FRICTION STIR PROCESSING: SIMULATION AND EXPERIMENTAL CHARACTERIZATIONS OF ALUMINIUM METAL MATRIX COMPOSITES

by

Adedotun Olanrewaju Adetunla

Student Number: 217094168

A thesis in fulfilment of the requirements for the degree

of

Doctor Philosophiae: Mechanical Engineering Science

Submitted to the

Faculty of Engineering and the Built Environment

University of Johannesburg

Johannesburg,

South Africa

June, 2019

Supervisor: Prof. Esther T. Akinlabi

DECLARATION

I, Adedotun Olanrewaju Adetunla, hereby declare that this thesis, which I herewith submit for the research qualification DOCTOR PHILOSOPHIAE IN MECHANICAL ENGINEERING to the University of Johannesburg, Department of Mechanical Engineering Science, is my own work; and it has not previously been submitted by me to any other institution.

DEDICATION

This work is dedicated to my lovely parents, Pastor and Barrister (Mrs) Samuel Omotayo Adetunla and my brother Gbenga Adetunla, I love and treasure them all so much.

ACKNOWLEDGEMENTS

I am grateful to many people who have contributed, in one way or another, to the achievement of this thesis.

First and above all, I want to thank the Almighty God, for His unconditional love. He made it possible for me to do all things through Jesus Christ, who strengthens me during hard times. I am sincerely grateful to Professor E. T. Akinlabi, my supervisor, for everything she has done to bring this research work to a happy conclusion. Her contribution to the achievement of this thesis is beyond calculation. I would like to appreciate the Global Excellence Scholarship (GES) from the University of Johannesburg for the financial assistance. I would like to express my appreciation to Prof. Satish Kailas at India Institute of Science in Bangalore, India for the support I received towards my experimental work.

I also appreciate the assistance of Dr. Kazeem Sanusi for his guidance at the early stage of this research work.

It remains for me to thank my parents, brother and his wife, and colleagues who have contributed financially, as well as morally, to the accomplishment of this task.

I think of:

- My parents, Pastor Samuel Omotayo Adetunla and Barrister (Mrs) Lucia Titilayo Adetunla for their financial support and for their endless love.
- My brother and his wife, Mr & Mrs Gbenga Adetunla
- My uncles and aunt, Mr Ayo Adetunla, Mr Yemi Ayejuyo and Mrs Adenike Okunrinmeta.
- Mr Michael Abegunde for his assistance during the experimental work
- My friends and all my colleagues from Modern and Advanced Manufacturing Systems (MAMS) research group for being there for me.

ABSTRACT

Aluminum (Al) and its alloys have been the prime materials of construction for many industries. The Al alloys are readily weldable and have excellent formability, good strength and excellent resistance to corrosion. While Al alloys are very strong and exhibit a high strength to weight ratio, they exhibit limited capabilities for wear and abrasion applications. The reinforcement of Aluminum and its alloys with various reinforcing powders has engineered a new type of material regarded as metal-matrix composites. The reinforcement of pure Al and its alloys with ceramic particles is expected to result in an improved mechanical property-to-weight ratio, as well as a superior resistance to wear, and to a high specific hardness. However, these composites suffer from a great loss in ductility and toughness due to the incorporation of non-deformable ceramic reinforcements as a result of inappropriate fabrication process and process parameters. The fabrication process used in this study is known as the friction stir processing technique.

Friction Stir Processing (FSP) has been established as a unique method to fabricate surface composites. FSP is a solid state processing method that has been employed to modify microstructures. The process was developed on the basis of the principle of Friction Stir Welding (FSW). A non-consumable and rotating tool, with a pin and shoulder, is inserted into the material and traversed along a chosen path. Due to the frictional heat produced, a severe plastic deformation takes place on the material, consequential in major microstructural modifications in the processed zone.

One major advantage of friction stir processing technique is that it enhances critical control of the processing parameters, which is necessary; in order to obtain an ideal solidified microstructure in

the surface layer, which also results in obtaining improved mechanical properties of the alloy. With improved mechanical properties, more potential application of FSP of Al and its alloys may be forthcoming.

Aluminium alloys, specifically the 1100 grade; which are commercially pure aluminium alloy, are used largely in the manufacturing industries. However, the alloy experiences wear and corrosion, while being used, which in turn causes reduction in the service life of this alloy. One of the most common causes of failure in aluminum alloy is wear, and with the aim to improve the wear resistance and other mechanical properties of this aluminum alloy, Ti-6Al-4V powders were incorporated to the surface of this alloy; and the fabrication was done via FSP. Titanium alloy (Ti6Al4V) Grade 5 have been regarded as the most useful alloys for the aerospace and automotive applications, due to their light weight and improved properties when compared to Aluminium and its alloys.

They have also been applicable for biomedical implants, due to their biocompatibility properties, and their ability to resist body, fluid attack, and to become predominantly attached to the tissues of the human body. The biocompatibility and mechanical properties can be greatly affected by the corrosion of the metal implants.

The current research project reinforced 1100 Al with Ti-6Al-4V powder, by using the friction stir processing technique (FSP). Different tool geometries namely square and threaded taper tool with varying number of passes from 1 to 3 passes, and a varying tool rotational speed of 600 and 1200 rpm) were employed. Limited research results exist on the fabrication of aluminum alloy with Ti-6Al-4V powder. However, the fabrication of these composite materials has the potential for many

applications in the industry. The fabricated samples were produced and characterized through optical microscopy and scanning electron microscopy for the microstructural evolution; while the chemical and phase identification were analyzed by using energy dispersive spectroscopy and X-ray diffraction, respectively.

Furthermore, tensile testing, microhardness profiling, heat input analysis, wear and corrosion performance tests were also conducted. These were done to investigate the relationship between the process parameters employed. The possibility of the formation of intermetallic compounds in the composite samples were analyzed by using the X-ray diffraction and energy dispersive spectroscopy. Additionally, microhardness measurements and tensile test were also conducted, in order to study the property of the composite samples, and to allow for a detailed evaluation of the quality of the composite samples.

The microstructure of the samples produced at different processing parameters was studied; and it was found that the Ti-6Al-4V particles were evenly distributed within the matrix, as the number of passes increase; while the samples produced at 1200 rpm for the two tool geometries employed exhibited improved particle distribution within the matrix. Good material mixing was achieved in all the composite samples fabricated with three number of passes. This further revealed the importance of multi-pass process, when fabricating Aluminum metal matrix composites.

The X-ray diffraction analyses using a 2 mm collimator revealed the intermetallics present in the composites. The intermetallics of Al_2Ti, Al_3Ti, $AlTi_3$ and TiAl, were found in the Stir Zone (SZ) of the three-pass samples produced with 1200 rpm for both tool geometries, while TiAl, Chromium

Carbide, Niobium Tungsten Carbide and Iron Carbide were found in the samples with lower rpm of 600 and with 1 to 2 FSP passes. On the other hand, in the HAZ, Al_2O_3 and Tungsten Carbide were found by using both tool geometries and varying revolution per minute. The increase in the tool-rotational speed contributes to the heat input associated with FSP; hence it causes severe plastic deformation, which affected the formation of the intermetallics and the properties of the base metal. However, the peaks of the intermetallics formed were low.

High failure loads of 5000 N and 4570 N were achieved when using a threaded taper and square tool geometry on all the 3-passes at 1200 rpm, respectively. It was observed that by increasing the number of passes, high strength composites were obtained. The composite sample fabricated via threaded taper tool on 3-passes also exhibited the highest ultimate tensile strength and yield stress. Furthermore, higher microhardness values were obtained in the stir zone for all the composites, which was as a result of the reinforcing particles. The particle distribution observed within the microstructure of the composites helps to improve the hardness values, which is in agreement with the Hall–Petch rule, which states that dynamic recrystallization results in reduced grain size which in turn results into increased hardness.

The samples with the highest hardness values were the 3-pass samples, also higher tool rotational speed helps to deform the material plastically, which in turn, helps to improve the hardness of the material.

A wear test and friction performance were carried out on the fabricated samples, to determine the composites with the best wear resistance and the wear mechanism encountered by the composites. The 1 to 2 passes composites showed higher friction during the test, with noticeable fluctuation across the test distance. However, all the 3-passes samples showed lower and stable friction coefficient. Furthermore, the mass losses were investigated after the wear tests; and it was revealed that the threaded-tool sample fabricated with 3-passes and 1200 rpm has the lowest loss of mass - even when tested with higher load of 50N. It was confirmed that the composites produced in this research are controlled by both adhesion and abrasion mechanisms.

Also, the corrosion behaviour of the composites was examined. Taffel extrapolation was used to calculate the current density and the corrosion potentials. The 3-pass samples with higher tool rotational speed showed good corrosion resistance; while the higher corrosion rates were seen with the 1 to 2 passes samples. These observations were attributed to the tendency of the composites with lower passes and lower tool rotational speeds to have particles clustering together on the grain boundaries. It can be said in this study that the addition of reinforcements to the base material improves the corrosion performance of the base material.

In conclusion, the heat generation due to friction during the process is simulated by using Finite Element Analysis Software i.e ABAQUS. The generated and distributed heat across the workpieces of 5 mm Aluminum composites was observed. Heat analysis and measurement during the process are carried out numerically and experimentally for validation. The simulated temperature history of FSP for the composites at different tool rotational speeds showed that the peak temperature increased when the tool rotational speed was increased - due to the increased strain rate and plastic dissipation in the stir zone.

A peak temperature of 423°C was observed with the 600 rpm processed sample; while a higher peak temperature of 471°C was observed with the 1200 rpm processed sample. The results of the simulation are in good agreement with those of the experimental results. The difference in the temperature during the processing between the experimental and simulated result is less than 15°C.

TABLE OF CONTENTS

DECLARATION ii

DEDICATION iii

ACKNOWLEDGEMENTS iv

ABSTRACT v

TABLE OF CONTENTS xi

ABBREVIATIONS xvii

LIST OF FIGURES xix

LIST OF TABLES xxv

LIST OF PUBLICATIONS xxvi

GLOSSARY OF TERMS xxviii

1 Introduction 1

- 1.1 Overview 1
- 1.2 Background 2
- 1.3 Justification of the study 7
- 1.4 Problem Statement 7
- 1.5 Aim and Objectives 8
  - 1.5.1 Aim 8
  - 1.5.2 Objectives 9

1.6 Hypothesis statement 10
1.7 Significance of the Research 10
1.8 Summary 10
1.9 Thesis Layout 11
2.0 LITERATURE REVIEW 15
2.1 Introduction 15
2.2 Aluminum and its alloys 16
2.3 1100 Al series 18
2.4 Processing Techniques 19
2.4.1 Metal Matrix Composites 20
2.4.2. Aluminium-matrix composites 22
2.4.3 Titanium alloys as reinforcing particles 25
2.5 Friction Stir Welding 26
2.5.1 Advantages and Limitations 27
2.5.2 Applications of FSW 29
2.6 Friction stir processing as a fabrication technique 30
2.6.1 Heat input during friction stir processing 32
2.6.2 Friction stir process parameters and tool design 34
2.6.3 Effect of number of passes on FSPed composites 38
2.6.4 Effect of tool rotational speed and transverse speed on composites 42

2.7 Typical Applications of FSP 46

2.8 Friction stir processing of aluminum matrix composites 48

2.8.1 Microstructural evolution and X-Ray Diffraction analyses 48

2.8.2 Hardness and Tensile properties of AMCs 55

2.8.3 Wear and Friction Performance of AMCs 59

2.8.4 Corrosion Behavior of AMCs 62

2.9 Finite Element Analysis (FEA) of the Heat Generated During FSP 65

2.10 Summary 69

3.0 METHODOLOGY 70

3.1 Introduction 70

3.2 Experimental set up 70

3.2.1 Parent material and reinforcing powder 70

3.2.3 Process parameters 73

3.2.4 Friction Stir Processing Procedure 76

3.3 Experimental techniques 77

3.3.1 Tensile Test 77

3.3.2 Microhardness Profiling 78

3.3.3 Sample Preparation for Microstructural Analysis 78

3.3.4 Optical Microscopy analysis 80

3.3.5 Scanning Electron Microscopy (SEM) coupled with Energy Dispersive Spectroscopy (EDS) 81
3.3.6 X-ray Diffraction (XRD) 82
3.3.7 Wear test analysis 83
3.3.8 Corrosion test analysis 86
3. 3.9 Prediction of the grain sizes within the Microstructure using Otsu Image Segmentation 88
3.4 Finite Element Simulation Using ABAQUS/CAE 90
3.4.1 Material Set up 90
3.4.2 Description of the Problem 91
3.4.3 Modelling Procedure 92
3.5 Summary 94
4.0 RESULTS AND DISCUSSIONS 95
4.1 Introduction 95
4.2 Parent Material and Powder Characterizations 95
4.3 Optical Microscope Analysis 99
4.4 Scanning Electron Microscope combined with the Energy Dispersive Spectroscopy (SEM/EDS) 102
4.5 Prediction of the grain sizes within the Microstructure using Image thresholding Technique 107
4.6 Effect of Process Parameters on the Output Response 113

4.7 A Torque-Based Predicted Heat-Input Analysis 115

4.8 Tensile test analysis 117

4.9 Microhardness Profiling 121

4.10 XRD Analysis of the Composites 124

4.11 Wear and Friction Behavior of the Fabricated Composites 128

4.12 Worn Surfaces of Fabricated Samples and Comparison Between the Reinforced and the Unreinforced Matrix 135

4.13 Corrosion Behavior 137

4.14 Heat Generation during FSP 144

4.14.1 Numerical Analysis of the Heat Generated 145

4.14.2 Finite Element Simulation Using ABAQUS/CAE 146

4.15 Summary 151

5.0 CONCLUSIONS AND RECOMMENDATIONS 153

5.1 Introduction 153

5.2 Conclusions 153

5.3 Recommendations for future work 157

REFERENCES 159

APPENDIX A 177

APPENDIX B 177

APPENDIX C 178

APPENDIX D 179

APPENDIX E 181

APPENDIX F 183

APPENDIX G 185

APPENDIX H 187

ABBREVIATIONS

AA	Aluminum Alloy
Al	Aluminum
AS	Advancing Side
ASTM	American Society for Testing and Materials
BM	Base material
BSE	Backscattered Electron
EDS	Energy-Dispersive X-ray Spectroscopy
FSW	Friction-Stir Welding
FSP	Friction-Stir processing
HAZ	Heat-affected zone
HV	Vicker's hardness
IISc	Indian Institute of Science
iCorr	Corrosion Density
kN	Kilo-Newton
mm/min	Millimeters per minute
MPa	Mega Pascal
OM	Optical Microscope
rpm	Revolutions per minute
RS	Retreating Side
Sec	Seconds
SEM	Scanning Electron Microscope
SZ	Stir zone

Ti	Titanium
TMAZ	Thermo-mechanically affected zone
WEDM	Wire Electrical Discharge Machining
XRD	X-Ray Diffraction
μ	Friction coefficient
ω	Tool angular rotation speed, rads-1
θ	Angle, deg
σ_{yield}	Yield stress, Pa
α	Alpha
β	Beta
µm	Micrometre
%	Percentage
<	Less than
(°)	Degrees

LIST OF FIGURES

Figure 1. Thesis layout 12

Figure 2. 1: Fan blades in airplane, (b) Gr/Mg airplane tubes made of MMC (Panwar & Chauhan, 2018) 21

Figure 2. 2 Car brake disc of Aluminum metal matrix composites, (b) Light metal diesel piston (Darras, Omar, & Khraisheh, 2007).. 23

Figure 2. 3 Example of FSW applications 30

Figure 2. 4 Friction stir processing set up (Hashemi & Hussain, 2015a) 31

Figure 2. 5 FSP tool design.. 32

Figure 2. 6 Showing the effect of tool on the force output (Koli et al., 2017) 34

Figure 2. 7 Various tool geometries used in the current study and their dimensions 35

Figure 2. 8 Schematic diagram and photographs of tool pin profiles (Vijayavel & Balasubramanian, 2017) 37

Figure 2. 9 Effect of tool pin profiles on the stir zone microstructure (Vijayavel & Balasubramanian, 2017) 38

Figure 2. 10 Multi-pass FSP sample with 25 percent overlapping: for low-magnification overview of transversal cross-section. And for micrograph presenting transition area between SZ and BM (El-Rayes & El-Danaf, 2012) 39

Figure 2. 11 Engineering stress-engineering strain curves of the samples studied, along with the obtained tensile properties (Luo et al., 2018) 40

Figure 2. 12 SEM images revealing the particle distribution within the matrix via (a) single-pass, b) two-passes, c) three-passes and d) four-passes composites (Rahsepar & Jarahimoghadam, 2016) 41

Figure 2. 13 Scanning electron microscope images of AZ31 Mg showing different regions, (a) BM; (b) HAZ; (c) Interface of TMAZ/SZ; (d) SZ in Mg side; (e) SZ in Al side; (f) Intercalated microstructure (Z. Zhang et al., 2017) 44

Figure 2. 14 Effect of the traverse and rotational speeds on the microhardness of SZ (Faraji & Asadi, 2011) 46

Figure 2. 15 Existing applications of FSP 48

Figure 2. 16 (a), (b) SEM images revealing dispersion of particles within the matrix at two different magnifications. (c) High magnification BSE image showing clean particle- matrix interface (Shyam Kumar et al., 2016) 50

Figure 2. 17 XRD pattern of the 5083 Al–W composite (Shyam Kumar et al., 2016) 51

Figure 2. 18 The X-ray diffraction patterns for samples after 1–6 passes (Anvari et al., 2013) .. 53

Figure 2. 19 SEM images showing the titanium particle dispersion through the Aluminum matrix (Khodabakhshi et al., 2018) 54

Figure 2. 20 Hardness values increased marginally from 70.4 for first pass to 74 for the 12th pass (Ramesh et al., 2012) 56

Figure 2. 21 Vickers hardness profiles (Tajiri et al., 2015) 58

Figure 2. 22 (a) Micro-hardness profiles of annealed Al–Mg alloy before and after FSP, and FSPed Al–Mg–Ti composite. (b) Engineering stress-strain curves display (Khodabakhshi et al., 2015) 59

Figure 2. 23 Average friction coefficient of matrix and composite samples (Anvari et al., 2013) 60

Figure 2. 24 Friction behavior of parent metal and 4-passes composite samples (Anvari et al., 2013) 61

Figure 2. 25 Effect of load on wear rate of composites for different speeds: 05, 07 and 09m/s (Anvari et al., 2013) 62

Figure 2. 26 Cyclic potentiodynamic polarization curves for 6061 Al and R-Mg in aerated 3.5% NaCl solution at room temperature (Gobara et al., 2015).......... 64

Figure 2. 27 Temperature evolution of a generic node lying in the advancing side 6mm from the welding line at the mid-thickness – 500 rpm and100 mm/min case study (Buffa et al., 2017).... 66

Figure 2. 28 Response of the heat- traversing source on the FS-welded materials (Chen et al., 2017) 67

Figure 2. 29 Variation of calculated and measured peak temperature with the tool pin eccentricity for FSPed (a) AA1050-H12, (b) AA5754-H24 at different welding speeds of 100, 300 and 500 mm/min (Ramadan et al., 2016) 68

Figure 3. 1 5-Axis friction stir-welding machine used for the friction stir processing of the composites.......... 72

Figure 3. 2 Schematic and Images of FSP tool used in this project: (A) Threaded taper tool geometry (B) Square tool geometry.......... 73

Figure 3. 3 Damaged sheet and tool fabricated with 3-passes rectangular tool geometry with 1200rpm and transverse speed of 20mm/min 74

Figure 3. 4 The FSP set up showing the backing plate, the tool holder, the tool, the aluminium plate, and the clamping system 76

Figure 3. 5 Aluminium sheet filled with Titanium powder 77

Figure 3. 6 Dimension of Tensile sample 78

Figure 3. 7 Hot-mounted samples.......... 79

Figure 3. 8 Optical Microscopy, University of Johannesburg ....**Error! Bookmark not defined.**

Figure 3. 9 SEM images..**Error! Bookmark not defined.**

Figure 3. 10 XRD machine 83

Figure 3. 11 The wear test set up 85

Figure 3. 12 The Profilometer... 86

Figure 3. 13 Cold Mounting of Sample for Corrosion test 87

Figure 3. 14 The corrosion test set up... 88

Figure 3. 15 Dimension of the 1100 Aluminum alloy as the base material................................ 90

Figure 3. 16 Dimension of the FSP tool 91

Figure 3. 17 Showing (a)Surface contact of the FSP tool and Aluminum composite plate(b) Graphical representation of FSP 92

Figure 4. 1 SEM micrographs of the 1100 Al, (a) Surface, (b) Cross Section 96

Figure 4. 2 EDS analysis of the 1100 Al alloy 96

Figure 4. 3 (a) SEM image of the Ti-6Al-4V powder (b) SEM image showing the average particle size of the Ti-6Al-4V powder... 98

Figure 4. 4 Crown appearance of the processed sample... 99

Figure 4. 5 Microstructure of the parent material (1100 Al) 99

Figure 4. 6 Optical micrographs of composites (a)A1, (b)X1, (c)B1, (d)Y1 (e)A3, and (f) X3 101

Figure 4. 7 Backscatter electron images of some composites samples using one and two passes (a) A1, (b) X1, (c) B2 and (d) Y2... 103

Figure 4. 8 SEM images of the three passes fabricated samples (a) X3 and (b) A3.................. 104

Figure 4. 9 SEM images of composites showing the grain structure (a) A3, (b) B2 and (c) A1 105

Figure 4. 10 EDS analysis of the 3-passes composites (A3) 107

Figure 4. 11 Original microscopic image (a) and segmented image (b) at one pass(X1)........... 110

Figure 4. 12 Original microscopic image (a) and segmented image (b) at two passes (B2) 111

Figure 4. 13 Original microscopic image (a) and segmented image (b) at three passes (B3) 112

Figure 4. 14 Force feedback of the downward force against time of B3 sample 114

Figure 4. 15 Force feedback of the downward force against time of Y3 sample 115

Figure 4. 16 Output parameters of temperature measured against Time for Samples B3 and Y3 composites.. 117

Figure 4. 17 (a) Photographs of the tensile specimens before the test (b) after the test 118

Figure 4. 18 Stress-strain graph of the samples fabricated with the threaded taper tool geometry 119

Figure 4. 19 Stress-strain graph of the samples fabricated with the square tool geometry 119

Figure 4. 20 Showing the effect of process parameters and tool geometry on the maximum failure load of the composites 121

Figure 4. 21 Microhardness values of the composite samples produced with various process paramters (i.e tool rotational speed, number of passes and tool geometries) 122

Figure 4. 22 Mean hardness values of some composites 123

Figure 4. 23 Average Hardness Values of Specimen 124

Figure 4. 24 XRD pattern of 1100 Al Alloy 125

Figure 4. 25 XRD pattern of Ti-6Al-4V particles... 125

Figure 4. 26 XRD pattern of the Al/Ti-6Al-4V composites (Y3).. 126

Figure 4. 27 XRD pattern of the Al/Ti-6Al-4V composites (B3).. 127

Figure 4. 28 Friction behaviour of 1100 Al alloy and various composite samples (All the samples were tested under a normal load of 20N) (a) 1100 Al, (b) B1), (c) Y2, (d) Y3 and (e) B3........ 130

Figure 4. 29 Average coefficient of friction of 1100 Al and composite samples (All the samples were tested under normal load of 20N 131

Figure 4. 30 Wear-volume losses calculation of the B3 sample using SEM 132

Figure 4. 31 Average mass loss of all samples during wear test at 20N 133

Figure 4. 32 Mass loss of composites during wear test at further testing of 50 N 134

Figure 4. 33 SEM images of the worn surfaces of 1100 Al, 1-pass composite (B1) and 3-passes composite (B3) 135

Figure 4. 34 Analysis of the worn surface of B3 sample via EDS 136

Figure 4. 35 Potentiodynamic polarization curves of some samples (a) A1, (b) B1, (c) B2, (d) X2, (e) B3 and (f) Y3 139

Figure 4. 36 SEM images revealing the corroded surfaces after the potentiostatic polarization test (a) A1, (b) X2, (c)B3 and (d) X3 142

Figure 4. 37 Composition in the intergranular and transgranular regions at a corrosion site of the B3 composite 144

Figure 4. 38 Temperature distributions obtained by ABAQUS on the Aluminum composite for ω=600 rev/min and v= 30mm/min 149

Figure 4. 39 Temperature distributions obtained by ABAQUS on the Aluminum composite for ω=1200 rev/min and v= 30mm/min 149

Figure 4. 40 Temperature profiles of simulated and experimented values at 600rpm (constant transverse speed of 30 mm/min) 150

Figure 4. 41 Temperature profiles of simulated and experimented values at 1200 rpm (constant transverse speed of 30 mm/min) 151

LIST OF TABLES

Table 2. 1 Various aluminum alloys and their strength 18

Table 2. 2 Mechanical Properties of 1100 Al 19

Table 2. 3 Some applications of AMCs in Automotive industry 24

Table 2. 4 Benefits of FSW 27

Table 2. 5 Tensile properties (Tajiri et al., 2015) 57

Table 3. 1 Chemical composition of the 1100 Aluminum Alloy 71

Table 3. 2 Chemical composition of the Ti-6A-4V particles 71

Table 3. 3 Design of Experiment 75

Table 4. 1 Chemical composition of the 1100 Al Alloy 97

Table 4. 2 Chemical Composition of Ti-6Al-4V 98

Table 4. 3 Design of Experiment 110

Table 4. 4 Average heat input prediction during the fabrication of the composites 116

Table 4. 5 Tensile properties of the composites and the 1100Al alloy 120

Table 4. 6 List of Intermetallic compounds found at the stir zone of all fabricated samples 127

Table 4. 7 Wear behaviour of the parent material, unreinforced and reinforced 1100 Al 137

Table 4. 8 Rate of corrosion of fabricated composites 141

Table 4. 9 Simulation Parameters used for the Fabricated Aluminum composites 148

LIST OF PUBLICATIONS

1. Adedotun Adetunla and Esther Akinlabi "**Mechanical characterization of Al/Ti-6Al-4V surface composite fabricated via FSP: a comparison of tool geometry and number of passes**". Materials *Research Express* (2018) Volume 5 issue 11, ISSN: 2053-1591
2. Adedotun Adetunla and Esther Akinlabi "**Influence of reinforcements in friction stir processed magnesium alloys: insight in medical applications**". *Materials Research Express* (2018) Volume 6 issue 2, ISSN: 2053-1591
3. Adedotun Adetunla and Esther Akinlabi "**Fabrication of Aluminum Matrix Composites for Automotive Industry via Multipass Friction Stir Processing Technique**". *International Journal of Automotive Technology* (2019) Volume 2 Issue 1, ISSN: 1229-9138
4. Adedotun Adetunla and Esther Akinlabi "**Significantly Improved Mechanical Properties Of AZ31 Mg Alloy via Particle Reinforcement**". Submitted to *Materiali in Tehnologije* (2019). ISSN 1580-2949. ***(Accepted for publication)***
5. Adedotun Adetunla, Esther Akinlabi, and Adeyinka Adebayo "**Experimental and Numerical Analysis of Friction Stir Processed 1100 Aluminum Alloy: effect of process parameters".** *Materials Characterization* (2019) ISSN 1044-5803. ***(Accepted for publication)***
6. Adedotun Adetunla and Esther Akinlabi "**Analysis of Fabricated Al Metal Matrix Composites Reinforced with Ti-62222 via Multi Pass Friction Stir Processing**". *International Academy of Science, Technology, Engineering and Management, Norway (Dec,2018)*

7. Adedotun Adetunla and Esther Akinlabi “**Effect of Reinforcement on Mechanical properties of Aluminum alloy**”. *International Academy of Science, Technology, Engineering and Management, Norway (Dec,2018).*
8. Adedotun Adetunla and Esther Akinlabi “**Improving the Mechanical Properties of Aluminum alloy for automotive Industries**". *9th International Conference on Key Engineering Materials, Oxford, United Kingdom 2019***.** ISSN: 1662-9795 **. *(Accepted for publication)***
9. Adedotun Adetunla and Esther Akinlabi, **“Investigating the mechanical integrity of reinforced 1100 Aluminium Alloy via Particle Reinforcement”.** *5th International Conference on Innovation in Science and Technology, December 2018, Spain*. ISBN: 978-609-8239-25-6
10. Adedotun Adetunla and Esther Akinlabi. “**Corrosion Performance of Reinforced Magnesium Alloy: Insight in Automotive Industry**”. *International Conference of Nanotechnology and Smart Materials, Design Artificial Intelligence, Manufacturing and Engineering. September 2019, Singapore*.

GLOSSARY OF TERMS

A

Alloy – A substance having metallic properties and being composed of two or more chemical elements, of which at least one is a metal.

Alloying element – The alloying element is an element added to and remaining in the metal, which changes its structure and properties.

Agglomeration of particles – This is the clustering of particles in a particle region

B

Backing plate – A layer of material that is placed below the joint interfaces of the materials to be welded. It provides a surface to oppose the vertical downward force on the material; and it protects the machine bed.

Bending stress – If a beam is subjected to a bending moment, the fibres in the upper part are extended; and those in the lower part are compressed. Tensile and compressive stresses are thereby induced, which vary from zero at the neutral axis of the beam, to a maximum at the outer fibres. These stresses are called bending stresses.

Breaking load – the load at which fracture occurs.

Brittle fracture – rapid fracture preceded by little or no plastic deformation.

Brittleness – the tendency of a material to fracture without first undergoing significant plastic deformation.

C

Clamping System – Is the device used to hold, locate and prevent the workpiece from moving during the large forces involved in the FSW process. Coalescence –the merging of two or more materials (metals) into one.

Coefficient of friction – This is a value that shows the relationship between the force of friction between two objects and the normal reaction between the objects that are involved.

Composite –A is a material made from two or more constituent materials with significantly different physical or chemical properties, that when combined, produce a material with characteristics different from the individual components

Corrosion - is the gradual destruction of materials (usually metals) by chemical and/or electrochemical reaction with their environment.

Corrosion rate - rate of corrosion is the speed at which any given metal deteriorates in a specific environment

Corrosive substance- This is one that will damage or destroy other substances with which it comes into contact - by means of a chemical reaction

D

Defect - A discontinuity or discontinuities that accumulate to render a weld or part thereof unable to meet the minimum acceptance standards or criteria of the design specifications.

Deformation – Is a change in the form of a body due to stress, heat, or other causes.

Degrees of Freedom – The number of available independent comparisons that are needed to estimate a parameter.

Diffraction – The scattering of electrons by any crystalline material, through discrete angles, and it depends only on the lattice spacing of the material and the velocity of the electrons.

Ductility – The ability of a material to deform plastically before fracture. Design Model –This is the model designed for the experiment to estimate when the design was first created.

Design space – It is an imaginary area bounded by the extremes of the tested factors.

Dwell time – The period of time after the rotating tool has been plunged into the work, and for which it remains stationary, generating frictional heat and plasticizing the materials, before commencing the traverse along the joint (seconds)

E

Electrical discharge machining (EDM)– This is a manufacturing process whereby a desired shape is obtained using electrical discharges (sparks).

Elastic region – a material is said to be stressed within the elastic region, when the working stress does not exceed the elastic limit.

Elastic deformation – This is the deformation of the material that is recovered when force is applied to it.

Elastic limit – This is the greatest stress, which a material is capable of sustaining without any permanent strain remaining upon complete release of the stress.

Elongation – the increase in gauge length of a body subjected to a tension force, referenced to a gauge length of a body. Usually expressed as a percentage of the original gauge length.

Elongation (%) – the total percentage increase in the gauge length of a specimen after a tensile test.

Engineering strain – this is a dimensionless value that is the change in length (ΔL) per unit length of the original linear dimension (L_o) along the loading axis of the specimen; that is $e = \Delta L$, L_o the amount that a material deforms per unit length in a tensile test.

Equilibrium – A state of dynamic balance between the opposing actions, reactions, or velocities of a reversible process.

Etchant – A chemical solution used to etch a metal to reveal the structural details.

Etching – Subjecting the surface of a metal to preferential chemical or electrolytic attack to reveal the structural details for metallographic subsequent examination.

Extrusion – The process whereby a material is shaped by force or squeezed through a die or nozzle.

F

Friction – The force required to cause one body in contact with another to begin to move.

Friction Stir Welding (FSW) – This is a process developed at The Welding Institute (TWI) that utilizes local friction heating to produce continuous solid-state seams. It allows butt and lap joints to be made, without the use of filler metals. The solid-state low distortion welds produced are achieved with relatively low costs, using simple and energy-efficient mechanical equipment.

Friction Stir Processing (FSP) - This process has same working principle as FSW, the rotational tool is plunged into the workpiece to deform the material plastically, which in turn, may lead to improved mechanical properties

G

Grain – An individual crystallite in metals.

Grain growth – This is a phenomenon, which occurs when the temperature of a metal is raised; the grains begin to grow and their size may eventually exceed the original grain size.

Grain size – A measure of the areas or volumes of grains in a polycrystalline metal or alloy, usually expressed as an average when the individual sizes are fairly uniform. Grain size is reported in terms of the number of grains per unit area or volume, the average diameter, or as a number derived from the area measurements.

Grain boundary – An interface separating two grains, whereby the orientation of the lattice changes from that of one grain to that of the other. When the orientation change is very small, the boundary is sometimes referred to as a sub-boundary structure.

Grinding – Removing material from the surface of a work piece by using a grinding wheel or abrasive grinding papers.

H

Hardness – This is a term used for describing the resistance of a material to plastic deformation.

Hardness test – This measures the resistance of a material to penetration by a sharp object.

Hardening – Increasing the hardness by means of a suitable treatment.

Heat-Affected Zone (HAZ) – The portion of the base metal which has not been melted, but whose mechanical properties have been altered by the heat of welding or cutting.

Homogeneous – The chemical composition and the physical state of any physical small portion, and one, which is the same as that of any other portion.

Hot working – A deformation under conditions that result in recrystallization.

I

Indentation hardness – This is the hardness, as evaluated from the measurements of an area of an indentation, made by pressing a specified indenter into the surface of a material under specified static loading conditions.

Intensity (X-rays) – The energy per unit time of a beam per unit area, which is perpendicular to the direction of propagation.

Interfacial region – A weld joint boundary of the workpieces indicating the positions of the pin and shoulder diameters during the welding process.

Intermetallic compounds – These are any solid materials, composed of two or more metal atoms in a definite proportion, which have a definite structure, which differ from those of its constituent metals.

M

Macrograph – A graphic reproduction of a prepared surface of a specimen at a magnification not exceeding 25x.

Macrostructure – The structure of metals, as revealed by macroscopic examination of the etched surface of a polished specimen.

Magnification – The ratio between the length of a line in the image plane to the length of a line on the imaged material.

Mass loss – It is a property of a physical body and a measure of its resistance to acceleration when a net force is applied.

Matrix – It refers to a fine-grained material in which larger objects are embedded.

Mechanical properties – These are the properties of a material that reveal its elastic or inelastic behaviour, when a force is applied, indicating the suitable mechanical applications.

Microstructure – The structure of a prepared surface of a metal, as revealed by a microscope at a particular magnification.

Model – The model is the empirical mathematical model that is fitted to the data

O

Oxidation – the addition of Oxygen to a compound.

P

Parameter – The minimum and maximum parameters that would describe the operating range of a variable.

Parent material – This is the sheet-metal plate in its ‘as manufactured form’, as supplied.

Particles/Powder – This is a dry, bulk solid composed of a large number of very fine particles that may flow freely when shaken or tilted. In particular, powders refer to those granular materials that have the finer grain sizes, and that therefore have a greater tendency to form clumps when flowing.

Plastic deformation – this is the distortion of material continuously and permanently in any direction. The deformation that remains or would remain permanent after the release of the stress that caused it.

Polished surface – This is a surface that reflects a large proportion of the incident light in a peculiar manner.

Position control – This is a mode in FSP, in which the machine automatically adjusts the forces acting during the process.

Plunge depth – This is the maximum depth that the tool shoulder penetrates into the processed sheets.

Plunge force – During the plunging stage of the tool pin in FSP, the vertical force in the direction of the Z-axis movement is normally referred to as the plunging force.

Predicted Value – This is the value of the response predicted by the mathematical model

R

Recrystallisation – This is a change from one crystal structure to another, such as that occurring upon heating and/or cooling through a critical temperature.

Residual stress – This is the stress in a body, which is at rest, in equilibrium, and at a uniform temperature in the absence of any external force.

Retreating side – The retreating side of the tool is where the local direction of the weld surface, due to tool rotation and the direction of the traverse, are in the opposite direction.

Rotational speed – The tool rotation speed is the rate of angular rotation (usually specified in rpm) of the tool around its rotational axis.

S

Scanning-Electron Microscope – An electron microscope, in which the image is formed by a beam operating simultaneously with an electron probe scanning the object.

Solid-phase – A physically homogeneous and distinct portion of a material system in the solid state.

Solution - A liquid mixture in which the minor component (the solute) is uniformly distributed within the major component (the solvent)

Specimen – This refers to the sample of something

Spindle speed – This is also referred to as the rotational speed; and it is the speed of the work holding device (chuck), measured in revolutions per minute.

Spindle torque – This is the spindle torque required to rotate the FSW tool, when plunging it into and traversing through the work piece along the joint (Nm).

Stir zone – This refers to the recrystallized central area of the processed interface

Stress – This is the load applied to a piece of material; and it tends to cause deformation, which is resisted by the internal forces set up within the materials, which are referred to as stresses. The intensity of the stress is estimated as the force acting on the unit area of the cross-section, namely: as Newtons per square metre, or as Pascals.

T

Tensile strength – This is the maximum tensile stress, which a material is capable of sustaining. Tensile strength is calculated from the maximum load during a tension test carried out to rupture, and from the original cross-sectional area of the specimen.

Tensile test – This measure the response of a material to a slowly applied axial force. The yield strength, tensile strength, modulus of elasticity and ductility are thereby obtained.

Tool displacement – This refers to the offset of the tool at a certain distance from the weld centre line.

Tool shoulder – This refers to that part of the welding tool, which rotates, and is normally disk shaped.

Tool pin – This refers to that part of the tool that rotates in contact with the surface of the work piece.

Tool plunge – This is the process of forcing the tool into the material at the start of the weld.

Tool tilt angle – The angle, at which the FSW tool is positioned relative to the work piece surface; that is, when zero tilt tools are positioned perpendicular to the work piece surface (degrees).

Traverse speed – This is also referred to as the feed rate; it is the speed at which the rotating FSW tool is translated along the joint line (mm/min).

Tunnel hole – This is a defect in the microstructure of a material caused by lack of plastic deformation

V

Vickers hardness number – This is a number related to the applied load and the surface area of the permanent impression made by a square-based pyramid diamond indenter.

Void – This is the space that exists between the particles or grains. Normally, in welding, voids are associated with defects

U

Unaffected material – This refers to the bulk of material, which is not affected by either heat or deformation, during the welding process.

Uneven distribution – This refers to particles that are not properly dispersed within the matrix

W

Wear – It is the damaging, gradual removal or deformation of material at solid surfaces caused from continuous use

Wear rate – It is the volume loss per unit distance and its unit is (m3/m)

Wear resistance – Loss of material from a surface by means of some mechanical action

Welding – This is the process of joining, in which the materials are enabled to form metallurgical bonds under the combined action of heat and pressure.

Work piece – The component to be welded.

Worm holes – This refers to a defect in a FS processed specimen, usually on the advancing side of the rotating tool, due to the lack of mixing and re-bonding of the plasticized material

Y

Yield stress – This is the material property defined as the stress at which a material begins to deform plastically whereas; it is the amount of stress that an object needs to experience for it to be permanently deformed.

CHAPTER ONE

1 Introduction

1.1 Overview

Aluminium and its alloys have been utilized in numerous industries as an essential material of construction. The Al alloys have good corrosion resistance, easily weldable, and have excellent formability (Davis, 2001). Al alloys possess excellent strength to weight ratio, however, they are not hard enough for wear and abrasion. The addition of ceramic particles to Al alloys which serves as reinforcement can improve the mechanical property such as hardness, strength and wear resistance. However, these composites suffer from a great loss in ductility and toughness due to the incorporation of non-deformable ceramic reinforcements as a result of inappropriate fabrication technique. Numerous ceramic particles such as Al_2O_3, SiO_2, SiC, C, B_4C, AlN, TiC, BN and $ZiSiO_4$ have been used to reinforce Al metal matrix composites (Tajiri et al., 2015; Narayana Yuvaraj, Aravindan, & Vipin, 2015).

The Ti-6Al-4V alloyed with Aluminium, Molybdenum, Chromium and Silicon is the most broadly used titanium alloy (B. S. Li, Shang, Guo, & Fu, 2004). This titanium alloy (Ti6Al4V) Grade 5, an $\alpha + \beta$ alloy, has been produced for aerospace applications to enhance the better mechanical properties of titanium, while keeping intact its resistance to corrosion behaviour (Crist, 2012). The Ti-6Al-4V is an alloy which has been produced for higher toughness, this alloy is majorly used as implants due to its biocompatibility property and also its ability to overcome body fluid attacks (Alpas & Inagaki, 2000). This alloy has also been used in industries such as: the marine, power generation, automotive, chemical, sport etc. Fabricating Al alloy with this powder might improve the mechanical properties of the alloy. Reinforcement of aluminum alloys with various ceramic particulates has engineered a new family of materials that are marketed under the trade name of metal matrix composites.

Friction stir processing (FSP) is one of the techniques used to fabricate these composites, since it enhances critical control of the processing parameters, which is necessary, in order to obtain an ideal solidified microstructure in surface layer. As a result of the controlled process parameters, the processing of surface composite is carried out at temperatures below melting point of the substrate. FSP is a reliable way to fabricate metal-matrix composites; as it overcomes the drawbacks experienced by the traditional methods such as stir casting, powder metallurgy etc. FSP is considered to be the most significant method to fabricate metal-matrix composites, and it has been successfully used to produce metal composites of aluminum, titanium and other alloys**.**

1.2 Background

Friction Stir Processing (FSP) utilizes similar working principle as Friction Stir Welding (FSW) which was an invention of The Welding Institute (TWI) in the year 1991 (Salih, Ou, Sun, & Mccartney, 2015). A rotating tool, which is non-consumable with a tool shoulder and a pin probe; is inserted into the workpiece, and travel along the processed part. Due to interfacial friction between the rotating tool and the workpiece, heat is generated. The tool shoulder and pin probe produce heat, which allows the material to be soften under its melting point.

In FSP, the rotating tool pin has a different design according to types of processed base metal and other processing parameters. As the rotating tool travels along the workpiece, the material flows around the tool is forged under the tool shoulder, and this causes new structural and mechanical conditions (Arab, Karimi, Jahromi, Javadpour, & Zebarjad, 2015; R. S. Mishra, Ma, & Charit, 2003).

In the recent years, Metal Matrix Composites (MMCs) are used to replace conventional materials for practical engineering applications, such as those in the aerospace, transportation, defense and sports industries due to their superior properties in hardness, tensile, wear and corrosion behavior(Kangazian & Shamanian, 2019). MMCs have attracted considerable attention for critical applications in industrial sectors, such as spacecraft structures, deck panels and the automotive and railway brake discs. The global demand for MMCs has increased from about 5496 tons to nearly 8000 tons in the period from 2012 to 2019. Light metals like aluminum, magnesium and titanium alloys are considered as ideal base matrices to produce MMCs reinforced by carbide, nitride, boride and oxide in the form of particles, whiskers and fibres.

Advanced materials like aluminum matrix composites (AMCs) have attracted considerable attention, due to their appealing mechanical properties, and their clear potential for aerospace applications. They are viewed as a new generation of light-weight and high-strength materials. In addition, AMCs have found a wide range of applications in the military sector, such as armour, due to the combined static strength and the high ballistic performance. Among the grades of aluminum used is the commercially available 1100 Al alloy. The 1100 Al has excellent welding characteristics; it is soft and ductile, so it’s ideal for applications that require intricate forming. as it work-hardens slower than other Al alloys.

The 1100 Al grade is however non-heat treatable, but it has excellent resistance to corrosion. It is the most heavily alloyed of the 1000 series. It is also the mechanically strongest alloy in the series;

and is the only 1000-series alloy that is commonly used in rivets. At the same time, it has the benefits of being relatively, lightly alloyed.

Many researchers have investigated reinforcing metal alloys with ceramic particles via FSP. Process parameters, such as tool geometry, tool speed and number of passes, are factors that play significant roles in successfully fabricating these metal matrix composites. Multi-pass, with 100% overlap was carried out using in situ fabricated Cu/SiC composite via FSP by Barmouz et al 2011 (Barmouz, Asadi, Besharati Givi, & Taherishargh, 2011). They reported that the hardness results of 1Pass, 4Pass and 8Pass increased about 30%, 50% and 58% with respect to the base metal. Mishra et al 2018 (M. K. Mishra, Rao, Balasundar, Kashyap, & Prabhu, 2018) investigated the evolution of the microstructure of 6068 aluminum alloy by varying the traverse speed (from 50 to 150 mm/min) during FSP; and they reported continuous refinement of the grain size with increasing traverse speed and concurrent improvement in the corrosion resistance of Stir Zone(SZ). The Influence of tool rotational speed, tool traverse speed, the number of passes, shift of rotational direction between the passes and the particle size was studied on the distribution of SiC particles in the 5052 aluminum SiC metal matrix composites by Dhayalan et al 2014 (Dhayalan, Kalaiselvan, & Sathiskumar, 2014). The results proved that a change of the tool-rotational direction between FSP passes, increase with number of passes; and a decrease of SiC particles size enhances the hardness and the wear properties.

Charit and Mishra investigated the effect of multi-pass FSP on the superplasticity of 7075 Al rolled plate, by using mini-tensile specimens cut from the center of each stir zone on the staggered pass samples (Charit & Mishra, 2017). The result showed good superplastic ductility in each stir zone of the multi-pass FSP 7075 Al samples. The study also indicated that overlapping the FSP passes is a feasible method to create a large, fine-grained aluminum alloy plate. Sunil et al studied the effect of multipass FSP on the microstructure and tensile properties of a cast aluminum-silicon alloy A356 (Sunil et al., 2017).

Their work reported that in the multi-pass processed material, the strength of the previously processed zones was lower than that of the subsequent processed zones, because of an over-ageing of the thermal cycles.

Ramesh et al (Ramesh, Pradeep, & Pancholi, 2012) reported an improvement in the mechanical properties of an aluminum die casting alloy subjected to 14 pass FSP. The average tensile strength in the parallel direction was higher than in the perpendicular direction.

Yuvaraj et al (Narayana Yuvaraj et al., 2015) studied the wear and hardness properties of A390/graphite and A390/Al_2O_3 composites by changing the rotational to traverse speed ratio. They observed that homogenous distribution of reinforcement and higher hardness were evident as the rotational speed increases, while lower damages as a result of wear were observed and traverse speed has lesser effect on the properties of the composites when compared to the effect of tool rotational speed on the mechanical properties.

FSP was also used to fabricate AA6082/TiC surface composite, this was done to study the effect of TiC particles on the microstructure, wear and other mechanical properties by Thangarasu et al (A. Thangarasu, Murugan, & Dinaharan, 2014). They found out that the reinforcing particles have great significance on the micro-hardness, grain size of the matrix, UTS and the wear performance of the AA6082/TiC composites. The fabrication process employed could disperse the particles homogenously within the matrix regardless of the volume fraction of the TiC particles. However, the Ultimate Tensile Strength (UTS) and microhardness increased when the volume fraction was increased. Furthermore, formation of voids was reduced, wear rate reduced and an increase in the stiffness of the matrix were observed with the addition of the TiC particles.

Several advances have been made by using friction stir processing (FSP) to fabricate metal matrix composites by considering various process parameters. The 1100 Aluminium has excellent resistance to corrosion. It is the mechanically strongest and the most heavily alloyed of the 1000 series. It is also the only 1000-series alloy commonly used in rivets. The 1100 Al alloys are highly resistant to chemical attack and weathering; they also have low cost, they are ductile for deep drawing, and easy to weld. They are also used for high-purity applications, such as chemical-processing equipment, fan blades in aircrafts, flue lining, sheet metal work, and fin stock. While the Ti-6Al-4V is an alloy, which have been produced for higher toughness; and because of its biocompatibility, the alloy is largely used as implants, because it can overcome attacks from the fluid in the body; while being attached to the tissues found in human body (Alpas & Inagaki, 2000). This alloy has also been used in industries such as: the marine, power generation, automotive, chemical, sport etc. Furthermore, the front fan blade of turbo-fan engines is usually manufactured from titanium alloys. To be more precise, the front fan blades are most commonly manufactured from Ti-6Al-4V alloy, which is considered as a workhorse among all other grades of titanium alloy because of its properties.

Furthermore, it is obvious that several advances have been made in the fabrication of metal matrix composites; however, it has to be well understood that the study on this topic is far from being exhausted; and it is still in the feasibility phase. In conclusion, from the discovery of FSP up to the present, the systematic investigation of the fabrication of 1100 Aluminum alloy with Ti-6Al-4V powder has not yet been reported. An FSP composite specimen is affected by the distribution of the reinforcing particles within the matrix, and this distribution is dependent on the tool geometry, the tool speed and number of FSP passes employed. Hence, the aim of this research is to find out the best combination of the processing parameters that produces excellent corrosion resistance, good resistance to wear and superior mechanical properties.

In other words, the deeper fundamental understanding of the different properties of the fabricated composites would extend the applicability of 1100 Al in various industries, such as that of the aerospace, medical and manufacturing industries

1.3 Justification of the study

Friction stir processing has advantages when compared to the conventional techniques. Limitations, such as liquation cracking, solidification cracking and porosity can be eliminated by employing FSP since it’s a solid-state process (R. S. Mishra et al., 2003). Friction stir processing display the presence of deformations and microstructural differences in the processed zone, including the nugget zone (NZ), the thermo-mechanically affected zone (TMAZ) and the heat-affected zone (HAZ). The two base materials used in this research have peculiar characteristics, and new alloys may be fabricated from these materials. Moreover, in order to extend the use of FSP as a technique in fabricating metal matrix composites, this project focuses on generating data on the characterization of FSP of the 110Al and Ti-6Al-4V powder by using different tool geometries and process parameters. The experimental results will be characterized, analyzed and compared with those of the computed/numerical method

1.4 Problem Statement

Metal matrix composites suffer from poor wear resistance, lower hardness and tensile strength as a result of uneven distribution of particles within the matrix leading to an inhomogeneous structure. Since wear and corrosion are the most common cause of failure in Al alloys, improvement of these properties can be done by choosing an appropriate surface modification technique that will ensure even distribution of reinforcing particles across the matrix. While traditional modification methods present inadequate level of control over the distribution of reinforcing particles within the matrix, FSP can be used as a suitable method to ensure microstructural refinement and even distribution of particles across the surface of the base material(Yaw, Cho, Das, Lee, & Hong, 2019). However, a single pass FSP with a pin diameter of 6mm may produce a processed zone 6 to 8 mm wide and a depth depending on the length of the tool pin. Such a narrow-processed zone is not suitable for practical engineering applications.

The extension of FSP to multi-pass FSP addresses this issue, whereby the overlapping of passes can be used to produce bulk-processed material. Also, process parameters such as tool speed and tool geometries play significant roles in fabricating MMCs, a need for appropriate combination of these process parameters offering good mechanical properties of fabricated composites is essential, which will provide a good insight into the possible applications of the fabricated composites.

1.5 Aim and Objectives

1.5.1 Aim

The aim of this research work is to successfully fabricate 1100 Aluminum alloy and Ti-6Al-4V particles using multi-pass Friction Stir Processing. The effect of process parameters, such as tool rotational speed, tool geometries and number of passes will be investigated; and the fabricated samples will be characterized through metallurgical evaluation, mechanical testing and chemical means. The focus will be to present a set of process parameters offering good mechanical properties during service conditions.

1.5.2 Objectives

The objectives of this study are highlighted as follows:

- To characterize properties of the fabricated samples (i.e. thermal, mechanical, metallurgical and chemical properties).
- To study the effect of the process parameters and tool geometry on the wear and corrosion performance of the samples.
- To study and report the formation of intermetallic compounds as a result of the process parameters and the reinforcing particles used, and the impact of these intermetallic on the mechanical properties of the composites.
- To investigate the effect of number of passes on the reinforced samples and their feasible applications
- To investigate the heat generated due to friction during FSP using Finite Element Analysis (FEA)
- To analyze the particle distribution within the microstructure of the fabricated samples using MATLAB

1.6 Hypothesis statement

The mechanical behaviour of the fabricated samples is expected to be determined through mechanical testing and fracture mechanics analysis. The particle distribution and the tensile behavior of the samples will be analyzed with MATLAB. The heat generated due to friction will be examined using ABAQUS, and the computed results is expected to correlate with the experimental results to ascertain the efficiency of the new alloys produced. The produced samples should be suitable for typical surface engineering applications.

1.7 Significance of the Research

Within the university, this project will add value in the research field of metal matrix composites; since it is to the best of our knowledge, it is the first project on multi-pass friction stir processing of 1100 Al plates with Ti-6Al-4V powder as reinforcing particles. In the industries, with the fabrication of these composites; new alloys will be formed, and this will extend the potential applications of 1100 Al in biomedical implants, as well as the aerospace and the manufacturing sectors. Finite element modeling of the effect of tool rotational speed on the peak temperature of the composites is also investigated and reported in this research project.

1.8 Summary

The reinforcement of aluminum alloys with ceramic particulates has engineered a new family of materials that are marketed under the trade name of Al matrix composites; and to successfully reinforce metals with ceramic particulates, appropriate process parameters have to be used. This thesis focuses on using multi-pass friction stir processing method to fabricate 1100 Al alloy with

Ti-6Al-4V powder based on an experimental investigation and advanced computational modeling. A crucial aspect of the research is to compare and analyze the results that were obtained.

1.9 Thesis Layout

This thesis layout is schematically represented by a flow-diagram, as shown in Figure 1.1. The flow-diagram shows the sequential arrangement of the thesis in a logical order. The fabricated samples were characterized for microstructure analysis, mechanical testing, electrochemical testing and finite element analysis.

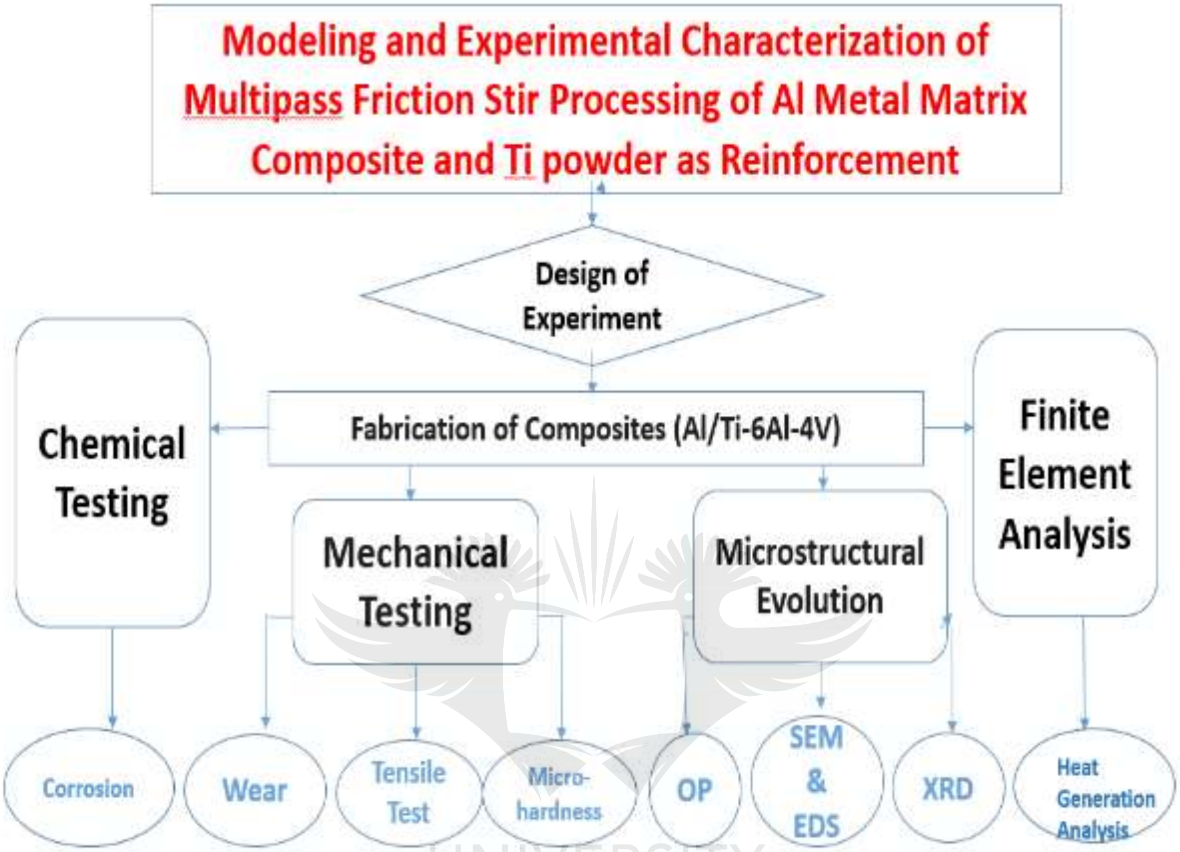

Figure 1.1: Thesis layout

The structural arrangements of this thesis are accomplished with five chapters; and each chapter has been linked with the others, in order to provide an insight into the complete and unabridged thesis.

Chapter One comprises the introduction, which is the main section in this chapter. The subsection includes the overview, background to the study, justification of study, a statement of the problem, as well as the aim, the objectives, the hypothesis statement, and the significant of research, summary, a summary, and the structural arrangement of the thesis.

Chapter Two covers the studies that have been conducted by different authors and researchers with respect to metal-matrix composites and the FSP technique used to fabricate various alloys. The literature survey investigated other conventional methods used to fabricate metals, the importance of aluminum and titanium alloys, the application of titanium and aluminum alloys; the design of experiment, in addition to the types and applications. This chapter ends with a summary of all the literature surveys.

Chapter Three runs through the approach in the fabricating and characterizing of the samples; the design methodology and the experimental set-up; the metallurgical preparation and characterization of the composites, such as the OM, SEM, microhardness, tribological dry testing, electrochemical corrosion test, FEA analysis of the fabricated samples, XRD and the design of the experiment – in order to obtain the desired parameters. This chapter ends with a summary of the material characterization; design and experimental set-up and testing thereof.

Chapter Four presents the results, and a discussion of the characterizations conducted on the fabricated composites. This includes an analysis of the results and variance, as well as the mechanical testing, in addition to the electrochemical testing and the microstructural evolution of composites. The results from the tests and analyses conducted on the microhardness, microstructures, dry sliding wear, tensile, corrosion and XRD analysis are clearly presented.

Chapter Five focuses on the main points in the conclusions of the research work, alongside the recommendations for the purpose of future drives and their applications; and for the optimization of material selection for engineering applications, which would guarantee a prolonged material lifespan in the manufacturing and production industries.

References: All the literature sources quoted in the dissertation appear at the end of the thesis.

Appendix section: To be found in this section, are some of the selected analyses and the relevant data. The next chapter presents the literature surveys

Chapter Two

2.0 LITERATURE REVIEW

2.1 Introduction

Aluminium is one of the most abundant elements present in the earth's crust. It has a high consumption demand compared to other metals, due to its light weight. It has a low density coupled with attractive mechanical strength, which makes it perfect for domestic and structural applications. The additional unique properties of aluminium alloy include: low electrical resistance, high ductility and high corrosion resistance. The combination of these desirable properties makes aluminium alloys an ideal substitute for steel; although the proportionately low weldability and high cost makes its application less general. 1100 Aluminium has excellent resistance to corrosion, it is the mechanically strongest and the most heavily alloyed of the 1000 series, which is also used for rivets.

The 1100 Al alloys are highly resistant to chemical attack and weathering, low cost, ductile for deep drawing, and easy to weld. The invention of FSP has made the fabrication of aluminium alloys a simpler process. Fabricating Al alloys with powders have been used by many researchers to improve the mechanical properties.

The Ti-6Al-4V alloyed with Aluminium, Molybdenum, Chromium and Silicon is the most broadly used titanium alloy, an $\alpha + \beta$ alloy (B. S. Li et al., 2004). This titanium alloy (Ti-6Al-4V) Grade 5 has been produced for aerospace applications, in order to enhance better mechanical properties of titanium, while keeping intact the metal's resistance to corrosive behavior (Crist, 2012). The

Ti-6Al-4V is an alloy created for higher toughness and because of its biocompatibility, the alloy is largely used as implants; because it can overcome attacks from the fluid in the body, while being attached to the tissues found in human body (Alpas & Inagaki, 2000). This alloy has consequently been used in industries, such as: the marine, power generation, automotive, chemical, sport etc.

2.2 Aluminum and its alloys

The peculiar characteristic exhibited by aluminum and its alloys make aluminum one of the most economical and highly sought-after material used in various applications, ranging from highly ductile wrapping foil to the key engineering material in manufacturing industry. Aluminum is the second most-used alloy after steel in structural metals, with a density of 2.7 g/cm3, which is about one-third of the density of steel (7.83 g/cm3). Aluminum alloys are light weight, with high strength alloys (exceeding that of structural steel), which permits the design and the construction of strong, lightweight structures that are essentially required for moving structures, such as aircraft, all types of vehicles (including space, land and water-borne vehicles). Aluminum has higher resistance to oxidization than steel; hence it doesn’t rust quickly (Yashpal, Jawalkar, & Kant, 2015).

Aluminum surfaces are highly reflective, and if the protective layer is scratched, an instant resealing will occur. The thin oxide layer itself clings tightly to the metal; and is colorless and transparent; consequently, it is invisible to the naked eye. Aluminum can withstand corrosion to water, salt and other corrosive media if well-treated and alloyed. When polished, aluminum is highly reflective over a broad range of wavelengths; this attribute makes aluminum useful for many decorative and functional uses. Generally, aluminum alloys have good electrical and thermal conductivity, which makes the alloy useful in high-torque electric motors. When compared to copper of the same weight in terms of electrical conductivity, aluminum is nearly twice as conductive as copper.

The requirements of high conductivity and mechanical strength can be met by the use of long-line, high-voltage, Aluminum steel-cored reinforced transmission cable. Aluminum are preferred material used in heat-exchangers, utensils, radiators, electrically-heated appliances and cylinder heads used in automotive, due to its thermal conductivity, which is about 60% more than copper. Aluminum is used as containers for beverages and food because its non-toxic; it is also non-pyrophoric, which means it can be used in applications involving explosive or inflammable materials. Aluminum is also generally used in electronic industries; because it is non-ferromagnetic.

The appearance of aluminum is attractive; because it is always shiny and bright in its natural state. It can be fabricated into any form, which make it essentially sought-after; and it comes in any texture and color. Aluminum can be used in place of other cheaper materials because of its easy formability and workability; its mechanical strength is however low, which makes it inappropriate for structural applications. Aluminum is highly ductile; hence it is used mostly in its alloyed state, in which other elements serve as reinforcement to make it a composite; and its mechanical properties are thereby enhanced.

The strength of various grades of aluminum alloys are shown in Table 2.1. The reinforcements are either solid solutions; or they are found in their secondary phase, serving as resistance to dislocation movement, which in turn, would result in the improved tensile and yield strength of aluminum.

Table 2. 1 Various aluminum alloys and their strength

Aluminum Series	Type of composition	Strengthening Method	Tensile Strength Ranges (UTS)
1 x	Al	Cold Work	70-175
2 x	Al-Cu-Mg	Heat Treat	170-310
3 x	Al-Mn-Mg	Cold Work	140-280
4 x	Al-Si	Cold Work	105-350
5 x	Al-Mg	Cold Work	140-280
6 x	Al-Mg-Si	Heat Treat	150-380
7 x	Al-Zn-Mg-Cu	Heat Treat	520-620
8 x	Al-Li-Cu-Mg	Heat Treat	280-560

2.3 1100 Al series

The 1100 Aluminum alloy is used largely in the chemical, aerospace and electrical industries. The 1 and 7 series alloys are mostly used in aerospace industry, and in applications, such as automobile body panels, fuselage skins of an aircraft and bumpers; these applications are mostly made of the 1000 series because this aluminum grade is less expensive than the 7-series alloys(Yaw et al., 2019). The 1100 Al alloys are also used in automotive industry and home appliances, such as cooking utensils, foils, cover for electronic equipment and numerous other areas. The 1100 Aluminum alloys are of 99% purity; hence, it has many applications in electrical and chemical areas. This series of aluminum possesses good resistance to corrosion, good electrical and thermal conductivity, high workability, but low mechanical properties.

Strain-hardening can improve the strength of the Al 1100 alloy; and the Al alloy contains impurities, such as Iron and Silicon. This alloy has high resistance to weathering and chemical attacks, it has low cost, and easily weldable. 1100 Al can also be used for chemical-processing equipment, fan blades, sheet metal work, nameplates, fin stock and spun hollowware. The mechanical properties of the 1100 Al alloy are shown in Table 2.2.

Table 2. 2 Mechanical Properties of 1100 Al

Tensile Strength	**Yield Strength**	**Elongation**	**Hardness**
110 MPa	85 MPa	15%	59 HV

2.4 Processing Techniques

The mechanical properties of a material are enhanced by the processing parameters used. Different specific properties are required for different applications; and the processing techniques ensure that the material attains a desirable property. Various microstructural patterns can be observed with Aluminium alloys, these patterns can be as a result of thermo-mechanical treatment to enhance the mechanical property, i.e., grain boundary hardening, stress corrosion, toughness and ductility, solid solution hardening, dispersion hardening etc(Maja, Falodun, Obadele, Oke, & Olubambi, 2018; Ramana & Sanke, 2019; Sanusi, Afolabi, & Member, 2014). High strength can be achieved by the use of an adequate processing technique and with proper alloying elements.

With proper optimization of deformation and ageing processes, this alloy can achieve high levels of strength compared with other processed aluminum alloys (Kondaiah et al., 2017)

- The fabrication of composites

This refers to the recent method of improving the mechanical properties of Aluminium and its alloy; the strength and the hardness behaviour of these alloys have been determined by this method. This is done in a way that different materials come together to form new composite material, with improved mechanical properties.

2.4.1 Metal Matrix Composites

Metal-Matrix Composites (MMCs) have replaced conventional materials in recent years due to the attractive and unique properties offered by this composite. MMCs have been largely used in engineering applications such as transportation, sports and aerospace industries. Furthermore, these composites are greatly utilized in automotive and railway brake disc, and also for critical applications in the construction of spacecraft as shown in Figure 2.1. These materials are highly sought after, hence the global demand has increased from between 5496 tons to 8000 tons from 2012 to 2019 (Buffa, Campanella, & Fratini, 2017).

Figure 2. 1: A fan blades in airplane, (b) Gr/Mg airplane tubes made of MMC (Panwar & Chauhan, 2018)

MMCs are combination of materials, with a base material mixed with a reinforcement, usually in powder form; since this approach gives the material superior properties. The base materials largely used are: magnesium, titanium and aluminum alloys; while the reinforcements are usually titanium, boride and carbide. The mechanical performance of MMCs are higher than the unreinforced alloys in all the structural applications; and MMCs also have low coefficient of thermal expansion, great thermal conductivity, low specific densities, improved strength-to-weight ratio, high specific stiffness, good dimensional stability (Abegunde, Akinlabi, & Madyira, 2017; Ajay Kumar, Murari, & Dey, 2018).

Due to the unique properties offered, MMCs have been used to withstand temperature changes associated with environmental condition. Many studies focused on aluminum-matrix composites because of their superior performance in many applications. These unique properties include: the modulus of elasticity, good temperature resistance and high specific strength (Pandey, Purohit, Agarwal, & Kumar Singh, 2018).

MMCs can be fabricated by several mean. These range from mechanical-alloying method, powder metallurgy, and many other surface-modification techniques (Panwar & Chauhan, 2018).

2.4.2. Aluminium-matrix composites

Al and its alloys have been greatly used in the production of metal matrix composites. Aluminium matrix composites have numerous advantages in many industrial applications as a result of their unique properties such as, wear resistance, stiffness, good strength and stability. AMCs are perceived as ideal candidate for materials with light weight and good strength (Thangarasu *et al.*, 2014; Avareji *et al.*, 2017; Sunil *et al.*, 2017).

Additionally, AMCs have been used in military applications such as armour due to its static strength, also in automotive industry as shown in Figure 2.2. AA1100 is a popular type of Al alloys and used greatly as the base material among aluminium alloys, as a result of its highly formable characteristics, the commercial availability and also the option of modifying the mechanical strength by incorporating appropriate reinforcement particles.

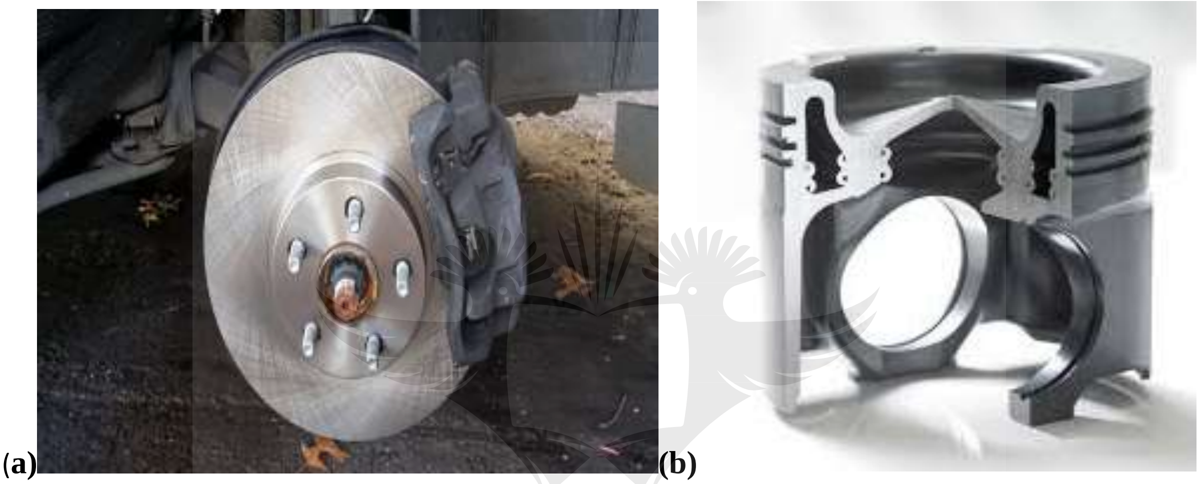

Figure 2. 2 Car brake disc of Aluminum metal matrix composites, (b) Light metal diesel piston (Darras, Omar, & Khraisheh, 2007)

Ramnath et al (Ramnath, Elanchezhian, Atreya, & Vignesh, 2014) studied the machinability and mechanical behavior of SiC particles on Aluminium, and reported an increase in tensile strength, hardness and density of the Al-MMC as the reinforcement ratio increases but impact toughness reduced. Tamer et al (Tamer *et al.*, 2017) examined the behavior of Al reinforced with SiC particle under different conditions of temperature. The behaviour of the composites was influenced by the weak matrix-reinforcement bond, agglomeration of particles and particles cracks. Duhan 2017 (Duhan, 2017) examined the differences in the properties of Al6063 MMC reinforced with four different volume fractions of Zircon sand and Alumina with varying volume fractions of (0+8)%, (6+2)%, (2+6)%, (4+4)% and (8+0)%. The (4+4)% volume fraction composites showed a higher tensile strength and hardness, also using this volume fraction, the reinforcement particles was evenly distributed with lesser pores at the formation of inter-metallic. Sharma and Das.(Sharma & Das, 2009) studied the differences in the wear property of Al-Cu alloy reinforced with Alumina and Zircon sand particles, they reported that the addition of both reinforcements improved the wear resistance of the alloy. However, a significant improvement in wear resistance was seen with the zircon reinforced composites than that of alumina as a result of the particle matrix bonding.

The addition of ceramic particles within the matrix of the alloy for the production of MMCs have been reported to have economical and other significant advantages as a result of its strength and resistance to corrosion. Table 2.3 shows some of the existing applications of AMCs in automotive industry.

Table 2. 3 Some applications of AMCs in Automotive industry

Manufacturer	Composites	Component
Honda	Al/Al_2O_3-Cf	Engine Blocks
Volkwagen	Al/SiCp	Blade Rotor
Toyota	Al/Al_2O_3	Piston Rings
Nissan	Al/SiCw	Connecting Rods
Duralcan, Lanxide	Al/SiCp	Brake rotors, Calipers, Liners
Hitachi	Cu/Graphite	Current Connectors
Martin Marietta	Al/TiCp	Piston, Connecting rods

2.4.3 Titanium alloys as reinforcing particles

Reinforcements in the form of ceramic particles have been added to matrix of MMCs to improve the wear and corrosion resistance, mechanical damping, to reduce weight and also increase the strength and stiffness of the material (Maja et al., 2018; Nabhani, Razavi, & Barekat, 2018). Additionally, proper fabrication of MMC with reinforcement particles have helped to minimize drawbacks such as interfacial reaction, fibre damage and mismatch and microstructural heterogeneity. Pandey et.al (Pandey et al., 2018) used in-situ technique to fabricate Al alloy with TiC, they reported that the yield strength increased by 18% after the mixing of the TiC particles within the matrix of the Aluminum-alloy. Also, a noticeable increase of 20% was observed with the hardness property. Lastly, the wear resistance of the composite was improved with the addition of the TiC particle when compared to the unreinforced aluminum-alloy.

Stephens et. al. examined 4043 grade of Al alloy with dimension of (300 × 200 × 1) cubic mm reinforced with Ti-62222 particles having average particle size of 50 nm. TiC-62222/Al compound fillers of gas tungsten arc welding through dissimilar contents of TiC Nano particles were effectively made-up by accumulative roll bonding (ARB) (Stephens, Stephenst, Veitt, & Albertson, 1997).

Their aim was to form a good interfacial bond between Ti-62222 and Al-alloy, and also to examine the surface morphology, mechanical properties and the microstructure of the composites. The addition of the Ti-62222 particles resulted in improved mechanical properties such as tensile strength and hardness. The enhanced mechanical properties observed after their experiment was attributed to the proper usage of Titanium particles within the matrix.

Candan used sessile drop method to examine different grades of Aluminium-alloys such as 2024, 6061, 1010 and 7075 by reinforcing them with TiC and the phase development at the metal–

ceramic boundary was investigated at 900 °C (Candan, 2002). It has been reported that the Ti-6Al-4V alloy accounts for almost 50% of all alloys used in aircraft applications (Brewer, Bird, & Wallace, 1998) and numerous factors such as process parameters, fabrication techniques, interfacial bonding and volume fraction of reinforcements used influences the mechanical properties of the composite fabricated by Candan.

2.5 Friction Stir Welding

Friction stir welding (FSW) was invented and patented at the Welding Institute (TWI), UK in the year 1991, as a solid-state welding process, initially used to join aluminum alloys(Komarasamy, Mishra, Grant, Northwest, & Hovanski, 2013). The fundamental principle of FSW is simple. A rigid and non-consumable rotating tool, with an exclusively designed shoulder and pin is inserted into the abutting surface of the plates to be joined; and it is later traversed along the joint line. The descriptions of all the terms associated with the process are stated in the nomenclature section.

In the description, the FSW tool rotates in the counterclockwise direction; and it travels from left to right. During friction stir welding, the pressure outpaces the yield strength of the workpiece; and the weld/thermal cycle is considerably shortened. The advancing side is positioned on the right, where the tool direction of rotation is the same as the tool traverse direction and the retreating side is located on the left, where the tool rotation is opposite to the direction of the tool propagation. A compelling benefit of the 'solid-state' welding approach is the complete recrystallized, equiaxed, and refined grain microstructure produced in the weld nugget through an intense plastic deformation, as the temperature increases (Rhodes et al. 1997; Liu et al. 1997; Jata and Semiatin 2000; Benavides et al., 1999). The more the refined grains' microstructure and recrystallization, the better the metallurgical properties and the mechanical properties.

2.5.1 Advantages and Limitations

Friction stir welding is referred to as a “green” technology, because of its environmentally friendly nature, power efficiency and versatility. When compared with the conventional joining approach, it uses considerably less power – without using any consumables (i.e. flux or cover gas); and no toxic emission is released, making it an environmentally friendly welding method. In addition, FSW does not involve the melting of metal alloys; and as a result, no filler metal is required; consequently, most of the Aluminium grade can be fabricated or joined without any worry of solidification fracture, or composition compatibility, or any of the challenges associated with the conventional fusion welding. Furthermore, dissimilar Aluminium grades and metal-matrix composites can be joined with ease (Murr et al., 1998; Li et al. 2000, 1999).

FSW has numerous advantages over the traditional welding methods, due to its solid-state nature. Drawbacks such as solidification cracking, solute redistribution, porosity and liquation cracking can be avoided by using FSW. FSW technique have been generally used to produce welds with minimum defects and also showed high tolerance to adapt to various tool parameters and materials (Sivakumar, Bose, Raguraman, & Muruganandam, 2014). Materials joined together by using FSW have shown good mechanical properties, improved safety due to the absence of toxic fumes or the spatter of molten material and thinner materials with same joint strength can be used. Table 2.4 summarizes the important benefits of FSW against conventional fusion welding.

Table 2. 4 Benefits of FSW

Metallurgical benefits	Environmental benefits	Energy benefits

Solid phase process	No shielding gas required	Improved materials use (e.g., joining different thickness) allows reduction in weight
Low distortion	Minimal surface cleaning required	Only 2.5% of the energy needed for a laser weld
Good dimensional stability and repeatability	Eliminated grinding wastes	Decreased fuel consumption in light weight aircraft, automotive and ship applications
Excellent mechanical properties in the joint area	Consumable materials Saving, such as rugs, wire or any other gases	

However, some defects are associated with FSW if the process is not properly implemented. Weld material may not be subjected to critical deformation during the welding process, as a result of inadequate weld temperatures; this inadequacy is caused by high traverse speeds or low tool rotational speeds. This in turn may result to tunnel hole defects along the fabricated specimen. Also, the bond between the materials being joined together may be reduced by low temperatures. Furthermore, the interface and the surface of the materials may be affected by the length of the

FSW tool pin, which may deform the welds or leads to potential area where fatigue cracks will propagate.

2.5.2 Applications of FSW

FSW is the fastest welding technology adopted in the aerospace and automotive industries. It is an indication of a technology flux due to its global acceptance. Basically, some alloys of Aluminium are categorized as 'non-weldable' by the conventional fusion-welding method. Examples of such alloys are 2XXX and 7XXX Aluminium series. However, new doors of opportunity were opened, when FSW was discovered in 1991 – especially for welding high- strength Aluminium alloys. This definitely received a glorious acceptance in the aerospace industry; which has been faced with the challenge of joining high-strength Aluminium alloys. Afterwards, other characteristics of FSW, like lower residual stresses, defect-free welds and lower distortion, led to a diverse utilization adopting reduced-strength Aluminium alloys.

The new illustration of economic prospect of FSW including the joining of Ford GT central tunnel assembly, Orion spacecraft of NASA, back and front segments of the iMac monitor, an elongated panel for constructing train-body parts in Chinese high-speed trains etc. A descriptive illustration of this FSW application is shown in Figure 2.3

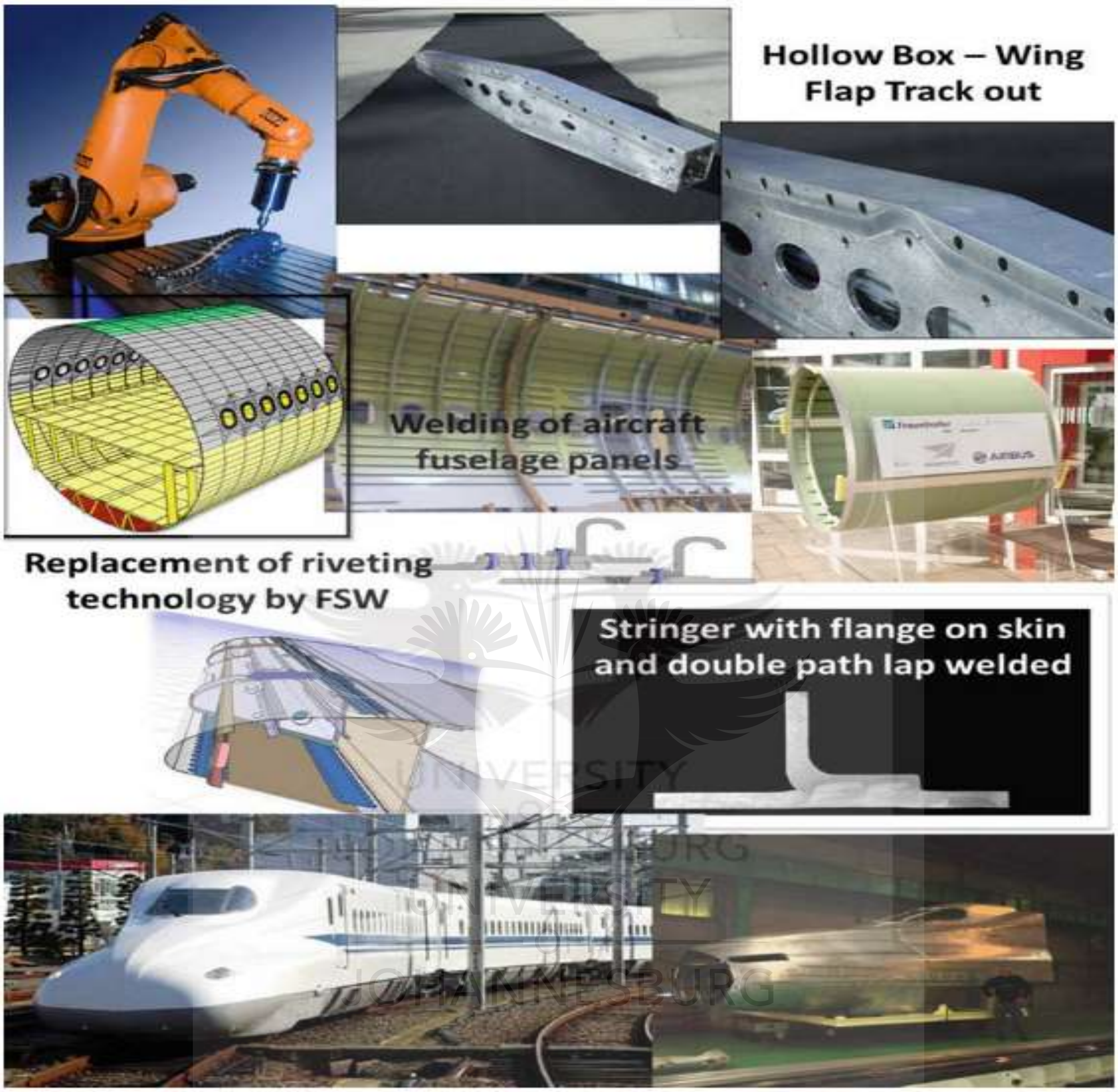

Figure 2. 3 Example of FSW applications (Asif, Chandra, & Misra, 2011)

2.6 Friction stir processing as a fabrication technique

Numerous methods have been used to produce MMCs which includes, ball milling, mechanical alloying, nano-sintering etc. Friction Stir Processing has been successfully used to produce metal matrix composite. Friction Stir Processing has a working principle where a non-consumable rotating tool with a pin probe and a shoulder is plunged into the metal surface and travel along the path to be processed (R. S. Mishra et al., 2003). Due to interfacial friction between the rotating tool and the workpiece Localized, heating is generated. The tool probe and shoulder produce heat, which softens the material under its melting point. This process uses same working principle as FSW.

In FSP, the rotating tool pin has a different design, according to the types of the processed base metal and other processing parameters as shown in Figure 2.4. As the rotating tool travels along the workpiece, the material flows around the tool; is forged under the tool shoulder, and it causes plastic deformation of the workpiece.

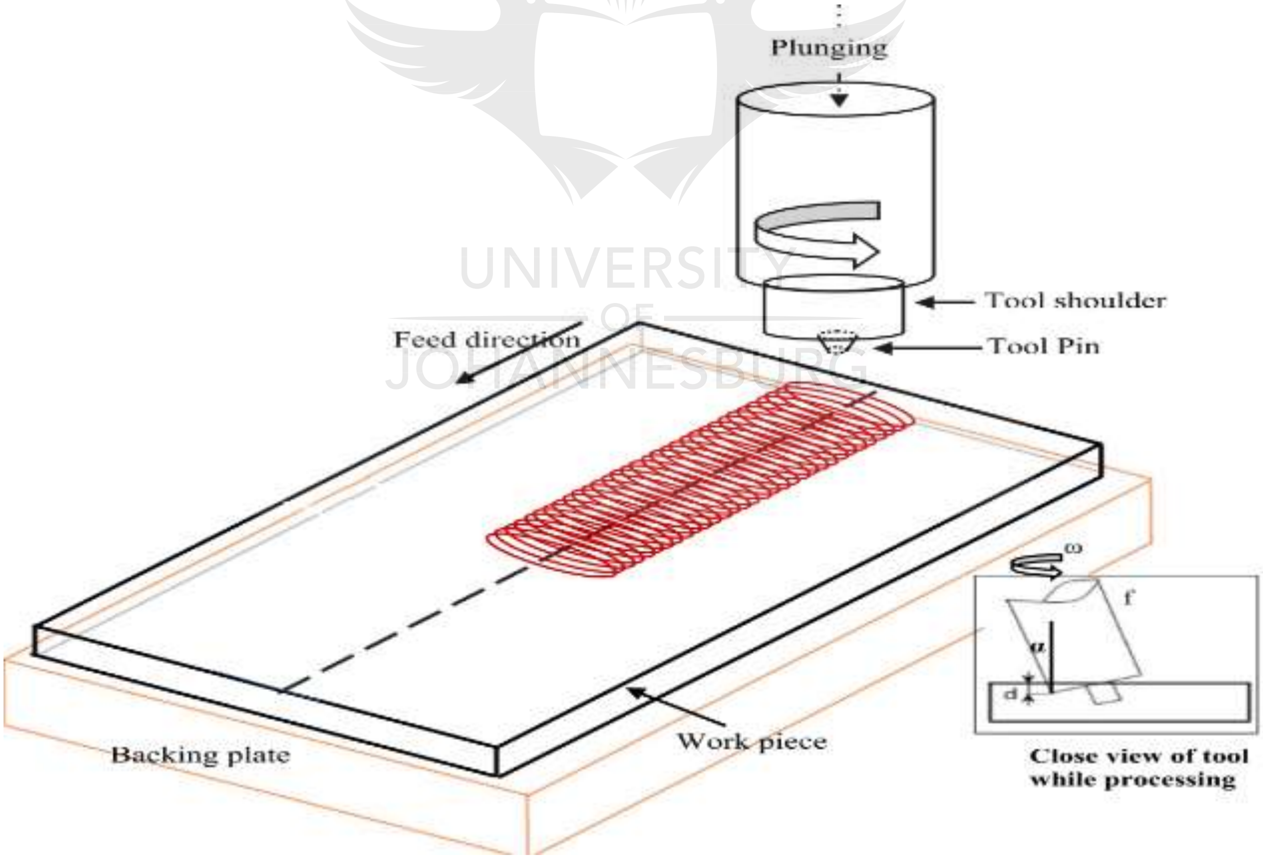

Figure 2. 4 Friction stir processing set up (Hashemi & Hussain, 2015a)

The advantage of friction stir processing technique is that it has a more homogeneous microstructure and uniform particle distribution with stronger interfacial bonding of the reinforcements particles with the base matrix (R. S. Mishra & Ma, 2005). FSP helps in providing the following functions; (i) severe plastic deformation to promote mixing and refining of the constituent phases in the material, (ii) elevated temperature to facilitate the chemical reactions, and (iii) hot consolidation to form a fully dense solid. A basic and conventional design for FSP tool is shown in Figure 2.5. They generally comprise three generic features, including: a shoulder, a probe also known as a pin, and any external features on the probe.

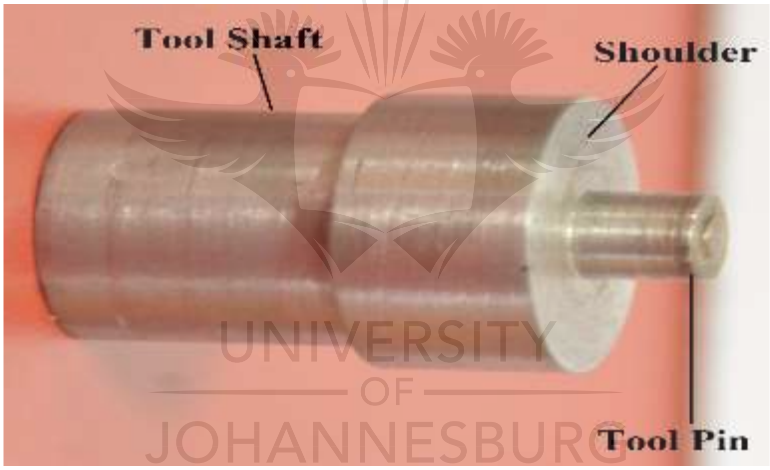

Figure 2. 5 FSP tool design

2.6.1 Heat input during friction stir processing

During FSP, the tool moves over the base metal, stirring, deforming, and mixing it. The parent material, the anvil and the tool increase in temperature, due to the influence of the tool on the parent material. This variation in temperature is a clear indication of the heat generation caused by frictional contact that takes place during the fabrication process (Al-Fadhalah, Almazrouee, & Aloraier, 2014).

In FSP, the heat input is calculated by integrating the torque curve, then using the equation 2.1 (Gadakh & Adepu, 2013)

$$U= \frac{2\pi}{60}\omega \int_{t0}^{ts} T dt \qquad 2.1$$

Where,

ω: Tool rotation speed

T: Torque

And t_0 and t_1 are the tool contact and withdrawal times

U: Heat input

FSP involves plunging a specially shaped rotating tool between the abutting faces of the materials to be processed. Heating arises from rubbing between the tool and the substrate and by visco-plastic dissipation of mechanical energy at high strain rates developed through interaction with the tool, as shown in Figure 2.6 (S. K. Singh, Immanuel, Babu, Panigrahi, & Janaki Ram, 2016). Control of forces and temperature during the fabrication process should assist with minimizing the defects in the composites, particularly if links can be established between the process parameters and the strain partitioning ductility-drop defects (Koli et al., 2017)

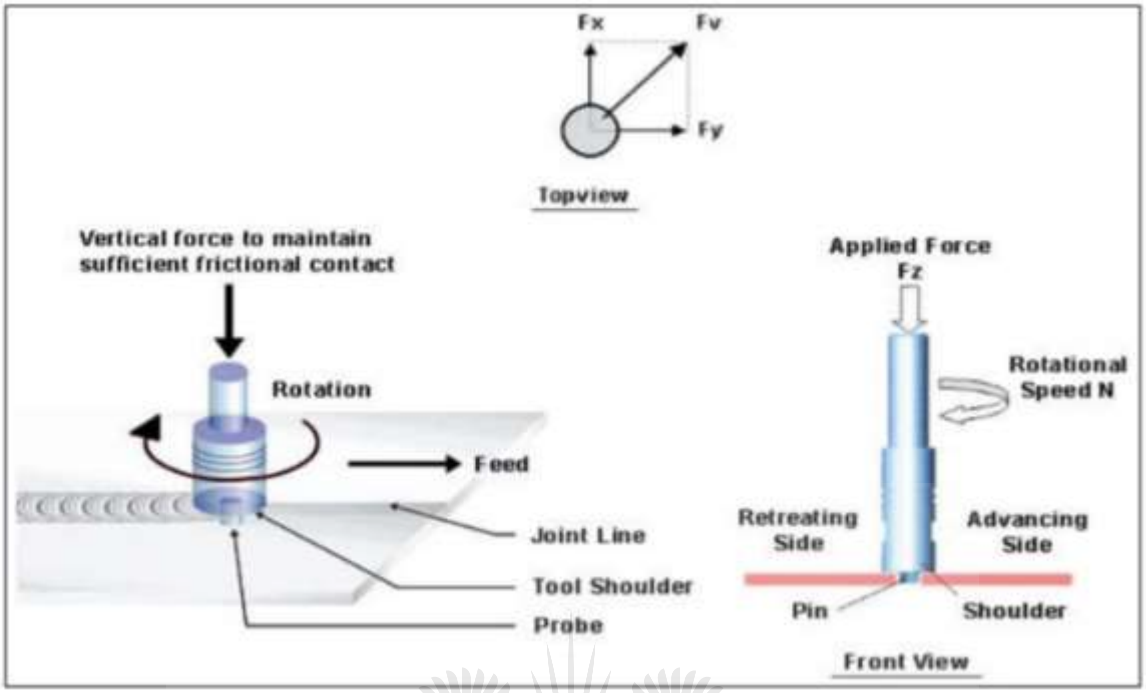

Figure 2. 6 Showing the effect of tool on the force output (Koli et al., 2017)

2.6.2 Friction stir process parameters and tool design

One major advantage of friction-stir processing technique is that it enhances the critical control of processing parameters, which is necessary, in order to obtain an ideal solidified microstructure in surface layer, which also transcends to obtaining improved mechanical properties of the alloy. The suitable execution of the process and the control of a number of parameters are highly required, in order to get quality processed samples. Process parameters, such as the rotational speed, traverse speed, number of passes are of importance (Charit & Mishra, 2017); and these factors will all be investigated in the current research work.

Furthermore, the FSP tool used is considered to be an important factor to be considered in producing composites, the tool heats the workpiece material by friction, the shoulder part of the tool frictionally heats a portion of the workpiece.

Three different shapes of the tool pin are commonly used: threaded taper shape, rectangular and square shape tool geometry, which are depicted in the Figure 2.7. A review of the previous research work done in the field of FSP using different process parameters, such as the rotational speed, the traverse speed, and the tool geometries, is conducted and summarized in the paragraphs to follow. The effects of the cited parameters and the different tool geometries are outlined.

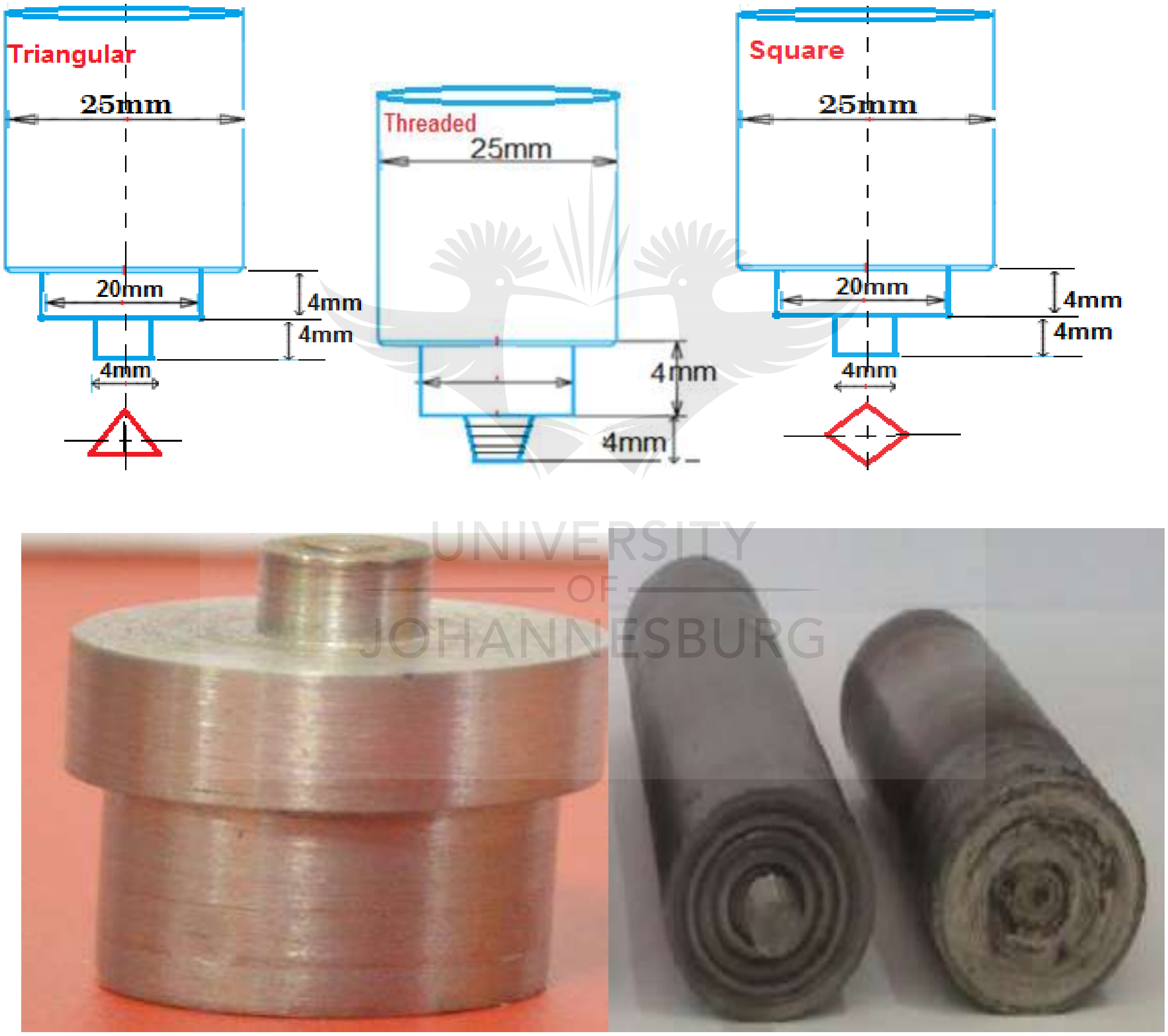

Figure 2. 7 Various tool geometries used in the current study and their dimensions

Hashemi et al 2015 investigated wear performance of Al/TiN dispersion strengthened surface composite produced through friction-stir process - by comparing various tool geometries, it was concluded that the tool geometry affects the particles' dispersion (Hashemi & Hussain, 2015b). In their work, the threaded tool was the most appropriate geometry among all used, in which higher hardness and good wear resistance were experienced, when the composites were fabricated with threaded tool shape.

Sarmadi et al 2013 fabricated copper-graphite surface composites via FSP, by using five different tool geometries, namely; straight cylindrical (SC), tapered cylindrical (TC), threaded cylindrical (TH), square (SQ), and triangular (TR) (Sarmadi, Kokabi, & Seyed Reihani, 2013). It was concluded that using a tool with a triangular pin leads to better distribution of the particles, rather than other tools. This is because of the flow pattern of materials against this tool.

The area of composite produced with this tool is larger in comparison with composites produced by other tools. Adetunla et al 2018 carried out an investigation on the mechanical properties of Al reinforced with Ti-6Al-4V particles by comparing various tool geometry and number of FSP passes (Adetunla and Akinlabi, 2018). It was reported that the tool geometry formed in threaded taper shape is the most suitable tool shape to produce even distribution of particles within the matrix and the adequate number of passes should be at-least 3-passes. They reported a 30% increment in the tensile strength with the combination of their processing parameters.

Vijayavel et al 2015 studied the effect of various pin profiles, by considering the pin volume ratio (PVR) on the stir zone of the material, and its resulting effects on the tensile properties, microhardness and the microstructural evolution. They concluded that the PVR plays a significant role in the particle distribution and grain refinement within the microstructure of the stir zone; and subsequently, it has an effect on the mechanical properties of the various pin profiles examined in their research, as shown in Figure 2.8 (Vijayavel & Balasubramanian, 2017).

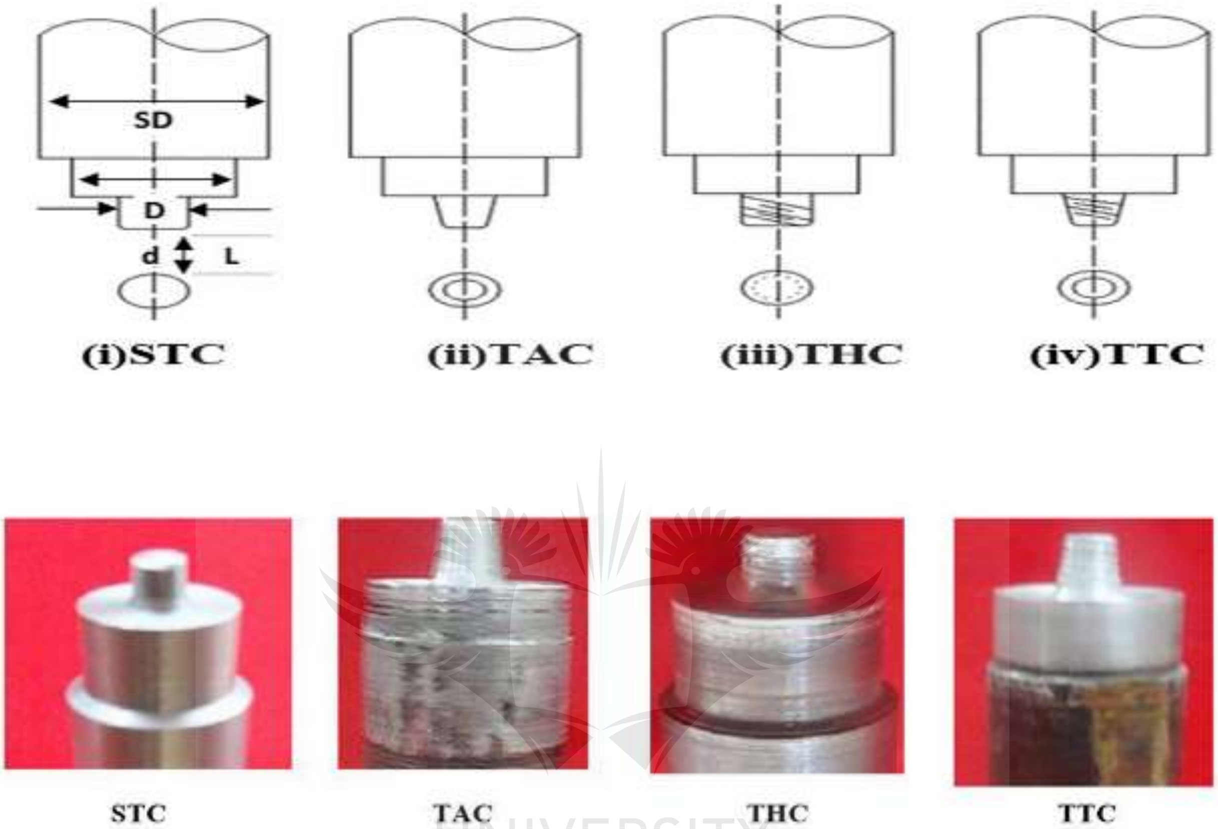

Figure 2. 8 Schematic diagram and photographs of tool pin profiles (Vijayavel & Balasubramanian, 2017)

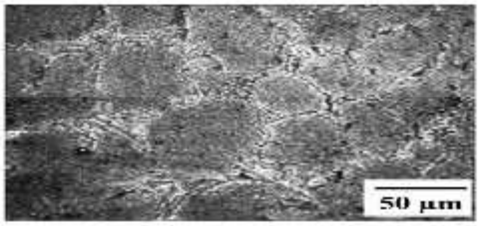

(a) Base material

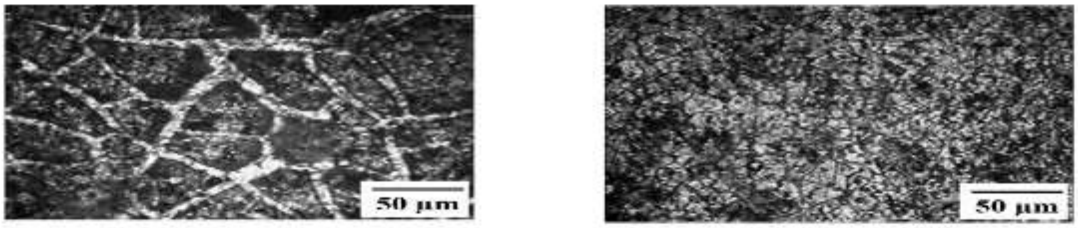

(b) PVR=1.0 (STC)

(c) PVR=1.15 (TAC)

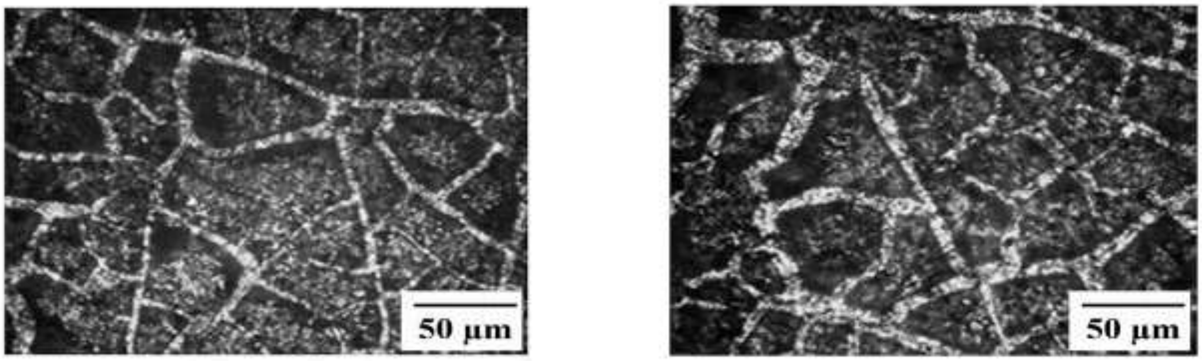

(d) PVR=1.28 (THC)

(e) PVR=1.63 (TTC)

Figure 2. 9 Effect of tool pin profiles on the stir zone microstructure (Vijayavel & Balasubramanian, 2017)

2.6.3 Effect of number of passes on FSPed composites

The effect of multi-pass FSP on the microstructure, the microhardness, and the tensile strength on the metal alloy and on the composites, have been studied by many investigators(Choi, Liu, Ushioda, & Fujii, 2019; Costa, Verdera, Vieira, & Rodrigues, 2014; Sivakumar et al., 2014). The importance of these additional passes is to improve the mechanical properties and to obtain a fine and homogenous distribution of the reinforcement particles in the metal-matrix composites. The effect of FSP passes on the microstructure of the fabricated matrix, the distribution of SiC nanoparticles, and the mechanical properties of the stir zone have been carried out by Rahsepar et al 2016 (Rahsepar & Jarahimoghadam, 2016).

These researchers revealed that the increase in the FSP number of passes does not have a significant effect on the stir zone of the sample subjected to FSP without reinforcement particles; while the samples fabricated with SiC nanoparticles can intensely affect the distribution of nanoparticles and then microstructural evolutions and mechanical properties of the stir zone. The effect of overlap multi-pass friction stir processing on the mechanical properties of Aluminum Alloy 6082 was investigated by Rayes et al 2012 (El-Rayes & El-Danaf, 2012).

The relation between hardness and grain size is inversely proportional in multi-pass processing; where increasing the number of passes led to an increase in the SZ-grain size, and also thereby increasing the traverse speed, which increases the mean hardness and the UTS of the SZ, as shown in Figure 2.10.

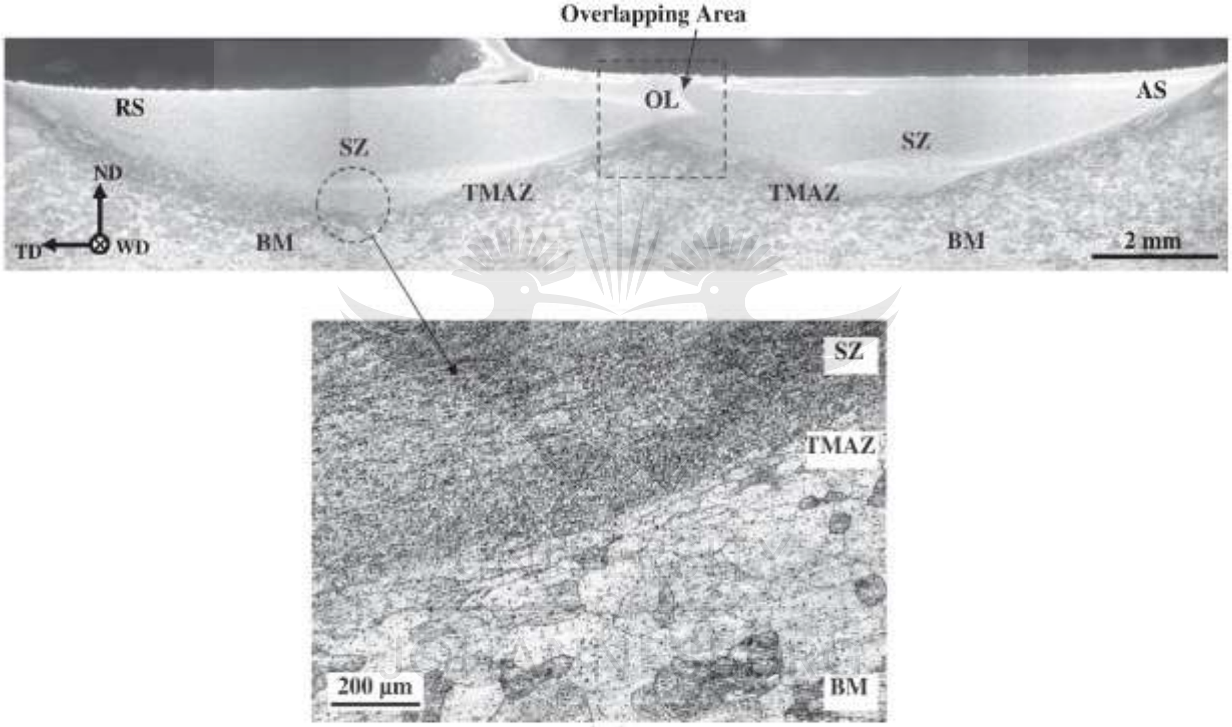

Figure 2. 10 Multi-pass FSP sample with 25 percent overlapping: for low-magnification overview of transversal cross-section. And for micrograph presenting transition area between SZ and BM (El-Rayes & El-Danaf, 2012)

Multi-pass friction stir processing has been carried out on commercial A356 alloy fabricated by adding inorganic salt K_2TiF_6 powder to forming 6% vol. Al_3Ti/A356 compost. The microstructure and mechanical properties were improved, as reported by Koli et al 2017 (Koli et al., 2017).The authors concluded that multi-pass FSP improved the distribution of Al_3Ti and Si particles.

Furthermore, it reduced the grain sizes, the refinement of the metal-matrix grains; and it eliminated any cavity or porosity.

Therefore, both the strength and the elongation of the specimens were gradually improved. The effect of particle types and size distribution was studied by Luo et al 2018 in Al-alloy metal matrix composites (Luo, Zhang, Zhang, Q, & Chen, 2018). It was observed that by increasing the number of FSP passes, the distribution of the reinforcing particles become more homogeneous than that of the base metal. Furthermore, the third pass friction-stir processed composite shows an improvement in the tensile strength by 15 % compared with all processing passes, as shown in Figure 2.11.

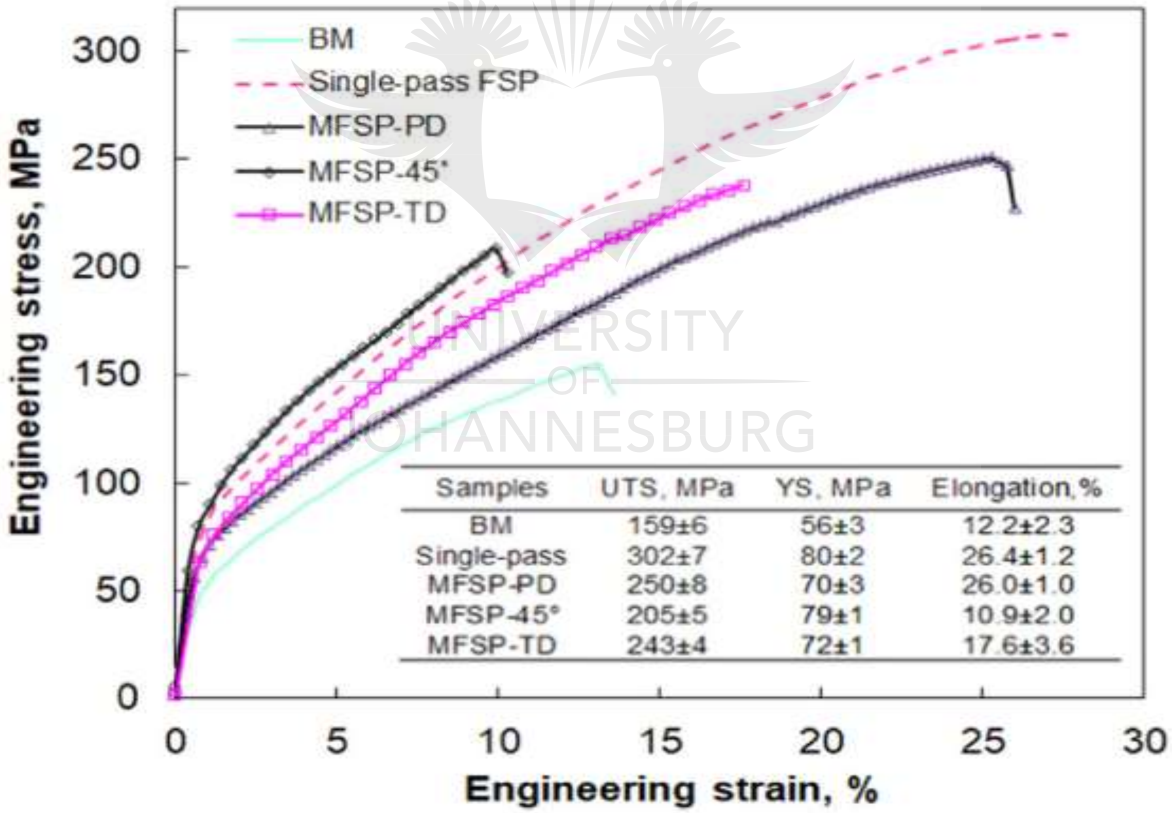

Samples	UTS, MPa	YS, MPa	Elongation, %
BM	159±6	56±3	12.2±2.3
Single-pass	302±7	80±2	26.4±1.2
MFSP-PD	250±8	70±3	26.0±1.0
MFSP-45°	205±5	79±1	10.9±2.0
MFSP-TD	243±4	72±1	17.6±3.6

Figure 2. 11 Engineering stress-engineering strain curves of the samples studied, along with the obtained tensile properties (Luo et al., 2018)

Rahsepar et al 2016 investigated the influence of multi-pass friction stir processing on corrosion behavior and on the mechanical properties of the zircon-reinforced Al metal matrix composites. The microstructural observation of their study is shown in Figure 2.12. They concluded that a significant way to improve the properties of the fabricated composites is to increase the number of FSP passes (Rahsepar & Jarahimoghadam, 2016). While the composites fabricated with four cumulative passes has the highest tensile strength and the composites with the best corrosion resistance observed with the samples fabricated via three cumulative passes.

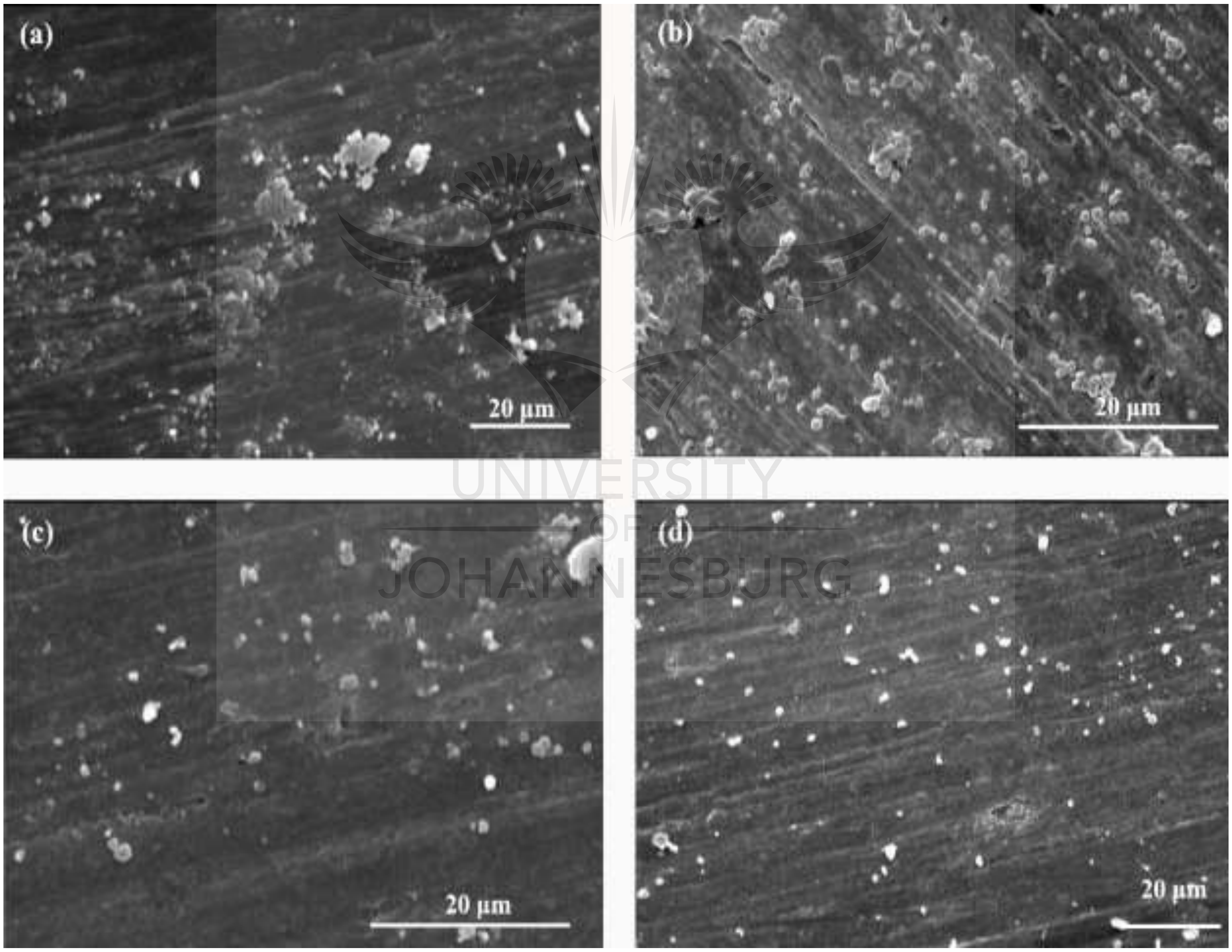

Figure 2. 12 SEM images revealing the particle distribution within the matrix via (a) single-pass, b) two-passes, c) three-passes and d) four-passes composites (Rahsepar & Jarahimoghadam, 2016)

2.6.4 Effect of tool rotational speed and transverse speed on composites

Yuvaraj et al 2015 (Narayana Yuvaraj et al., 2015) fabricated SiC with 5083 Al alloy, they recorded that the highest tensile strength of 273 MPa observed with sample fabricated with 950 rpm and a square pin shape. Lastly, they attributed the differences in the tensile strength with the tool parameters used, behaviour of the flow of material, the dissolution and the over-ageing of the reinforcing particles, as well as the formation of macroscopic defects in the processed samples. Sunil et al. (Sunil et al., 2017) joined two dissimilar metals by investigating the microstructural and mechanical properties of these metals after reinforcing it with titanium at the joint interface. The materials were welded at 254mm/min feed rate and with varying tool speed of 400,1000 and 2000 rpm.

Aluminijeve et al 2017 (Aluminijeve et al., 2017) examined the mechanical behaviour of welded AA6082 and AA2024 via FSW. They reported that a noticeable increment in the vertical force was observed as the traverse speed increases. They also noticed that the tool speed plays significant role in achieving good mechanical properties such as tensile strength and hardness. Yuvaraj et al 2015 (Narayana Yuvaraj et al., 2015) employed FSW to join two different aluminium alloy grades. They observed that the presence of defects at the weld zone of the specimen caused damage to some of the blanks during the formability tests. Zhang et al 2018 (C. Zhang, Cui, Wang, Liu, & Li, 2018) welded aluminium-alloy and magnesium-alloy together using FSW; they were able to successfully produce some welds at only a particular process parameter of 600 rpm tool rotational speed and 40 mm/min tool speed. The examined microstructure of the welds showed fine and equiaxed grains when observed at the stir zone. Also, a perfect bond consisting of both aluminium and magnesium bands was formed. The microstructure of the parent material and three weld zones are shown in Figure 2.13.

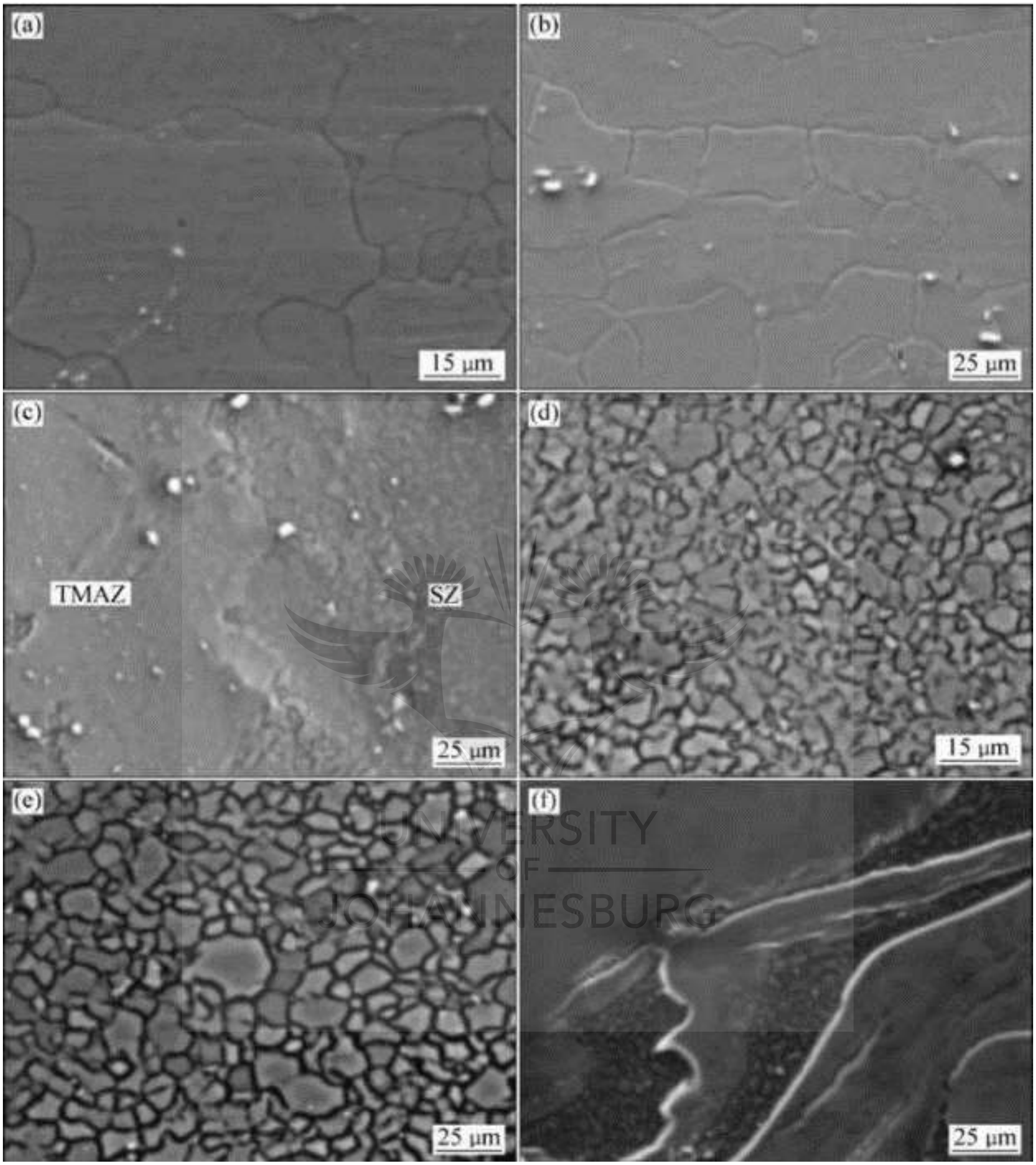

Figure 2. 13 Scanning electron microscope images of AZ31 Mg showing different regions, (a) BM; (b) HAZ; (c) Interface of TMAZ/SZ; (d) SZ in Mg side; (e) SZ in Al side; (f) Intercalated microstructure (Z. Zhang et al., 2017)

Faraji et al 2011 fabricated AZ91/alumina nanocomposite via FSP, they reported that FSP is an appropriate technique to mix Al_2O_3 particles into the base material (Faraji & Asadi, 2011). FSP is a viable method that helps to modify microstructure in order to produce homogenous and fine grain structures with evenly distributed particles within the matrix. They also reported that fine surface layer of composites was achieved using tool rotational speed of 900 rpm and traverse speed of 40 mm/min. Ensuring fine and equiaxed grain structure are majorly dependent on the FSP parameters such as number of passes, traverse speed and tool rotational speed. Lastly, they concluded that the FSP parameters used affected the hardness results as shown in Figure 2.14.

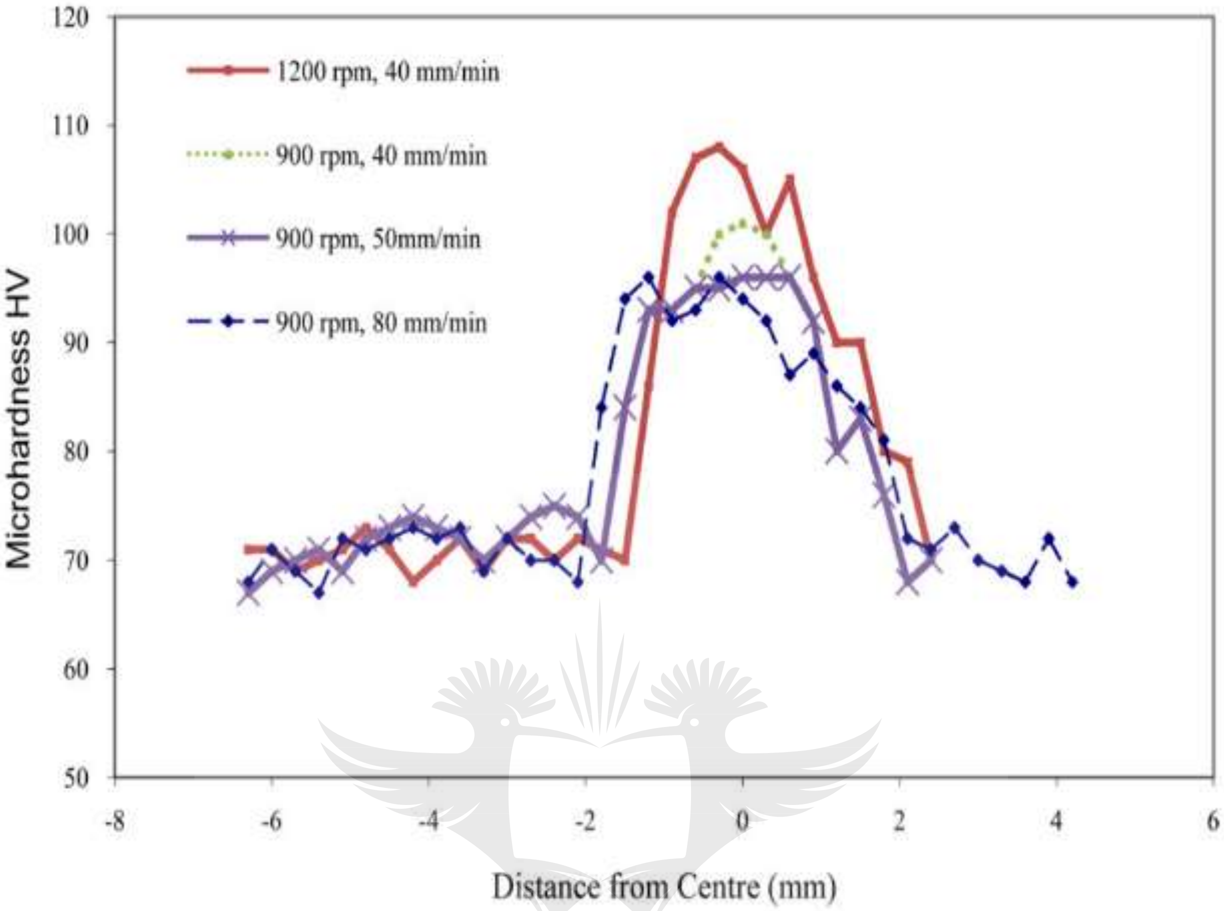

Figure 2. 14 Effect of the traverse and rotational speeds on the microhardness of SZ (Faraji & Asadi, 2011)

2.7 Typical Applications of FSP

Friction Stir Process is utilized when the mechanical properties of a metal need to be improved by employing other metals as reinforcements to improve the first. This technique has been used largely in aerospace and automotive industries, by developing new materials with improved wear resistance, and fatigue life (Ahmadkhaniha, Heydarzadeh Sohi, Salehi, & Tahavvori, 2016). Numerous materials have been processed by employing the FSP technique. The mechanical properties of Aluminium, Magnesium and Stainless Steel have been enhanced successfully by various researchers (Swaminathan *et al.*, 2017; Rahsepar and Jarahimoghadam, 2016; Yuvaraj, Aravindan and Vipin, 2017).

- Casting

Metallic parts produced by casting are comparatively inexpensive, but are often subject to metallurgical flaws like porosity and microstructural defects. Friction stir processing can be used to introduce a wrought microstructure into a cast component and eliminate many of the defects. By vigorously stirring a cast metal part to homogenize it and reduce the grain size, the ductility and strength are increased.

- Powder metallurgy

Friction stir processing can also be used to improve the microstructural properties of powder metal objects. In particular, when dealing with aluminium powder metal alloys, the aluminium oxide film on the surface of each granule is detrimental to the ductility, fatigue properties and fracture toughness of the workpiece. While conventional techniques for removing this film include forging and extrusion, friction stir processing is suited for situations where localized treatment is desired.

- Fabrication of metal matrix composites (MMC)

Friction stir processing (FSP) can also be used to fabricate MMC at the nugget zone where we need the change of properties. Al 5052/SiC and some other composites were successfully fabricated. Even nano-composites can also be fabricated by FSP. FSP have been used to produce locomotive train, carriage panels, aircraft fuselage, truck bodies, caravans, heat sinks, ship panel sections, aluminium bridge sections, architectural structures, pipelines and electrical motor housings. Figure 2. 15 shows existing applications of FSP.

Figure 2. 15 Existing applications of FSP

2.8 Friction stir processing of aluminum matrix composites

2.8.1 Microstructural evolution and X-Ray Diffraction analyses

The development of laboratory work on the friction stir processing of Aluminum matrix composites should provide insight into the potential applications of this alloy which will facilitate industrial development. Shyam et al 2016 investigated the microstructural and XRD analysis of 5083 Al-W surface composite fabricated by FSP (Shyam Kumar, Bauri, & Yadav, 2016). They reported that the particles used were homogenously distributed in Al matrix in the stir zone (surface).

The SEM images of the 5083 Al–W composite are shown in Figure 2.16. The volume of the tungsten particles was found to be 18%. The interfacial bonding between the base material and the particles were observed. The observed micrograph shown in Figure 2.17 reveals a superior interfacial bonding and no intermetallic was detected. At the observation of the XRD pattern of the composite, the peaks reveal only Al and W and no intermetallic phase was formed. This observation showed that there was no particle-matrix reaction; and the tungsten particles were retained in their elemental form.

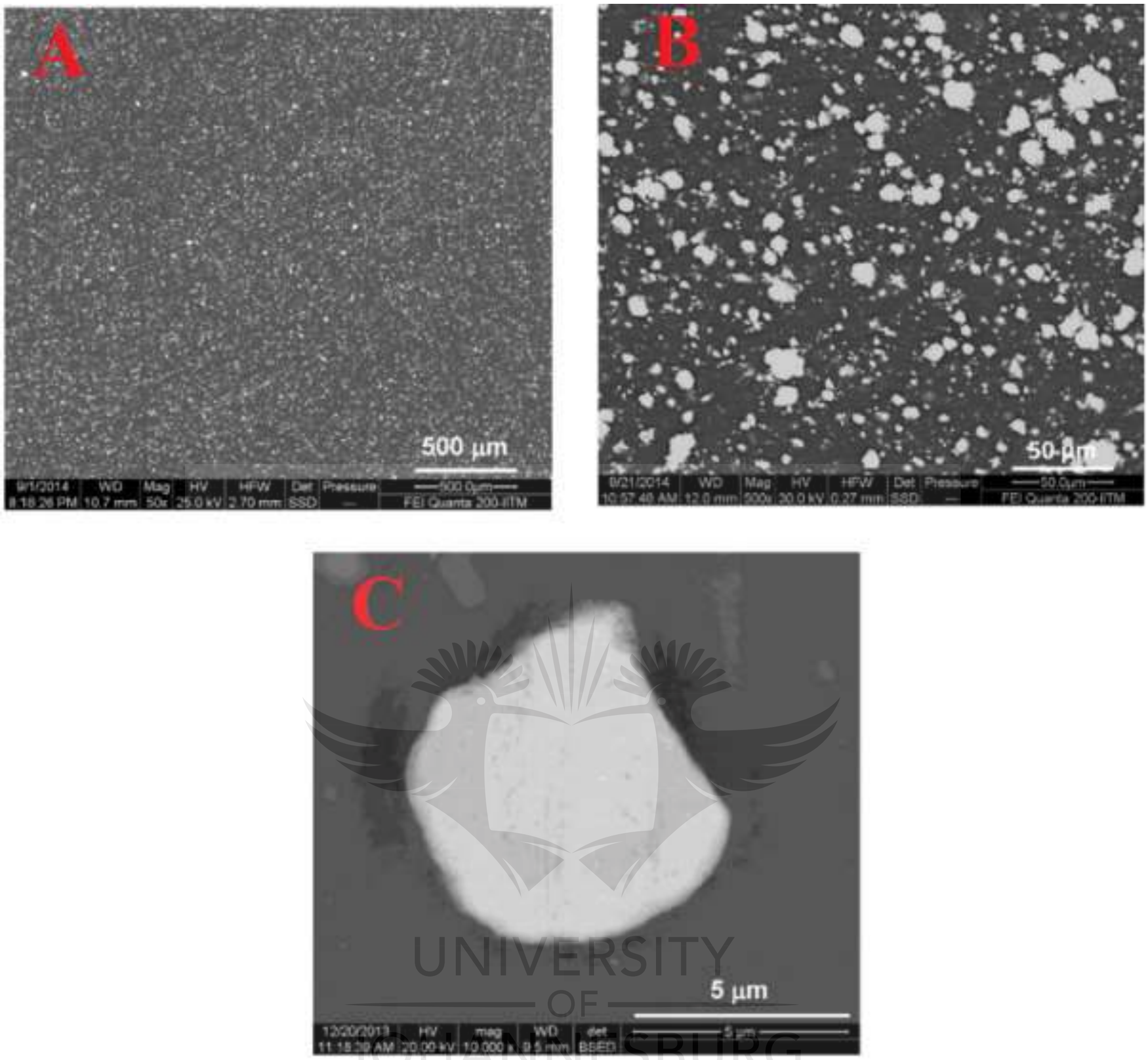

Figure 2. 16 (a), (b) SEM images revealing dispersion of particles within the matrix at two different magnifications. (c) High magnification BSE image showing clean particle- matrix interface (Shyam Kumar et al., 2016)

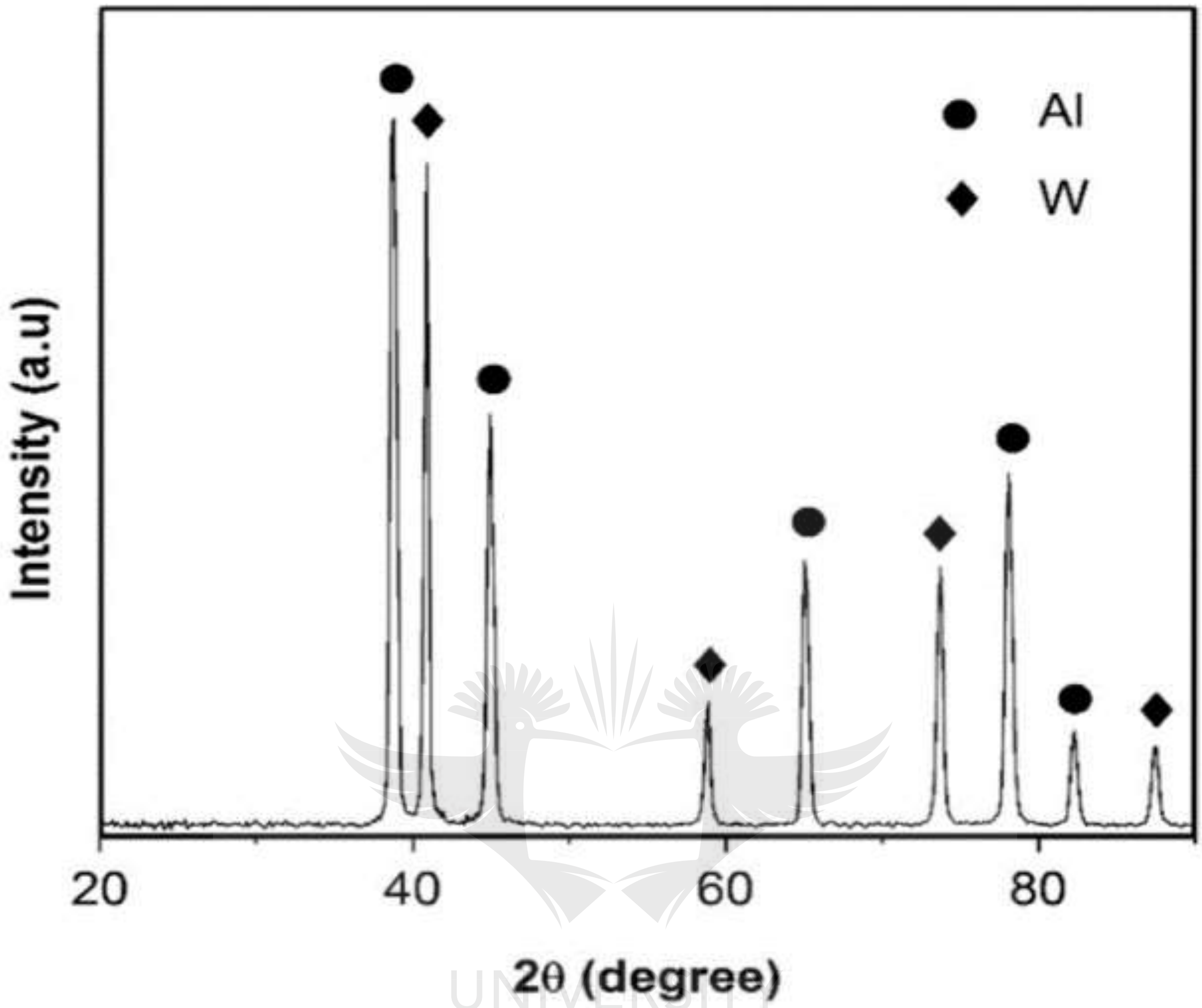

Figure 2. 17 XRD pattern of the 5083 Al–W composite (Shyam Kumar et al., 2016)

Yuvaraj et al 2015 Fabricated Al5083/B_4C surface composite by friction stir processing. They concluded that the microstructure in the FSP-ed specimens with nano B_4C particles three passes exhibits fine grain size, higher hardness (124.8 HV), ultimate strength (360 MPa) and wear rate (0.00327 mg/m) in comparison to the base material hardness (82 HV), the ultimate strength (310 MPa) and the wear rate (0.0057 mg/m) (Narayana Yuvaraj et al., 2015). The XRD profile of the nano B_4C reinforced aluminum alloy specimen subjected to three stir passes were observed; and it was concluded that the peaks were the base materials.

Anvari et al 2013 investigated the XRD pattern of Al-Cr-O surface nano-composite layer fabricated on Al6061 plate by friction stir processing after six passes, as shown in Figure 2.18 (Anvari, Karimzadeh, & Enayati, 2013). They concluded that until the third pass of FSP, due to thermomechanical condition, Cr_2O_3 was reduced by the Al; consequently, pure Cr and Al_2O_3 were produced. Thereafter, with increasing FSP passes, intermetallic compounds of Al–Cr appeared as a result of the reaction between Al and Cr during the FSP. With respect to the results, a reaction mechanism in FSP was suggested.

According to this mechanism, during the FSP, Cr was surrounded by a continuous Al matrix. Al is easily deformed and wrapped around the Cr. The reaction between Al and Cr is exothermic, in which $Al_{13}Cr_2$ and $Al_{11}Cr_2$ phases grow at the Cr–Al interface, as a spherical shell.

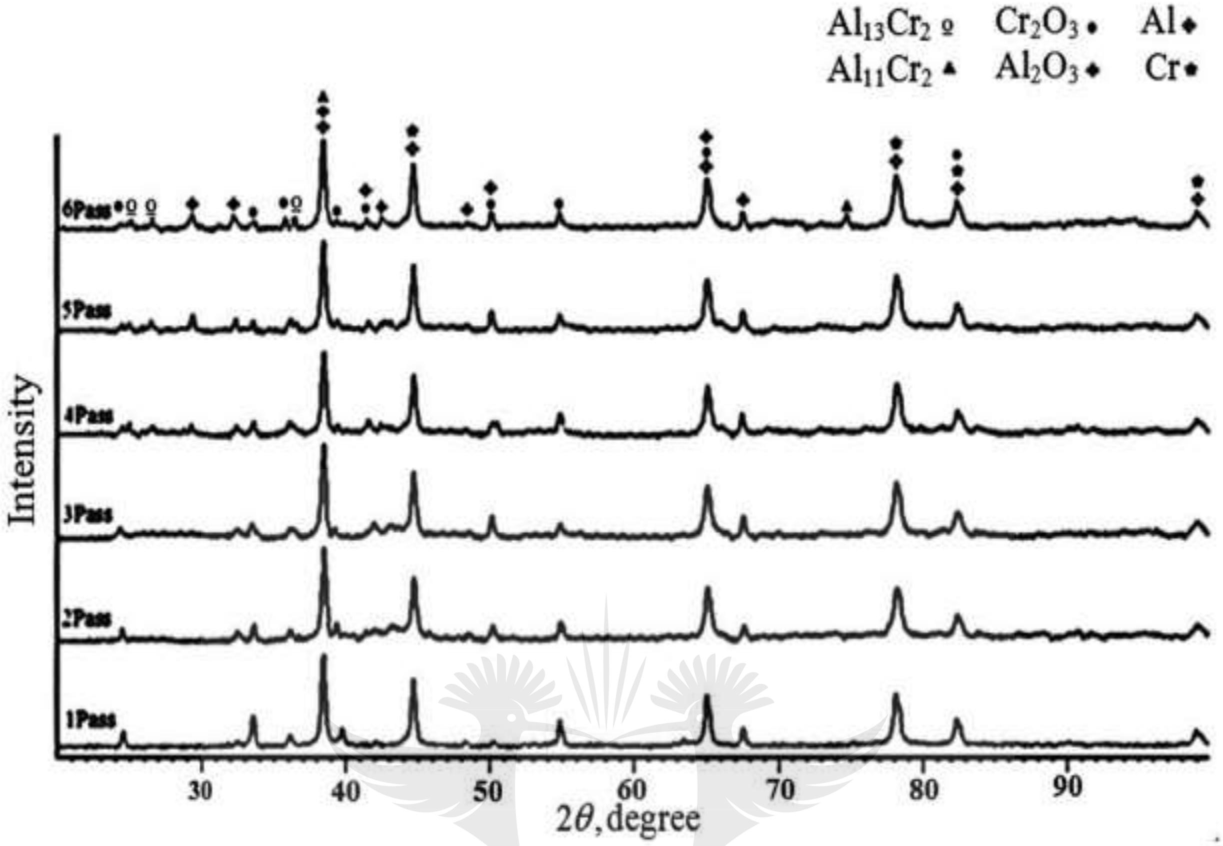

Figure 2. 18 The X-ray diffraction patterns for samples after 1–6 passes (Anvari et al., 2013)

Khodabakhshi et al 2012 investigated Al–Mg/A_{l3}Ti (b100 nm, 4 vol%) nanocomposite was produced via FSP of an Al–Mg alloy (AA5052) with Titanum as the reinforcing particles. They observed and reported the mechanical properties of the composites as well as the intermallic phases and the microstructure of the composites. Also, a comparison was made with the un-reinforced alloy (Khodabakhshi, Nosko, & Gerlich, 2018). The authors reported that FSP helped to reduce the grain size of the Al-Mg alloy from an average of ~49 µm down to 20 µm as shown in Figure 2.19. The pre-placing of the titanium particles accelerated the grain refinement, so that a fine-grained metal matrix was achieved. The average grain size of the composite was about 1.5 µm but the size distribution was broad with a sign of bimodal distribution. The plastic strain and high temperature associated with the use of friction stir processing influenced the solid- state chemical reactions between Aluminium and Titanium to form Al_3Ti. The size of the hard inclusions was smaller than 100 nm with an approximate volume fraction of 4%. Ultra-fine Mg_2Si particles were also detected in the microstructure. As a result of the some particles serving as inclusions, the strength of the composite was greatly increased when compared to the unreinforced alloy with a moderate tensile elongation of ~22%.

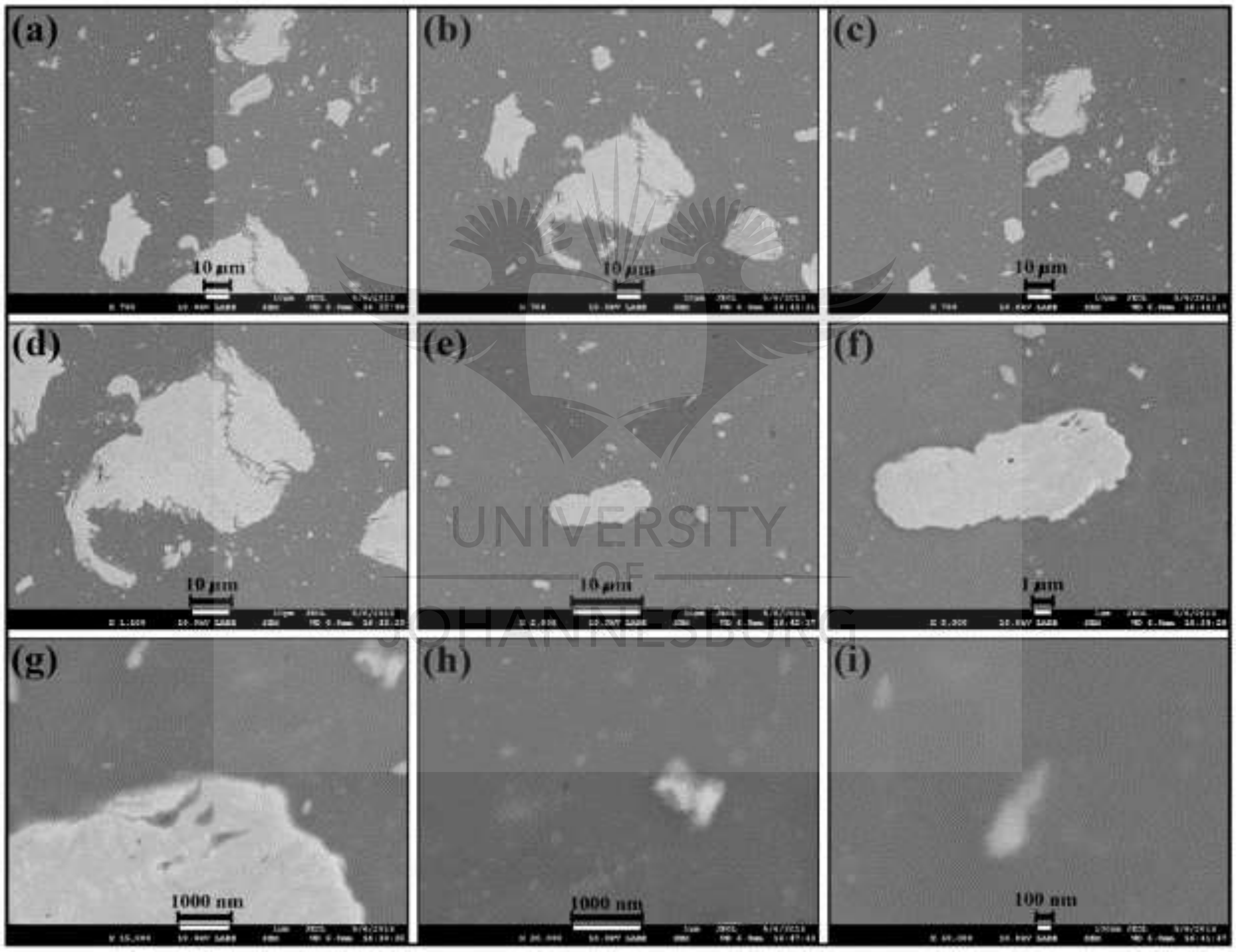

Figure 2. 19 SEM images showing the titanium particle dispersion through the Aluminum matrix (Khodabakhshi et al., 2018)

2.8.2 Hardness and Tensile properties of AMCs

Ramesh et al 2012 investigated the effect of Multi-pass friction-stir processing on the mechanical heat input associated with multi-pass FSP; and they found that the multi-pass FSP heating cycle of one pass affects the microstructure and the mechanical properties of the other passes; and two different variants of the process known as intermittent multipass FSP (IMP) and continuous multipass FSP (CMP) were postulated (Ramesh et al., 2012). In their work, it was concluded that the hardness Vickers hardness values was a function of traverse speed. For the samples processed up to the traverse speed of 110 mm/min, the hardness values obtained for IMP and single pass processed samples were found to be higher than the values obtained for the CMP processed samples.

The hardness values in the transition zone were higher than those obtained from the nugget zone; and there was a variation in the hardness values in the nugget zone of different passes. The hardness values increased marginally from 70.4 for the first pass to 74 for the 12th pass, as shown in Figure 2.20.

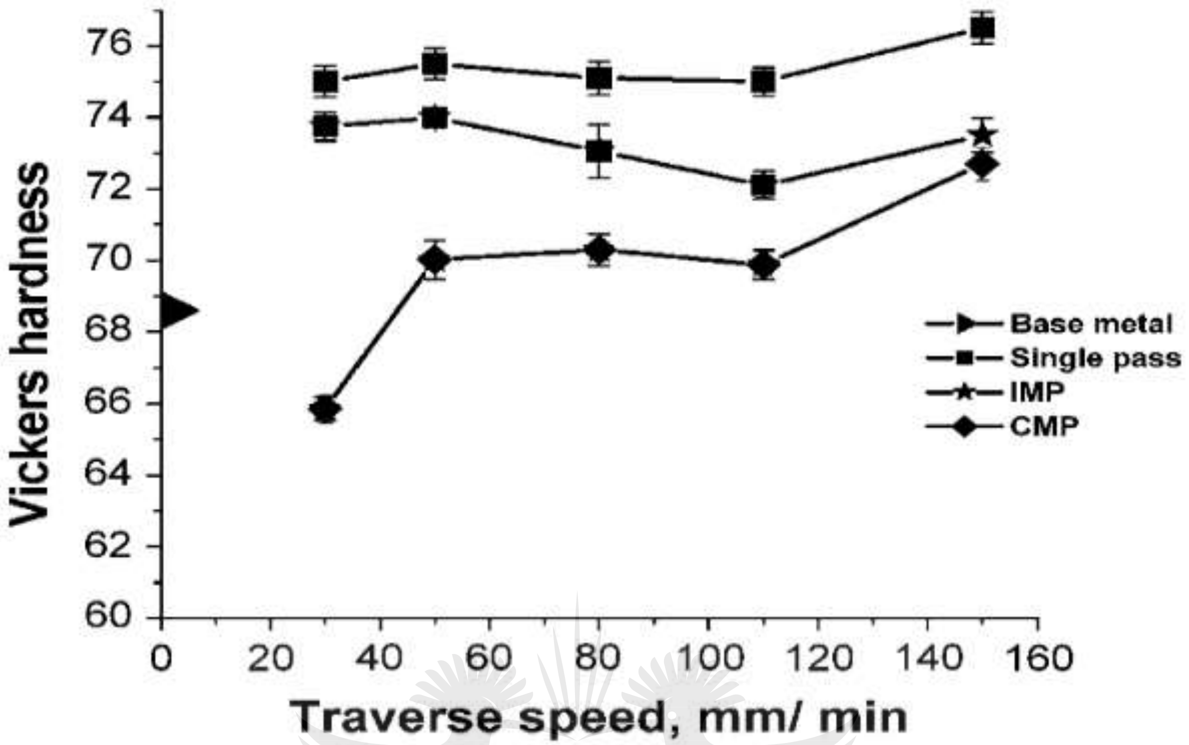

Figure 2. 20 Hardness values increased marginally from 70.4 for first pass to 74 for the 12th pass (Ramesh et al., 2012)

Tajiri et al 2015 investigated the effect of the friction-stir processing conditions on the fatigue behaviour and the texture development in A356-T6 cast aluminum alloy. The tensile properties are summarized in Table 2.5 (Tajiri et al., 2015). The proof stress samples fabricated at 500rpm and 1000rpm were decreased 23% and 12% by FSP, respectively, compared with the as-received material. Subsequently, the tensile strength, was decreased 8.7% and 1.4% for 500 and 1000 rpm specimens, respectively. It could be concluded that the proof stress was more sensitive to the softening by FSP, and the lower rotational speed gives slightly lower stress and tensile strength.

Table 2. 5 Tensile properties (Tajiri et al., 2015)

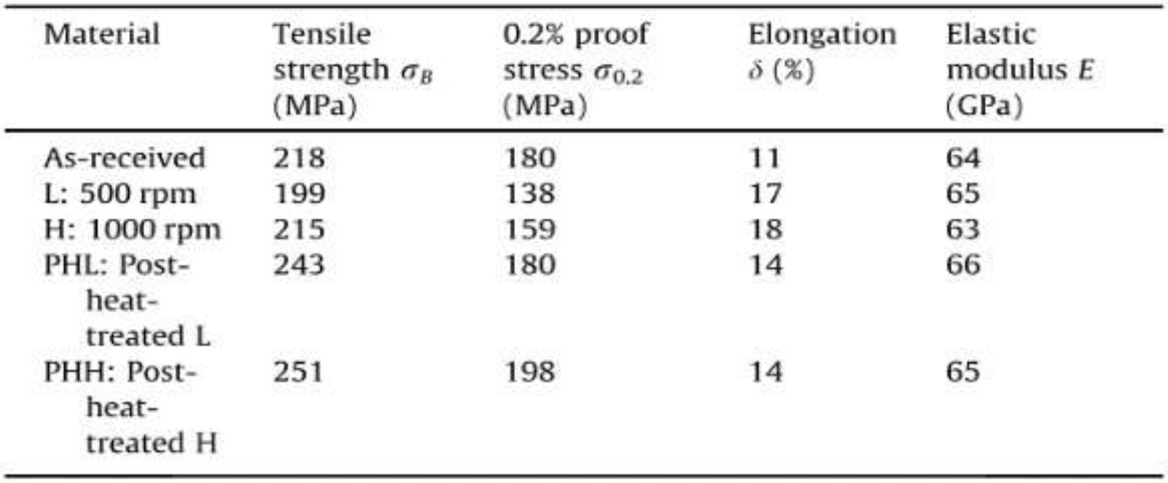

Material	Tensile strength σ_B (MPa)	0.2% proof stress $\sigma_{0.2}$ (MPa)	Elongation δ (%)	Elastic modulus E (GPa)
As-received	218	180	11	64
L: 500 rpm	199	138	17	65
H: 1000 rpm	215	159	18	63
PHL: Post-heat-treated L	243	180	14	66
PHH: Post-heat-treated H	251	198	14	65

Tajiri et al further tested the samples for hardness, and the hardness profiles for both R-side and the A-side are almost same, indicating that the hardness profile is sensitive to the depth from the surface. The 500 rpm and the 1000 rpm samples exhibited lower hardness than the as-received one, because of the resolution of hardening precipitates by the heat input. Severe plastic deformation under high tool rotational speed resulted in the slightly higher hardness in the 1000rpm fabricated specimen than in 500 rpm specimen. It was concluded that the post-heat treatment had successfully increased the hardness, as shown in Figure 2.21.

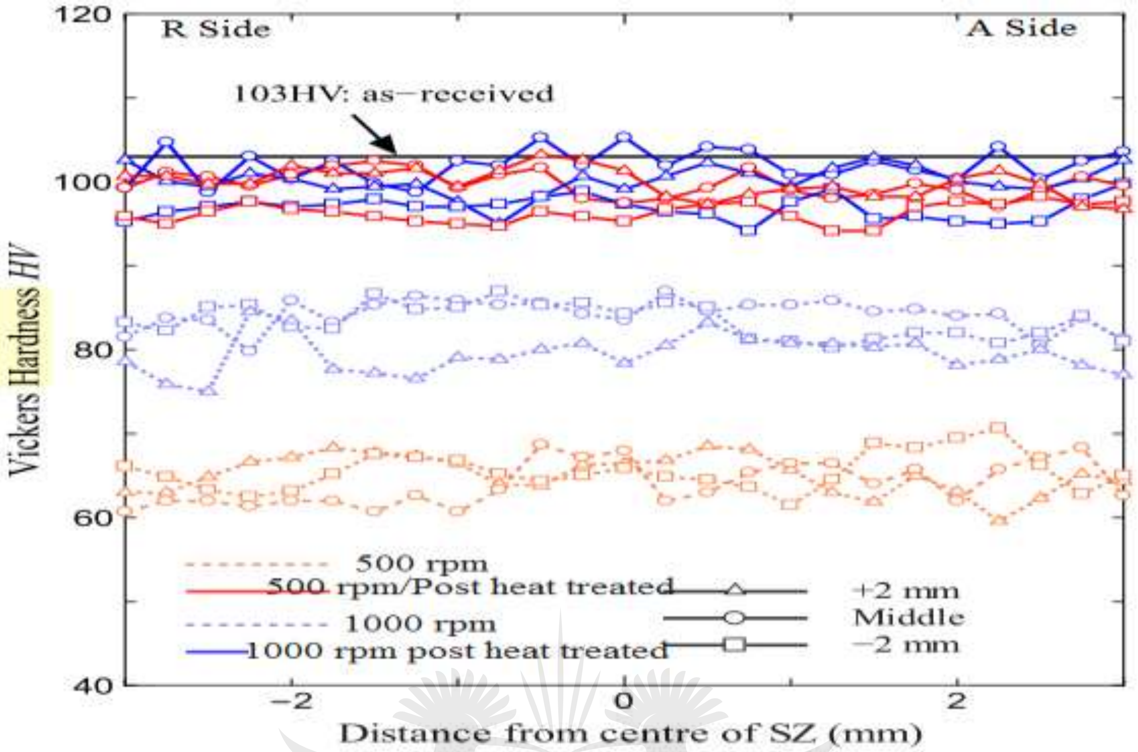

Figure 2. 21 Vickers hardness profiles (Tajiri et al., 2015)

Khodabakhshi et al 2015 investigated Friction-stir processing of an aluminum-magnesium alloy with pre-placing of the elemental titanium powder. It was concluded that a uniform hardness values were observed with the base material with an average hardness value of ~51 HV (Khodabakhshi, Simchi, Kokabi, & Gerlich, 2015). An increased (~16%) in the hardness of the stir zone was achieved after the fabrication process with the addition of reinforcements serving as secondary particles. Nevertheless, the hardness value was ramped up in SZ to ~131 HV (~156% increment) when the secondary particles were incorporated into the matrix. The improved hardness value was attributed to the addition of the well distributed reinforcements particles within the matrix, as shown in Figure 2.22a . Furthermore, the tensile properties were examined, and the engineering stress-strain curves are shown in Figure 2.22b. The annealed Al–Mg alloy exhibited a relatively low yield stress (YS, ~68 MPa) and ultimate tensile strength (UTS, ~180 MPa) with high elongation (~29.5%). The tensile strength was improved by the addition of the titanium particles, with the composites having a yield stress and UTS of 151 MPa and 246 MPa respectively.

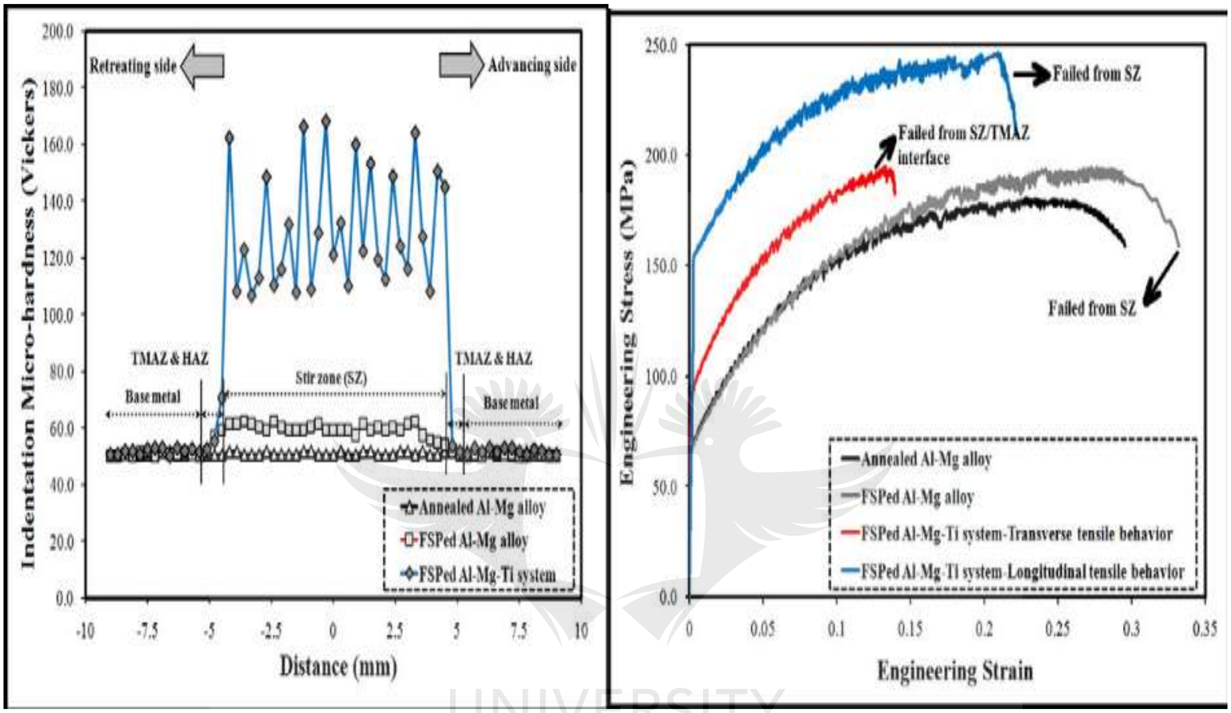

Figure 2. 22 (a) Micro-hardness profiles of annealed Al–Mg alloy before and after FSP, and FSPed Al–Mg–Ti composite. (b) Engineering stress-strain curves display (Khodabakhshi et al., 2015)

2.8.3 Wear and Friction Performance of AMCs

Anvari et al 2013 investigated the wear characteristics of the Al-Cr-O surface composite layer produced on Al6061 plate by the friction stir processing. They concluded that friction-stir processing reduces friction coefficient of Al 6061-T6. The reason for their results was caused by the periodical accumulation and elimination of wear debris on the worn track and repeated banding structure in the tool-travelling direction. The mean friction coefficients for the as-received Al

6061- T6, fabricated sample and the nano-composite were 0.28, 0.45 and 0.17 respectively (Anvari et al., 2013).

Hashemi et al 2015 investigated the wear performance of an Al/TiN dispersion strengthened surface composite produced through the friction stir process: a comparison of tool geometries and the number of passes. From their results, the average friction coefficients of the composite samples are shown in Figure 2.23.

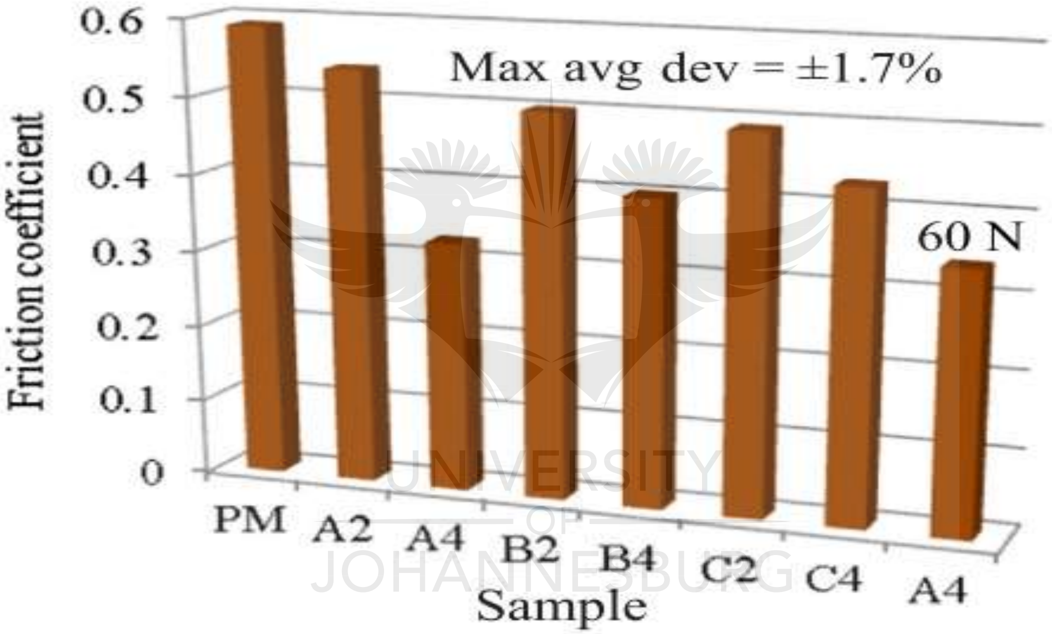

Figure 2. 23 Average friction coefficient of matrix and composite samples (Hashemi & Hussain, 2015c)

They concluded that the samples produced when using 4 passes (i. e., A4, B4 and C4) offer a lower friction coefficient than those fabricated using 2 passes(i.e.,A2, B2 and C2) (Hashemi & Hussain, 2015c). This is because the increase in the number of passes improves the distribution of the TiN particles. The friction coefficient of the samples fabricated with more FSP passes remained lower throughout the test distance. Also, the coefficient remained almost stable. This means that samples fabricated with more passes can perform consistently for longer period of time and; therefore, they may exhibit a long service life. The other samples shown in Figure 2.24 show more or less similar behavior.

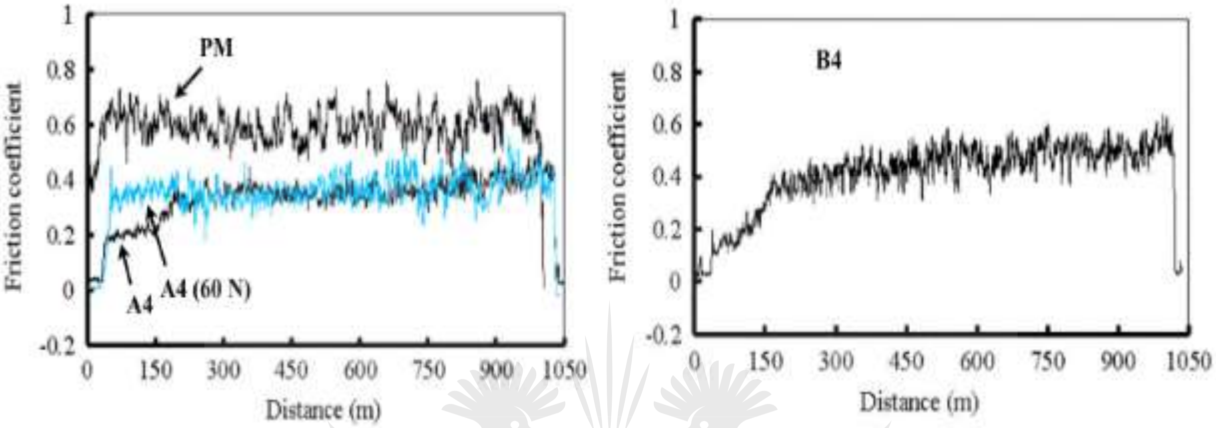

Figure 2. 24 Friction behavior of parent metal and 4-passes composite samples (Anvari et al., 2013)

Rahbar et al 2014 predicted the mechanical and wear properties of Aluminum-surface composites fabricated by using the friction stir processing with different traverse speeds. They concluded that the wear rate was found to be 219 X 10^{-5} mm^3/m at 20 mm/min and 171 X 10^{-5} mm^3/m at 60 mm/min. The increase in the microhardness of the surface composite offers resistance to metal removal during the sliding wear. Hence, the wear rate decreases when traverse speed increases (Rahbar-Kelishami, Abdollah-Zadeh, Hadavi, Seraj, & Gerlich, 2014).

Asif et al 2011 developed Aluminium Based Hybrid Metal Matrix Composites for Heavy-Duty Applications. They studied the wear behavior of their fabricated composites. It was concluded that a drastic increment in the wear rate of the binary composite was observed when the load increased from 50-80N (Asif et al., 2011).

The wear rate shows little variation with increasing sliding speed over the load range 30-50N and for higher load ranges 50-80N, only a slight reduction is observed, with increases in sliding speed from 07 to 09 m/s, as shown in Figure 2.25. It has been concluded that the wear resistance is improved with the incorporation of SiC particles with more solid lubricants than those of the binary Al-alloy.

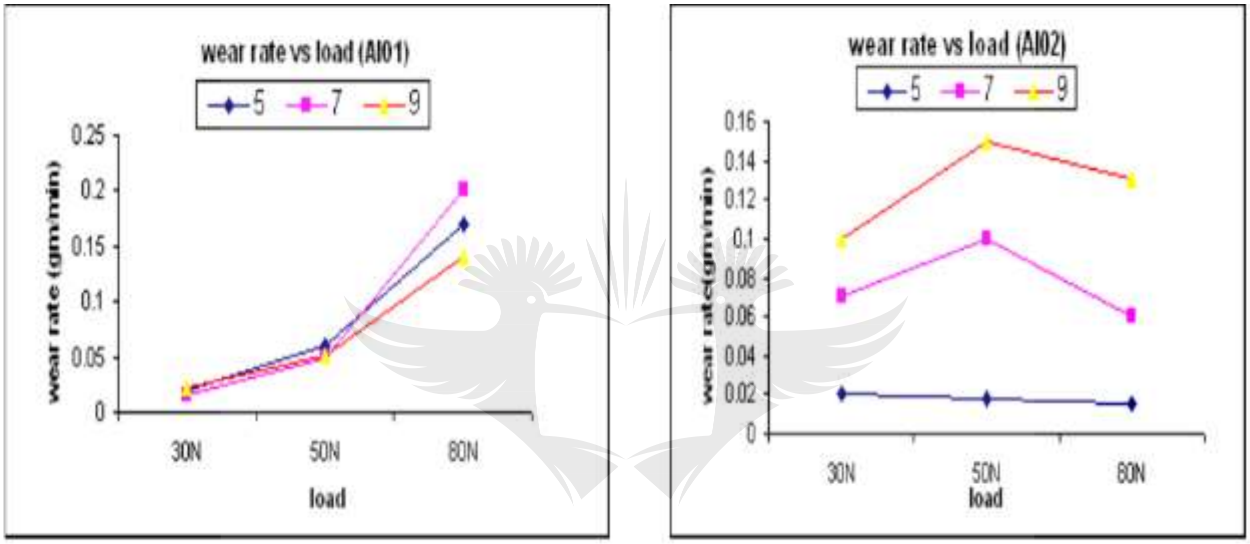

Figure 2. 25 Effect of load on wear rate of composites for different speeds: 05, 07 and 09m/s
(Anvari et al., 2013)

2.8.4 Corrosion Behavior of AMCs

Kondaiah et al 2017 investigated the Influence of TiC particles reinforcement on the corrosion performance of 6061 Al alloy. The Al-TiC composites showed a great potential for applications requiring high temperature (Kondaiah et al., 2017). SEM, EIS and EDX investigation of the microstructures reveals that the polarization resistance (Rp) amplifies with the addition of the TiC powder when compared to unreinforced alloy. The superior corrosion resistance of the composites is attributed to the excellent matrix bond between the TiC particles and the Aluminium alloy. It was concluded that TiC particles serve as good reinforcements that enhance the corrosion performance of Aluminum matrix composites.

Tang et al 2018 enhanced the surface integrity and corrosion resistance of Ti-6Al-4V titanium alloy through cryogenic burnishing. They found out that the surface integrity and corrosion resistance of a cryogenic burnished Ti-6Al-4V alloy increased greatly, due to the high density of the grain boundary and the dislocations (Tang, Zhao, Xiang, Liu, & Jia, 2018).

Yashpal et al. (2015) compared the Al-Li alloys (2099 and 2199) for aerospace applications, with 2024. As compared to 2024, the 2199 (T8E80 and T8E79 tempers) plates have less density, better corrosion resistance, better toughness and yield strengths.

The 2099-T83 extrusion alloys have high tensile, compression, shear strength compared to 2024-T83, and they also have better corrosion resistance, higher modulus and lower density (Yashpal et al., 2015). Gobara et al 2015 attempted to improve the corrosion resistance of 6061 aluminum alloy through reinforcement with titanium carbides and borides (Gobara, Shamekh, & Akid, 2015). The cyclic potentiodynamic polarization of the 6061 aluminum alloy sample, shown in Figure 2.26, shows negative hysteresis in comparison with corrosion current density of the R-Mg alloy. In addition, the corrosion potential (-1087 mV) that is higher than that of the 6061 Al sample(-1576) thereby implying a higher corrosion resistance for the R-Mg sample. They concluded that reinforcing magnesium with unreinforced 6061 aluminum alloy with titanium carbides and borides particulates improves the corrosion resistance in the aerated 3.5% NaCl corrosive medium compared to that of the 6061 aluminum alloy.

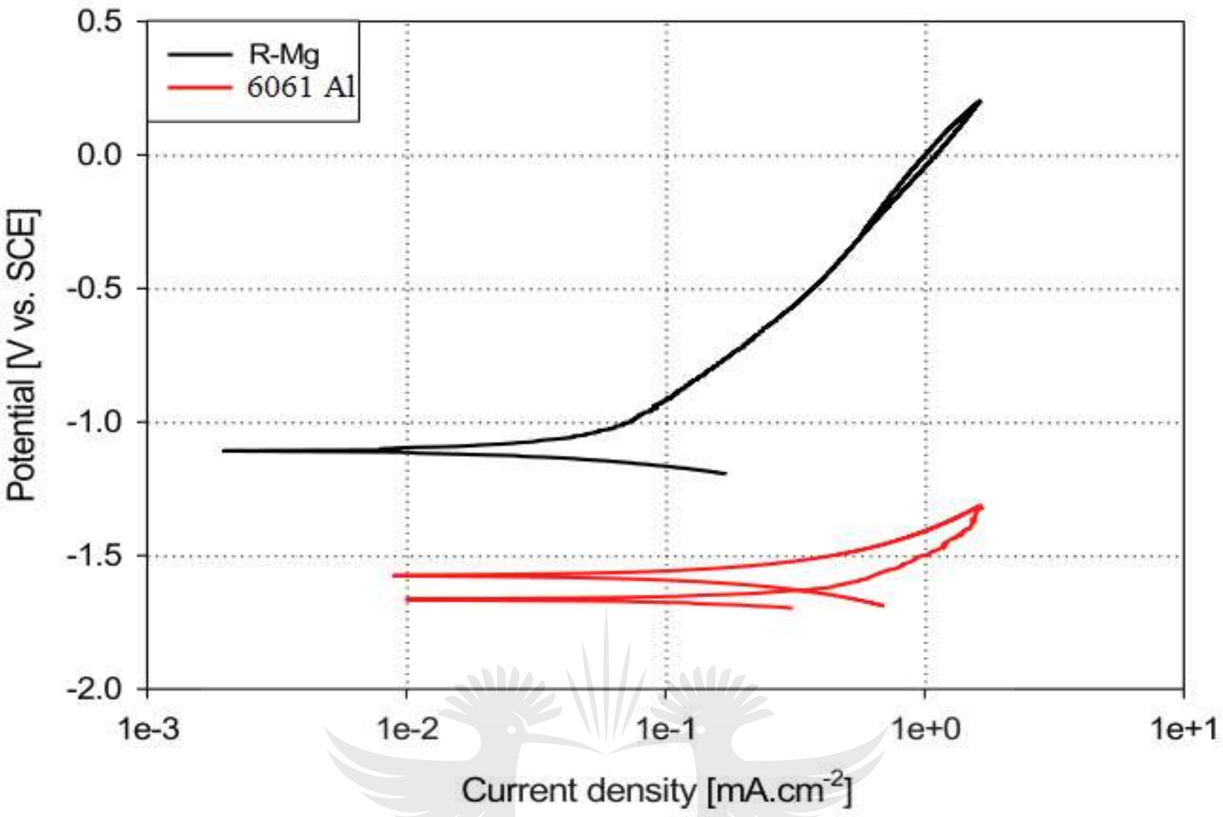

Figure 2. 26 Cyclic potentiodynamic polarization curves for 6061 Al and R-Mg in aerated 3.5% NaCl solution at room temperature (Gobara et al., 2015)

The increased usage of composites is being driven by their performance improvement, when compared with those of the conventional aluminum alloys. The composites offer benefits in both reduced weight and maintenance costs (longer inspection intervals, better corrosion resistance). The incorporation of second phase particles in the alloy matrices to produce metal-matrix composites has also been reported to be more beneficial and economical due to its high specific strength and corrosion resistance properties (Yashpal, Sumankant, Jawalkar, Verma, & Suri, 2017).

2.9 Finite Element Analysis (FEA) of the Heat Generated During FSP

Darras et al 2007 attempted to derive a correlation between the induced thermal fields and the resulting temperature generation of enough heat to soften the material, while limiting any significant grain growth. They observed that the thermal variation in the rotational or the translational speed settings, as the tool moves along the sample to maintain uniform temperature field in order to avoid the non-homogeneity in the longitudinal microstructure, which resulted from the lateral conduction (Darras et al., 2007). Assidi et al 2010 adopted a subjective Lagrangian Eulerian concept incorporated into the Forge3R simulation software through an adaptive re-meshing scheme and a splitting approach that is based on error computation (Asadi, Akbari, & Karimi-Nemch, 2014).

Koli et al 2017 developed a model that was meant for solving complex temperature and high strain-rate problem processes formed from non-linear and numerical material response. The modelling and simulation of the complete FSW process was implemented by using the elasto-plastic constitutive law developed by Johnson–Cook, as it is presented in the FE ABAQUS code (Koli et al., 2017).

Khandkar et al 2006 and Chao et al 2008, numerically predicted the residual stresses and thermal analysis for Aluminium alloys and Stainless steel. The analysis was based on analytical models that are properly configured, where its main objective is to emphasize the residual stress condition associated with the thermal history of the material produced during the process (Asadi et al., 2014)(C. Zhang et al., 2018). Their research work shows a new numerical approach predicting the residual stress distributions in FSW processes through an elastoplastic and a rigid viscoplastic model that is thermo-mechanically coupled, as against the full elasto-plastic model that has a lot of setbacks in terms of computational or iteration time and output accuracy. They applied the principle of FSW of AA6060-T4 Aluminium alloy in butt configuration. Excellent results were obtained, when the computed data were compared with the experimental results. Buffa et al 2017 built a mode to forecast longitudinal-residual stresses. Figure 2.27 shows a typical temperature evolution curve at 500 rpm and 100 mm/min acquired for a node positioned on the advancing side (AS) at 6 mm from the welding-faying surface and 2 mm from the basement of the joint closer to mid-geometry (Buffa et al., 2017).

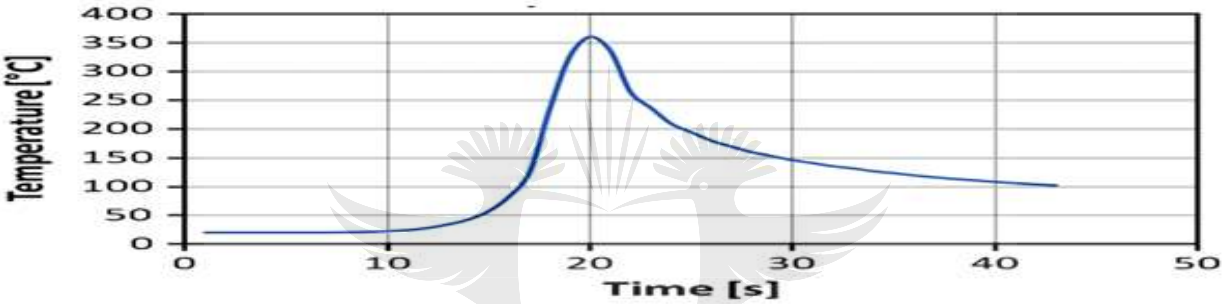

Figure 2. 27 Temperature evolution of a generic node lying in the advancing side 6mm from the welding line at the mid-thickness – 500 rpm and100 mm/min case study (Buffa et al., 2017)

Chen and Kovacevic (2017) developed a model that can be used to produce a commercial finite-element method (FEM) software, as shown in Figure 2.28. Moreover a commercial software known as ANSYS is a coupled Lagrangian and thermo-mechanically FE model, which integrates a multi-linear strain-hardening and temperature process, for the 3-D modelling of solid structures (Chen *et al.*, 2017). The temperature-gradient generation is employed to model the thermal action of the tool, as a traversing heat/thermal source. However, no consideration was made for a material model that is strain-rate dependent. In conclusion, the authors examined the response of the heat-traversing source on the FS-welded materials.

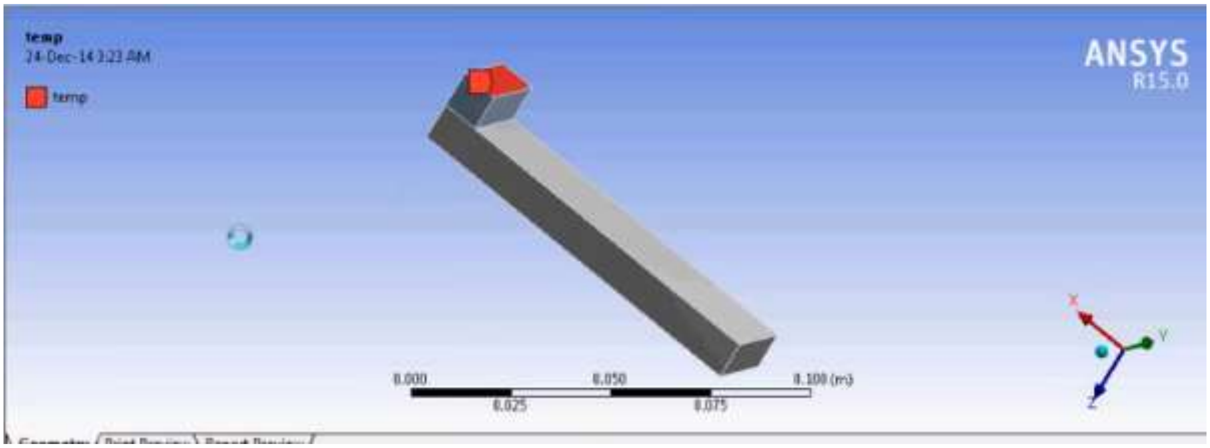

Figure 2. 28 Response of the heat- traversing source on the FS-welded materials (Chen *et al.*, 2017)

Ramadan et al 2016 developed an analytical model for heat generation, for an eccentric cylindrical pin in FSP of Al alloys. They concluded that there is a good agreement between the generated heat energy and the associated maximum temperature by the proposed model; and they measured the results, as shown in Figure 2.29. With the proposed analytical model approach one can directly predict the peak temperature for respective tool pin's eccentricity, under given process conditions. This would be helpful for further predicting the mechanical properties for that Al alloy, and hence, for the elimination of the post-weld testing cost and time (Ramadan et al., 2016).

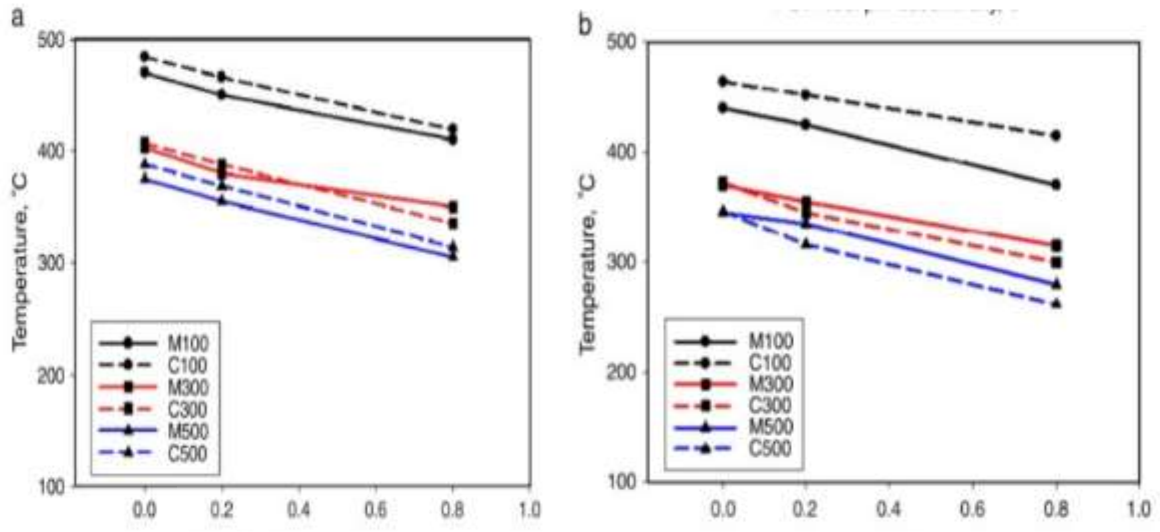

Figure 2. 29 Variation of calculated and measured peak temperature with the tool pin eccentricity for FSPed (a) AA1050-H12, (b) AA5754-H24 at different welding speeds of 100, 300 and 500 mm/min (Ramadan et al., 2016)

In conclusion, modelling is another effective way of checking the heat generated due to friction, which in turn affects the mechanical properties of the composites. Until now, no studies have reported heat generated due to friction of the composites as a result of varying the tool rotational speed. The knowledge gap in forecasting the effects of the heat generated during FSP, by using either mechanical testing, or via the computational approach, is urgently needed. Simulation of the process was a major challenge; but with the availability of some commercial software, like ANSYS and ABAQUS, it becomes easier to model.

The choice of the appropriate mesh type, materials and geometry properties, thermal properties and heat input model are key to getting an accurate model.

2.10 Summary

A literature review has been conducted on the background of the friction stir processing as a means to fabricate metal-matrix composites and in particular Aluminum-matrix composites. It shows that not much importance has been shown on producing FSP composites on 1100 Al and Ti-6Al-4V by considering the process parameters, such as the number of passes, the tool rotational speed and the tool geometries. Ti-6Al-4V powder has numerous advantages as a reinforcement to Aluminum alloys; the fabrication of this alloy could be an alternative in applications of AMCS in automotive, medical and aerospace industries.

In this study, we have focused on the usage of the FSP method by using various process parameters and tool geometries to produce composites fabricated with Ti-6Al-4V and 1100 Al alloy. Furthermore, the related review of the literature to the current study has been successfully conducted and published. The next chapter will present the research methodology.

CHAPTER 3

3.0 METHODOLOGY

3.1 Introduction

This chapter addresses the main experimental procedure and the outcome of the preliminary laboratory experiment conducted to explore the feasibility of the friction stir processing technique. With a basic understanding of the process of friction-stir processing technique, a design of the experimental approach was carried out, in order to get a better understanding of the effect of the tool geometries and the process parameters on the friction-stir processed Ti-6Al-4V and 1100 Al alloy composites. Tools with two different geometries were designed and machined to produce the composites. Additionally, a detailed experimental procedure and the methods of analysis used in this research will be discussed in this chapter.

3.2 Experimental set up

3.2.1 Parent material and reinforcing powder

The parent material used in the research work is 1100 aluminum alloy and the reinforcement is Ti-6Al-4V particles. The aluminum sheet with 5mm thickness was cut in a rectangular form of measurement 250 x 200 mm and four grooves were machined into every single sheet, the grooves have a width and depth of 2.5mm and 2 mm, respectively. The aluminum sheets were clamped on the FSP machine and subsequently processed, as shown in Appendix A. The chemical composition of the parent material was determined, using a spectrometer (Q4 TASMAN). Emery paper was used to remove the oxide layer; and the plates were then washed with ethanol. Table 3.1 shows the chemical composition of 1100 Al**.**

Table 3. 1 Chemical composition of the 1100 Aluminum Alloy

Element	**Al**	**Cu**	**Zn**	**Fe**	**Si**	**Others**
Percentage(%)	97	0.15	0.09	0.95	0.95	0.86

The powder used is a Ti-6Al-4V alloy powder, the as-received Ti-6Al-4V powder was characterized using a Particle Size Analyzer and the average size of the particles was found to be 65.23 µm and the chemical composition of the powder is shown in Table 3.2. The particles have a spherical structure, which is also non-porous; with particles attached with bigger ones, forming satellites, the formation of these satellites shows that gas atomization was used to fabricate the Ti-6Al-4V powder.

Table 3. 2 Chemical composition of the Ti-6A-4V particles

Element	Ti	Al	Fe	O	C	Ni	V
Weight (%)	89.18	6.25	0.03	0.20	0.08	0.06	4.2

3.2.2 FSP Tools

The tools were machined to fit the FSP machine at Indian Institute of Science, Bangalore, India as shown in Figure 3.1.

Figure 3. 1 5-Axis friction stir-welding machine used for the friction stir processing of the composites

The tool material is H13 tool steel hardened to 50-52 HRC, this tool produces adequate frictional heat required for the process as well as fruitful mixture of the powder into the alloy structure. FSP tool made of H13 tool steel with a shoulder of 20mm diameter and the constant tool pin length of 4mm and pin diameter of 5mm. Some specimens fabricated via with rectangular tool geometry were damaged due to unfavorable heat input on the base material as a result of the tool pin geometry. The choice of the pin length was motivated by the fact that the pin length must not be equal to the total thickness of the base materials. The tool dimensions and tool features are shown in Figure 3.2.

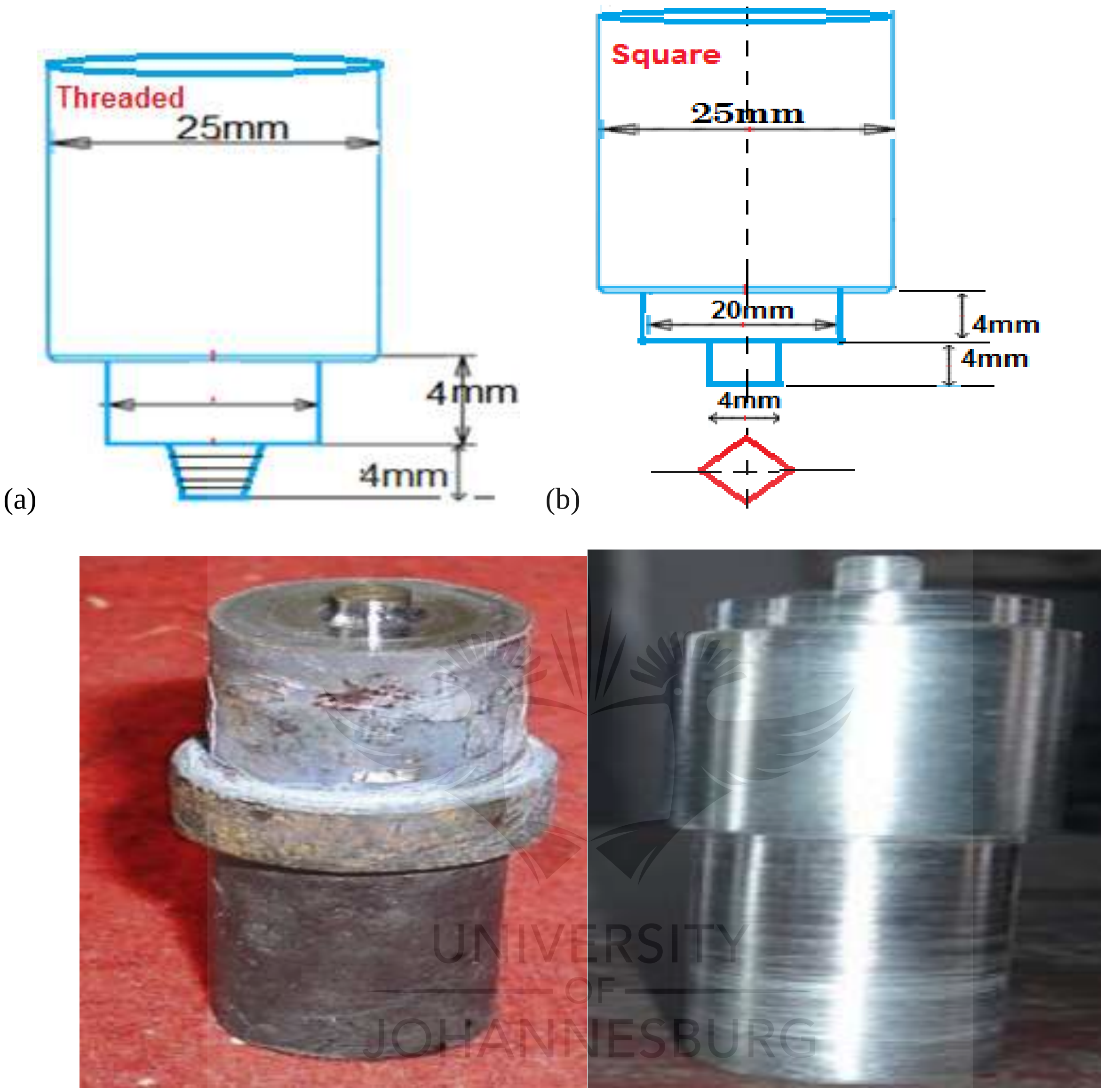

Figure 3. 2 Schematic and Images of FSP tool used in this project: (A) Threaded taper tool geometry (B) Square tool geometry

3.2.3 Process parameters

The variables that mostly influence the outcome of the FSP specimens are identified as: the rotational speed, the number of passes, the transverse speed and the tool geometry. The traverse speed was optimised during the preminary work and the traverse speed of 30mm/min was considered adequate for the current research work. The rotational speed, the number of passes and the tool geometry were varied for each of the fabricated samples.

In addition, the axial forces and the torques were recorded and correlated to the tool geometry and the process parameters. Two different rotational speeds were used in this investigation, namely; 600 and 1200 rpm. The fabricated samples were subjected to three cummulative passes with different plunge depths for each FSP pass.

Prior to the production of the final matrix, preliminary samples using different rotational speeds, tool design and three cummulative passes were conducted; and the results were analysed. It was noticed that almost all of the samples produced with rectangular tool geometry, on1200 rpm and 20mm/min transverse speed were damaged, as shown in Figure 3.3.

Figure 3. 3 Damaged tool and materials, produced via three passes/rectangular tool geometry/1200rpm and transverse speed of 20mm/min

Thus, the optimized rotational speeds and the chosen tool geometry were used to produce the final matrix. Subjecting the workpiece to numerous passes may lead to an excessive heat input, which may have a negative effect on the resulting properties of the processed sample (Abraham, 2012).

Hence, this research was limited to three cumulative passes. After three(3) cumulative FSP passes, twelve different specimens were fabricated (named A1, B1, X1, Y1, A2, B2, X2, Y2, A3, B3, X3, and Y3). A summary of the final design of the experiment and definition of terms are presented in Table 3.3.

Table 3. 3 Design of Experiment

Samples	Tool Geometries	Number of Passes	RPM/ Plunge depth	Fixed Parameters
A-1	Threaded	1	600/ 2.5 mm	Feed rate (f): 30 mm/min.
A-2	Threaded	2	600/ 3.0 mm	
A-3	Threaded	3	600/ 3.5 mm	Tilt angle (α): 2.51.
B-1	Threaded	1	1200/ 2.5 mm	Shoulder penetration (d) 0.2mm.
B-2	Threaded	2	1200/ 3.0 mm	
B-3	Threaded	3	1200/ 3.5 mm	
X-1	Square	1	600/ 2.5 mm	Plunge speed 10mm/min.
X-2	Square	2	600/ 3.0 mm	
X-3	Square	3	600/ 3.5 mm	
Y-1	Square	1	1200/ 2.5 mm	100% Inter-pass overlap
Y-2	Square	2	1200/ 3.0 mm	
Y-3	Square	3	1200/ 3.5 mm	

To ensure accuracy of the results, two replicates were produced for every sample. Figure 3.4 illustrates the FSP set up: the backing plate and clamping system during the process, the backing plate used in this project was a mild steel plate bolted to the welding bed.

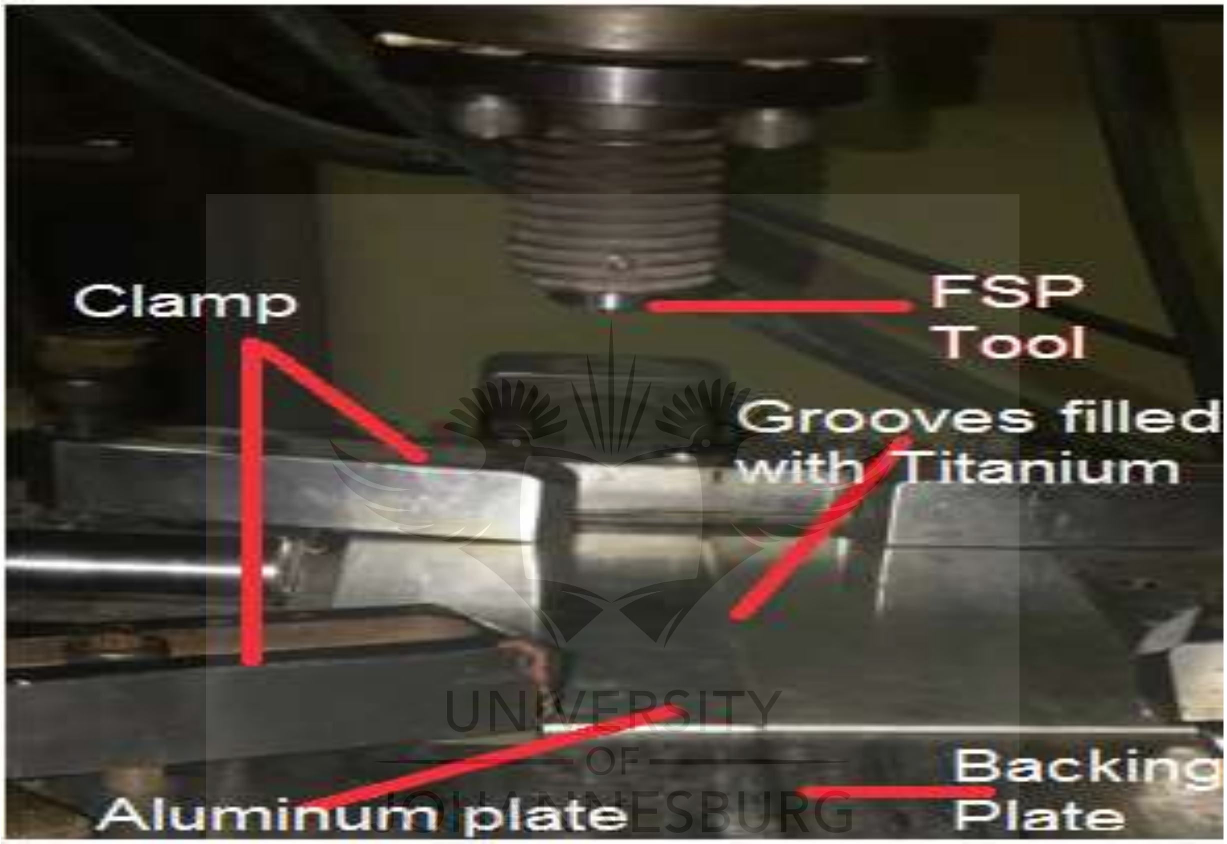

Figure 3. 4 The FSP set up showing the backing plate, the tool holder, the tool, the aluminium plate, and the clamping system

3.2.4 Friction Stir Processing Procedure

The 1100 Al alloy sheets were cleaned with Silicon Carbide paper and acetone, to remove the oxide layer; and the Ti-6Al-4V particles of 25% volume was poured into the grooves, and subsequently covered with aluminum strips, in order to prevent loss of the reinforcing particle. The sheets were subjected to three cumulative passes. After each pass, it was ensured that the tool, the tool holder and the processed sheets were cooled to room temperature, before the next FSP pass, by streams of compressed air at the end of each process.

This is performed, in order to prevent preheating of the next processed sample by the tool. Figure 3.5 shows aluminum sheet filled with Titanium powder.

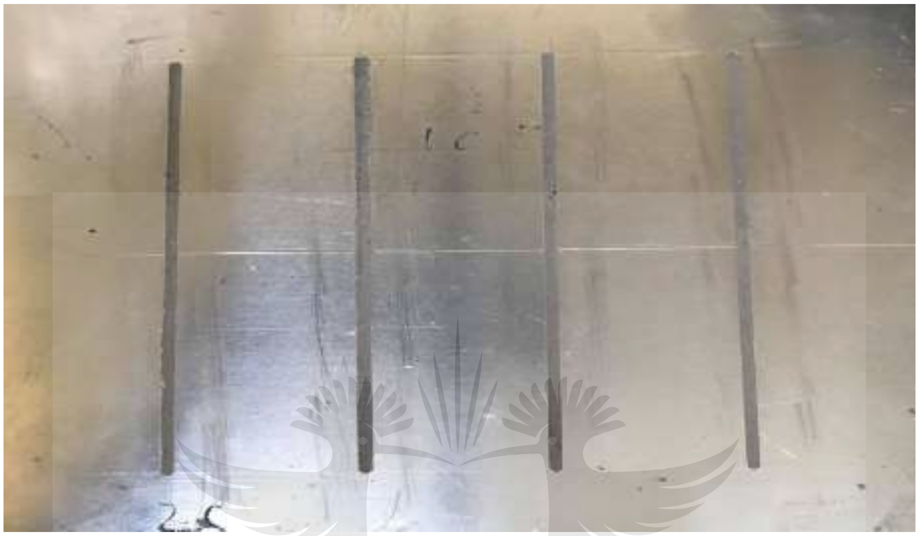

Figure 3. 5 Aluminium sheet filled with Titanium powder

3.3 Experimental techniques

3.3.1 Tensile Test

To test for the tensile properties, the 3mm sheet thickness of the 1100 Al alloy were cut by using an EDM machine, in compliance with ASTM standard (G133-05 ASTM standard). Tensile tests were carried out at 25 ºC (room temperature) using an electronic tensile machine with 2.0×10−3 s^{-1} strain rate. This is located at the mechanical laboratory in Indian Institute of Science, Bangalore, India. The equipment was used to pull the samples less than 200kg. Figure 3.6 shows the dimension of the tensile specimen prepared for mechanical testing.

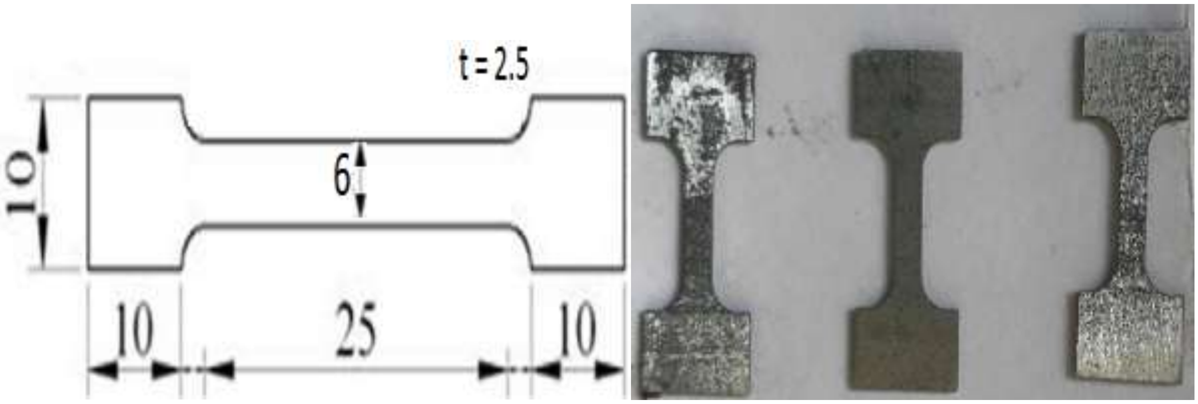

Figure 3. 6 Dimension of Tensile sample

3.3.2 Microhardness Profiling

All the fabricated specimens were cut by a metallographic cutting tool with high accuracy, so as to examine the micro-hardness of the material along its cross section. The cut samples were mounted inside thermoset resin; and upon solidification of the hot mounting process, the samples were polished to have an unscratched surface finishing having a mirror-like look. The micro-hardness tests were done by using a digital microhardness tester that has a diamond indenter and in accordance with ASTM standard (ASTM E2651-13 standard), using a 200 g load with dwell time of 15 secs as shown in Appendix B. Upon examination of the specimens under the micro-hardness machine, some indentation lines were made across the cross section of the samples. A 1mm interval was maintained throughout the test, and the test measurements were carried out on the composites at three different zones (the stir zone, the thermo-mechanical affected and the heat affected zones).

3.3.3 Sample Preparation for Microstructural Analysis

Processed samples were hot-mounted with poly-fast as shown in Figure 3.7; and subsequently ground and polished on the round magnetic table of the grinding and polishing machine. Three samples were accommodated in the slots of the machine and fixed under the friction-forced rods. Two stages were involved in the grinding operation. The first stage is the plain grinding. All the samples were rough-ground using a 320#, 500# and 800# grain size silicon carbide paper. The silicon carbide paper was attached to a MD Gekko circular plate, and placed on the grinding magnetic rotary table, as a shown in Appendix C. The plain grinding was done under low pressure running water for about 5 minutes at a speed of 300 rpm. The samples were removed after the stoppage of the machine. The surfaces of the samples were washed carefully with liquid soap, rinsed with clean water, acetone was applied, and then dried off with a hand dryer.

Figure 3. 7 Hot-mounted samples

The next stage is the fine grinding; and this was done on the same rotary table attached with MD-Largo circular disc and a Dia-pro suspension applied to achieve the correct level of lubrication.

The samples were ground at a speed of 150 rpm for 5 minutes. The samples were removed again; and they followed the same principle of cleaning and drying of samples, as initially explained.

On the same machine, the polishing was done using the MD-Chem circular plate with the OP-S suspension; and it ran at a speed of 150 rpm for about 5-10 minutes. A mirror-like surface of the samples was observed with no scratches; and this serves as an indication of a good grinding and polishing operation.

3.3.4 Optical Microscopy analysis

The BX51M Olympus microscope, the image of which is displayed in Figure 3.8, was used for capturing the microstructures. The friction-stir processed samples were prepared by using ASTM standard (E3-11 ASTM Standard). Prior to the microscopic observation, the Kroll's reagent was prepared for the bulk samples and the deposited Ti-6Al-4V/1100 Al composites. The Kroll's reagent is prepared [100 ml distilled H_2O, 2 ml HF and 4 ml HNO_3]. Etching was done for a period of between 20 to 30 seconds. Both the un-etched and the etched samples were observed on the BX51M Olympus microscope - at both low and high magnifications, in order to assess the microstructures, porosities and grain sizes of all the participating samples.

Figure 3. 8 Image of an Optical Microscopy

3.3.5 Scanning Electron Microscopy (SEM) coupled with Energy Dispersive Spectroscopy (EDS)

Metallographic observations and EDS analyses were carried out, in order to investigate the distribution of the Ti particles within the matrix and their grain sizes after three cumulative passes. A TESCAN Scanning Electron Microscope (SEM) equipped with the EDS, was employed to study the dispersion of the particles and the surface morphology at different magnifications, by using the ASTM metallographic standard procedure (E384 -11^{e1} ASTM standard). The SEM equipment shown in Figure 3.9 is incorporated with an EDS, and the EDS revealed the elemental distribution of the surface appearance.

Figure 3. 9 Scanning Electron Microscope

3.3.6 X-ray Diffraction (XRD)

X-ray diffraction (XRD) examinations were conducted for the qualitative analyses (phase identification) to determine the possible intermetallic compounds and their possible composition. The prepared specimens were studied by using a D8 Advance diffractometer as shown in Figure 3.10; the recording range was 10^o to 120^o, a step size of 0.04^o using a 2 mm collimator. Furthermore, an X-ray diffractometer Rigaku Ultima IV equipped with PDXL analytical software with Cu (K α) was also used to confirm the phase identification of the parent materials. The 2 theta scan was from 5^o to 90^o at 0.02^o per step. A 5 mm thickness of 1100 Al sheet was exposed to the X-Ray for 5 minutes. The radiation source used was Gamma Ray (Iridium isotope i.e. Ir-192) and ASTM standard industrial X-Ray Film (E-1815 ASTM standard) was used as a viewer. The film density is 2 to 4kg/m3 with a sensitivity of 2%. The source film distance (SFD) of 304.8mm was adopted for the geometry sharpness; while lead screens of 0.1 mm front and 0.15 mm back were positioned. Additionally, intermetallic compound analyses were carried out in the TMAZ, SZ, and in the HAZ of the samples.

Figure 3. 10 XRD machine

3.3.7 Wear test analysis

The wear performance of composites and the parent material were examined using Pin-on-Disc wear testing machine on a sample size of 4mm width and 4mm length, in accordance with the ASTM standard (G133-05 ASTM standard). The wear test machine is a universal micro-tribotester

(UMT-2, Center for Tribology, Inc.) located in the Metallurgy department of University of Johannesburg. Before the wear examination, each sample was ground down by using abrasive paper with a micron of 1000. Some parameters were fixed during the test such as; pin diameter of 6mm, 5mm pin length, wear radius of 13.5 mm, disc radius of 17.5mm, average hardness value of steel disc of 60HV, rate of acquisition as 100 Hz, surface roughness of 0.2 μm, the sliding distance as 1000m, while the sliding speed was set at 4.19cm/s. All tests were initially subjected to normal load of 20N, and these tests were carried out at room temperature of 25^{o} C, and relative humidity of 50%. For this wear operation, both the frictional force (Fx) and the normal force (Fz) are set at zero; and this was done so that the load of 20 N could be achieved.

The control unit is a part basic system and a computer-based unit with Dalton control software using windows 2000 or XP operating system and the friction coefficient of these composites were generated with this software as shown in Figure 3.11.

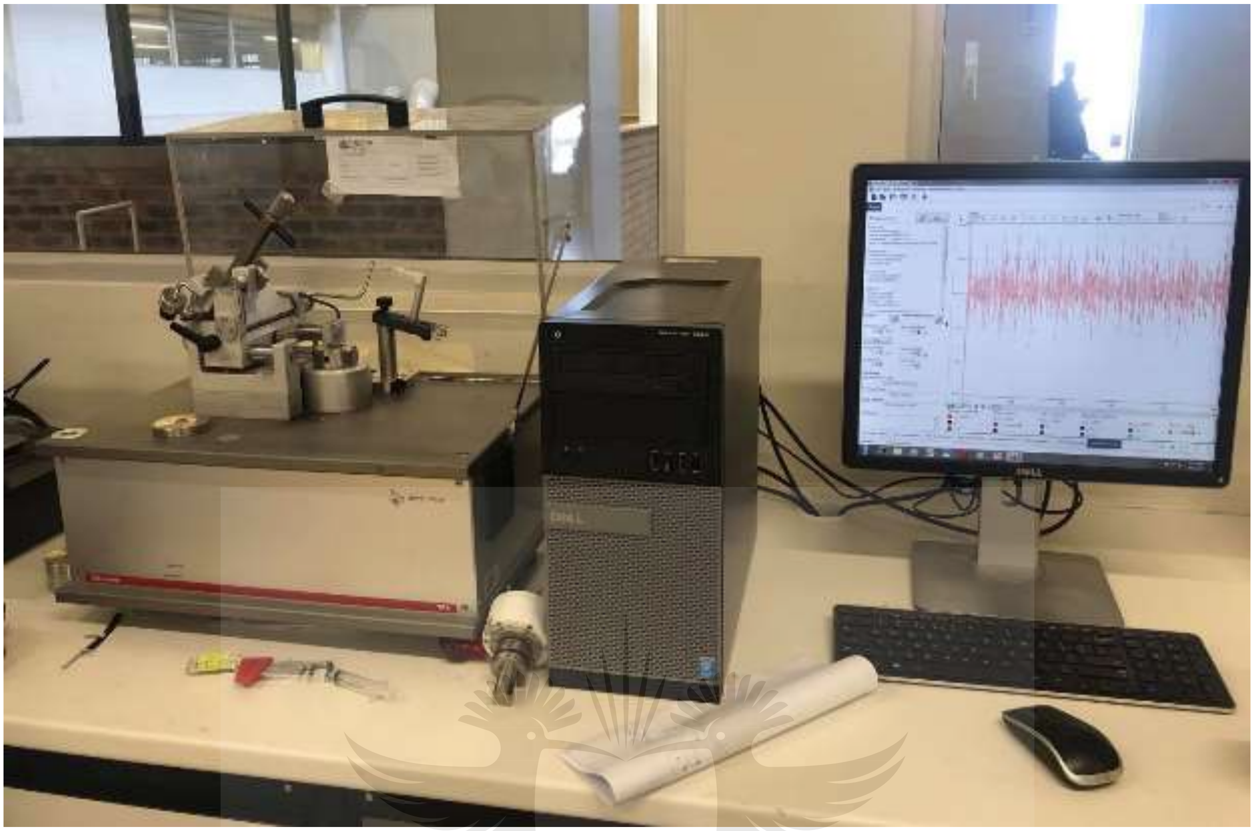

Figure 3. 11 The wear test set up

The mass loss of all samples was measured by using a profilometer; the wear volume was calculated from the length of the stroke, the width of the wear scar, and the depth of wear that were made on the surface of the deposited samples by the tungsten ball, the profilometer is shown in Figure 3.12.

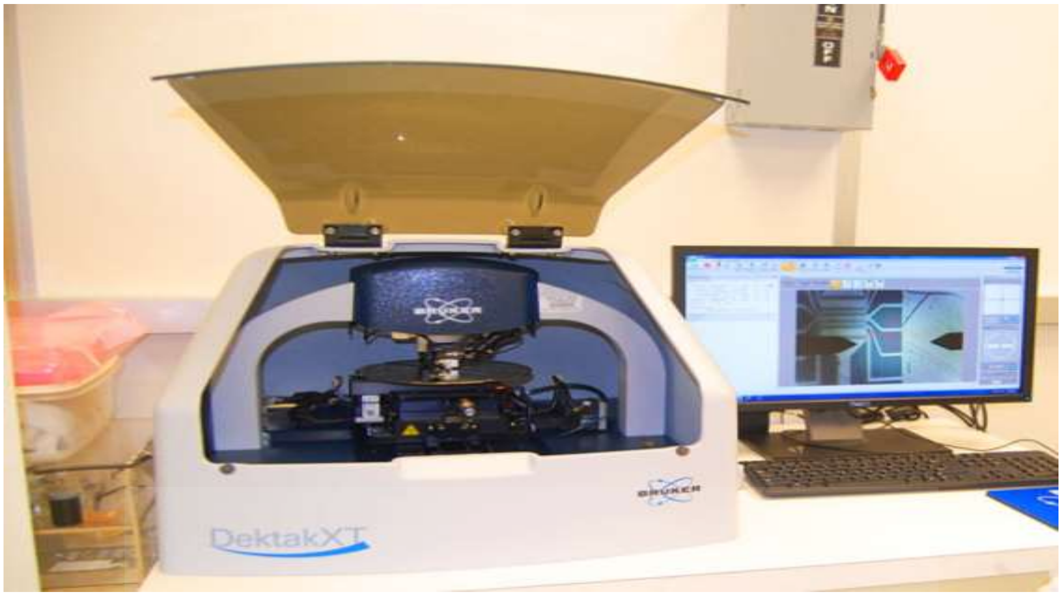

Figure 3. 12 The Profilometer

3.3.8 Corrosion test analysis

To test for the corrosion resistance of the composites and the parent material, samples were cut with EDM across the surface of the processed sheets in a square shape of 25 mm width and 25 mm breadth. The electrochemical measurements for the corrosion rate were conducted using the standard practice, according to the ASTM standard (ASTM G102-89, 1999). The processed samples were cold mounted and the surface ground down with 1000# emery sheet to obtain a smooth surface.

The samples were subsequently placed on the copper rod by connecting them electrically using epoxy resin as shown in Figure 3.13, and the measurement of potentiodynamic polarization was carried out in 3.5 wt.% Sodium Chloride (NaCl) solution.

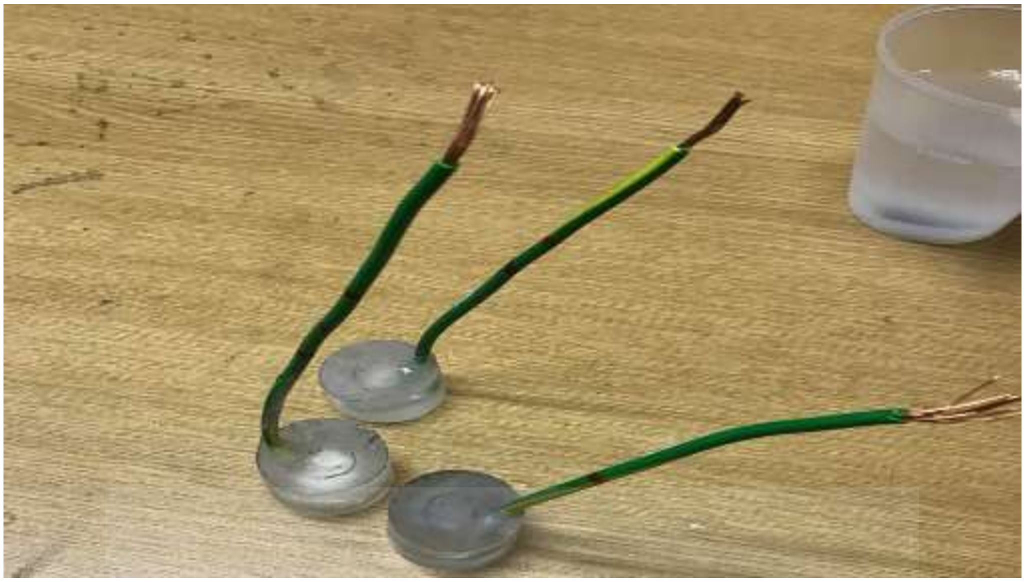

Figure 3. 13 Cold Mounting of Sample for Corrosion test

The samples, having an exposed area of 1 cm^2 were used as the working electrode. The electrochemical tests were carried out at 25^{o}C (room temperature) by using a Parstat 4000 model potentiostat/galvanostat, which has a corrosion analysis software installed in the computer as shown in Figure 3.14. A saturated calomel electrode was used as the reference electrode. Between −250 mV and 250 mV potential was applied versus open circuit potentials (OCP), which were determined after 3600 secs of immersion in NaCl solution. 1 mV/s was set at the scan rate.

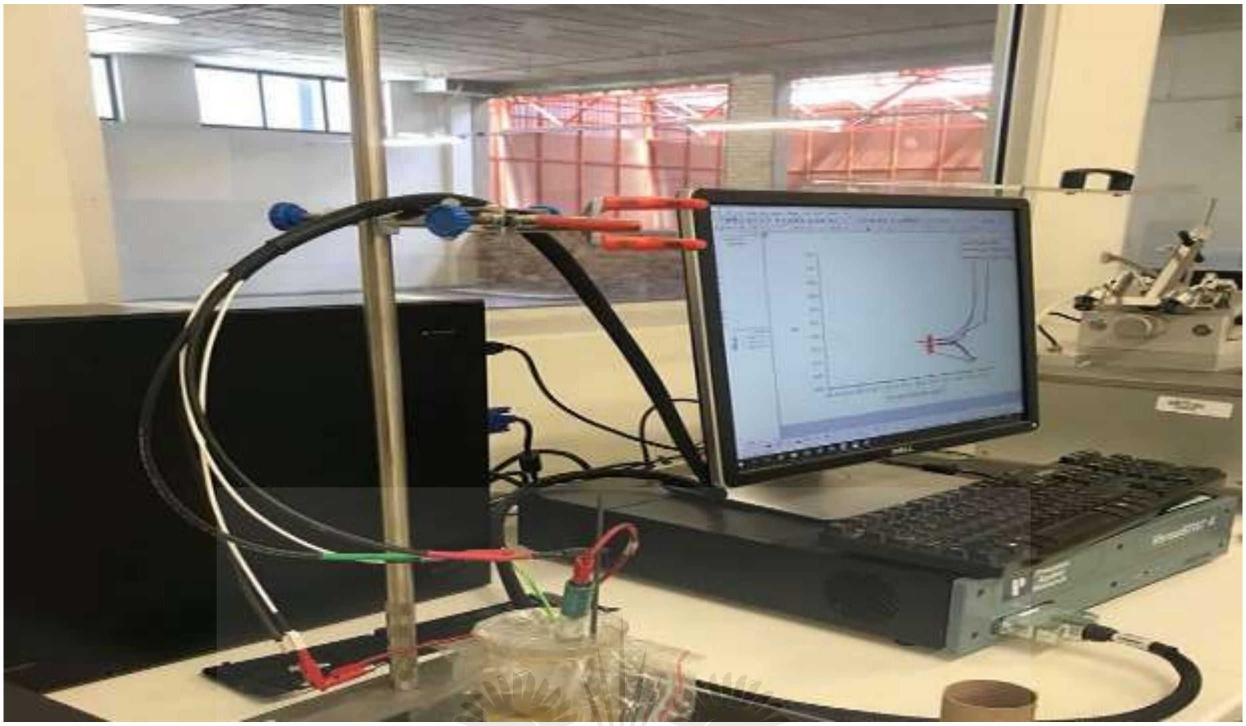

Figure 3. 14 The corrosion test set up

3. 3.9 Prediction of the grain sizes within the Microstructure using Otsu Image Segmentation

Otsu’s method (Otsu, 1979) was used for image thresholding. The technique is a nonparametric as well as unsupervised thresholding technique, which selects optimum thresholds from a maximization of intraclass variance of binary images. A significant assumption in the algorithm is the bimodal class of the image, this includes the foreground and background pixels which the microscopic images in this study satisfy. The method is apparently a 1-dimensional. The global optimal threshold value was obtained for the microscopic images. Particle size in the material samples for the three passes were identified using the difference in intensity if resulting images after thresholding.

Given the local thresholds $t_1, t_2, t_3, \ldots\ t_n$ to be selected from, the thresholds subdivide the images into n+1 classes of $C_1, C_2, C_3, \ldots\ C_n$ by maximizing the objective function given by the sum of all threshold variances (Khairuzzaman & Chaudhury, 2017);

$$J_1(t_1, t_2, t_3, \ldots\ t_n) = \sigma_0^2 + \sigma_1^2 + \sigma_2^2 + \sigma_3^2 + \cdots \sigma_n^2 \tag{3.1}$$

Where;

$$\sigma_0^2 = \omega_0(\mu_0 - \mu_T)^2, \omega_0 = \sum_{i=0}^{t_1-1} p_i\,, \mu_0 = \sum_{i=0}^{t_1-1} \frac{ip_i}{\omega_0}$$

$$\sigma_1^2 = \omega_1(\mu_1 - \mu_T)^2, \omega_1 = \sum_{i=t_1}^{t_2-1} p_i\,, \mu_1 = \sum_{i=t_1}^{t_2-1} \frac{ip_i}{\omega_1}$$

$$\sigma_2^2 = \omega_2(\mu_2 - \mu_T)^2, \omega_2 = \sum_{i=t_2}^{t_3-1} p_i\,, \mu_2 = \sum_{i=t_2}^{t_3-1} \frac{ip_i}{\omega_2}$$

$$\sigma_3^2 = \omega_3(\mu_3 - \mu_T)^2, \omega_3 = \sum_{i=t_3}^{t_4-1} p_i\,, \mu_3 = \sum_{i=t_3}^{t_4-1} \frac{ip_i}{\omega_3}$$

$$\sigma_n^2 = \omega_n(\mu_n - \mu_T)^2, \omega_n = \sum_{i=t_n}^{t_{n+1}-1} p_i\,, \mu_n = \sum_{i=t_n}^{t_{n+1}-1} \frac{ip_i}{\omega_n}$$

and $\sigma_0^2, \sigma_1^2, \sigma_2^2, \sigma_3^2, \ldots\ \sigma_n^2$ are the class variances, $\omega_0, \omega_1, \omega_2, \omega_3, \ldots\ \omega_n$ represents the class probabilities, $\mu_0, \mu_1, \mu_2, \mu_3, \ldots\ \mu_n$ represents the mean values of the segmented classes. The intensity of the whole image is $\mu_T \subseteq \mu_T = \omega_0\mu_0 + \omega_1\mu_1 + \omega_2\mu_2 + \omega_3\mu_3 + \cdots + \omega_m\mu_m$ and $\omega_0 + \omega_1 + \omega_2 + \omega_3 + \omega_n = 1$.

Segmentation of the SEM images was performed at different milling time using a MATLAB script implemented in MATLAB R2015a installed on a desktop computer workstation with configuration 64 bits, 32GB RAM Intel (R) Core (TM) i7 5960X.

3.4 Finite Element Simulation Using ABAQUS/CAE

3.4.1 Material Set up

The modelling of the aluminum plate with a length of 150mm, breadth of 50mm and base extrusion depth of 200mm was performed using ABAQUS 2019 edition, in order to check for the heat generated due to friction caused by the base material and the FSP tool during the process as shown in Figure 3.15.

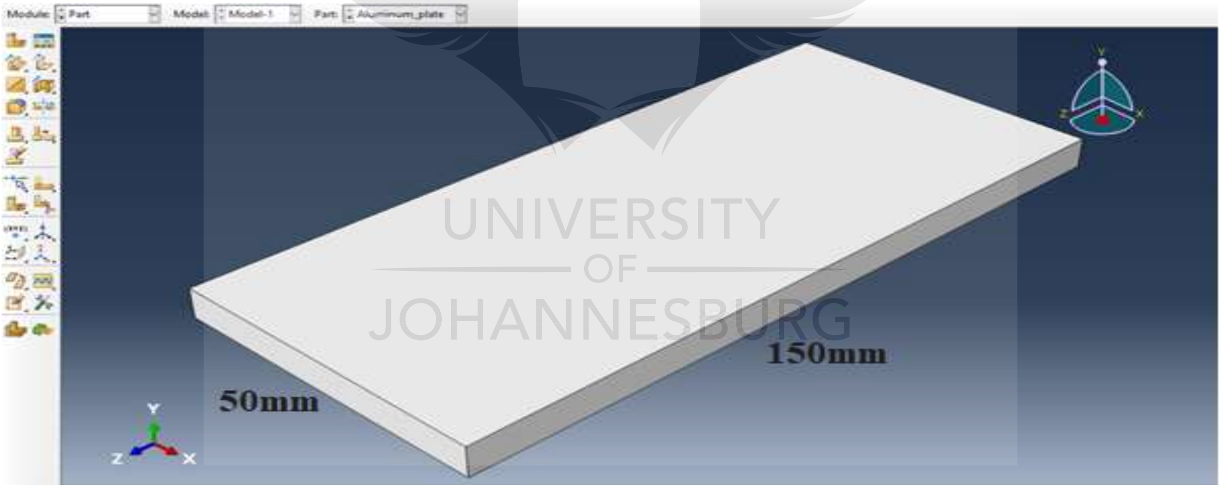
Module: Part
Model: Model-1
Part: Aluminum_plate

Figure 3. 15 Dimension of the 1100 Aluminum alloy as the base material

The FSP tool image is shown in Figure 3.16, it should be noted that heat is generated by the contact between the tool shoulder and the base metal hence the tool pin has little or no effect on the heat generated during the process (Mil & Stamenkovi, 2009). A linear static and non-linear transient modelling method for the nodal temperature at nodes was used to predict the heat generated during the process.

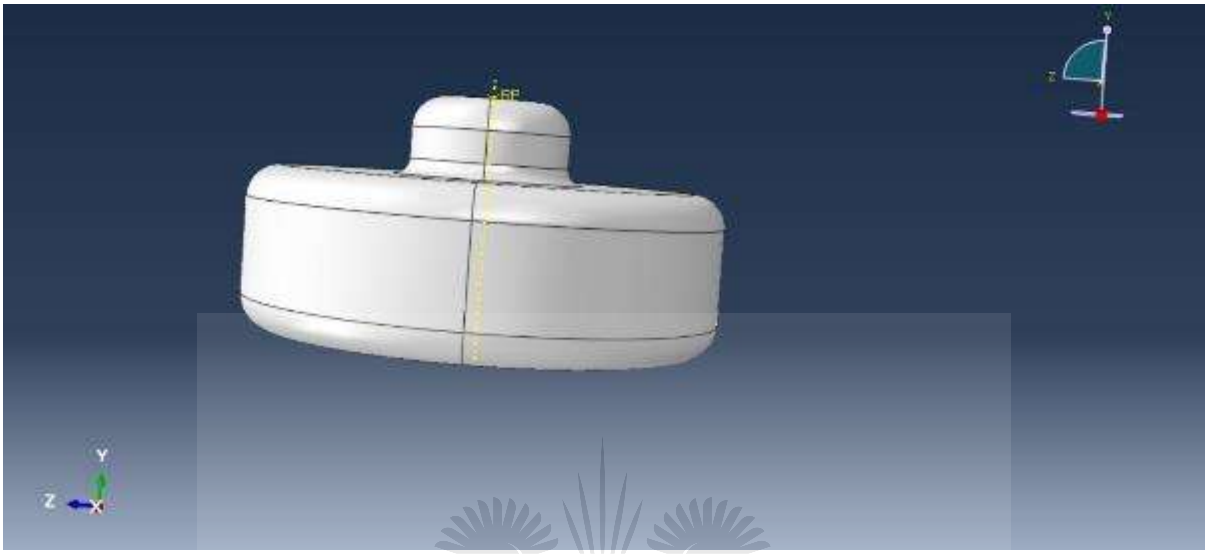

Figure 3. 16 Dimension of the FSP tool

3.4.2 Description of the Problem

The material property of the Aluminum matrix composites fabricated experimentally was used, the 3-pass composites has mass density of 2,700 kg/m^3, Young Modulus (E) of 70 GPa and Poisson ratio (υ) of 0.3. The Aluminum plate was subjected to 5000 kN load by exerted pressure on the FSP tool across a distance of 40mm as shown in Figure 3.17.

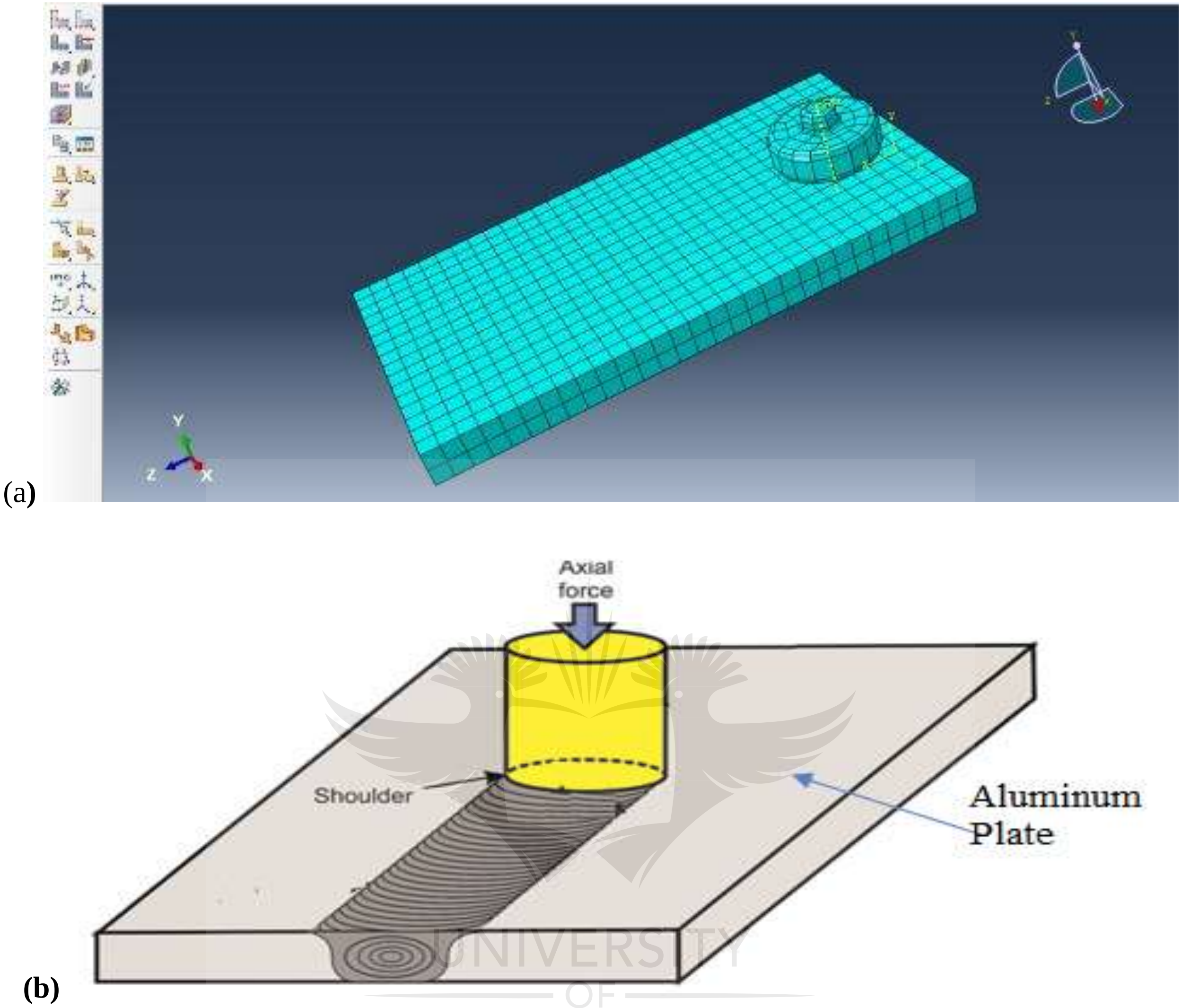

Figure 3. 17 Showing (a)Surface contact of the FSP tool and Aluminum composite plate(b) Pictorial representation of FSP set up

3.4.3 Modelling Procedure

The modelling procedure of the friction stir processed composite is stated as follows:

1. Creation of a new ABAQUS database file.

2. Creation of the aluminum plate and the FSP tool

3. Assemble both parts together as shown in Figure 3.17 (a).

4. Create Initial step by choosing Dynamic, Temp-displacement, Explicit of time period 0.1

4. Create an interaction by choosing “contact property options:

- Tangential Behavior by putting penalty of 0.3 friction coefficient
- Normal Behavior
- Heat Generation
- Friction Coefficient of 0.3”

5. Define the contact as surface-to-surface explicit by making the Base material (Aluminum plate) “SLAVE” while making the bottom of the FSP tool “MASTER” and the top of the tool as “PRESSURE”.

6. Apply boundary condition to the bottom plate on X and Z axis

7. Define the load by making the top of the tool (PRESSURE) and initial condition of -5000mm/sec velocity.

8. Put a mesh in parts (not assembly) of a global size of 5mm, by selecting the base material as explicit and coupled Temperature-Displacement.

9. Create a job, then put a data check to find if there is any pre-processor related issue, and lastly submit the job

10. Post-processing of results are generated from the field output where the nodal temperature at nodes, stress-displacement and other outputs are displayed.

3.5 Summary

Some preliminary investigations have been conducted on the parent materials. A design of the experiments was used, in order to set up the experiments to be conducted. The Aluminium sheet of 5mm thickness was cut to a rectangular shape with 250 x 200 mm; and having grooves cut across the surface of these sheets with width and depth of 3.5mm and 3mm respectively. The volume of the Ti-6Al-4V reinforcing powder poured into the grooves of the sheets, were made to undergo 100% overlap of multi-pass FSP.

The process parameters were set at two different too rotational speed of 600 and 1200 rpm, with a constant traverse speed of 30 mm/min, and two different tool geometries. The experiment was limited to three cumulative passes to avoid excessive heat input caused by excessive number of passes, which could affect the properties of the aluminum sheet. The next chapter will present and discuss the results generated.

CHAPTER FOUR

4.0 RESULTS AND DISCUSSIONS

4.1 Introduction

This chapter covers the results and a discussion of the analyses conducted on multi-pass Friction Stir process, using different process parameters and tools. The analyses included the microstructure characterization by using the optical microscope (OM), the scanning electron microscope (SEM), the chemical analysis, as well as the phase identification- by using energy dispersive spectroscopy (EDS), and X-ray diffraction (XRD), respectively. Mechanical analyses, such as the tensile strength, and the microhardness were also conducted. Additionally, wear and corrosion-resistance tests were also investigated. Furthermore, Image thresholding and Finite-element simulation were also carried out, in order to predict the grain size of the particles and the tensile strength of the composites. The results are presented and discussed.

4.2 Parent Material and Powder Characterizations

Analysis was done by using SEM on the surface and on the cross section of the parent material (1100 Al), as shown in Figure 4.1. The dark precipitates in the as-received alloy indicate a continuous distribution inside the grains and within the grain boundaries; and the grain boundaries were detected to be elongated or stretched, the cell format of these precipitates are eutectic. The weight percentage of the elements in the aluminum alloy was determined using EDS as shown in Figure 4.2. Other elements were also detected in the 1100 Al alloy, which are indicated as “others” in the chemical composition shown in Table 4.1, these elements can be said to be oxides and carbides because of impurities and inclusions often found during the preparation process of the 1100 Al alloy.

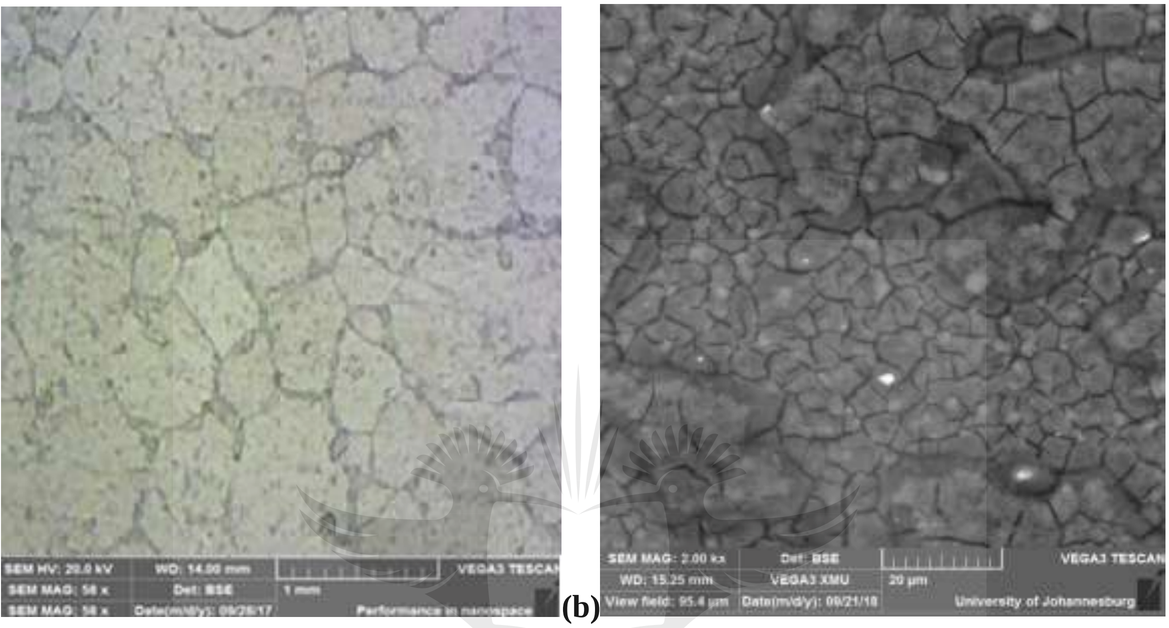

.**(a)** **(b)**

Figure 4. 1 SEM micrographs of the 1100 Al, (a) Surface, (b) Cross Section

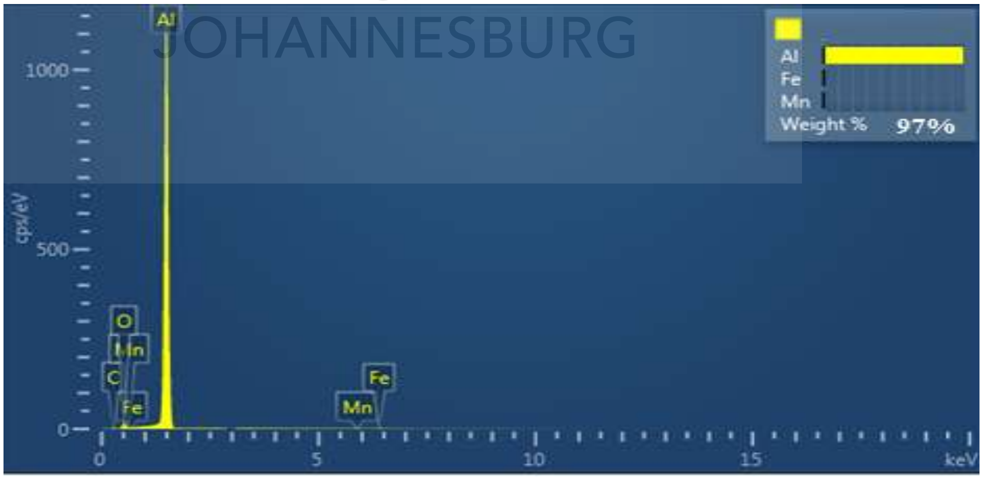

Figure 4. 2 EDS analysis of the 1100 Al alloy

Table 4. 1 Elements and Chemical composition of the Al Alloy(1100)

Element	**Al**	**Cu**	**Zn**	**Fe**	**Si**	**Others**
Percentage(%)	97	0.15	0.09	0.95	0.95	0.86

The particle size analyzer was used to characterize the as-received Ti-6Al-4V powder and the average particles size was found to be 65.23 µm, as shown in Figure 4.3. Table 4.1 shows the chemical composition of the Ti-6Al-4V powder, Ti was observed to show the highest atomic and weight percentage composition, as compared with Al and V. Both the atomic and weight percentage compositions were indicated to be close to 90 %. The powder shows a spherical structure which is non-porous, having bigger particles joined together as satellites, the Ti-6Al-4V particles was fabricated via gas atomization due to the presence of the satellites.

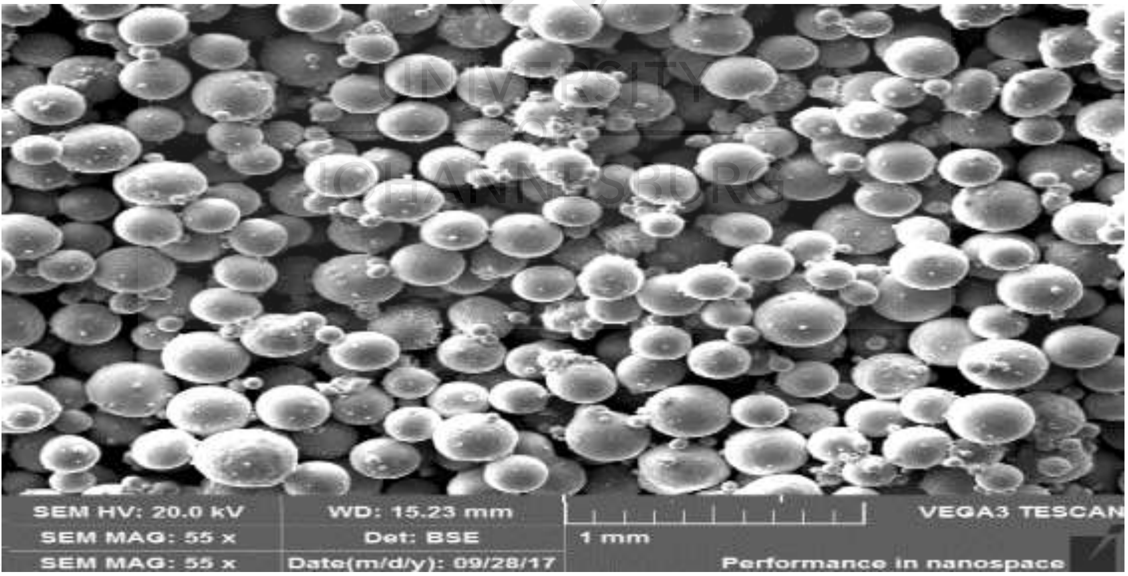

(a)

(b)

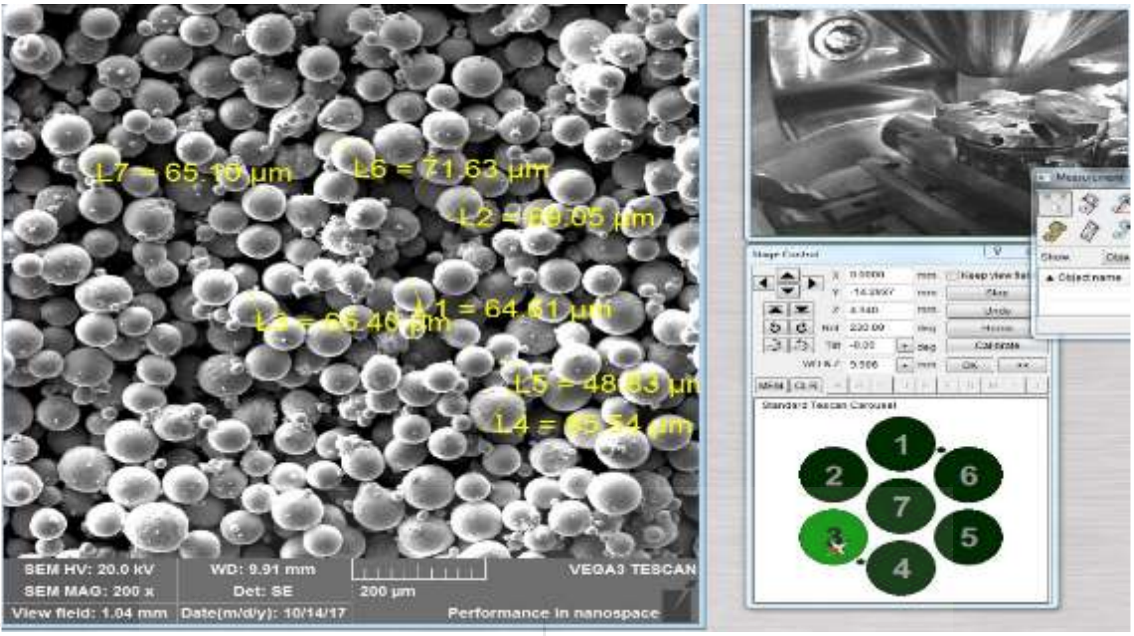

Figure 4. 3 (a) SEM image of the reinforcing powder, (b) SEM image showing the average particle size of the Titanium powder

Table 4. 2 Elements and Chemical Composition of Ti-6Al-4V powder

Element	Ti	Al	Fe	O	C	Ni	V
Weight (%)	89.18	6.25	0.03	0.20	0.08	0.06	4.2

The samples were subjected to FSP with various process parameters. Figure 4.4 shows the crown appearance of the sheets that has been subjected to FSP. 12 different samples were fabricated, and each sample are assigned a different name for proper clarification, as earlier presented in Chapter 3 (Table 3.3).

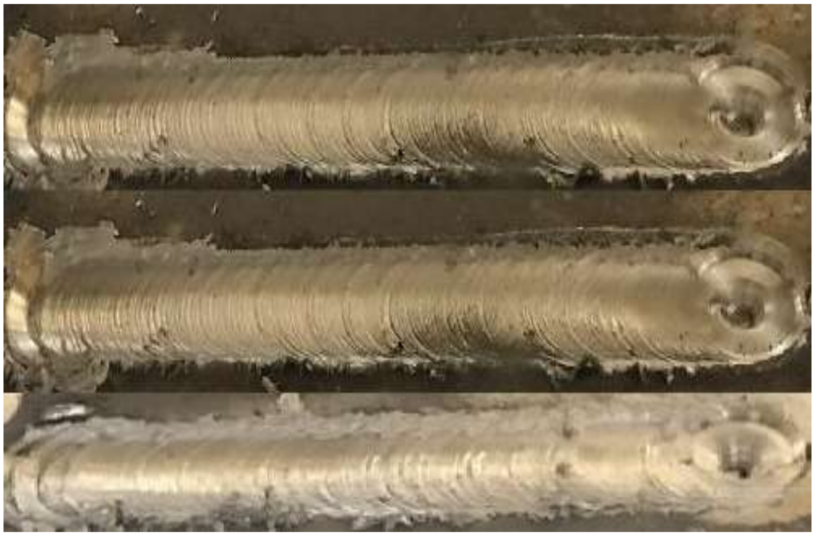

Figure 4. 4 Crown appearance of the processed sample

4.3 Optical Microscope Analysis

The micrograph of the parent material is presented in Figure 4.5. The micrograph of the Ti-6Al-4V particles are observed in Figure 4.3.

Figure 4. 5 Microstructure of the parent material (1100 Al)

The optical micrographs of some fabricated composites are shown in Figure 4.6; and the stir zones of the samples were examined to reveal the particle distributions across the matrix. Some microstructural defects were observed by the samples fabricated with 1 pass (i.e A1, B1, X1, and Y1), defects such as agglomeration of particles, pin and tunnel hole. The grain of these composites was coarse, as a consequence of the heat input and inappropriate combination of process parameters, which resulted into a reduced plastic deformation. Also, worm-hole defect was detected, which was caused by insufficient mixing within the matrix. From the images of A3(Threaded taper tool geometry) and X3(Square tool geometry), the stir zone of the X3 sample revealed a lower dispersion of the Titanium powder while that of A3 revealed a more even distribution. These examinations showed that the threaded taper tool geometry combined with 3-FSP passes give a better dispersion of particles within the matrix when compared to the square tool geometry.

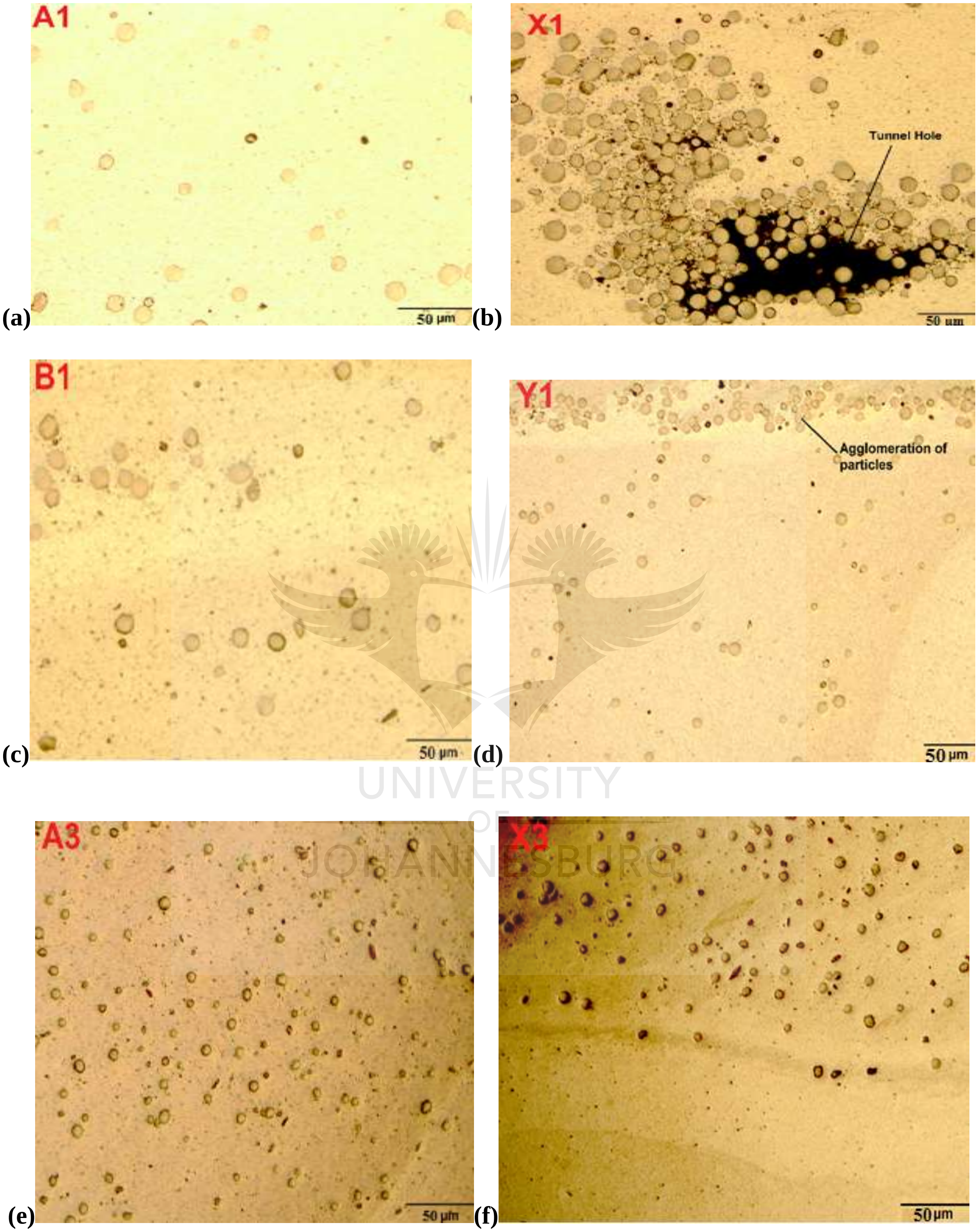

Figure 4. 6 Optical micrographs of composites (a)A1, (b)X1, (c)B1, (d)Y1 (e)A3, and (f) X3

4.4 Scanning Electron Microscope combined with the Energy Dispersive Spectroscopy (SEM/EDS)

The effect of process parameters on the microstructural evolution was examined on the SEM images of selected composites, as shown in Figure 4.7. This was done to reveal the dispersion of the particles within the matrix. In similar observations with the images from the optical microscope, microstructural defects such as tunnel holes and agglomeration of particles are observed with the composites fabricated using one and two passes, regardless of the tool geometry. This observation shows that tool geometry has little effect in mixing the particles within the matrix. Back scattered electron images are used to clearly reveal the particles within the matrix.

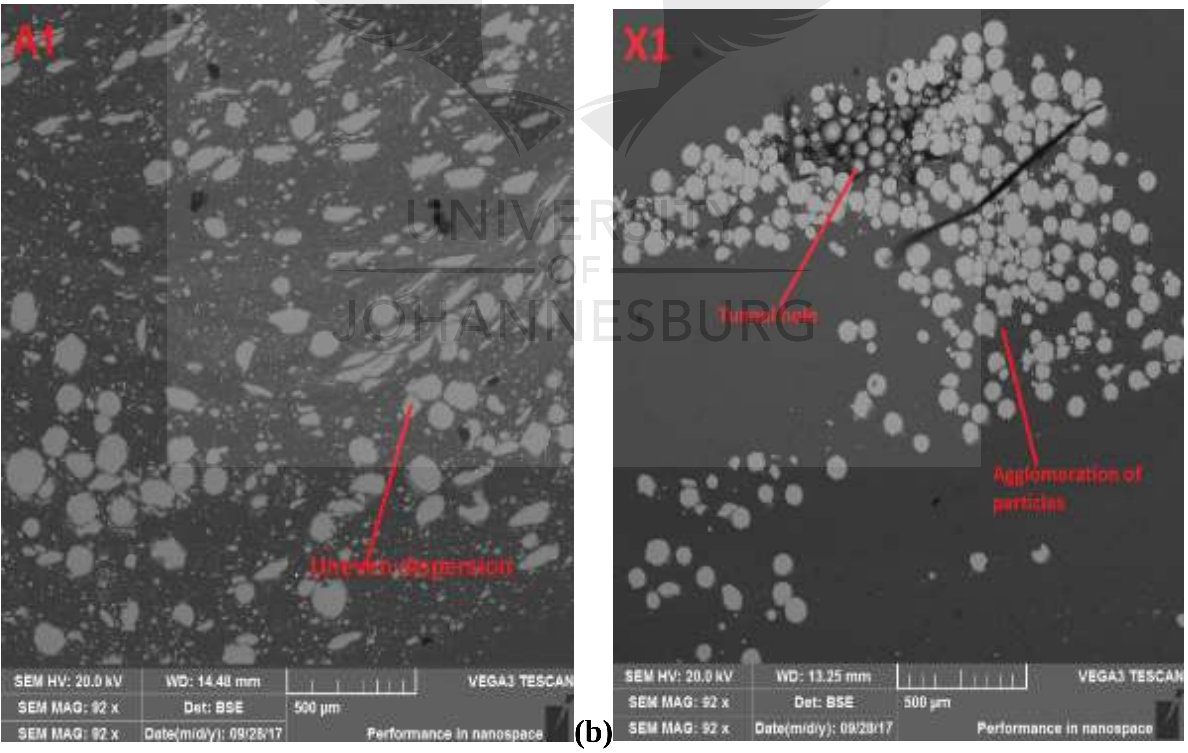

(a) **(b)**

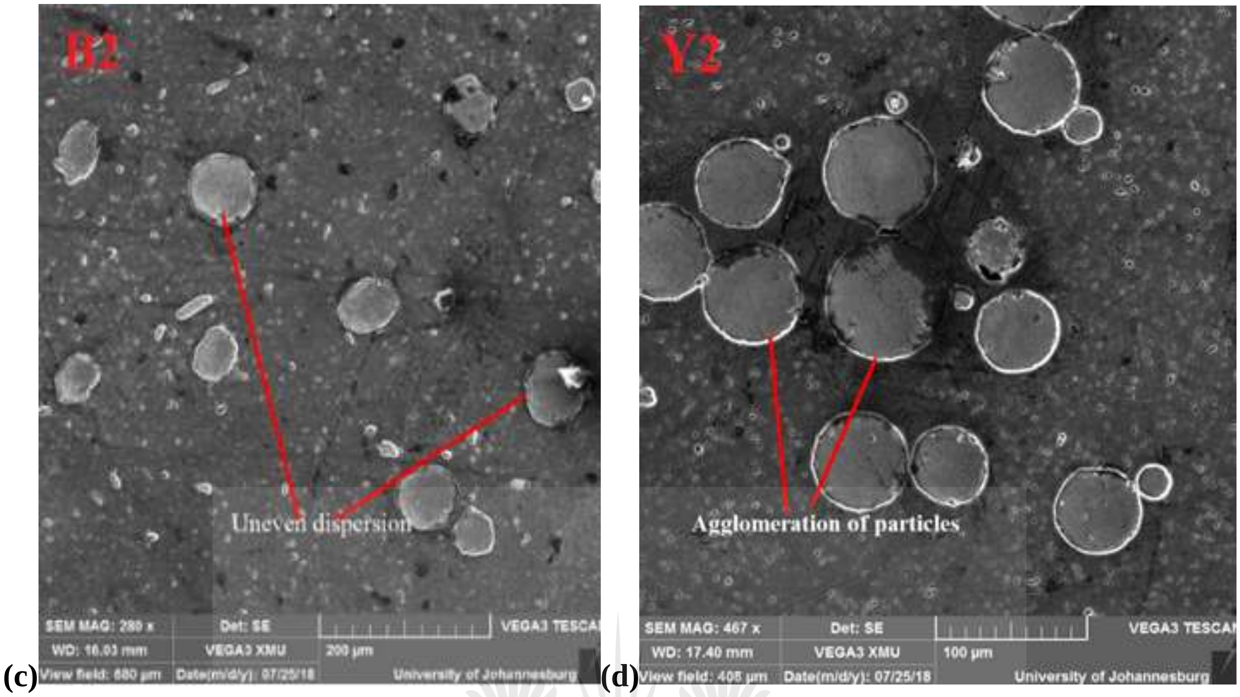

Figure 4. 7 Backscatter electron images of some composites samples using one and two passes (a) A1, (b) X1, (c) B2 and (d) Y2

However, with the composites produced via three cumulative passes with both tool geometries (i.e, A3 and X3), the SEM images reveal a uniform distribution of particles without microstructural defects within the matrix as shown in Figure 4.8. It is necessary to have a uniform distribution of particles within the matrix, as the Ti-6Al-4V powder helps to improve the mechanical properties, such as hardness and tensile properties, as explained earlier within the stir zone. Additionally, the sample with the most dispersed particles within the matrix is shown to be the A3 sample. These sample was produced, by using tool speed of 600 rpm and threaded taper tool geometry. This observation reveals that the reinforcements are well distributed by the threaded tools after three cumulative passes on both 600 and 1200 rpm. However, the stir zones of other samples fabricated with 1 to 2 passes reveal a lesser dispersion of Ti-6Al-4V particles.

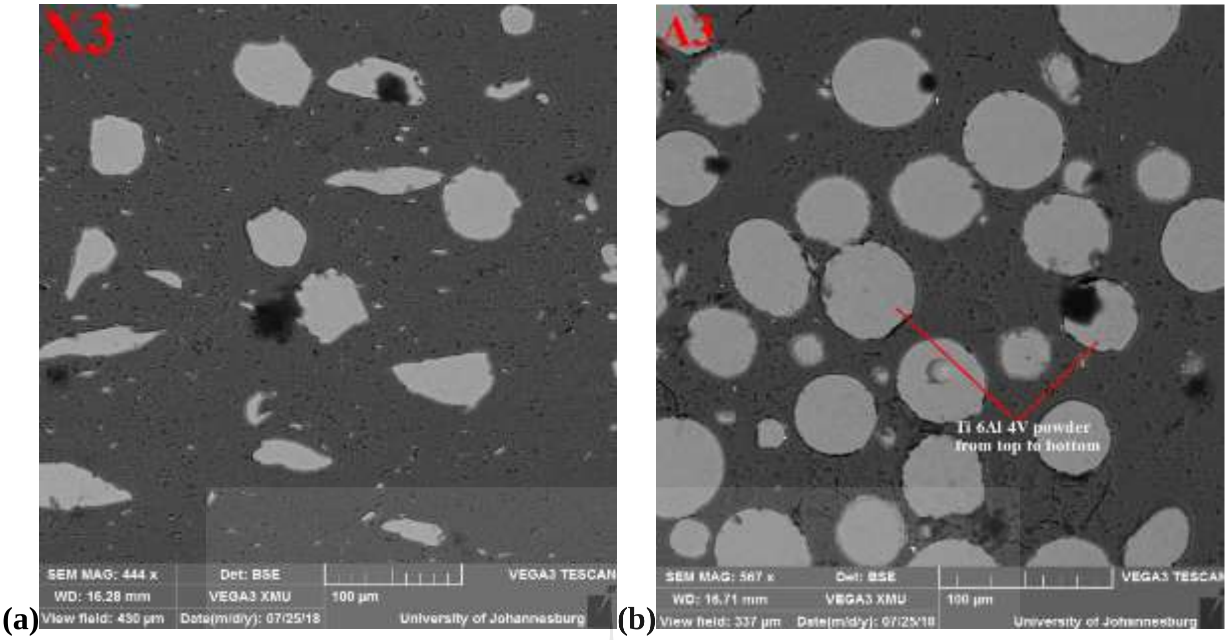

Figure 4. 8 SEM images of the three passes fabricated samples (a) X3 and (b) A3

A further examination of the microstructures of the composites was done to reveal the multi-pass FSP on the grain structures, as shown in Figure 4.9. A more refined grain structures are observed with the samples produced via three FSP passes; this was due to a complete dynamic recrystallization in the stirred zone, as a result of three cumulative passes. Material mixing was effective; and no defect was observed. The specimens produced via square geometry and at lower tool speeds of 600 rpm have less grain refinement. The grain structure was coarse, due to the reduced plastic deformation. The worm-hole defect was observed; as a result of the insufficient mixing of the materials, due to the inappropriate combination of process parameter. The SEM images of the rest of the composites can be found in Appendix D

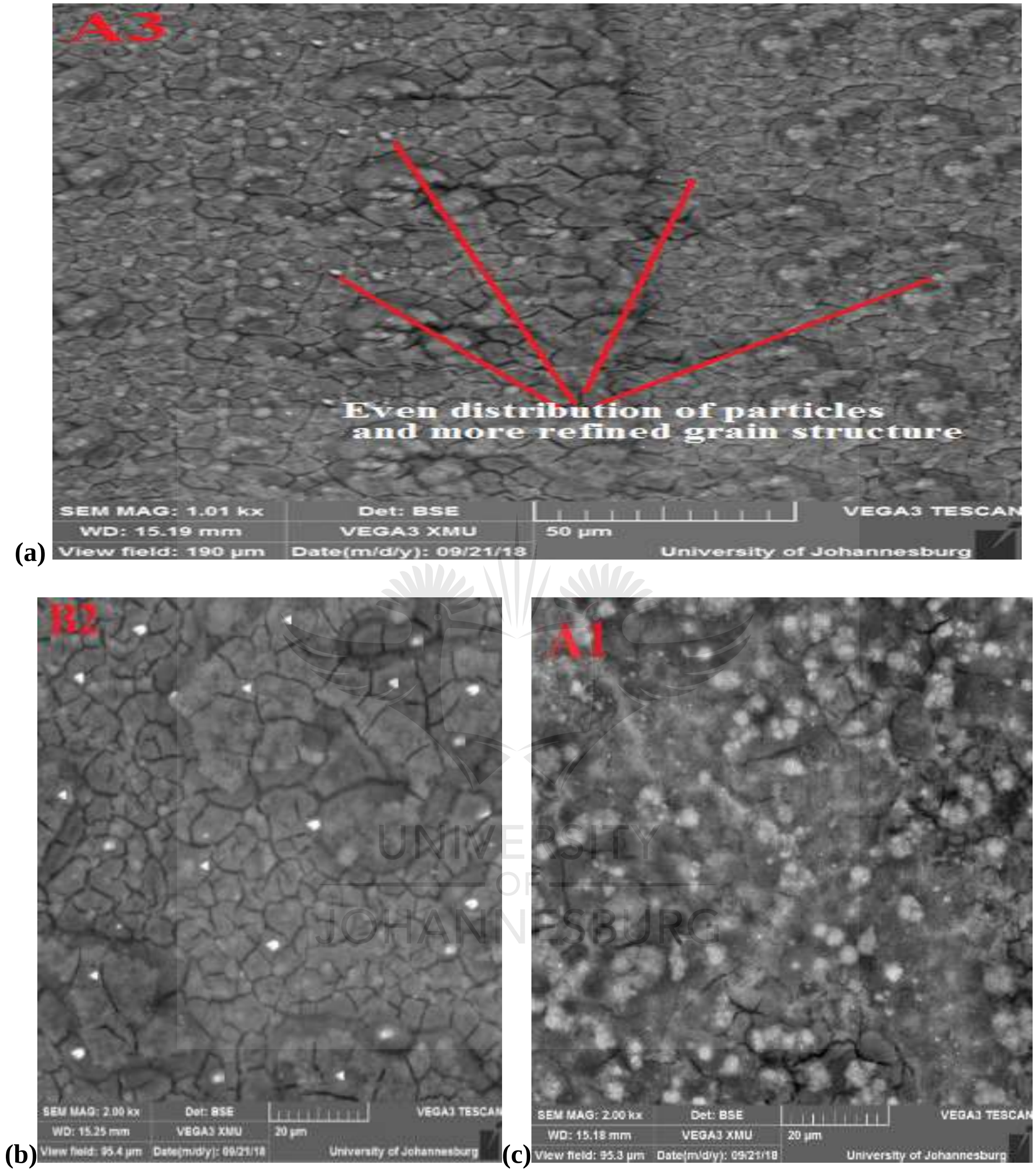

Figure 4. 9 SEM images of composites showing the grain structure (a) A3, (b) B2 and (c) A1

With Hall-Petch equation, it has also been proven that the refinement of grains during the process can result in improved mechanical properties, such as the hardness value, due to the dynamic recrystallization at the stir zone (Vedabouriswaran & Aravindan, 2018). The rate of deformation, the temperature distrubtion and the type of reinforcing particles are the major factors controlling grain-size refinement (Faraji & Asadi, 2011). In this project, the presence of the Ti-6Al-4V particle as second-phase particles and at a deformation rate associated with the appropriate combination of process parameters are the factors responsible for the refined grains.

EDS analysis was carried out on the stir zone of the three passes sample, in order to examine the element presents and the effect of the reinforcing particle. The presence of Ti-6Al-4V particles in the aluminium matrix can be clearly seen at all the selected points. As revealed with XRD analysis earlier, the difference led to the formation of hard and brittle intermetallic compounds. The EDS analysis of selected points within the matrix, using threaded taper tool were presented Figure 4.10m while other EDS analysis can be found in Appendix E.

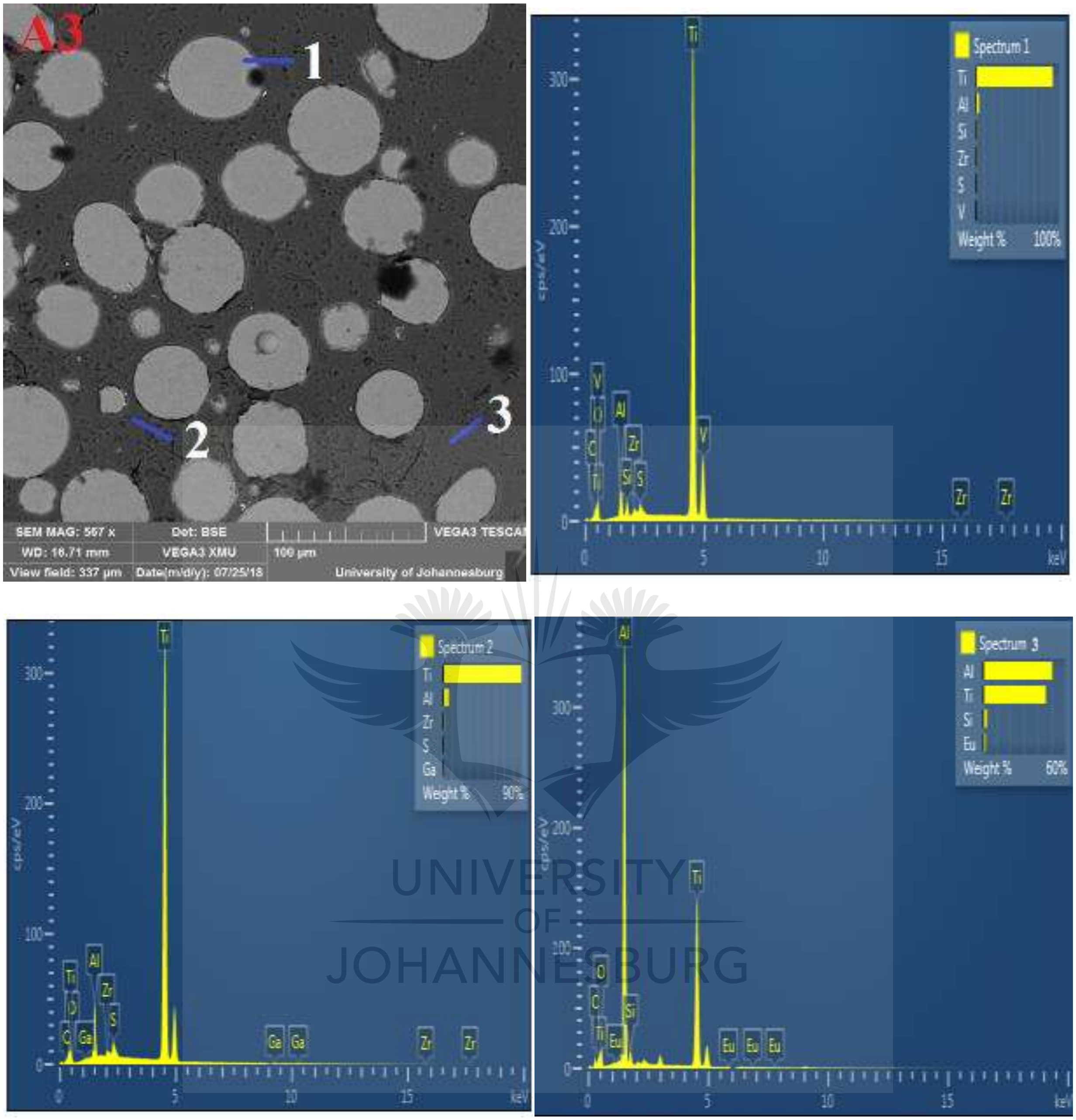

Figure 4. 10 EDS analysis of the 3-passes composites (A3)

4.5 Prediction of the grain sizes within the Microstructure using Image thresholding Technique

Thresholding technique is one of the methods of image processing used to detect morphological maps (Rohilla, Garg, Mallick, & Setia, 2018) and image colour intensity. It is one of the commonest parallel techniques of segmentation. It distinguishes foreground pixel from background pixel, as well as enhances better visual perception of the image (Zhu, Xia, Zhang, & Belloulata, 2007)(Kuruvilla, Sukumaran, Sankar, & Joy, 2016). Greyscale microscopic images were converted into binary images, in order to reduce data complexity. The binary images consist of important data with respect to the shape and the location of the objects. One of the merits of threshold segmentation is its speed of operation and simplicity of its calculation (Zaitoun & Aqel, 2015). It helps in recognizing the patterns of the images; and by so-doing, it gives high quality and resolutions of the final result of the analysis (Aly, Deris, & Zaki, 2011).

Otsu's method (Otsu, 1979) was used for image-thresholding, as explained earlier in section 3.9. The global optimal threshold value was obtained for the microscopic images. Particle size in the material samples of the threaded-tool fabricated composites, using 1,2 and 3 passes, were identified by using the difference in intensity of resulting images after thresholding.

Given the local thresholds $t_1, t_2, t_3, \ldots\ t_n$ to be selected from, the thresholds subdivide the images into n+1 classes of $C_1, C_2, C_3, \ldots\ C_n$ by maximizing the objective function given by the sum of all threshold variances (Khairuzzaman & Chaudhury, 2017);

$$J_1(t_1, t_2, t_3, \ldots\ t_n) = \sigma_0^2 + \sigma_1^2 + \sigma_2^2 + \sigma_3^2 + \cdots\ \sigma_n^2 \qquad (4.1)$$

Where;

$$\sigma_0^2 = \omega_0(\mu_0 - \mu_T)^2, \omega_0 = \sum_{i=0}^{t_1-1} p_i\,, \mu_0 = \sum_{i=0}^{t_1-1} \frac{ip_i}{\omega_0}$$

$$\sigma_1^2 = \omega_1(\mu_1 - \mu_T)^2, \omega_1 = \sum_{i=t_1}^{t_2-1} p_i\,, \mu_1 = \sum_{i=t_1}^{t_2-1} \frac{ip_i}{\omega_1}$$

$$\sigma_2^2 = \omega_2(\mu_2 - \mu_T)^2, \omega_2 = \sum_{i=t_2}^{t_3-1} p_i\,, \mu_2 = \sum_{i=t_2}^{t_3-1} \frac{ip_i}{\omega_2}$$

$$\sigma_3^2 = \omega_3(\mu_3 - \mu_T)^2, \omega_3 = \sum_{i=t_3}^{t_4-1} p_i\,, \mu_3 = \sum_{i=t_3}^{t_4-1} \frac{ip_i}{\omega_3}$$

$$\sigma_n^2 = \omega_n(\mu_n - \mu_T)^2, \omega_n = \sum_{i=t_n}^{t_{n+1}-1} p_i\,, \mu_n = \sum_{i=t_n}^{t_{n+1}-1} \frac{ip_i}{\omega_n}$$

And $\sigma_0^2, \sigma_1^2, \sigma_2^2, \sigma_3^2, \dots\ \sigma_n^2$ are the class variances, $\omega_0, \omega_1, \omega_2, \omega_3, \dots\ \omega_n$ represents the class probabilities, $\mu_0, \mu_1, \mu_2, \mu_3, \dots\ \mu_n$ represents the mean values of the segmented classes. The intensity of the whole image is: $\mu_T \subseteq \mu_T = \omega_0\mu_0 + \omega_1\mu_1 + \omega_2\mu_2 + \omega_3\mu_3 + \cdots + \omega_m\mu_m$; where $\omega_0 + \omega_1 + \omega_2 + \omega_3 + \omega_n = 1$.

SEM images with the different passes were identified with distinctiveness in the image threshold. The results of these are presented as follows:

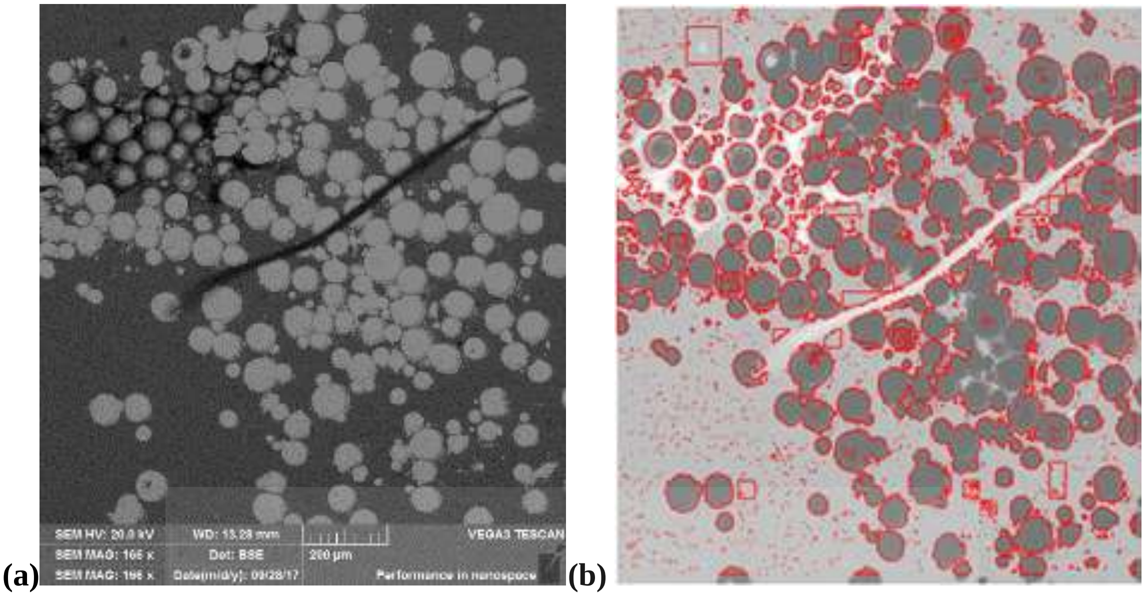

Figure 4. 11 Original microscopic image (a) and segmented image (b) at one pass(X1)

Shown in Figure 4.11 (a) and (b) are the original SEM image and the segmented SEM image, respectively. At one pass, the particle sizes are closely distributed and clustered with bigger particle sizes across the sample. Using a magnification of X166, the particle, the mean particle size of the segmented image obtained was 2.26×10^3 µm. The particle sizes obtained for one pass was observed to exhibit spherical structures closely packed, which were identified to the smallest possible particle size in Figure 4.11(b).

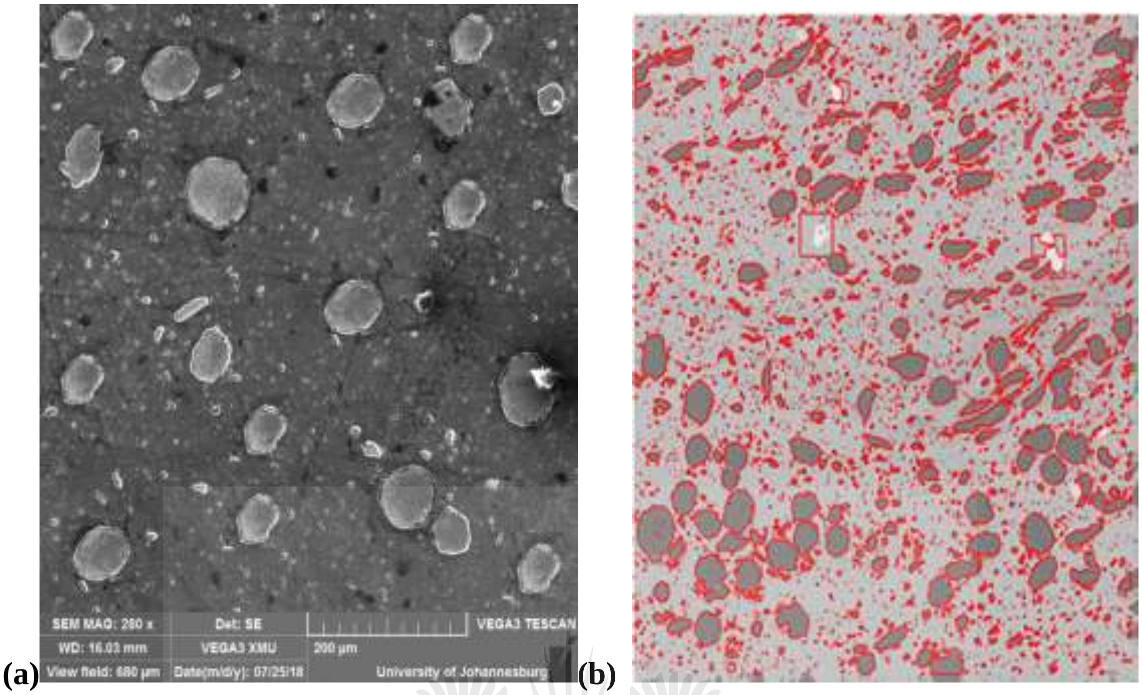

Figure 4. 12 Original microscopic image (a) and segmented image (b) at two passes (B2)

Figure 4.12(a) and (b) shows the original SEM image and the segmented SEM image, respectively. Unlike the one pass, the particle sizes in two passes are widely distributed with bigger particles dispersed across the sample. Using a magnification of X155, the mean particle size of the segmented image obtained was 2.69×10^3 μm. The particle sizes obtained for two passes were observed to exhibit less of spherical structures, but irregular structures, which illustrates the flow process in the Friction Stir Process.

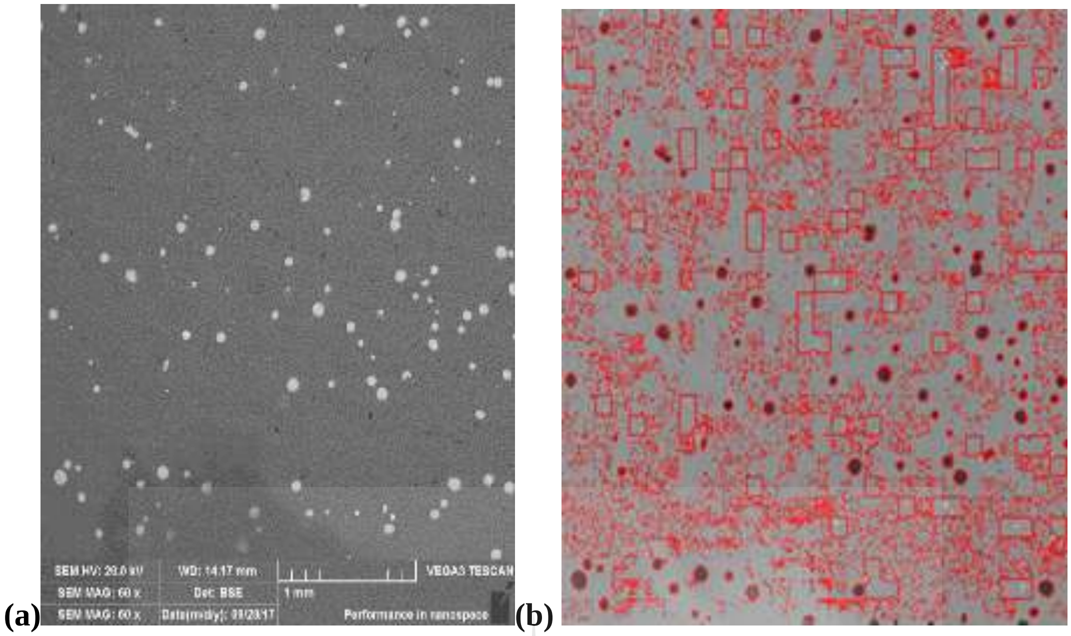

Figure 4. 13 Original microscopic image (a) and segmented image (b) at three passes (B3)

Shown in Figure 4.13(a) and (b) are the original SEM image and the segmented SEM image for the three passes respectively. Using a magnification of X60, the particle, the mean particle size of the segmented image obtained was 1.36×10^3 μm, which illustrates a significant reduction compared to those obtained from one pass and two passes. The particle sizes in three passes were widely distributed, like that of the two passes. The particle sizes obtained for the three passes exhibit more spherical structures, with smaller particle sizes of the reinforcements detected by the Otsu Segmentation algorithm.

The mean particle sizes decrease across the passes of the FSP. Irrespective of the magnification used, there is a deviation in the reinforcement distribution across the sample.

4.6 Effect of Process Parameters on the Output Response

The tool in FSP experiences forces in three co-ordinate axes, namely: longitudinal or transverse force Fx; lateral force Fy; and downward force Fz - due to rotational and linear movement of the tool. These output parameters act around the tool on the workpiece; and vary with the process parameters, the tool, and composition of the workpiece. During the FSP, the force reaction should be taken into consideration; but more attention should be given to the torque and axial force; because the heat generated during the process can be estimated by the axial force and the torque.

Fz, which is the downward force, is needed to put the tool below the surface of the material. Since this force arises as a result of the resistance of the material to the motion of the tool, it is expected that this force will decrease; as the temperature of the material around the tool is increased. The samples subjected to three cumulative passes with 1200 rpm were examined (i.e. B3 and Y3) to determine the force feedback of the downward force against time during FSP. The plunging of the material generates the initial heat required to plasticize the material before the traverse is started.

At the initial displacement of the B3 sample, the compressive downward force increases during the plunging stage; and then decreases when the FSPed seam becomes uniform. After a while, the Fz force becomes uniform for the latter part of the process. Once the thermal equilibrium has been reached, these output-response parameters become constant. The peak axial force for the B3 sample is 25 kN as shown in Figure 4.14.

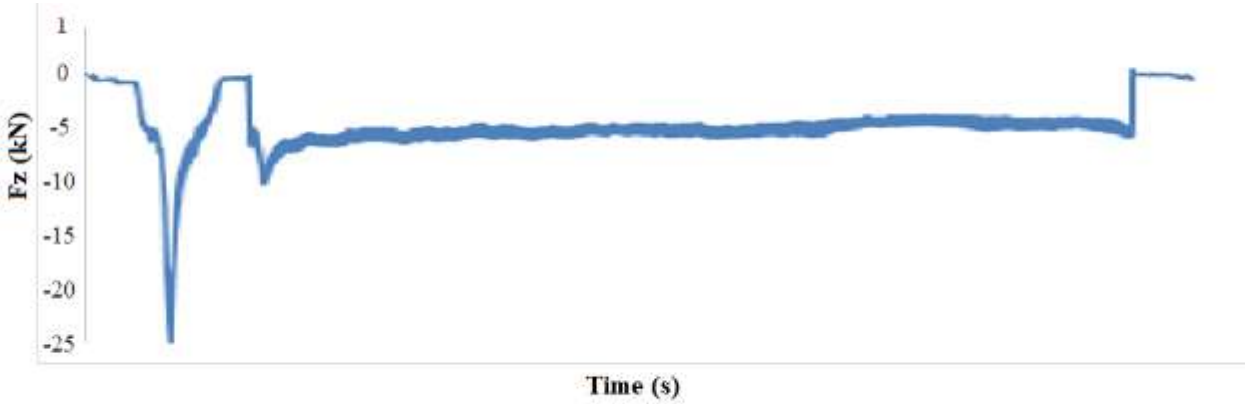

Figure 4. 14 Force feedback of the downward force against time of B3 sample

A similar observation was seen with the Y3 Sample, as shown in Figure 4.15. At the plunging of the material, the tool traverses; and a ramp-up occurs due to the forging, resulting in an increase in the downward vertical force. Then, a stable vertical downward force takes over. This period can be referred to as the steady state of the process, i.e., the period during which the force, the torque and heat reach a near equilibrium state (Chainarong, Muangjunburee, & Suthummanon, 2014). However, the Y3 sample experiences less force to deform the material; and more time required for the processed beam to become uniform, which translates to more time being therefore required for thermal equilibrium to be reached.

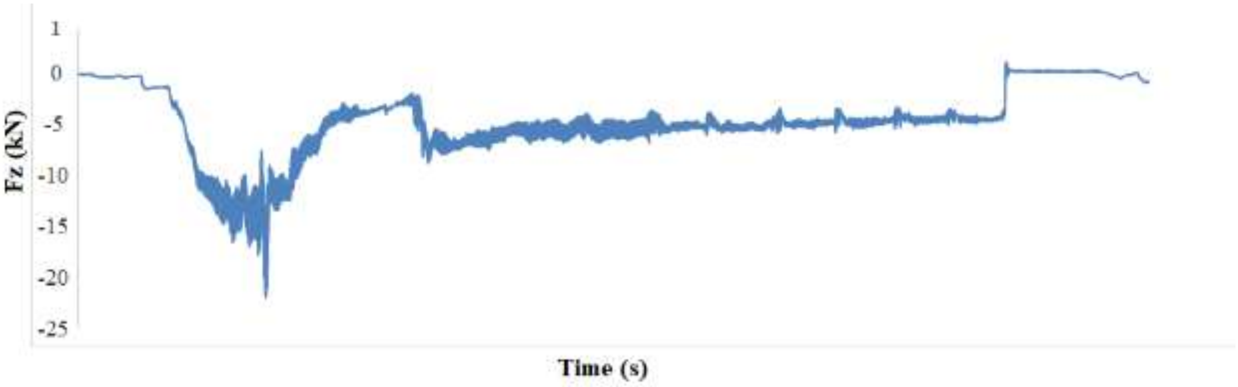

Figure 4. 15 Force feedback of the downward force against time of Y3 sample

The peak axial force for the Y3 sample is 23.87 kN. It can be inferred that the forces during FSP can help in understanding the flow of the materials; and it can consequently predict the occurrence of these voids in the nugget.

4.7 A Torque-Based Predicted Heat-Input Analysis

The 1100 Al alloy is not heat treatable, however, the FSP technique generates heat input, as a result of the severe plastic deformation of the metal(Aa et al., 2017). A torque-based energy model, as suggested by Asadi et al 2014 (Asadi et al., 2014), was used in estimating the FSP heat input. The predicted processed M (Nm), the tool rotational speed, Ω (rpm) and the processing power (Pw) can be related by using the model in Equation 4.2

$$\text{Processing Power} = \frac{2\pi\Omega m}{60} \qquad 4.2$$

The tool rotational speed is converted from rpm to radian per second by multiplying M with 2π/60. Further, the forecasted heat input (H.I) can be estimated by finding the quotient of the processing power Input, (Pw.I.)(watts) by the transverse speed, (ν), (mm/min), as expressed in Equation 4.3.

$$\mathrm{H.i} = \frac{\mathrm{Pw.i}}{\mathrm{v}} \qquad 4.3$$

The sheets were subjected to three cumulative passes; however, it should be noted that the workpiece material was allowed to return to room temperature, before being subjected to another pass. The predicted heat input, based on the excel data generated from the friction-stir processing of the composites fabricated by using different tool geometries with 1-pass, are shown in Table 4.3.

Table 4. 3 Average heat input prediction during the fabrication of the composites

Composites	Tool design	Average Heat Input
A1 (600rpm/ 30mm/min)	Threaded Taper	206.23 KJ
B1 (1200rpm/ 30mm/min)	Threaded Taper	253.54 KJ
X1 (600rpm/ 30mm/min)	Square tool	199.16 KJ
Y1 (1200rpm/ 30mm/min)	Square tool	244.66 KJ

The torque decreases with increasing rotational speed, due to the higher temperature caused by the higher heat generation rate (heat input/time), the indicator of which is the power input. The result indicates that the threaded taper tool has higher heat input on the workpiece, which may help to deform the workpiece plastically. The temperature during the process was measured with thermocouple. Three different readings were taken at 10 seconds interval during the fabrication of the composites. Heat was generated due to friction; and the output parameters of temperature against time for the 3-pass composites fabricated with two different tool geometries on 1200rpm, are shown in Figure 4.16. As shown, the peak temperature for the B3 composite is 430°C; while the peak temperature of the Y3 sample is 423°C. There is little effect of the tool geometry on the heat generated during the process.

The effect of this heat on the quality of the composites will be further investigated in the subsequent experimental characterizations carried out in this chapter.

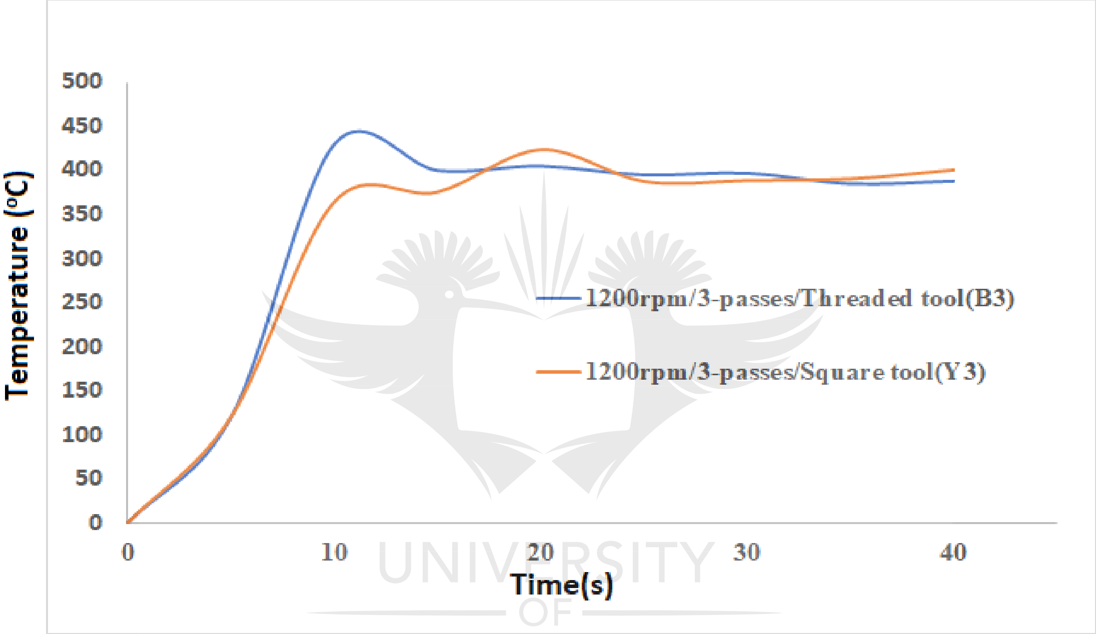

Figure 4. 16 Output parameters of temperature measured against Time for Samples B3 and Y3 composites

4.8 Tensile test analysis

The effect of the process parameters on the tensile properties of the fabricated composite samples were analyzed. The images of the fabricated specimens before and after testing are shown in Figure 4.17, all samples fractured at different load.

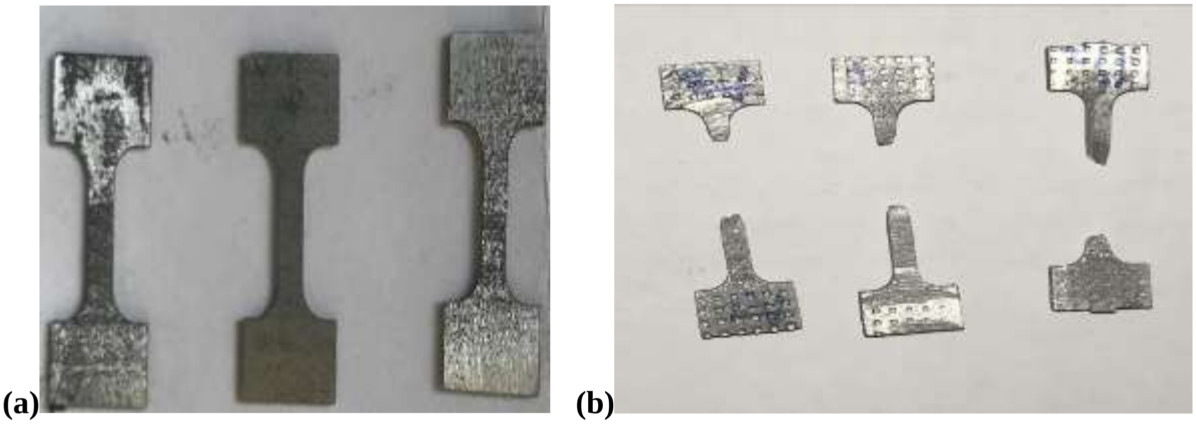

Figure 4. 17 (a) Photographs of the tensile specimens before the test (b) after the test

The load-displacement are shown in Figure 4.18 and 4.19; the composites “B-1”, “B-2”, “B-3”, “A-1”, “A-2” and “A-3” were fabricated by using threaded taper tool geometry, while “Y-1”, “Y-2”, “Y-3”, “X-1”, “X-2” and “X-3” were fabricated by using square tool geometry. PM represents the as-received 1100 Al (i.e the parent material). From these figures, all the reinforced samples show better tensile properties when compared to the parent material. This is to show that the addition of Ti-6Al-4V improves the tensile properties of the 1100 Al alloy. Also, an increase in the number of passes and an increase in tool rotational speed directly increases the ultimate tensile strength (UTS) and the yield stress of the composites.

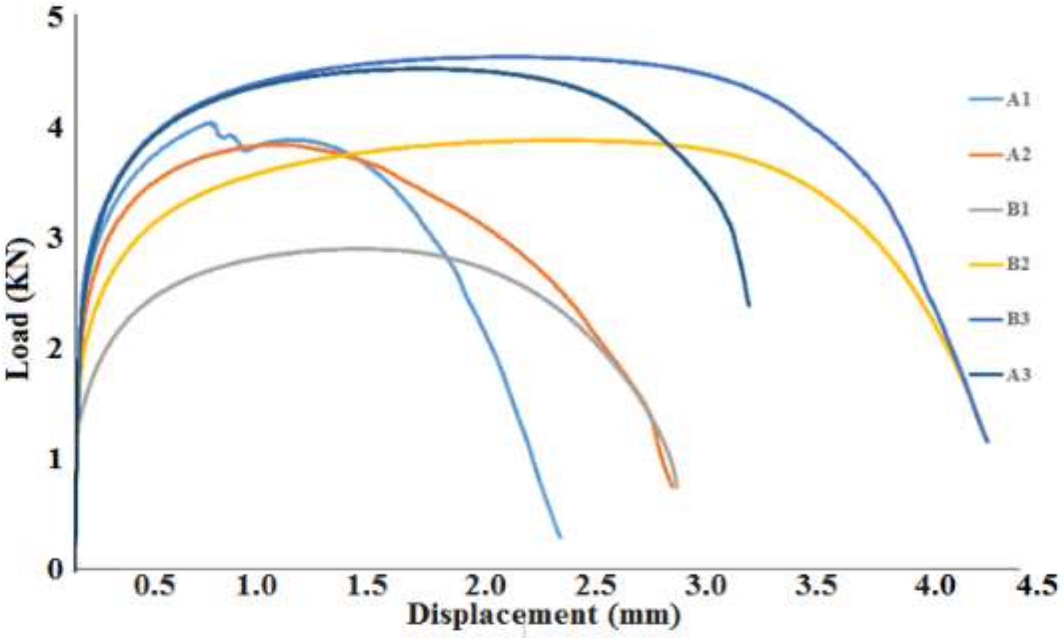

Figure 4. 18 Stress-strain graph of the samples fabricated with the threaded taper tool geometry

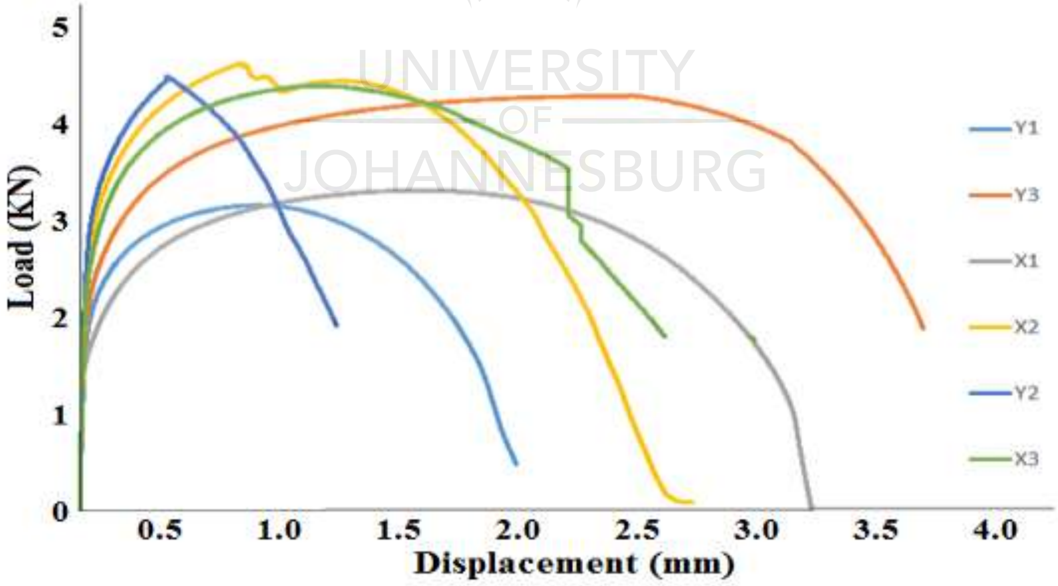

Figure 4. 19 Stress-strain graph of the samples fabricated with the square tool geometry

The sample fabricated at 1200rpm and 3-passes via the threaded taper tool geometry (B3) produced the peak UTS, i.e. 275.40MPa; while the sample produced at 600rpm and with 1 pass via the square tool geometry (X1) gave the lowest UTS, respectively. A synergy between the process parameters, which ensure adequate mixture of the powder within the matrix, plays an important role in the properties of the fabricated composites. The fluctuating waves seen with the A1, Y1 and X2 samples could be as a result of the uneven distribution of the reinforcement particles within the matrix. Sometimes, reinforcement particles act as inclusion and impurities in the matrix; if they are not evenly distributed (Khodabakhshi et al., 2015).

All the samples fractured in the HAZ – caused by the dissolution mechanism which led to the reduction in the hardness of the samples. A 33.4% increment in tensile strength was observed with the B-3 sample, when compared with the base material, as presented in Table 4.5.

Table 4. 4 Tensile properties of the specimens

Specimens	Yield stress (MPa)	UTS (MPa)	Elongation (%)
Base material	38.16	92.44	34.00
A1	44.66	91.71	43.57
A2	47.23	94.53	43.91
A3	58.90	162.38	51.83
B1	41.32	92.87	41.44
B2	51.63	110.21	48.72
B3	99.78	275.40	66.12
X1	36.51	88.20	40.57
X2	32.85	80.42	32.26
X3	70.11	197.69	54.53
Y1	42.46	92.4	35.13
Y2	66.31	108.75	47.83
Y3	82.25	226.61	59.21

It was seen that all the fractured samples were ductile; and the effect of the process parameters on the maximum fractured samples can be seen in Figure 4.20 for the 3-pass samples fabricated with Threaded taper and square tool geometries.

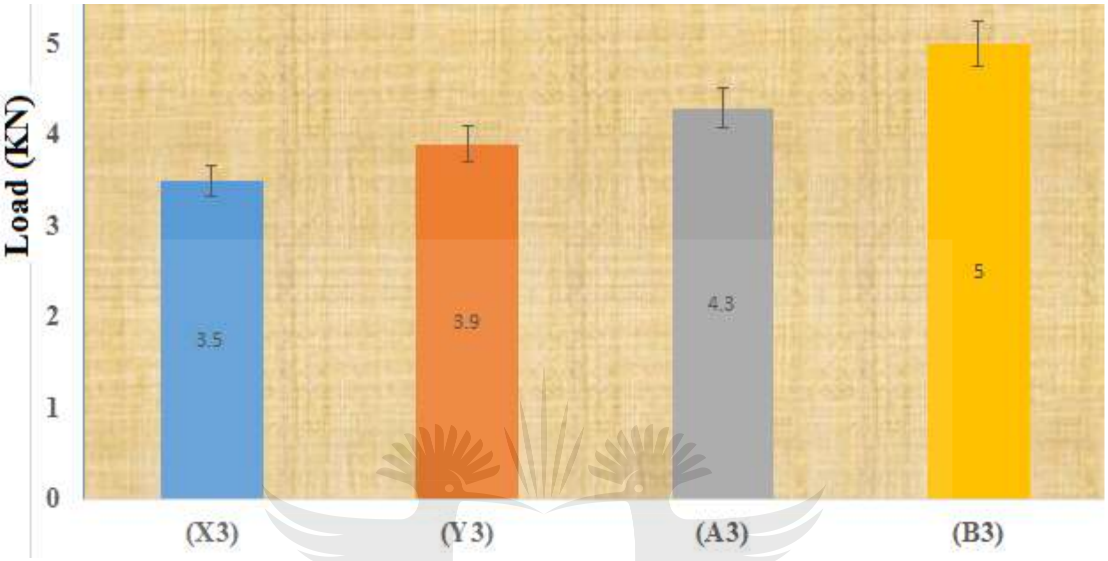

Figure 4. 20 The effect of process parameters and tool geometry on the maximum failure load of the composites

The sample fabricated with threaded tool shape and 1200rpm (i.e B3) has the highest failure load of 5kN. The severity of the barricading action of the particles increases as their distribution improves. The higher failure load exhibited by the B3 composite is due to a fact that the particles within the matrix are well distributed, also the composite comprise finer grains than the rest. This finding is also in agreement with other published works (Rathee, Maheshwari, Siddiquee, & Srivastava, 2017) (Hashemi & Hussain, 2015c).

4.9 Microhardness Profiling

A micro-hardness profiling was carried out across all the zones (i.e HAZ. SZ, TMAZ), as shown in Figure 4.21. As illustrated in Chapter 3, the Vickers microhardness measurements were conducted at the cross section of the sample. In all the samples, higher microhardness values were recorded in the region close to the groove fabricated on the sample (i.e, concentrated reinforcement). It has been reported that the presence of hard and brittle intermetallic compounds could have caused the sudden increase in the microhardness in the stir zone (Annigeri & B, 2018).

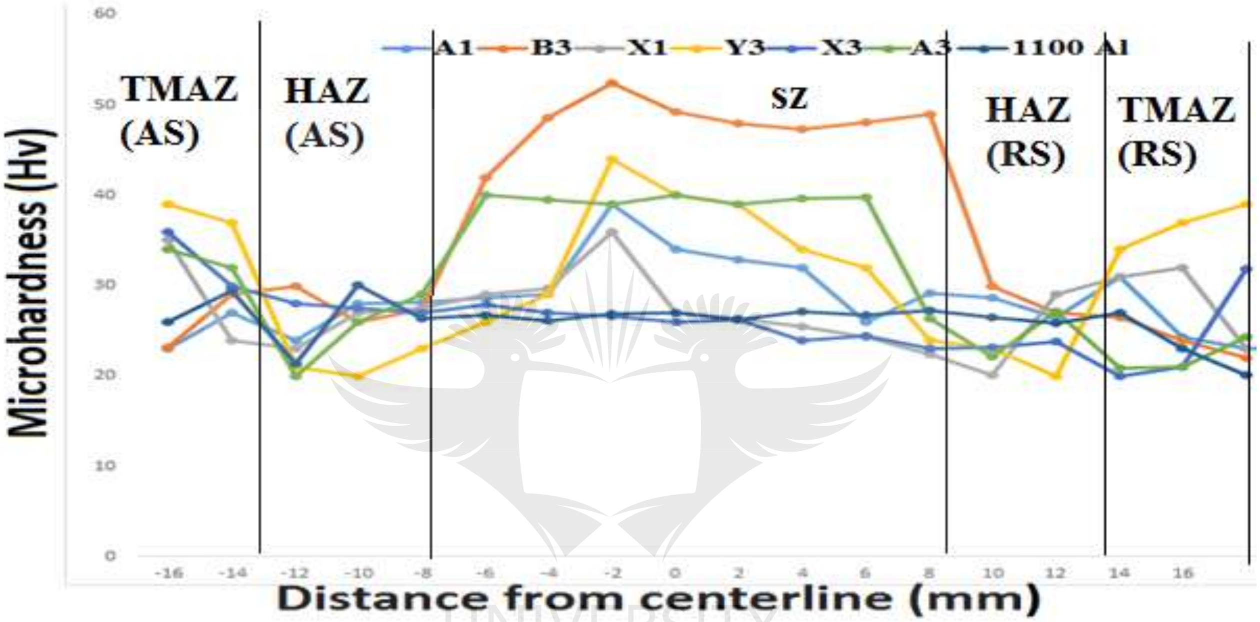

Figure 4. 21 Microhardness values of the composite samples produced with various process parameters (i.e tool rotational speed, number of passes and tool geometries)

The increment in the hardness value at the SZ observed in the result of the microhardness profiling can be attributed to grain refinement and the presence of the reinforcement particles. As the passes increase, finer grains are observed; this observation is in agreement with Hall-Petch rule, which states that decrease in the grain size results to an increase in the hardness value (Wu et al., 2015). From the tested zones, the minimum hardness value appeared at the HAZ; this is due to the thermal history experienced at this zone, which resulted in the coarsening of the precipitates.

The samples subjected to three cumulative passes were further examined, in order to determine the effect of the tool rotational speed and the tool geometry. The A3, B3, and Y3 samples were examined; and the microhardness profiles are presented in Figure 4.22.

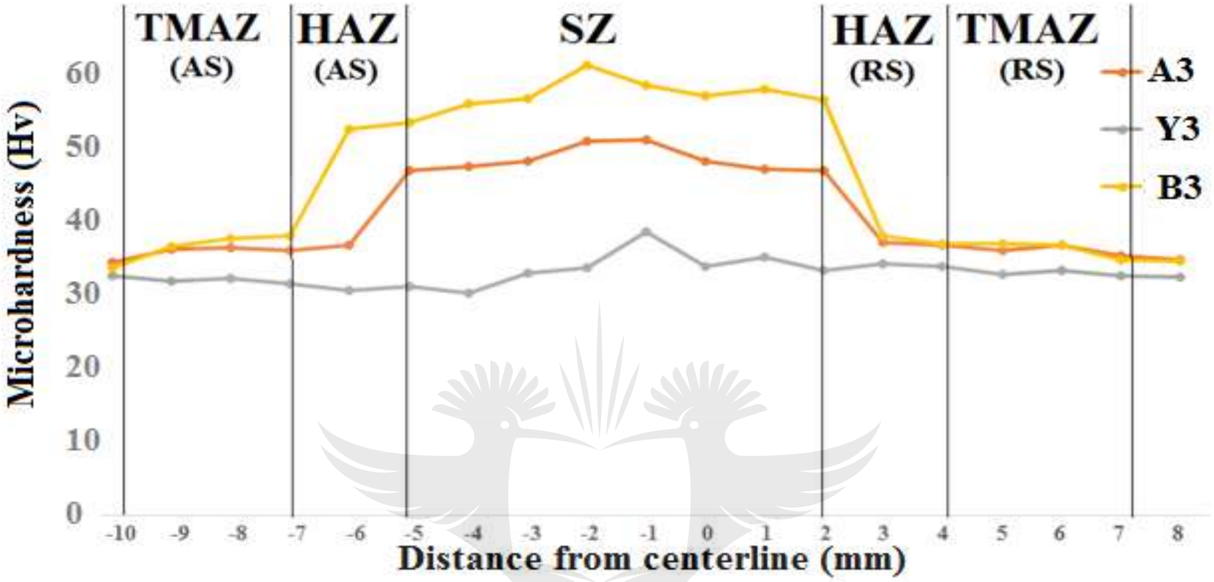

Figure 4. 22 Mean hardness values of some composites

It can be inferred from Figure 4.22 that the sample fabricated with 1200 rpm and threaded tool geometry exhibited the highest hardness, while the least hardness value is seen with the square-tool shape at 1200rpm. This is due to a fact that the samples fabricated via threaded tool with higher tool rotational speed comprise finer grains than the samples produced with square tool geometry on same tool rotational speed. This finding is consistent with the Hall–Petch rule, and this is to further show the importance of the appropriate tool shape on the hardness result when fabricating aluminum matrix composites.

The fabricated composite, after three cumulative passes, experienced a 62.5% increment than that of the 26.52 HV of the parent metal. The maximum microhardness value of 59.4 HV was obtained with the B3 sample; and the stirring action association with the Multi-pass FSP, with an appropriate combination of process parameter, such as the tool geometries and tool speed, help to improve the microhardness of the fabricated samples. The average hardness values of the processed samples are shown Figure 4.23.

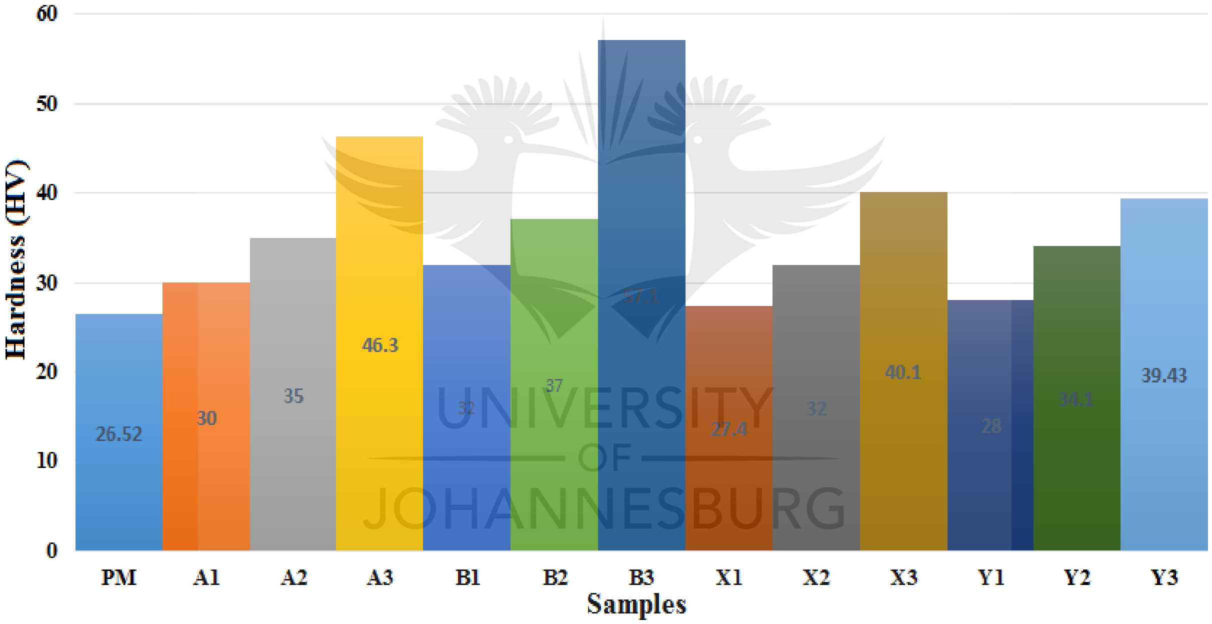

Figure 4. 23 Average Hardness Values of Specimen

4.10 XRD Analysis of the Composites

The XRD phase identification analysis was performed on the stir zone for all the samples; and the XRD spectrum of 1100 aluminum alloy and Ti-6Al-4V powder are shown in Figure 4.24 and 4.25 respectively; where the reinforcing powder is an α + β alloy.

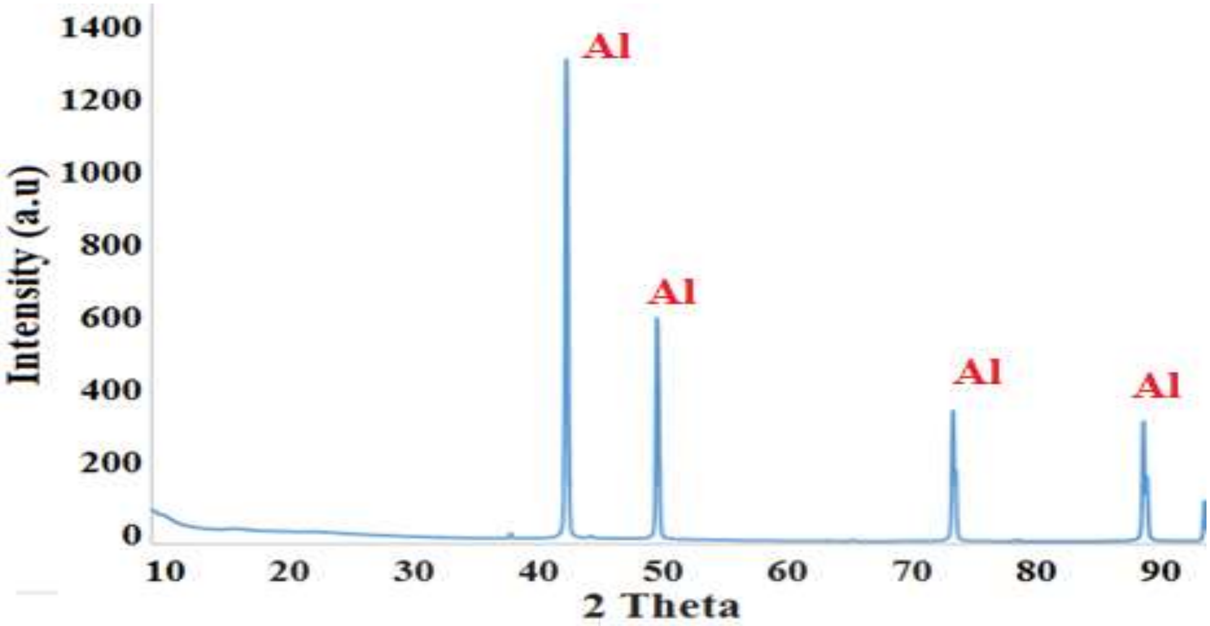

Figure 4. 24 XRD pattern of 1100 Al Alloy

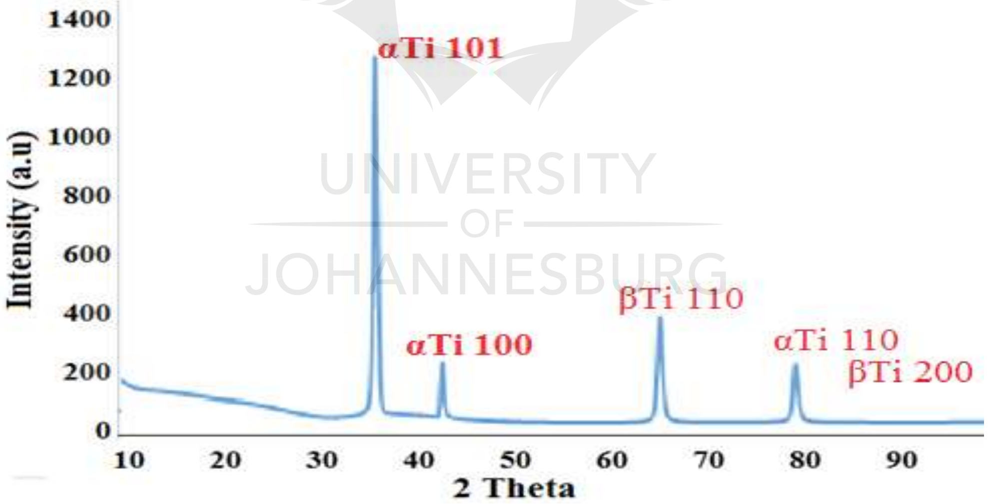

Figure 4. 25 XRD pattern of Ti-6Al-4V particles

A number of different intermetallics were detected in the fabricated composites. Intermetallics of Al_2Ti, Al_3Ti, $AlTi_3$ and TiAl, were found in the SZ of the three-pass samples produced with 1200 rpm and 30 mm/min traverse speed for both tool geometries as shown in Figure 4.26 and 4.27, while TiAl, Chromium Carbide, Niobium Tungsten Carbide and Iron Carbide were found in the samples fabricated with 1 to 2 passes, and lower rpm of 600.

On the other hand, in the HAZ, Al_2O_3 and Tungsten Carbide were found by using both tool geometries and rpm. The increase in the tool rotational speed contributes to the heat input associated with FSP, hence it causes severe plastic deformation which contributed to the formation of the intermallic compounds. Vinoth et al. have reported that the formation of intermetallics can be affected by low heats as well during FSP (Vinoth Jebaraj, Ajaykumar, Deepak, & Aditya, 2017). Furthermore, the highest peak XRD phase patterns identified in the stirred zone indicate an intense Aluminium alloys mixture; while the lowest XRD peaks illustrate the presence of new phases. An absolute scan range was approximately between 20^{o} and 92^{o} for the tested samples.

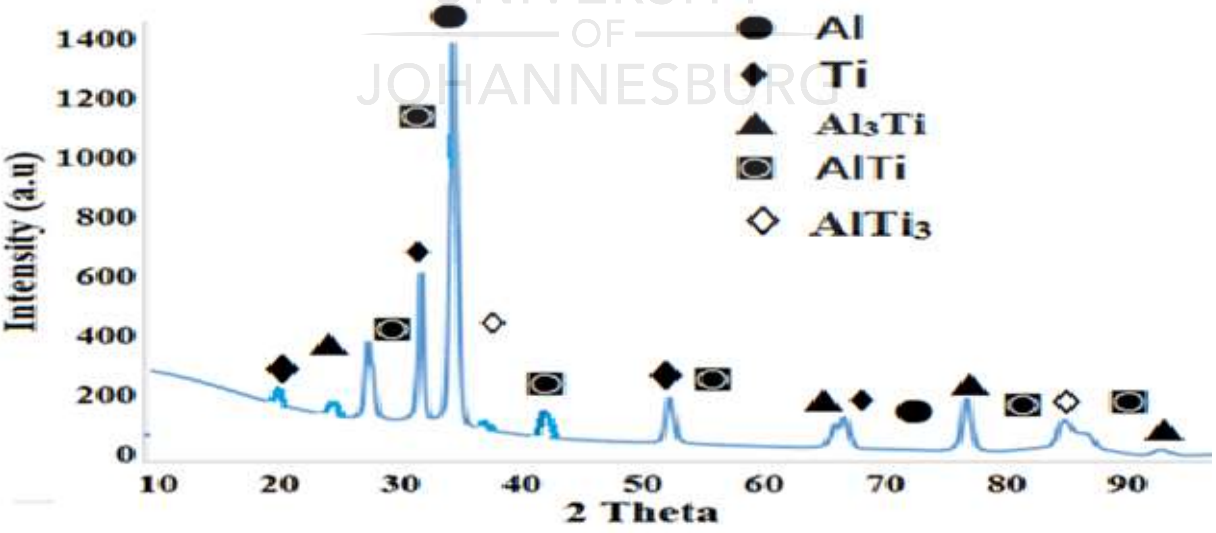

Figure 4. 26 XRD pattern of the Al/Ti-6Al-4V composites (Y3)

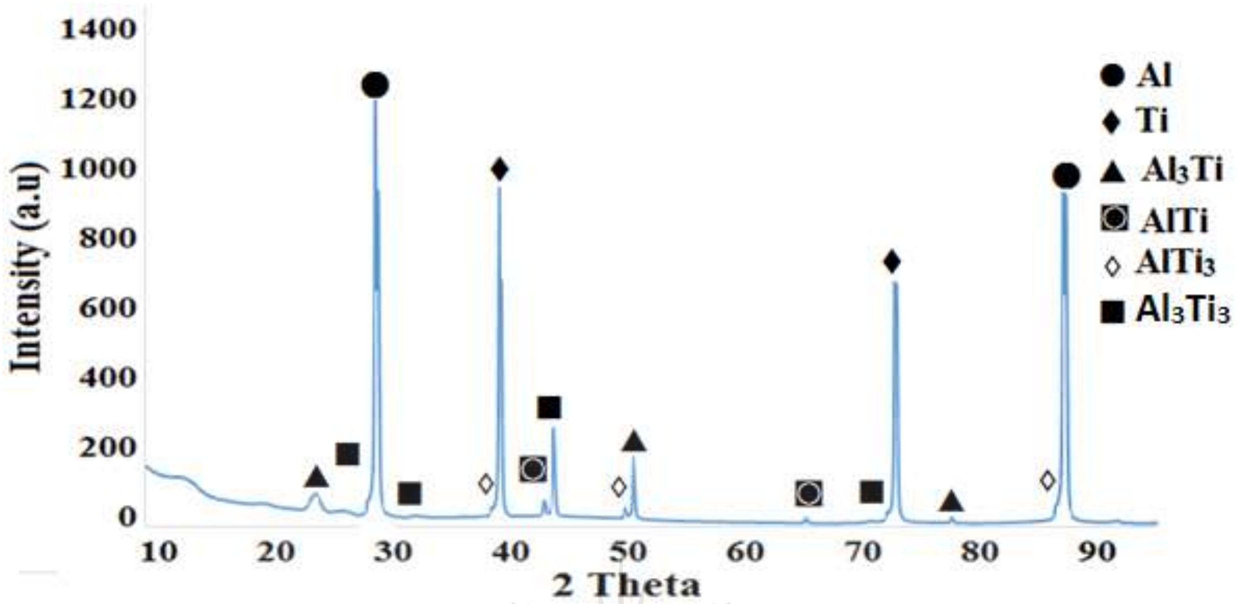

Figure 4. 27 XRD pattern of the Al/Ti-6Al-4V composites (B3)

A different intermetallics found in the stir zones of the composites are listed in Table 4.6. As it is established that low heats can affect the formation of intermetallics, this heat input is associated with the process parameters such as tool rotational speed and traverse speed (Xuo *et al.*, 2018). Hence, the intermetallics could not be well identified in some samples. Similar observations were made by Otunyo et al 2011(Otunyo, Nuaka, & Faith, 2011). The XRD results showing the presence of intermetallic compound in the samples were confirmed by the energy dispersive spectroscopy (EDS) analyses. The EDS results were discussed in the Section 4.5.

Table 4. 5 List of Intermetallic compounds found at the stir zone of all fabricated samples

Sample Number	Intermetallic Compounds

1100 Al	
A1	$AlTi_3$
A2	$AlTi$, $AlTi_3$
A3	$AlTi$, $AlTi_3$, Al_2Ti, Al_3Ti
B1	Al_2Ti
B2	Al_2Ti, $AlTi_3$
B3	$AlTi$, $AlTi_3$, Al_2Ti, Al_3Ti_3
X1	Al_3Ti, $AlTi_3$
X2	Al_3Ti, Al_3Ti_3
X3	$AlTi$, Al_3Ti, $AlTi_3$
Y1	Al_2Ti, Al_3Ti
Y2	$AlTi$, Al_3Ti, $AlTi_3$
Y3	$AlTi$, Al_3Ti, $AlTi_3$

4.11 Wear and Friction Behavior of the Fabricated Composites

The coefficient of friction of some selected samples are presented in Figure 4.28. A noticeable fluctuation across the test distance is observed with the parent material; while fluctuations are also observed with some composites fabricated with 1 and 2 passes, with both tool geometries. Further tests carried out on the samples fabricated with 3-passes on both tool geometries reveal lower and more stable friction coefficients across the test distance. This implies that the composites subjected to at least three cumulative passes can exhibit longer service life; and that they can withstand friction over longer period.

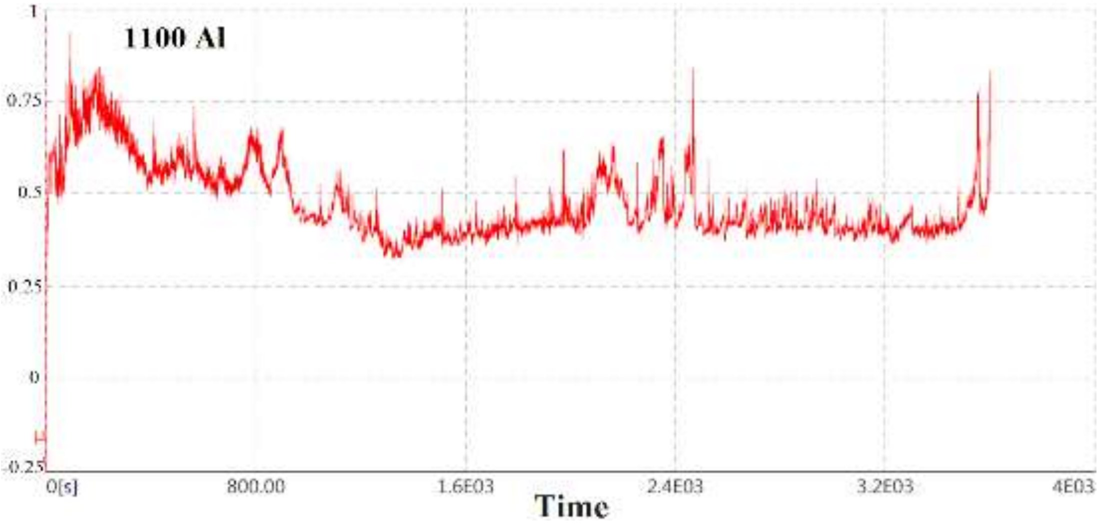
1100 Al
1
0.75
0.5
0.25
0
-0.25
μ
0[s]
800.00
1.6E03
2.4E03
3.2E03
4E03
Time

(a)

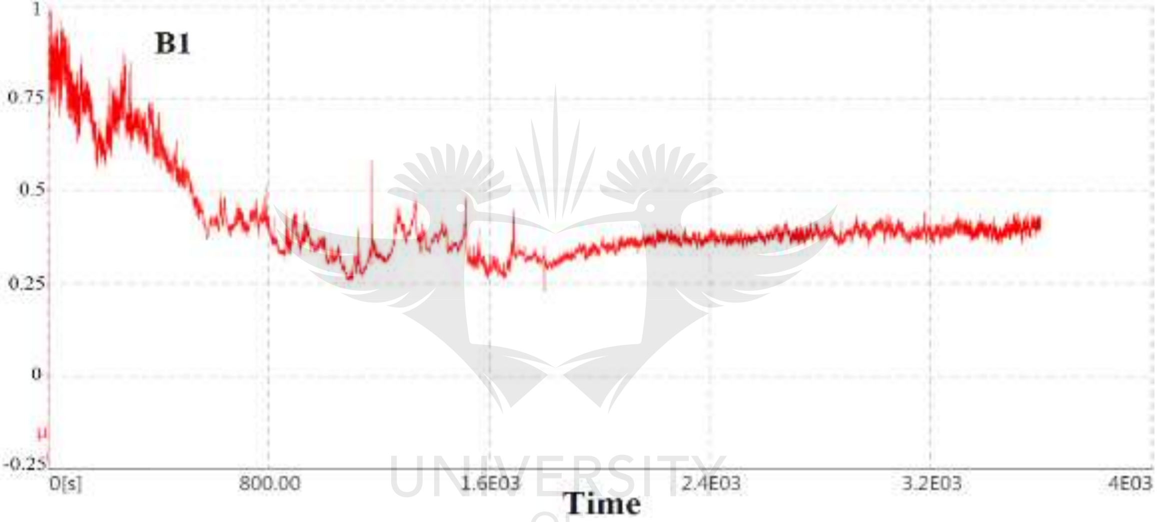
B1
1
0.75
0.5
0.25
0
-0.25
μ
0[s]
800.00
1.6E03
2.4E03
3.2E03
4E03
Time

(b)

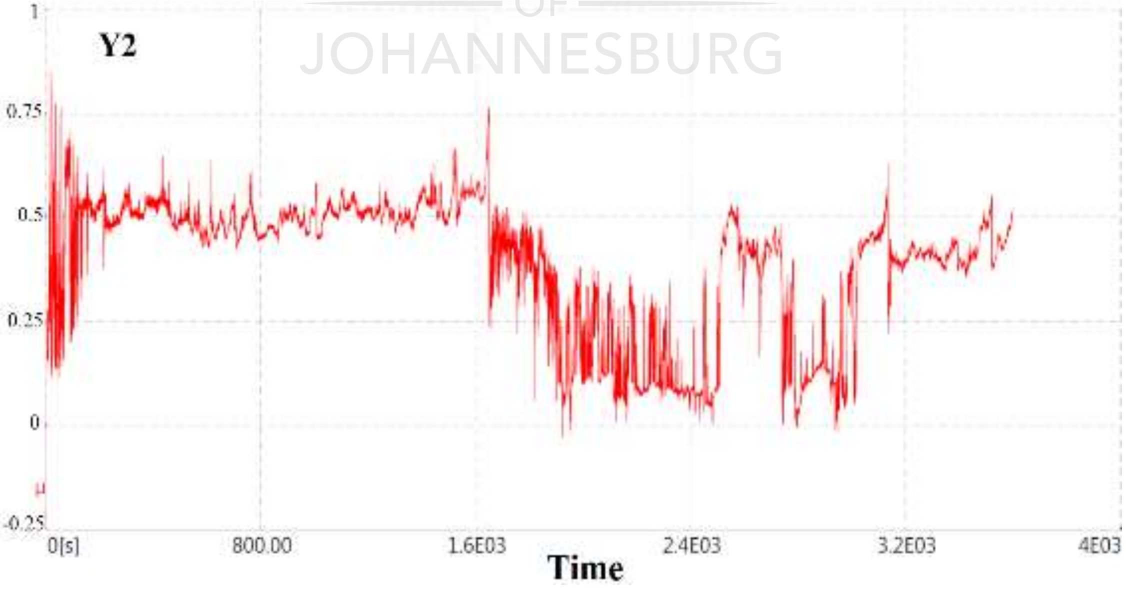
Y2
1
0.75
0.5
0.25
0
-0.25
μ
0[s]
800.00
1.6E03
2.4E03
3.2E03
4E03
Time

(c)

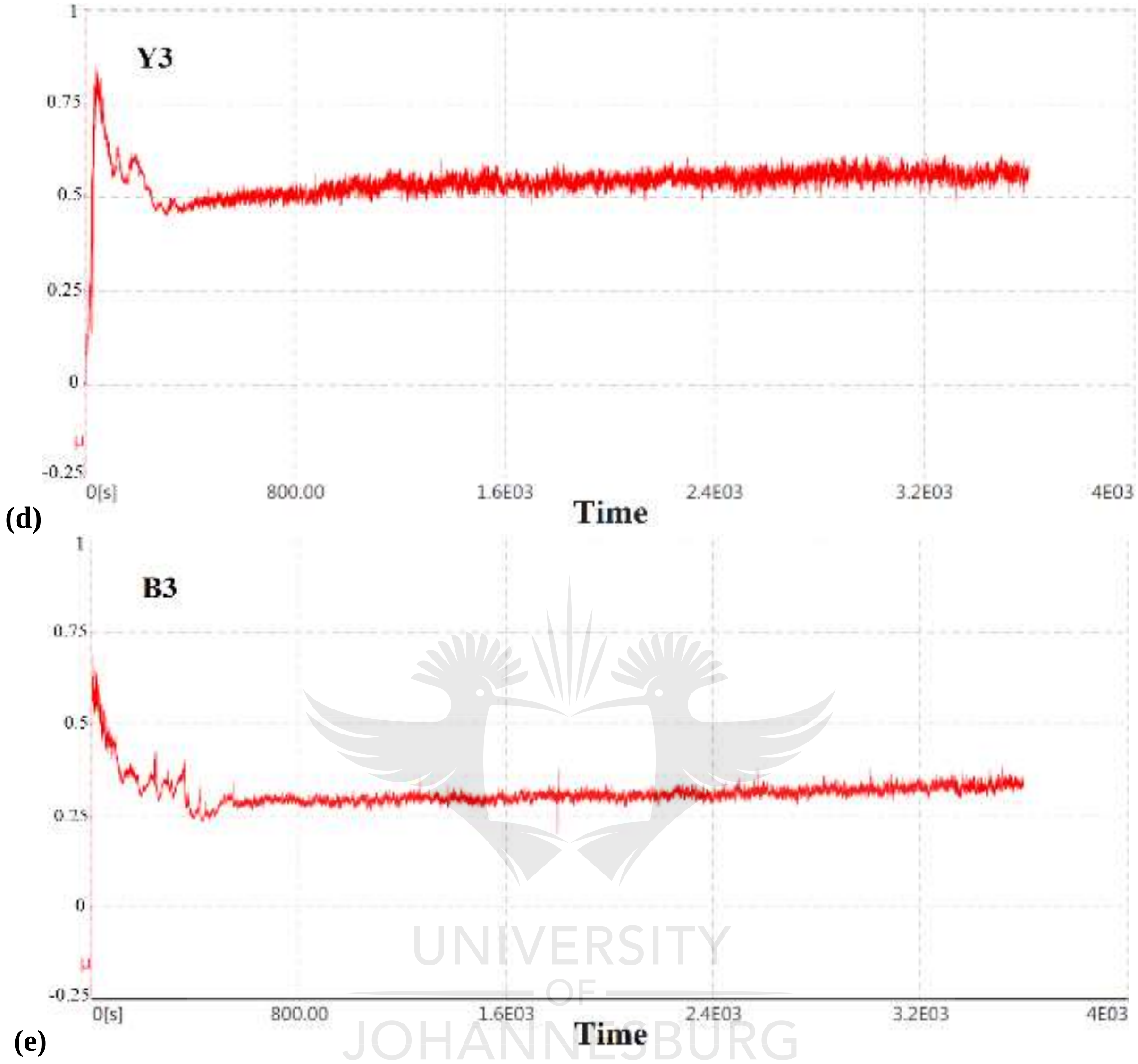

Figure 4. 28 Friction behaviour of the base material and some selected composites after being tested under 20 N load (a) 1100 Al, (b) B1), (c) Y2, (d) Y3 and (e) B3

The friction behavior exhibited by the 3-pass samples may be attributed to the improved distribution of the powder within the matrix observed in the sample produced via three passes, which has better particle distribution and finer grains. The rest of the results are to be found in Appendix F.

Figures 4.29 presents a graph showing the values of the friction coefficient of all the fabricated composites. It may be observed that the B3 composite (i.e. threaded taper/1200 rpm/ 3-passes) exhibit the least friction; while the parent material has the highest friction, which is about 50% higher than that of the fabricated composite (B3 sample). This friction behavior shows that the reinforcing particles help to improve the service life of the 1100 Al; and the results are in consistent with the hardness and tensile measurement.

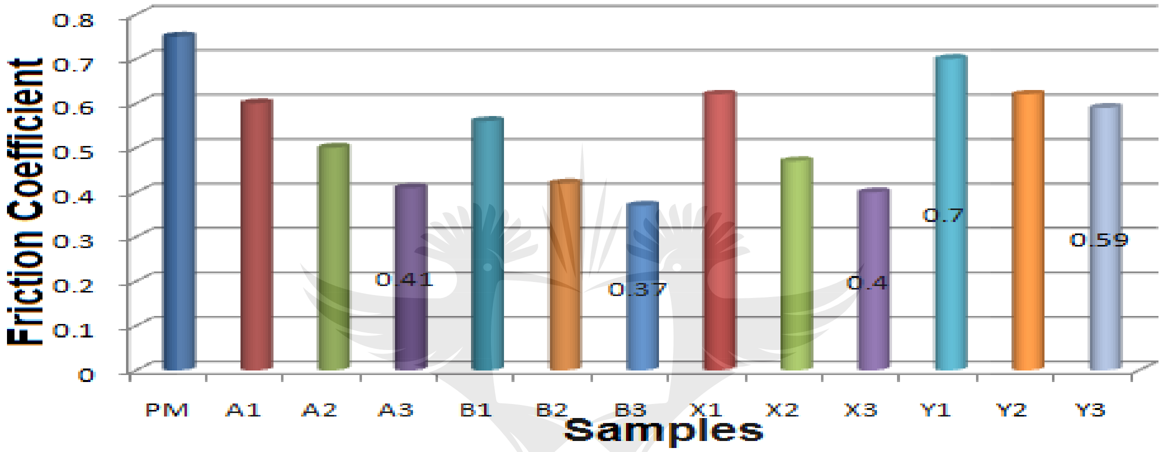

Figure 4. 29 Average friction coefficient of the base material and the fabricated composites

The wear rate of the composites was examined by using both the mass loss and the wear-volume lose for accuracy. The volume loss during the wear test was calculated from the width and the length of the wear scar SEM and profilometer, as shown in Figure 4.30. The dimensional wear coefficient, K, is generally used to calculate the wear rates of different types of materials; and it is defined by Equation 4.4.

$$K = \frac{V}{SL} \tag{4.4}$$

Where, V is the volume of the material worn away during testing (mm^3); S is the total sliding distance (1000m); L is the normal load (20N); and K is a dimensionless wear coefficient specific to the sample under test. From this calculation, the B3 and X3 samples have the least wear coefficient of 7.1844×10^{-6} mm^{2}N^{-1} and 8.6323×10^{-6}mm^{2}N^{-1} respectively, when compared to the rest.

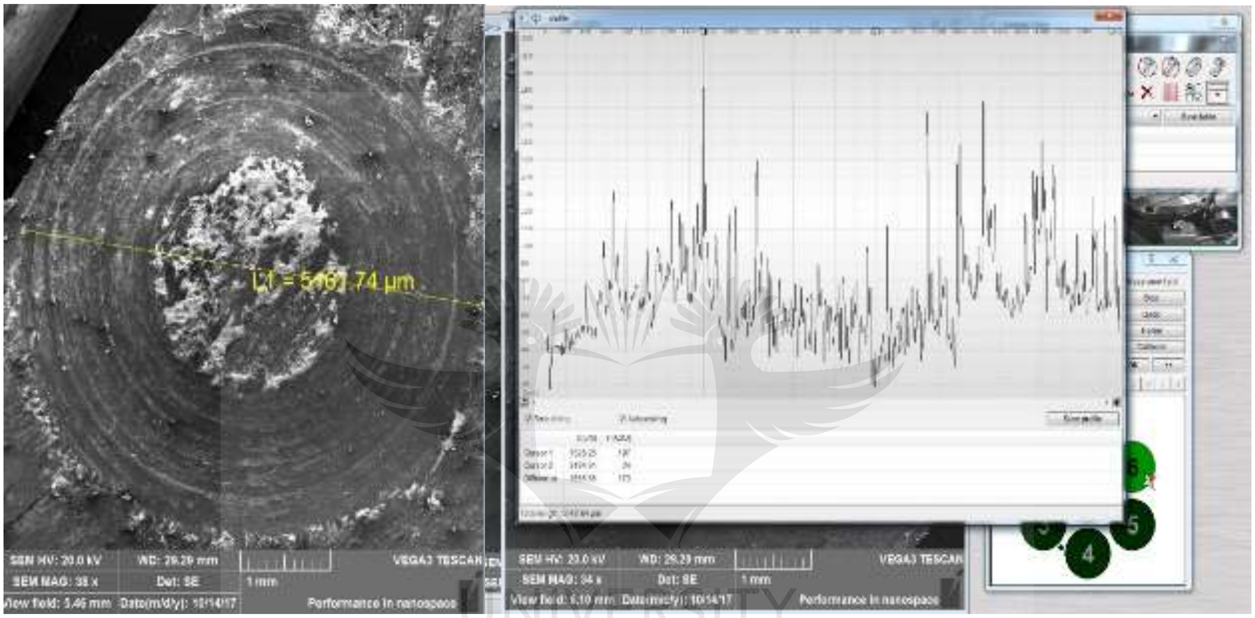

Figure 4. 30 Wear-volume losses calculation of the B3 sample using SEM

The loss of mass encountered by the samples was also investigated during the wear test. It is reasonable to expect that the materials after FSP would experience a smaller mass loss; so, the weights before and after the test were measured. Figure 4.31 presents the average loss of mass of the fabricated composites and the base metal; while a low mass loss is evident with all the 3-passes samples, when compared with the rest of the composites, which further reveals the importance of multi-pass FSP when fabricating metal matrix composites.

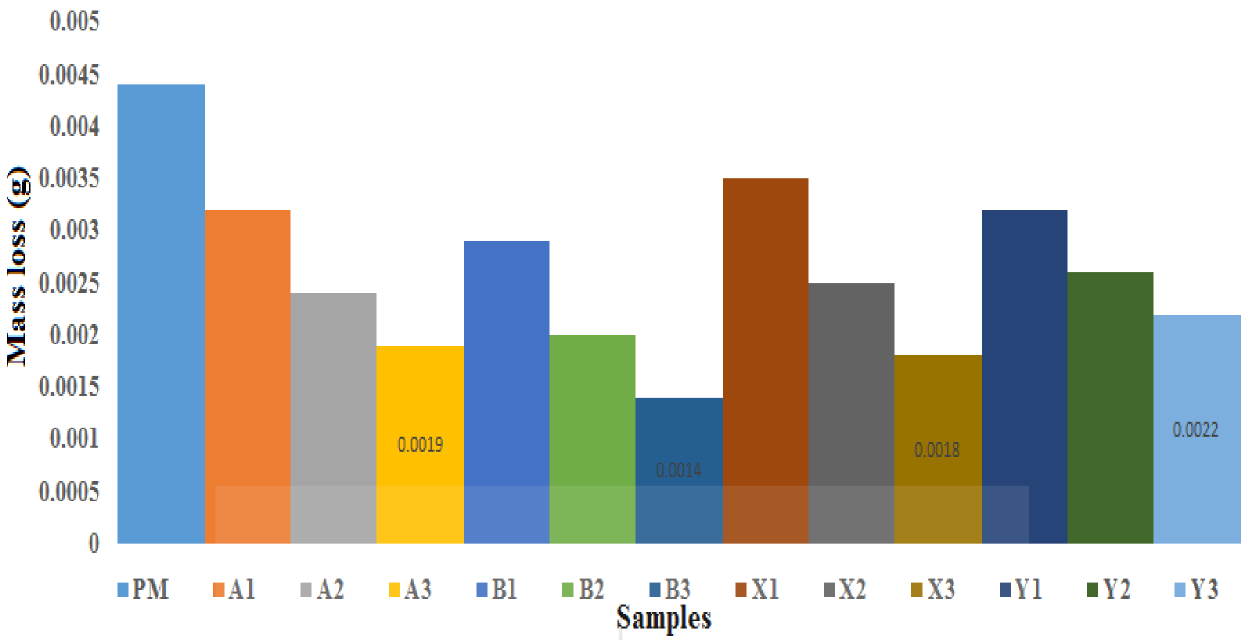

Figure 4. 31 Average mass loss of all fabricated specimens at 20N

Additionally, the B3 composite sample experiences the least mass loss, which is 67% lesser than the loss of mass encountered by the base material. This observation reveals that the wear performance of aluminium alloy might be improved by 67% with the addition of Ti-6Al-4V reinforcement particles. Although, as observed in some literatures, the wear properties of Ti-6Al-4V is not so good when used in some rubbing applications (Kgoete, Popoola, & Fayomi, 2018; B. Li, Shen, Luo, & Hu, 2013). However, it is useful in this case to improve the wear properties of Al.

For all the samples produced via 3-passes, a further test applying 50 N load was conducted. Here, the increase in the test load does not significantly affect the mass loss; and the friction remained stabled. For the B3 sample (i.e, sample fabricated via threaded-taper tool geometry on 1200rpn with 3-passes); the values of friction coefficient slightly increase from 0.37 to 0.40 and mass loss increased from 0.0014g to 0.0016g due to the additional 30 N load as shown in Figure 4.32.

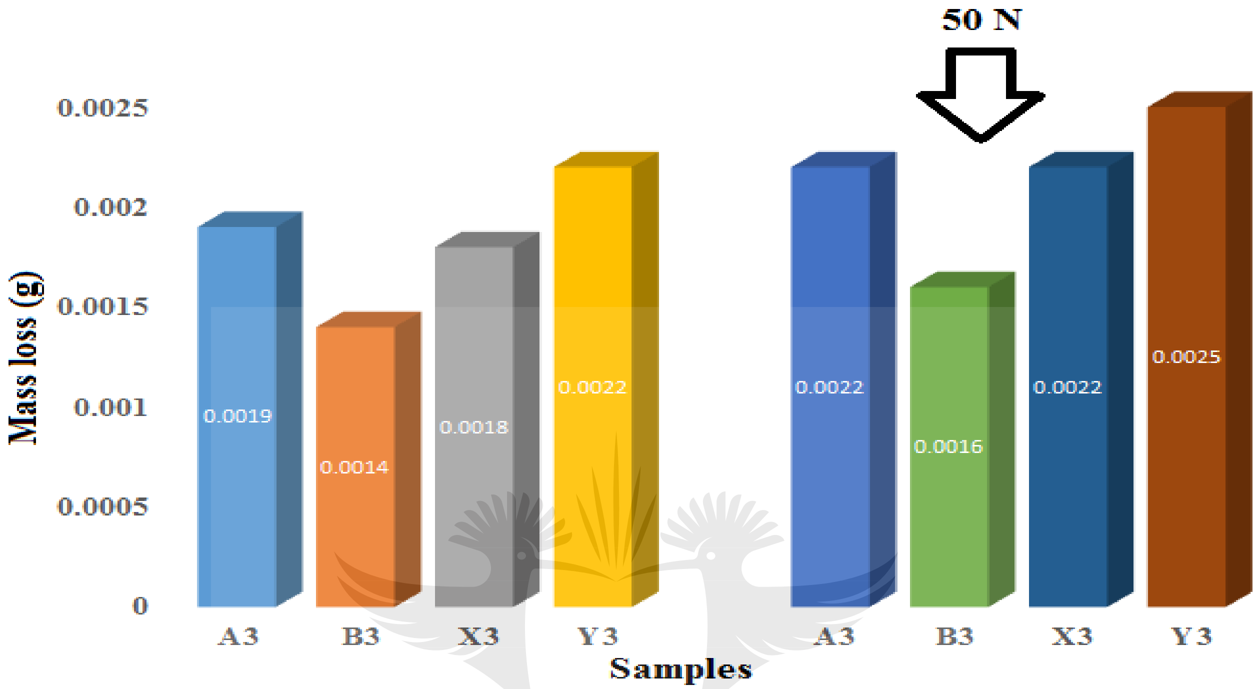

Figure 4. 32 Mass loss of composites during wear test at further testing of 50 N

From these findings, it follows that the Ti-6Al-4V/1100 Al fabricated via three passes can behave under higher loads satisfactorily right up to 50 N. Furthermore, as a result of the unique properties of the B3 composite in terms of wear resistance, particle distribution, hardness and fine grain structure, the importance of selecting appropriate combination of process parameters to produce 1100 Al/Ti-6Al-4V system cannot be overemphasized.

4.12 Worn Surfaces of Fabricated Samples and Comparison Between the Reinforced and the Unreinforced Matrix

The unreinforced 1100 Al alloy was subjected to three cumulative passes; and then it was compared with the B3 composite (i.e 3-passes reinforced with Ti-6Al-4V), the SEM micrographs showing the wear scars of both samples are seen in Figure 4.33. B-3 sample with the least mass loss, has its surface filled with striations during the test; and these striations indicate that B3 sample has been subjected to abrasive wear.

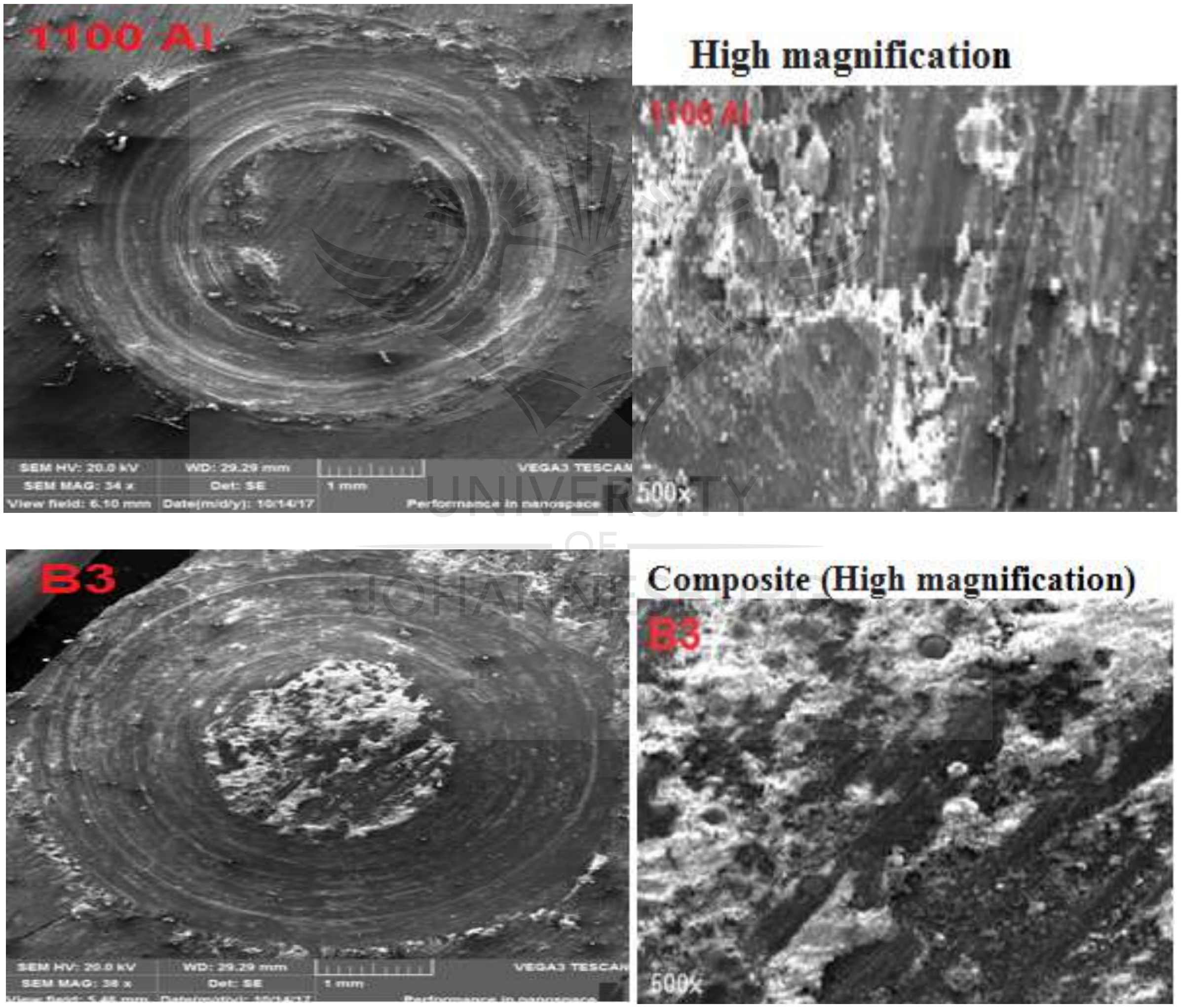

Figure 4. 33 SEM micrographs of the surfaces of the base material and the 3-passes composite (B3)

Two selected zones of the surface of the B-3 composite were further analyzed using EDS as shown in Figure 4.34. It was observed from the EDS peaks that some elements in the base metals are preset in the composite; elements such as Titanium, Aluminium and Nickel. These findings show that the composite also experienced adhesive wear, which is a confirmation that both the adhesive and the abrasive mechanisms controlled the composites. The worn surfaces of other composites can be found in Appendix G.

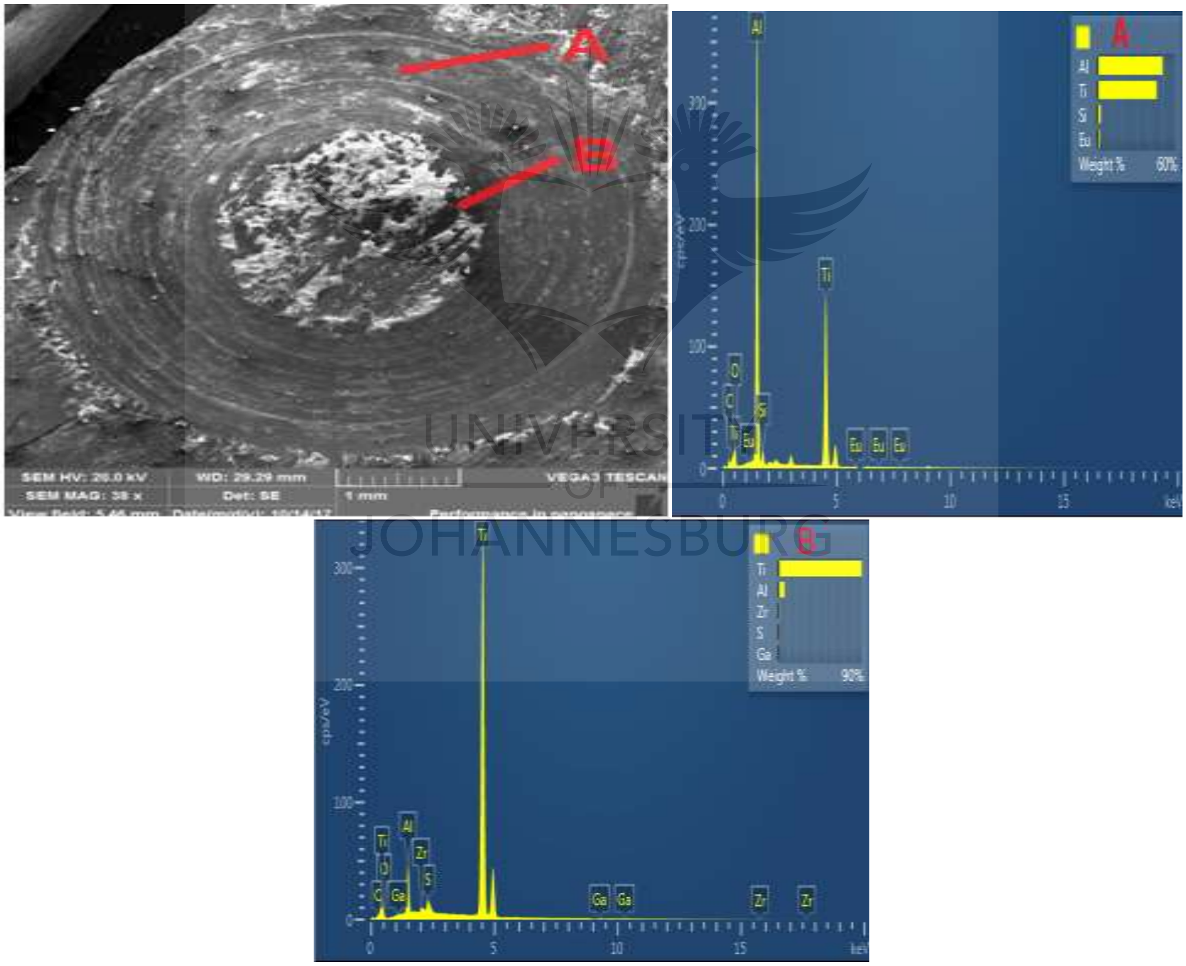

Figure 4. 34 Analysis of the B3 sample via EDS

The mass loss and friction coefficient of B3 sample are compared with unreinforced 3-passes specimen and the as-received base material (1100 Al alloy) shown in Table 4.7. The unreinforced sample subjected to three cumulative passes was fabricated via threaded tool geometry. From this table, the highest mass loss was observed to be the unreinforced 3-passes sample; due to the annealing effect of the generated heat during the fabrication of the samples. This observation reveals that the reinforced samples can perform better than the unreinforced samples, in terms of mass loss and friction coefficient. Lastly, it can be said that the Ti-6Al-4V reinforcements can overcome the annealing effect of the generated heat experienced during the fabrication process.

Table 4. 6 Wear behaviour of the parent material, unreinforced and reinforced 1100 Al

Properties	**Base material**	**3-passes Al Alloy**	**3-passes reinforced with Ti-6Al-4V (B-3)**
Mass loss (g)	**0.0046**	**0.0052**	**0.0014**
Coefficient of Friction	**0.75**	**0.056**	**0.37**
Dimensional wear coefficient(mm^2N^{-1})	**1.828×10^{-5}**	**1.5361×10^{-5}**	**7.1844×10^{-6}**

Summarily, the significance of tool geometry, tool speed and number of passes in fabrication of 1100 Aluminium alloy and Ti-6Al-4V particles can be observed on how uniformly the particles were dispersed within the matrix, can also be observed on the wear resistance, grain refinement and hardness of the composites.

4.13 Corrosion Behavior

Examinations were carried out on the corrosion behavior of the fabricated composites. Figure 4.35 presents the potentiodynamic polarization curves of some of these composites inserted in a 3.5wt

% of NaCl solution. The corrosion potentials (Ecorr) and current density (icorr) were generated via Tafel extrapolation. Non-symmetrical curves were observed with the composites; and the anodic branches of the composites show a lesser steep structure, when compared to the cathodic part. However, the cathodic and anodic kinetics reaction shows a similar trend pattern.

The B3 and Y3 samples (i.e 3-passes/1200rpm on different tool geometries) show increase in corrosion current, when compared with other composites fabricated in this research. Nevertheless, the highest current density in the anodic part is seen with the B3 composite. This results in a positive potential of the B3 and Y3 composites than the rest of the composites.

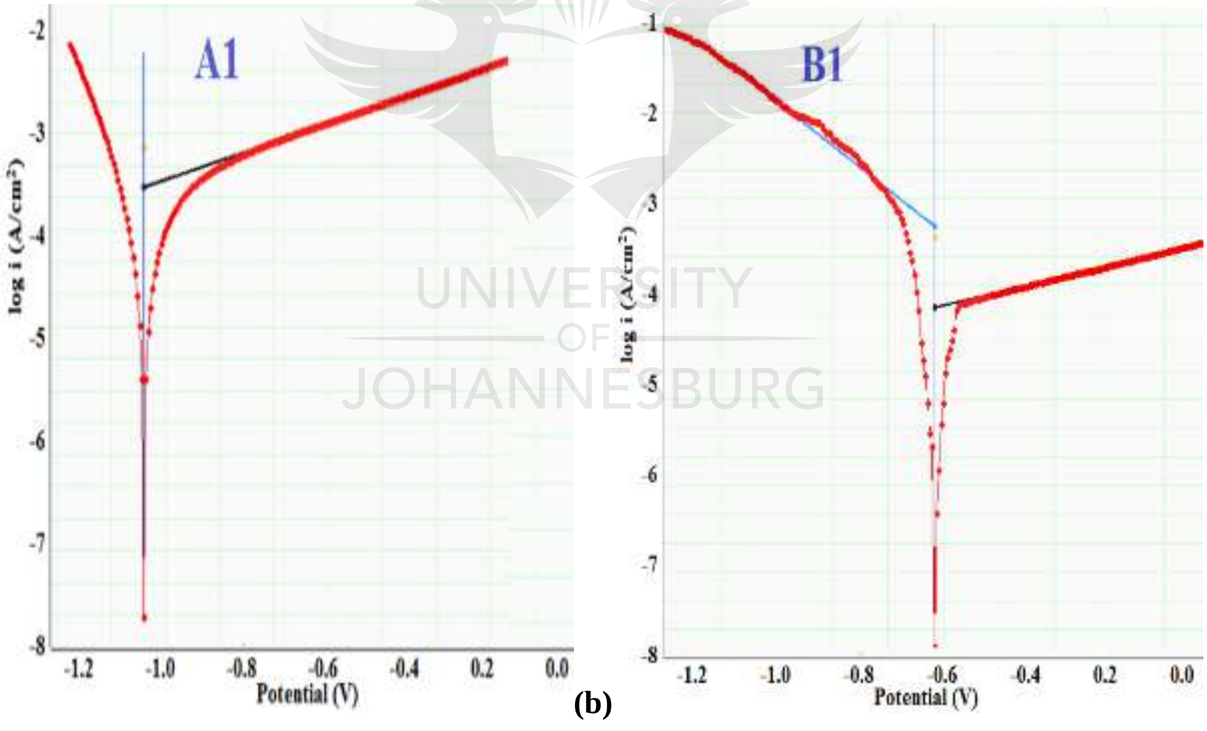

(a) **(b)**

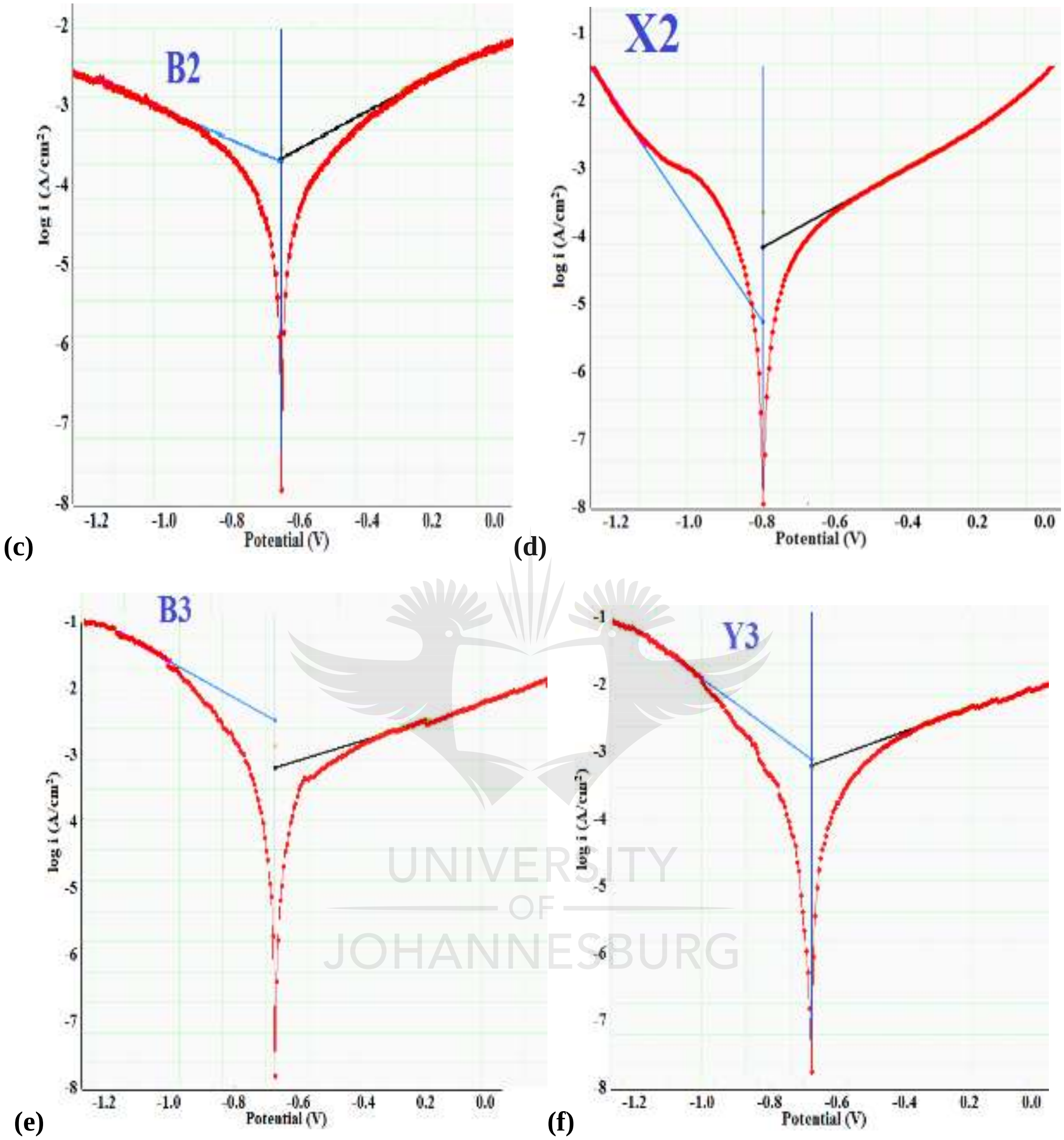
(c) (d) (e) (f)

Figure 4. 35 Potentiodynamic polarization curves of some samples (a) A1, (b) B1, (c) B2, (d) X2, (e) B3 and (f) Y3

The values obtained from the corrosion current density (icorr) of the composites can be used to calculate the corrosion rates of the composites by using the following equation (Gobara et al., 2015):

$$Corrosion\ Rate\ \left(\frac{mm}{year}\right) = \lambda.icorr.\frac{A.W.}{d} \qquad 4.5$$

$$Where;\ \lambda = \ 3.27 \times 10 - 3(mm.g)/(mA.cm.year)\ is\ a\ metric\ conversion\ factor$$

$$A.W. = Atomic\ Weight\ of\ \ Aluminium$$

$$d = \ Density\ (g/cm3)$$

From the calculation, the corrosion rates of the composites are generated and presented in Table 4.8. The highest corrosion rate is observed with the composites fabricated via 1-pass with a lower tool speed(600rpm). This result could be attributed to the tendency of these composites to have particles clustering together on grain boundaries, as observed by their SEM images. The composite with the least corrosion rate of 0.2020 mm/year has the highest resistance to corrosion, which is experienced by composite produced with threaded tool geometry/3 cumulative passes/1200rpm. From this observation, it may be inferred that the corrosion performance of the base material can be improved with the addition of Ti-6Al-4V powder, serving as a reinforcement. From several other studies, the corrosion rate of 1100 Al ranges from 0.732 to 0.940 mm/year, when inserted in NaCl solution(Chino, Hoshika, & Mabuchi, 2006; I. B. Singh, Singh, & Das, 2015).

Table 4. 7 Rate of corrosion of fabricated composites

Materials	OC potential (V)	Corrosion rate (mm/year)
3-passes/ 1200rpm/Square (Y3)	-0.6887	0.2421
2-passes/600rpm/Square (X2)	-0.8121	0.2696
3-passes/1200rpm/Threaded (B3)	-0.6542	0.2020
1-pass/600/Threaded (A1)	-1.0451	0.4771

After 3600 seconds of immersion in NaCl solution, the corroded surfaces of the composites were examined, in order to understand the corrosion mechanism encountered, as shown in Figure 4.36. The addition of the Ti-6Al-4V particles resulted into pitting formations; thereby indicating that corrosion may begin at the grain boundaries. Galvanic corrosion may occur between the reinforcement and the matrix, causing the particles to be separated from the matrix; while the matrix continuously dissolves. The 3-passes composite shows homogenous corrosive surface. The prominent bright regions observed with the A1 sample correspond to the sub-grain boundaries; and the X2 sample shows dendritic microstructures. The sub-grain boundaries appeared bright because of the presence of Titanium and oxide (Anil Kumar, Kumar, & Mukhopadhyay, 2018). The corroded surfaces of other composites can be found in Appendix H.

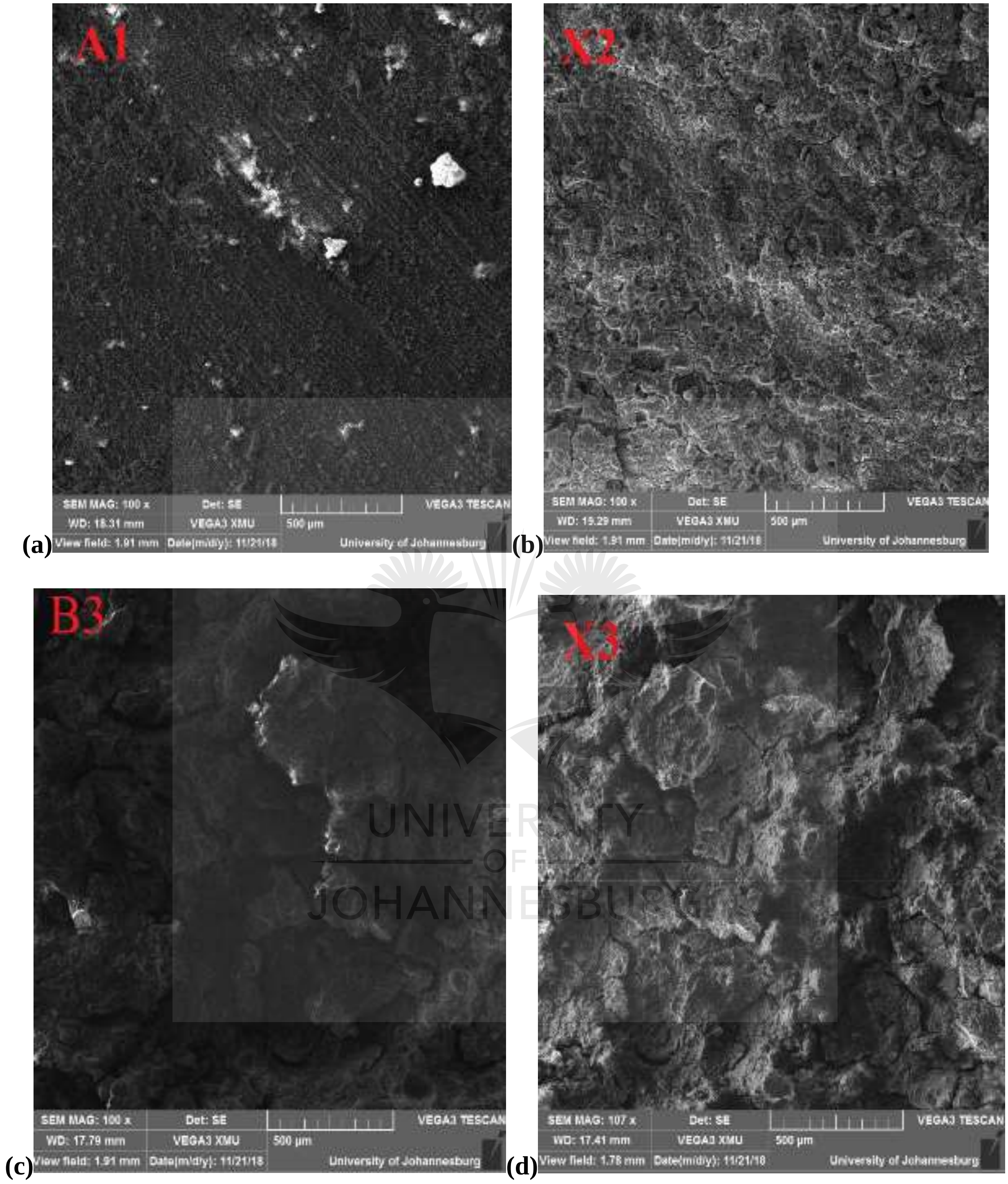

Figure 4. 36 SEM images revealing the corroded surfaces after the potentiostatic polarization test (a) A1, (b) X2, (c)B3 and (d) X3

In the case of the composites fabricated with 3-passes (i.e. B3 and A3), the valley-like features are evident. It can be observed that corrosion proceeded in a wide surrounding region of the grain boundary, in contrast to those samples fabricated with 1 to 2 passes. The shape of the grain boundary can be visibly seen because corrosion occurred at the grain boundary. The pit, which is deeper in the direction from transgranular region to the grain boundary, it can be said that the corrosion started from grain boundary and move to transgranular region. From this research, it was observed that the composites fabricated via 3-passes are more sensitive to intergranular corrosion than the rest of the composites. This is to further show that process parameters such as number of passes, helps to improve the corrosion performance of fabricated composites, which is in agreement with other published literatures (Jiang, Xiang, Atrens, Song, & Pan, 2017; Turan et al., 2018)

The chemical composition of elements in the grain boundaries of the B3 composite was analyzed via EDS. In the transgranular region, the major elements are Ti, Al, Na Cl and O. However, the Ti content was seen to be higher at the transgranular than the grain boundary, as shown in Figure 4.37.

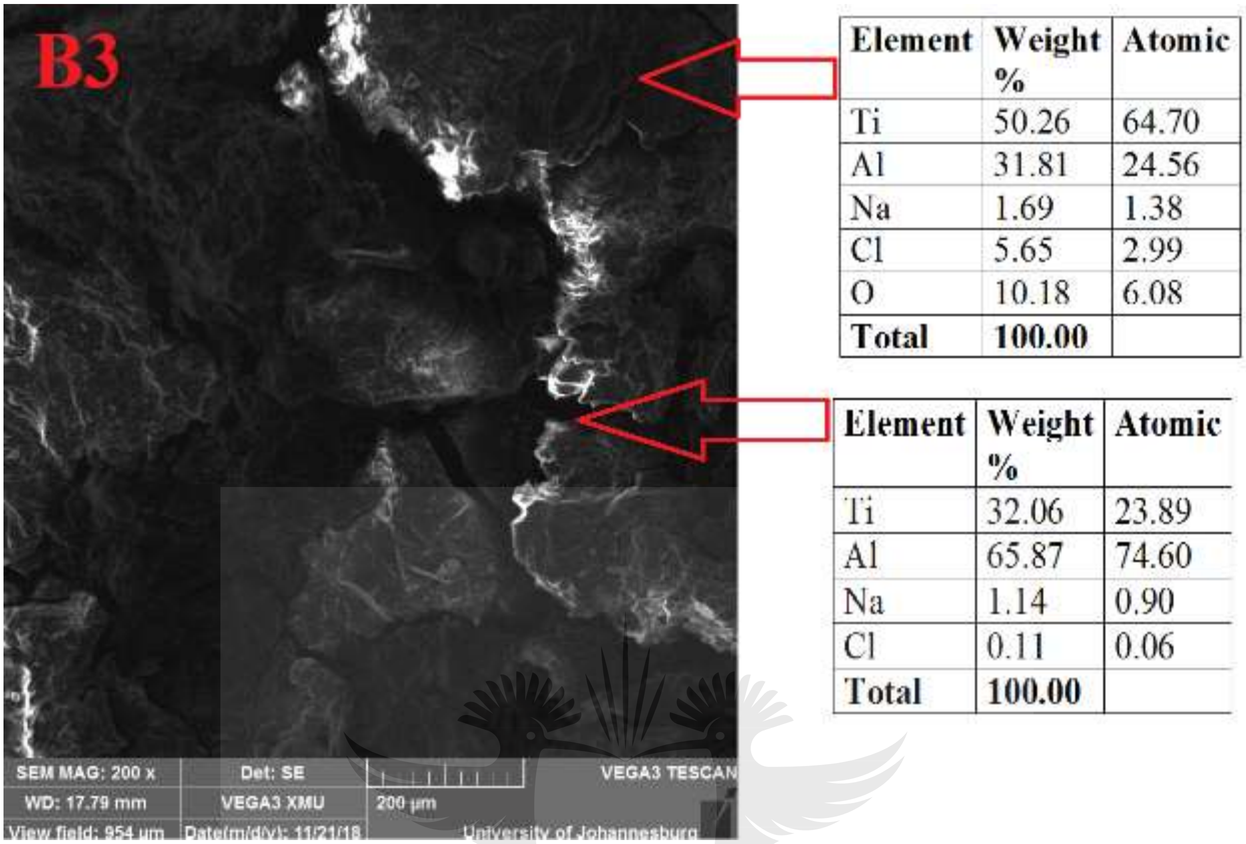

Element	Weight %	Atomic
Ti	50.26	64.70
Al	31.81	24.56
Na	1.69	1.38
Cl	5.65	2.99
O	10.18	6.08
Total	**100.00**	

Element	Weight %	Atomic
Ti	32.06	23.89
Al	65.87	74.60
Na	1.14	0.90
Cl	0.11	0.06
Total	**100.00**	

Figure 4. 37 Composition in the intergranular and transgranular regions at a corrosion site of the B3 composite

4.14 Heat Generation during FSP

Heat is a key factor in friction-stir processing, due to its capability to alter the microstructural evolution of the material, which in turn, affects the mechanical properties of the material. The required heat energy is generated in such away by mechanical friction between the rotating, traveling tool and workpieces itself. The heat generation during the FSP is determined by using Finite Element Analysis Software i.e ABAQUS. The numerical heat analysis and the experimentally measured result are compared for accuracy and validation.

4.14.1 Numerical Analysis of the Heat Generated

The temperature fields measured during the FSP of the composites can be calculated with the following heat transfer model. In the heat generation calculation, the transient temperature (T) which is a function of time (t) and the spatial coordinates (x, y, z) are estimated by the three-dimensional non-linear heat transfer in equation 4.6 based on Fourier's law of heat conduction (Ikumapayi, Akinlabi, & Majumdar, 2018).

$$\mathrm{K}\left(\frac{\partial^2 \mathrm{T}}{\partial \mathrm{x}^2}+\frac{\partial^2 \mathrm{T}}{\partial \mathrm{y}^2}+\frac{\partial^2 \mathrm{T}}{\partial \mathrm{z}^2}\right)+\mathrm{Q}_{\mathrm{int}}=\mathrm{c}\rho\frac{\partial \mathrm{T}}{\partial \mathrm{t}} \qquad 4.6$$

Where K is the thermal conductivity, $\mathrm{Q}_{\mathrm{int}}$ is the internal heat source rate, c is the heat capacity, and ρ is the material density (Veljic, Park, Rakin, Radakovic, & Todorovic, 2013)

The thermal history of the workpiece during FSP can be determined by the heat transfer coefficients on various surfaces of the workpiece, since these play a significant role in the determination of the thermal history of the workpiece in the friction-stir process. Convective and radiative heat loss to the ambient on all the workpiece surfaces, the heat loss (qs) is obtained by equation 4.7

$$\mathrm{qs}=\ \beta(\mathrm{T}-\mathrm{T}_0)+\varepsilon\sigma(\mathrm{T}^4-\mathrm{T}_0^4) \qquad 4.7$$

where, β is the convection coefficient (61 W/m2 K), T is in Kelvin, which is the absolute temperature of the workpiece materials; T_0 is the ambient temperature (300 K); ε is the emissivity of the plate surfaces (0.11 for Aluminium); and σ is the StefanBoltzmann constant (5.67 x 10^{-8} W/m^2 K^4).

With the assumptions made in this research, the heat produced due to friction between the material and the tool shoulder is the only source of heat generated; as the tool pin and the clamp only account for 2% of total heat loss; hence, this can be negligible, which is in agreement with another related study (Mil & Stamenkovi, 2009). The heat generation rate (qr) for this model is calculated based on the assumption of Johnson and Chen 2000 (Johnson & Chen, 2000) in equation 4.8

$$\mathrm{qr} = \frac{3\,\mathrm{Q_r}}{2\pi(\mathrm{r})} \qquad 4.8$$

Where, r is the tool shoulder radius; the coefficient of friction of the material is μ (0.3 for Aluminium); the tool speed is ω; the downward force of 25KN is represented by F; while the total heat input during the FSP of the composites is represented by $\mathrm{Q_r}$, and this is calculated by equation 4.9.

$$\mathrm{Q_r} = \frac{\pi\omega\mu\mathrm{F}(\mathrm{r}^2 + \mathrm{r})}{45(\mathrm{r})} \qquad 4.9$$

In this simulation, the heat flux (qr) obtained from the equation 4.8 is applied as surface load, by using the appropriate boundary conditions. The movement of FSP tool is implemented by creating a local co-ordinate system and calculating the heat load at each node at each instantaneous time step.

4.14.2 Finite Element Simulation Using ABAQUS/CAE

The modelling of the aluminum plate with a length of 50mm, breadth of 15mm and base extrusion depth of 200mm was performed by using ABAQUS/CAE 2019 edition, in order to check for the heat generated due to friction by the contact between the base material and the FSP tool during the process; while the fabrication process was performed. From the experimental result shown in Figure 4.3, the tool geometry, which is associated with the tool pin design, has little effect on the temperature difference. This observation is also in agreement with the literature (Swaminathan *et al.*, 2017).

A linear static and non-linear transient modelling method for the nodal temperature at the nodes was used to predict the heat generated during the process.

The assumptions made in developing the model are as follows;

- The material sheet is homogenous and isotropic.
- The workpiece material was cooled down to room temperature after each pass before subjecting it to another FSP pass
- Uniform boundary conditions existed along the processed part.
- The contact between the FSP tool and the base material have perfect contact, with 100% sticking condition.
- The tool pin only generates 2% of the total heat, which is negligible (Ramadan et al., 2016).
- The heat transferred to the clamp from the workpiece is negligible (Oladapo, Zahedi, Vahidnia, & Ikumapayi, 2018).

The experimental data obtained from the tensile test carried out on the composites were used to complete other parameters needed. The mechanical velocity used for the modelling is 30mm/min, which serves as the tool speed used for the experiment. The Aluminum composite at ambient temperature such as density (8930 Kg/m3), specific heat capacity (0.385 KJ/KgK), and thermal conductivity (400 W/mK) are used in finite element modelling, in which boundary conditions were specified. Table 4.9 shows the properties of Aluminum composite used in finite element modelling.

Table 4. 8 Simulation Parameters used for the Fabricated Aluminum composites

Parameters	Values
Young's Modulus of Elastic	70 GPa
Poisson's ratio	0.3
Thermal Conductivity	0.15 (W/(m·K))
Coefficient of Friction	0.1
Density	27000 Kg/ m^3
Specific Heat capacity	670000 J/K

The already established experimental results are compared with the results obtained from this model for validation. Figure 4.38 and 4.39 shows the Finite element model results generated with ABAQUS software. There is heat generated due to friction during the experiment. Initially, the temperature of the plate was 20^{o}C and it rose up to different peak temperatures when fabricated with different tool rotational speed, as seen in the simulated result in NT11 (423 ^{o}C for 600 rpm and 470 ^{o}C for 1200 rpm).

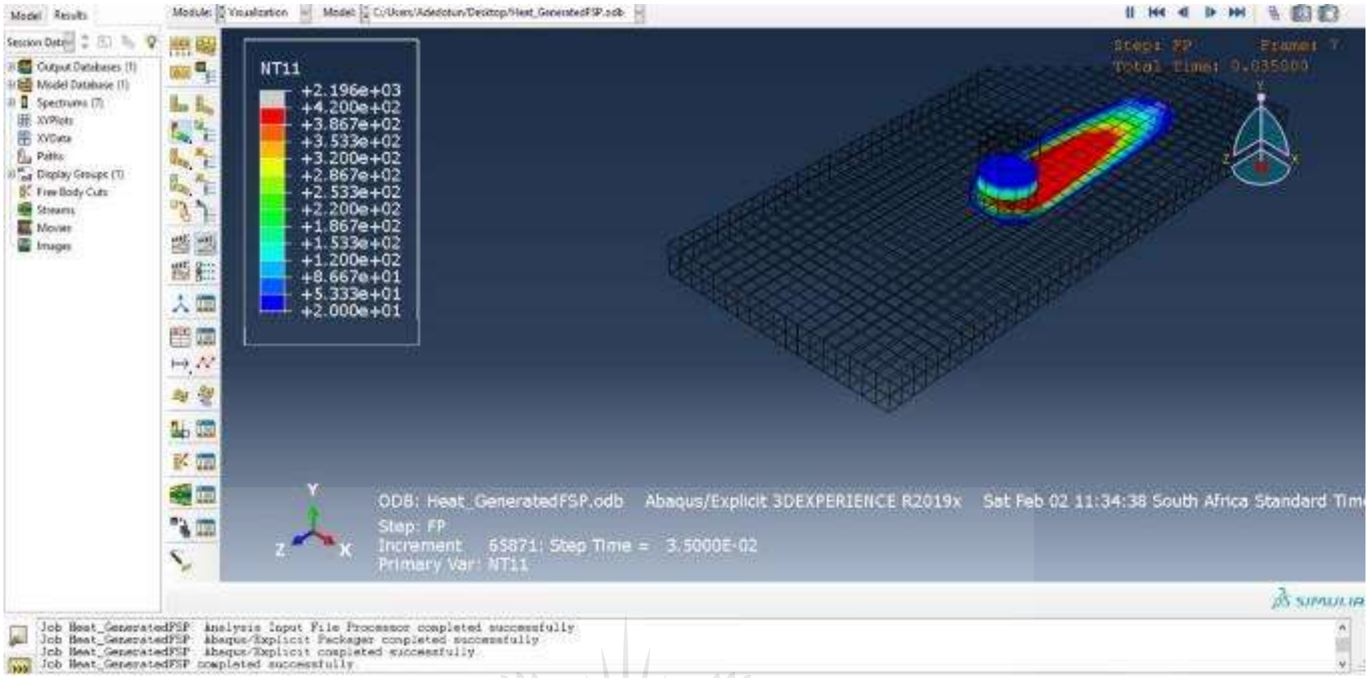

```
ODB: Heat_GeneratedFSP.odb    Abaqus/Explicit 3DEXPERIENCE R2019x    Sat Feb 02 11:34:38 South Africa Standard Tim
Step: FP
Increment    65871: Step Time =   3.5000E-02
Primary Var: NT11
```

```
Job Heat_GeneratedFSP: Analysis Input File Processor completed successfully
Job Heat_GeneratedFSP: Abaqus/Explicit Packager completed successfully
Job Heat_GeneratedFSP: Abaqus/Explicit completed successfully
Job Heat_GeneratedFSP completed successfully
```

Figure 4. 38 Temperature distributions obtained by ABAQUS on the Aluminum composite for ω=600 rev/min and v= 30mm/min

```
ODB: Heat_GeneratedFSP.odb    Abaqus/Explicit 3DEXPERIENCE R2019x    Wed Jan 30 04:13:47 South Africa St
Step: FP
Increment    141123: Step Time =   7.5000E-02
Primary Var: NT11
```

Figure 4. 39 Temperature distributions obtained by ABAQUS on the Aluminum composite for ω=1200 rev/min and v= 30mm/min

The temperature-time curve for the contact point (in situ) is compared with those of the simulation results. The simulated temperature history of FSP and the experimental result of the 3-passes sample produced with tool rotational speed of 600rpm are presented in Figure 4.40. While the 3-passes sample fabricated with 1200rpm are shown in Figure 4.41. Increasing the speed from 600 rpm to 1200 rpm causes significant changes in the thermal history; where the maximum temperature of 423^{o}C is observed at 600 rpm. However, at 1200rpm, a higher peak temperature of 470^{o}C is observed. These observations were consistent with those of other studies(Patel, Parlikar, Dhari, Mehta, & Pandya, 2019) (Lebaal, Chamoret, Schlegel, & Folea, 2017).

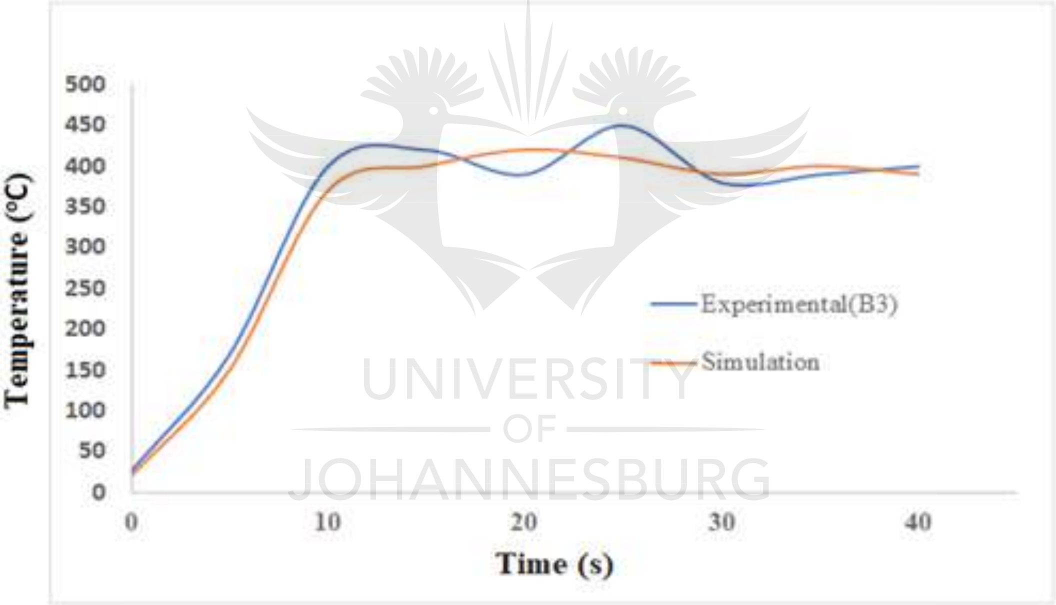

Figure 4. 40 Temperature profiles of simulated and experimented values at 600rpm (constant transverse speed of 30 mm/min)

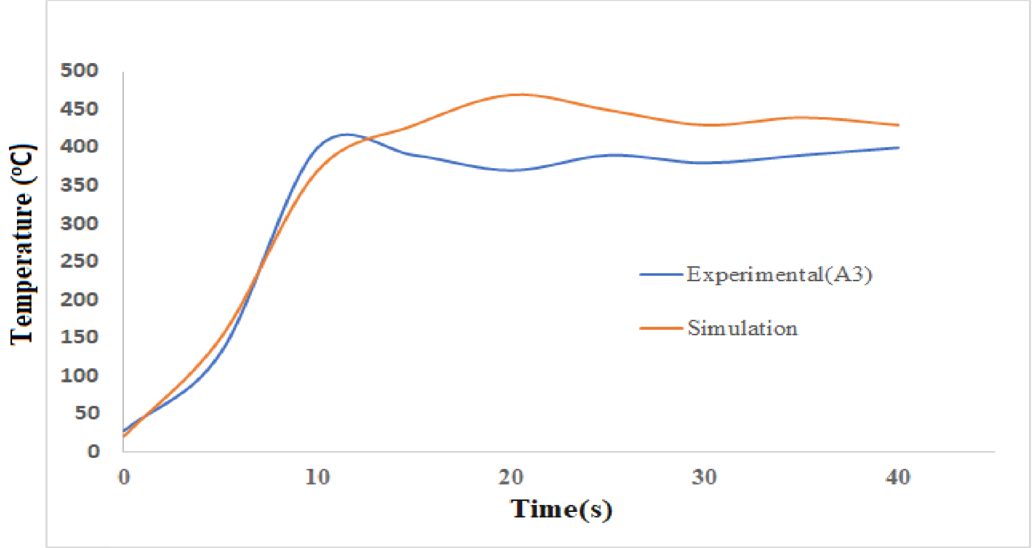

Figure 4. 41 Temperature profiles of simulated and experimented values at 1200 rpm (constant transverse speed of 30 mm/min)

It can be said that the varying tool speed used to fabricate these composites results in different peak temperature. The experimentally measured temperature results agree with the resulting generated heat energy of the developed model, with a temperature difference of less than 10°C.

4.15 Summary

To summarize this chapter, it is very important to simplify and extract the key findings and the facts from the selected composites through their characterizations and the analyses of the results. The macrographs of the composites have been examined. The SEM, Phase composition (XRD) and the EDS analyses of the composites were also presented, in order to study the distribution of the particles within the matrix; and also, to identify the intermetallic. The microhardness measurement of the reinforced and the unreinforced samples were compared. The tensile behavior of the composites and the base material were investigated. The wear resistance behavior of the fabricated composites was studied, as well as the wear volume/wear loss of the composites. The coefficient of friction and the wear mechanism of the Al/Ti-6Al-4V alloys were also examined. The open circuit potential (OCP), the polarization current density, the corrosion rate, and the Tafel plots of the composites inserted in NaCl solution were also investigated. The SEM images of the corroded samples were also presented, in order to show the morphologies of the corroded surfaces, after undergoing the electrochemical analyses in NaCl solution. Finite-element analysis was conducted, in order to analyze the heat generated due to friction during the process; and the effect of the varying tool rotational speed was investigated. Furthermore, the simulated results were compared with the experimentally measured temperature (in situ) for validation. The next chapter presents the conclusions and recommendations, which should serve as the inferences from all the results.

CHAPTER FIVE

5.0 CONCLUSIONS AND RECOMMENDATIONS

5.1 Introduction

The objective of this research project was to fabricate 1100 Aluminum alloy reinforced with Ti-6Al-4V powder, using the multi pass friction-stir processing technique with optimized process parameter, such as tool speed and tool shape geometry. In this chapter, the summary of the results obtained in the previous chapter are presented. This includes, the results of the microstructure evolution, chemical element analyses, and phase identification, the tensile test, the microhardness profile, the wear performance and the corrosion-resistance test. Additionally, the finite element analysis of the heat generated during the process, together with the experimental results are summarized. Some recommendations for further investigation are also presented.

5.2 Conclusions

The present research study has shown that 1100 Al can be successfully reinforced with Ti-6Al-4V particle via the multi-pass friction stir processing technique. A comprehensive literature review was conducted and discussed (Chapter Two) on Metal matrix composites and friction-stir processing as its fabrication technique. In the existing literature, there are very few published papers on friction-stir processing of Aluminum alloy and Titanium powder by considering the various process parameters. This was the main motivation of the current study, which was to characterize the evolving properties of 1100Al/Ti-6Al-4V composites, and to generate results to enhance the application of the fabricated composites. The produced composites were characterized and reported in this thesis. Investigations of the effects of the process parameters, such as tool rotational speed, tool geometry and the number of passes on the evolving microstructure, as well as the mechanical and electrochemical properties were conducted.

The following conclusions were made after the analysis:

The multi-pass FSP improves the particle distribution across the matrix and the grain structure becomes more refined, as the number of passes increase. The X-ray diffraction analyses were conducted by using a 2 mm collimator; and this revealed the presence of the AlTi, $AlTi_3$, Al_2Ti, Al_3Ti_3 intermetallic compounds at the stir zone of the composites. The X-ray diffraction results revealed the presence of intermetallics compounds at the stir zone which also correlates with the energy dispersive spectroscopy (EDS) analysis of the fabricated composites. Increase in the number of FSP passes is a viable method to enhance the mechanical properties of the 1100 Al. This study shows that to successfully reinforce metals during FSP and ensure uniform distribution of the particles, at least 3-passes of FSP should be employed.

From the investigation carried out in this research, the mechanical properties of 1100 Al alloy was greatly improved by the addition of Ti-6Al-4V powder. Process parameters, such as tool rotational speed, tool geometries and number of FSP passes were investigated, with the aim of attaining the best combination of process parameters that offers uniform distribution of particles within the matrix, which in turn, improves the mechanical properties of the fabricated composites.

The most suitable tool geometry employed in this research is the threaded taper tool geometry, and the most uniform distribution of particles within the matrix is observed with the composites subjected to three cumulative passes and tool rotational speed of 1200 rpm. When compared to the unreinforced Aluminium-alloy, the composites experienced 30% increment in tensile strength.

This research also observed that the increase in number of passes helps to modify the microstructure; defects elimination, pitholes, acicular breakup of Titanium particles and finer grain structures were noticed as the passes increases. The distribution of the Ti-6Al-4V particles within the matrix greatly influence the wear performance of the composites. Furthermore, the process parameters influenced the particle distribution, more heat input is generated by using higher tool rotational speed and the chosen tool geometries used in this research, which in turn helped to distribute the particles uniformly.

Ti-6Al-4V/1100 Al may have a good potential to be used in orthopedic application where corrosion resistance is of paramount importance. The B3 composites fabricated in this research shows an improved wear and corrosion resistance. This result can be attributed to the reinforcing powder used. Ti-6Al-4V is an alloy produced for higher toughness; and due to its biocompatibility, the alloy is largely used for implants; because it can overcome attacks from the fluid in the body, while being attached to the tissues found in human body.

Most importantly, the 1100 Al is the most commercially available and cheapest grade of aluminum alloy. However, the use of 1100 Al in automotive and aerospace is limited, due to its tensile strength, when compared with the higher grades of Aluminum, such as the 6000 and the 7000 series. With the fabricated composites in this research, the 1100 Al attain a tensile strength of 275 MPa, which is higher than 7075-T0 Al alloy.

In application where the cost and the availability of material are important, the fabricated composite using the process parameters combination of 1200rpm/3-passes/30mm/min/Threaded tool geometry is generally to be recommended.

Additionally, the heat generation due to friction, during the process is simulated by using Finite Element Analysis Software i.e ABAQUS. The simulated temperature history of FSP for the composites at different tool rotational speeds shows that the peak temperature was increased when increasing the tool rotational speed, due to the increased strain rate and the plastic dissipation in the stir zone.

A peak temperature of 423°C was observed with the 600 rpm processed sample while a higher peak temperature of 470°C was observed with the 1200 rpm processed sample. The experimentally measured temperature results are in agreement with the resulting generated heat energy of the developed model, with a temperature difference of less than 10°C.

Different process parameters, such as tool geometries, number of passes and tool rotational speed were used in this research work. This research has been able to provide valuable information on the fabrication of 1100 Al with Ti-6Al-4V powder, when using friction-stir processing technique. It was noticed that the samples fabricated using 1-pass and 600 rpm on both tool geometries used in this study exhibited lower mechanical properties. However, higher mechanical properties and corrosion resistance were reached when they were subjected to three cumulative passes. The produced composites were characterized; and the obtained results showed that the tools geometries and process parameters used in this research work can be recommended; and the effect of the heat generated due to the difference in tool rotational speed were validated with simulation. This information can be used in various industries, including the manufacturing, medical, automotive and aerospace.

5.3 Recommendations for future work

This thesis focused on some of the key issues in understanding the evolving properties of friction-stir processed 1100 Al alloy with Ti-6Al-4V powder. As a result of some of the findings, there are additional areas that need to be addressed in more detail in future research. These can be summarized in the following:

- Microstructure characterization should be extended to the use of advanced equipment, like Transmission electron microscopy (TEM), Scanning transmission electron microscopy (STEM), and Electron backscatter diffraction (EBSD).

- Extensive corrosion studies (galvanic and intergranular inclusive) need to be carried out on the composites on the heat affected zone, the thermo-mechanical affected zone, and the stir zone, in order to ascertain the susceptibility of the composites to corrosive media.

- A complete friction-stir process simulation using ANSYS or ABAQUE/CAE should be performed for a comprehensive understanding of the material flow during the process and for the particle distribution within the microstructure.

- A study of different tool geometries and dimensions needs to be used, to verify whether higher mechanical properties can be reached with 1100 Al, these will further increase the applicability of 1100 Al alloy.

- A more detailed application of these alloy in clinics should be investigated, in order to check for its reliability and biocompatibility when used as implants. A further corrosion resistance test is recommended, for 1 day, 30 days and more, when immersed in simulated body fluid solution.

- The friction stir process has been simulated, and the consideration has been on the heat generated due to friction during the process, and a further assessment of pin effect, shoulder design and material flow during FSP should be studied. The simulation process in this study can be further used to predict the microstructure evolution of the fabrication process.

REFERENCES

Aa, A. Z., Titanovim, O. J. A. A. N. E. S., Sanusi, K. O., & Akinlabi, E. T. (2017). FRICTION-STIR PROCESSING OF A COMPOSITE ALUMINIUM ALLOY (AA 1050) REINFORCED WITH TITANIUM CARBIDE POWDER, *51*(3), 427–435. https://doi.org/10.17222/mit.2016.021

Abegunde, O. O., Akinlabi, E. T., & Madyira, D. (2017). Microstructural evolution and mechanical characterizations of AL-TiC matrix composites produced via friction stir welding. *Materiali in Tehnologije*, *51*(2), 297–306. https://doi.org/10.17222/mit.2016.033

Abraham, F. (2012). Tensile properties and fracture behaviour of Multipass Friction Stir Processed Al-7Si-0 . 3Mg cast alloy by, (July).

Adetunla, A., & Akinlabi, E. (2006). Mechanical Characterization of Al / Ti-6Al-4V Surface Composite Fabricated via FSP : A comparison of Tool Geometry and Number of Passes.

Ahmadkhaniha, D., Heydarzadeh Sohi, M., Salehi, A., & Tahavvori, R. (2016). Formations of AZ91/Al2O3 nano-composite layer by friction stir processing. *Journal of Magnesium and Alloys*, *4*(4), 314–318. https://doi.org/10.1016/j.jma.2016.11.002

Al-Fadhalah, K. J., Almazrouee, A. I., & Aloraier, A. S. (2014). Microstructure and mechanical properties of multi-pass friction stir processed aluminum alloy 6063. *Materials and Design*, *53*, 550–560. https://doi.org/10.1016/j.matdes.2013.07.062

Alpas, A. T., & Inagaki, J. (2000). Effect of Microstructure on Fracture Mechanisms in, *40*(2), 172–181. https://doi.org/10.2355/tetsutohagane1955.87.1

Aly, A., Deris, S., & Zaki, N. (2011). Research review for digital image Segmentation techniques. *International Journal of Computer Science & …*, *3*(5), 99–106. https://doi.org/10.5121/ijcsit.2011.3509

American, A., & Standard, N. (1995). Standard Practice for Preparation of Metallographic Specimens 1, *03*(March).

Annigeri, U. K., & B, V. K. G. (2018). ScienceDirect Effect of Reinforcement on Density , Hardness and Wear Behavior of Aluminum Metal Matrix Composites : A Review. *Materials Today: Proceedings*, *5*(5), 11233–11237. https://doi.org/10.1016/j.matpr.2018.02.002

Anvari, S. R., Karimzadeh, F., & Enayati, M. H. (2013). Wear characteristics of Al-Cr-O surface nano-composite layer fabricated on Al6061 plate by friction stir processing. *Wear*, *304*(1–2), 144–151. https://doi.org/10.1016/j.wear.2013.03.014

Arab, S. M., Karimi, S., Jahromi, S. A. J., Javadpour, S., & Zebarjad, S. M. (2015). Fabrication of novel fiber reinforced aluminum composites by friction stir processing. *Materials Science and Engineering A*, *632*, 50–57. https://doi.org/10.1016/j.msea.2015.02.032

Asadi, P., Akbari, M., & Karimi-Nemch, H. (2014). *Simulation of friction stir welding and processing*. *Advances in Friction-Stir Welding and Processing*. Woodhead Publishing Limited. https://doi.org/10.1533/9780857094551.499

Asif, M., Chandra, K., & Misra, P. S. (2011). Development of Aluminium Based Hybrid Metal Matrix Composites for Heavy Duty Applications. *Journal of Minerals & Materials Characterization & Engineering*, *10*(14), 1337–1344.

Barmouz, M., Asadi, P., Besharati Givi, M. K., & Taherishargh, M. (2011). Investigation of mechanical properties of Cu/SiC composite fabricated by FSP: Effect of SiC particles' size and volume fraction. *Materials Science and Engineering A*, *528*(3), 1740–1749. https://doi.org/10.1016/j.msea.2010.11.006

Brewer, W. D., Bird, R. K., & Wallace, T. A. (1998). Titanium alloys and processing for high speed aircraft, *243*, 299–304.

Buffa, G., Campanella, D., & Fratini, L. (2017). Enhancement of mechanical properties of FSWed AA7075 lap joints through in-situ fabrication of MMC ઢ. *Journal of Manufacturing Processes*, *28*, 422–427. https://doi.org/10.1016/j.jmapro.2017.04.008

Candan, E. (2002). Effect of alloying elements to aluminium on the wettability of AL/SiC system. *Turkish Journal of Engineering and Environmental Sciences*, *26*(1), 1–5.

Chainarong, S., Muangjunburee, P., & Suthummanon, S. (2014). Friction stir processing of SSM356 aluminium alloy. *Procedia Engineering*, *97*, 732–740. https://doi.org/10.1016/j.proeng.2014.12.303

Charit, I., & Mishra, R. S. (2017). Effect of friction stir processed microstructure on tensile properties of an Al-Zn-Mg-Sc alloy upon subsequent aging heat treatment. *Journal of Materials Science and Technology*, *34*(1), 214–218. https://doi.org/10.1016/j.jmst.2017.10.021

CHEN, Y., DING, H., MALOPHEYEV, S., KAIBYSHEV, R., CAI, Z., & YANG, W. (2017). Influence of multi-pass friction stir processing on microstructure and mechanical properties of 7B04-O Al alloy. *Transactions of Nonferrous Metals Society of China*, *27*(4), 789–796.

https://doi.org/10.1016/S1003-6326(17)60090-6

Chino, Y., Hoshika, T., & Mabuchi, M. (2006). Mechanical and Corrosion Properties of AZ31 Magnesium Alloy Repeatedly Recycled by Hot Extrusion. *Materials Transactions*, *47*(4), 1040–1046. https://doi.org/10.2320/matertrans.47.1040

Choi, J., Liu, H., Ushioda, K., & Fujii, H. (2019). Materialia Dissimilar friction stir welding of immiscible titanium and magnesium. *Materialia*, *7*(June), 100389. https://doi.org/10.1016/j.mtla.2019.100389

Costa, M. I., Verdera, D., Vieira, M. T. F., & Rodrigues, D. M. (2014). Surface enhancement of cold work tool steels by friction stir processing with a pinless tool. *Applied Surface Science*, *296*, 214–220. https://doi.org/10.1016/j.apsusc.2014.01.094

Crist, E. (2012). (Ti - 62222) for Commercial Aerospace Applications Sesh Tamirisa.

Darras, B. M., Omar, M. A., & Khraisheh, M. K. (2007). Experimental Thermal Analysis of Friction Stir Processing, 3801–3806. https://doi.org/10.4028/www.scientific.net/MSF.539-543.3801

Davis, J. R. (2001). Aluminum and Aluminum Alloys. *Light Metals and Alloys*, 66. https://doi.org/10.1361/autb2001p351

Dhayalan, R., Kalaiselvan, K., & Sathiskumar, R. (2014). Characterization of AA6063/SiC-Gr surface composites produced by FSP technique. *Procedia Engineering*, *97*, 625–631. https://doi.org/10.1016/j.proeng.2014.12.291

Dinaharan, I., Kalaiselvan, K., Akinlabi, E. T., & Davim, J. P. (2017). Microstructure and wear characterization of rice husk ash reinforced copper matrix composites prepared using friction stir processing. *Journal of Alloys and Compounds*, *718*, 150–160. https://doi.org/10.1016/j.jallcom.2017.05.117

Duhan, S. (2017). Effect of Reinforcement on Property of Aluminium Metal Matrix Composite : A Review, *5*(10), 1–6.

El-Rayes, M. M., & El-Danaf, E. A. (2012). The influence of multi-pass friction stir processing on the microstructural and mechanical properties of Aluminum Alloy 6082. *Journal of Materials Processing Technology*, *212*(5), 1157–1168. https://doi.org/10.1016/j.jmatprotec.2011.12.017

Faraji, G., & Asadi, P. (2011). Characterization of AZ91/alumina nanocomposite produced by FSP. *Materials Science and Engineering A*, *528*(6), 2431–2440. https://doi.org/10.1016/j.msea.2010.11.065

Gadakh, V. S., & Adepu, K. (2013). Heat generation model for taper cylindrical pin profile in FSW. *Journal of Materials Research and Technology*, *2*(4), 370–375. https://doi.org/10.1016/j.jmrt.2013.10.003

Gobara, M., Shamekh, M., & Akid, R. (2015). Improving the corrosion resistance of AZ91D magnesium alloy through reinforcement with titanium carbides and borides. *Journal of Magnesium and Alloys*, *3*(2), 112–120. https://doi.org/10.1016/j.jma.2015.03.002

Hashemi, R., & Hussain, G. (2015a). Wear performance of Al/TiN dispersion strengthened surface composite produced through friction stir process: A comparison of tool geometries and number of passes. *Wear*. https://doi.org/10.1016/j.wear.2014.11.024

Hashemi, R., & Hussain, G. (2015b). Wear performance of Al/TiN dispersion strengthened surface composite produced through friction stir process: A comparison of tool geometries and number of passes. *Wear*, *324–325*, 45–54. https://doi.org/10.1016/j.wear.2014.11.024

Hashemi, R., & Hussain, G. (2015c). Wear performance of Al/TiN dispersion strengthened surface composite produced through friction stir process: A comparison of tool geometries and number of passes. *Wear*, *324–325*, 45–54. https://doi.org/10.1016/j.wear.2014.11.024

He, Z., Chen, Y., Yang, J., Tang, C., Lv, J., Liu, Y., … Hui, D. (2017). Fabrication of Polydimethylsiloxane films with special surface wettability by 3D printing. *Composites Part B*, *129*, 58–65. https://doi.org/10.1016/j.compositesb.2017.07.025

Ikumapayi, O. M., Akinlabi, E. T., & Majumdar, J. D. (2018). Review on thermal, thermomechanical and thermal stress distribution during friction stir welding. *International Journal of Mechanical Engineering and Technology*, *9*(8), 534–548.

Jayamathy, M., Kailas, S. V., Kumar, K., Seshan, S., & Srivatsan, T. S. (2005). The compressive deformation and impact response of a magnesium alloy: Influence of reinforcement. *Materials Science and Engineering A*, *393*(1–2), 27–35. https://doi.org/10.1016/j.msea.2004.09.070

Jiang, B., Xiang, Q., Atrens, A., Song, J., & Pan, F. (2017). Influence of crystallographic texture and grain size on the corrosion behaviour of as-extruded Mg alloy AZ31 sheets. *Corrosion Science*, *126*(August), 374–380. https://doi.org/10.1016/j.corsci.2017.08.004

Johnson, A. R., & Chen, T. (2000). Coupled thermo-mechanical analyses of dynamically loaded rubber cylinders 1, *1985*.

Journal, I., Technology, A. M., Reza, S., Zeidabadi, H., Daneshmanesh, H., Narimani, M., … Abraham, F. (2017). A Review on Properties, Behaviour and Processing Methods for Al-Nano Al2O3 Composites. *Procedia Engineering*, *97*(4), 24–27. https://doi.org/10.1016/j.jmst.2013.09.021

Kangazian, J., & Shamanian, M. (2019). Microstructure and mechanical characterization of Incoloy 825 Ni-based alloy welded to 2507 super duplex stainless steel through dissimilar friction stir welding. *Transactions of Nonferrous Metals Society of China*, *29*(8), 1677–1688. https://doi.org/10.1016/S1003-6326(19)65074-0

Kgoete, F. M., Popoola, A. P. I., & Fayomi, O. S. I. (2018). In fl uence of spark plasma sintering on microstructure and corrosion behaviour of Ti-6Al-4V alloy reinforced with micron-sized Si 3 N 4 powder. *Defence Technology*, 4–8. https://doi.org/10.1016/j.dt.2018.04.011

Khairuzzaman, A. K. M., & Chaudhury, S. (2017). Multilevel thresholding using grey wolf optimizer for image segmentation. *Expert Systems with Applications*, *86*, 64–76. https://doi.org/10.1016/j.eswa.2017.04.029

Khodabakhshi, F., Nosko, M., & Gerlich, A. P. (2018). Effects of graphene nano-platelets (GNPs) on the microstructural characteristics and textural development of an Al-Mg alloy during friction-stir processing. *Surface and Coatings Technology*, *335*(December 2017), 288–305. https://doi.org/10.1016/j.surfcoat.2017.12.045

Khodabakhshi, F., Simchi, A., Kokabi, A. H., & Gerlich, A. P. (2015). Friction stir processing of an aluminum-magnesium alloy with pre-placing elemental titanium powder: In-situ formation of an Al<inf>3</inf>Ti-reinforced nanocomposite and materials characterization.

Materials Characterization, *108*, 102–114. https://doi.org/10.1016/j.matchar.2015.08.016

Koli, D. K., Agnihotri, G., Purohit, R., Sunil, B. R., Reddy, G. P. K., Patle, H., … Abraham, F. (2017). Superplasticity of the rolled and friction stir processed Al-4.5 Mg-0.35Sc-0.15Zr alloy. *Procedia Engineering*, *27*(4), 214–220. https://doi.org/10.1016/S1003-6326(17)60089-X

Komarasamy, M., Mishra, R. S., Grant, G. J., Northwest, P., & Hovanski, Y. (2013). Friction Stir Welding and Processing VII, (October 2017). https://doi.org/10.1002/9781118658345.ch5

Kondaiah, V. V., Pavanteja, P., Afzal Khan, P., Anannd Kumar, S., Dumpala, R., & Ratna Sunil, B. (2017). Microstructure, hardness and wear behavior of AZ31 Mg alloy - Fly ash composites produced by friction stir processing. *Materials Today: Proceedings*, *4*(6), 6671–6677. https://doi.org/10.1016/j.matpr.2017.06.441

Kumar, A., Kumar, S., & Mukhopadhyay, N. K. (2018). Introduction to magnesium alloy processing technology and development of low-cost stir casting process for magnesium alloy and its composites. *Journal of Magnesium and Alloys*, *000*, 1–10. https://doi.org/10.1016/j.jma.2018.05.006

Kumar, A., Murari, K., & Dey, A. (2018). ScienceDirect Aluminium Metal Matrix Composite with Rice Husk as Reinforcement : A Review. *Materials Today: Proceedings*, *5*(9), 20130–20137. https://doi.org/10.1016/j.matpr.2018.06.381

Kuruvilla, J., Sukumaran, D., Sankar, A., & Joy, S. P. (2016). A review on image processing and image segmentation. *2016 International Conference on Data Mining and Advanced Computing (SAPIENCE)*, 198–203. https://doi.org/10.1109/SAPIENCE.2016.7684170

Lebaal, N., Chamoret, D., Schlegel, D., & Folea, M. (2017). THERMAL MODELLING OF FRICTION STIR PROCESS (FSP) AND IDENTIFICATION PARAMETERS, *32*, 14–20.

Li, B. S., Shang, J. L., Guo, J. J., & Fu, H. Z. (2004). In situ observation of fracture behavior of in situ TiB w / Ti composites, *383*(April), 316–322. https://doi.org/10.1016/j.msea.2004.04.071

Li, B., Shen, Y., Luo, L., & Hu, W. (2013). Materials Science & Engineering A Fabrication of TiC p / Ti – 6Al – 4V surface composite via friction stir processing (FSP): Process optimization , particle dispersion-re fi nement behavior and hardening mechanism, *574*, 75–85. https://doi.org/10.1016/j.msea.2013.03.019

Luo, X. C., Zhang, D. T., Zhang, W. W., Q, C., & Chen, D. L. (2018). Tensile properties of AZ61 magnesium alloy produced by multi-pass friction stir processing: Effect of sample orientation. *Materials Science and Engineering: A*, *725*(January), 398–405. https://doi.org/10.1016/j.msea.2018.04.017

Maja, M. E., Falodun, O. E., Obadele, B. A., Oke, S. R., & Olubambi, P. A. (2018). Nanoindentation studies on TiN nanoceramic reinforced Ti – 6Al – 4V matrix composite. *Ceramics International*, *44*(4), 4419–4425. https://doi.org/10.1016/j.ceramint.2017.12.042

Materials, H., Weinmann, M., Schnitter, C., Stenzel, M., Markho, J., Schulze, C., & Bader, R. (2018). International Journal of Refractory Metals Development of bio-compatible refractory Ti / Nb (/ Ta) alloys for application in patient-speci fi c orthopaedic implants, *75*(September 2017), 126–136. https://doi.org/10.1016/j.ijrmhm.2018.03.018

Mil, D. S. Č. I. Ć., & Stamenkovi, D. S. Ć. (2009). Heat Generation During Friction Stir

Welding Process, *31*(1), 8–14.

Mishra, M. K., Rao, A. G., Balasundar, I., Kashyap, B. P., & Prabhu, N. (2018). On the microstructure evolution in friction stir processed 2507 super duplex stainless steel and its effect on tensile behaviour at ambient and elevated temperatures. *Materials Science and Engineering A*, *719*(January), 82–92. https://doi.org/10.1016/j.msea.2018.02.032

Mishra, R. S., & Ma, Z. Y. (2005). Friction stir welding and processing, *50*, 1–78. https://doi.org/10.1016/j.mser.2005.07.001

Mishra, R. S., Ma, Z. Y., & Charit, I. (2003). Friction stir processing: A novel technique for fabrication of surface composite. *Materials Science and Engineering A*, *341*(1–2), 307–310. https://doi.org/10.1016/S0921-5093(02)00199-5

Nabhani, M., Razavi, R. S., & Barekat, M. (2018). An empirical-statistical model for laser cladding of Ti-6Al-4V powder on Ti-6Al-4V substrate. *Optics and Laser Technology*, *100*, 265–271. https://doi.org/10.1016/j.optlastec.2017.10.015

No Title. (n.d.).

Oladapo, B. I., Zahedi, S. A., Vahidnia, F., & Ikumapayi, O. M. (2018). Three-dimensional finite element analysis of a porcelain crowned tooth Beni-Suef University Three-dimensional fi nite element analysis of a porcelain crowned tooth. *Beni-Suef University Journal of Basic and Applied Sciences*, (April), 0–1. https://doi.org/10.1016/j.bjbas.2018.04.002

Otsu, N. (1979). A Threshold Selection Method from Gray-Level Histograms. *IEEE Transactions on Systems, Man, and Cybernetics*, *9*(1), 62–66.

https://doi.org/10.1109/TSMC.1979.4310076

Otunyo, A. W., Nuaka, B., & Faith, J. C. (2011). COMBINATION OF PALM KERNEL HUSK ASH (PKHA) AND FREE LIME (CaO) AS AN, *30*(1).

Pandey, U., Purohit, R., Agarwal, P., & Kumar Singh, S. (2018). Study of Fabrication, Testing and Characterization of Al/TiC Metal Matrix Composites through different Processing Techniques. *Materials Today: Proceedings*, *5*(2), 4106–4117. https://doi.org/10.1016/j.matpr.2017.11.671

Panwar, N., & Chauhan, A. (2018). Fabrication methods of particulate reinforced Aluminium metal matrix composite-A review. *Materials Today: Proceedings*, *5*(2), 5933–5939. https://doi.org/10.1016/j.matpr.2017.12.194

Patel, N. P., Parlikar, P., Dhari, R. S., Mehta, K., & Pandya, M. (2019). Numerical modelling on cooling assisted friction stir welding of dissimilar Al-Cu joint. *Journal of Manufacturing Processes*, *47*(September), 98–109. https://doi.org/10.1016/j.jmapro.2019.09.020

Rahbar-Kelishami, A., Abdollah-Zadeh, A., Hadavi, M. M., Seraj, R. A., & Gerlich, A. P. (2014). Improvement of wear resistance of sprayed layer on 52100 steel by friction stir processing. *Applied Surface Science*, *316*(1), 501–507. https://doi.org/10.1016/j.apsusc.2014.08.033

Rahsepar, M., & Jarahimoghadam, H. (2016). The influence of multipass friction stir processing on the corrosion behavior and mechanical properties of zircon-reinforced Al metal matrix composites. *Materials Science and Engineering A*, *671*, 214–220. https://doi.org/10.1016/j.msea.2016.05.056

Ramadan, A., Essa, S., Mohamed, M., Ahmed, Z., Ahmed, A. Y., & El-nikhaily, A. E. (2016). An analytical model of heat generation for. *Integrative Medicine Research*, *5*(3), 234–240. https://doi.org/10.1016/j.jmrt.2015.11.009

Ramana, G. V., & Sanke, N. (2019). Materials Today : Proceedings Effect of tool rotational speed and feed rate on similar and dissimilar Friction Stir welded joints of Al 5082 and Al 6061. *Materials Today: Proceedings*, (xxxx), 8–12. https://doi.org/10.1016/j.matpr.2019.08.228

Ramesh, K. N., Pradeep, S., & Pancholi, V. (2012). Multipass friction-stir processing and its effect on mechanical properties of aluminum alloy 5086. *Metallurgical and Materials Transactions A: Physical Metallurgy and Materials Science*, *43*(11), 4311–4319. https://doi.org/10.1007/s11661-012-1232-3

Ramnath, B. V., Elanchezhian, C., Atreya, T. S. A., & Vignesh, V. (2014). ALUMINIUM METAL MATRIX COMPOSITES - A REVIEW.

Rathee, S., Maheshwari, S., Siddiquee, A. N., & Srivastava, M. (2017). Effect of tool plunge depth on reinforcement particles distribution in surface composite fabrication via friction stir processing. *Defence Technology*, *13*(2), 86–91. https://doi.org/10.1016/j.dt.2016.11.003

Rohilla, L., Garg, V., Mallick, S. S., & Setia, G. (2018). An experimental investigation on the effect of particle size into the flowability of fly ash. *Powder Technology*, *330*, 164–173. https://doi.org/10.1016/j.powtec.2018.02.013

Sahoo, B. N., & Panigrahi, S. K. (2018). Effect of in-situ (TiC-TiB2) reinforcement on aging and mechanical behavior of AZ91 magnesium matrix composite. *Materials Characterization*, *139*(January), 221–232. https://doi.org/10.1016/j.matchar.2018.03.002

Saini, N., Dwivedi, D. K., Jain, P. K., & Singh, H. (2015). Surface modification of cast Al-17%Si alloys using friction stir processing. *Procedia Engineering*, *100*(January), 1522–1531. https://doi.org/10.1016/j.proeng.2015.01.524

Salih, O. S., Ou, H., Sun, W., & Mccartney, D. G. (2015). A review of friction stir welding of aluminium matrix composites. *JMADE*, *86*, 61–71. https://doi.org/10.1016/j.matdes.2015.07.071

Sanusi, K. O., Afolabi, I. A. S., & Member, E. M. (2014). Microstructure and Mechanical Properties of Ultra-fine Grained Copper Processed by Equal Channel Angular Pressing Technique, (October).

Sarmadi, H., Kokabi, A. H., & Seyed Reihani, S. M. (2013). Friction and wear performance of copper-graphite surface composites fabricated by friction stir processing (FSP). *Wear*, *304*(1–2), 1–12. https://doi.org/10.1016/j.wear.2013.04.023

Sharma, A., & Das, S. (2009). Study of age hardening behavior of Al – 4 . 5wt % Cu / zircon sand composite in different quenching media – A comparative study Study of age hardening behavior of Al – 4 . 5 wt % Cu / zircon sand composite in different quenching media – A comparative stud. *Materials and Design*, *30*(9), 3900–3903. https://doi.org/10.1016/j.matdes.2009.03.022

Shyam Kumar, C. N., Bauri, R., & Yadav, D. (2016). Wear properties of 5083 Al-W surface composite fabricated by friction stir processing. *Tribology International*, *101*, 284–290. https://doi.org/10.1016/j.triboint.2016.04.033

Singh, I. B., Singh, M., & Das, S. (2015). A comparative corrosion behavior of Mg, AZ31 and AZ91 alloys in 3.5% NaCl solution. *Journal of Magnesium and Alloys*, *3*(2), 142–148. https://doi.org/10.1016/j.jma.2015.02.004

Singh, S. K., Immanuel, R. J., Babu, S., Panigrahi, S. K., & Janaki Ram, G. D. (2016). Influence of multi-pass friction stir processing on wear behaviour and machinability of an Al-Si hypoeutectic A356 alloy. *Journal of Materials Processing Technology*, *236*, 252–262. https://doi.org/10.1016/j.jmatprotec.2016.05.019

Sivakumar, Bose, V., Raguraman, D., & Muruganandam, D. (2014). Review Paper on Friction Stir Welding of various Aluminium Alloys. *Journal of Mechanical and Civil Engineering*, 46–52. https://doi.org/10.17485/ijst/2015/v8i35/86774

Stephens, R. R., Stephenst, R. I., Veitt, A. L., & Albertson, T. P. (1997). Fatigue crack growth of Ti-62222 titanium alloy under constant amplitude and miniTWIST flight spectra at 25 ° C and 175 ° C, *19*(4), 301–308.

Sunil, B. R., Reddy, G. P. K., Patle, H., Dumpala, R., Kishan, V., Devaraju, A., … El-danaf, E. A. (2017). Superplasticity of the rolled and friction stir processed Al-4.5 Mg-0.35Sc-0.15Zr alloy. *Procedia Engineering*, *27*(4), 779–788. https://doi.org/10.1016/S1003-6326(17)60089-X

Suri, A., Sahai, A., Raj, K. H., & Gupta, N. K. (2017). Impact and Tensile testing of Al2024 Alloy Processed by Friction Stir Processing. *Procedia Engineering*, *173*, 679–685. https://doi.org/10.1016/j.proeng.2016.12.145

Swaminathan, S., Oh-ishi, K., Zhilyaev, A. P., Fuller, C. B., London, B., Mahoney, M. W., &

Mcnelley, T. R. (n.d.). Peak Stir Zone Temperatures during Friction Stir Processing.

Tajiri, A., Uematsu, Y., Kakiuchi, T., Tozaki, Y., Suzuki, Y., & Afrinaldi, A. (2015). Effect of friction stir processing conditions on fatigue behavior and texture development in A356-T6 cast aluminum alloy. *International Journal of Fatigue*, *80*, 192–202. https://doi.org/10.1016/j.ijfatigue.2015.06.001

Tang, H. P., Zhao, P., Xiang, C. S., Liu, N., & Jia, L. (2018). *3.3 - Ti-6Al-4V orthopedic implants made by selective electron beam melting*. *Titanium in Medical and Dental Applications*. Elsevier Inc. https://doi.org/10.1016/B978-0-12-812456-7.00011-1

Thangarasu, a., Murugan, N., Dinaharan, I., & Vijay, S. J. (2014). Influence of Traverse Speed on Microstructure and Mechanical Properties of AA6082-TiC Surface Composite Fabricated by Friction Stir Processing. *Procedia Materials Science*, *5*, 2115–2121. https://doi.org/10.1016/j.mspro.2014.07.547

Thangarasu, A., Murugan, N., & Dinaharan, I. (2014). Production and wear characterization of AA6082-TiC surface composites by friction stir processing. *Procedia Engineering*, *97*, 590–597. https://doi.org/10.1016/j.proeng.2014.12.287

Turan, M. E., Sun, Y., Aydin, F., Zengin, H., Turen, Y., & Ahlatci, H. (2018). Effects of carbonaceous reinforcements on microstructure and corrosion properties of magnesium matrix composites. *Materials Chemistry and Physics*, *218*(January), 182–188. https://doi.org/10.1016/j.matchemphys.2018.07.050

Vedabouriswaran, G., & Aravindan, S. (2018). Development and characterization studies on magnesium alloy (RZ 5) surface metal matrix composites through friction stir processing.

Journal of Magnesium and Alloys, *6*(2), 145–163. https://doi.org/10.1016/j.jma.2018.03.001

Veljic, D. M., Park, T., Rakin, M., Radakovic, Z., & Todorovic, P. M. (2013). Heat generation during plunge stage in friction stir welding, (January). https://doi.org/10.2298/TSCI120301205V

Vijayavel, P., & Balasubramanian, V. (2017). Effect of pin profile volume ratio on microstructure and tensile properties of friction stir processed aluminum based metal matrix composites. *Journal of Alloys and Compounds*, *729*, 828–842. https://doi.org/10.1016/j.jallcom.2017.09.117

Vinoth Jebaraj, A., Ajaykumar, L., Deepak, C. R., & Aditya, K. V. V. (2017). Weldability, machinability and surfacing of commercial duplex stainless steel AISI2205 for marine applications – A recent review. *Journal of Advanced Research*, *8*(3), 183–199. https://doi.org/10.1016/j.jare.2017.01.002

Wu, H., Li, Y., Tang, X., Hussain, G., Zhao, H., Li, Q., & Adedotun, A. (2015). Nano-mechanical characterization of plasma surface tungstenized layer by depth-sensing nano-indentation measurement. *Applied Surface Science*, *324*, 160–167. https://doi.org/10.1016/j.apsusc.2014.10.085

Yashpal, Jawalkar, C. S., & Kant, S. (2015). A Review on use of Aluminium Alloys in Aircraft Components. *I-Manager's Journal on Material Science, 3*(3), 33–38. https://doi.org/10.26634/jms.3.3.3673

Yashpal, Sumankant, Jawalkar, C. S., Verma, A. S., & Suri, N. M. (2017). Fabrication of Aluminium Metal Matrix Composites with Particulate Reinforcement: A Review. *Materials*

Today: Proceedings, *4*(2), 2927–2936. https://doi.org/10.1016/j.matpr.2017.02.174

Yaw, S., Cho, H., Das, H., Lee, J., & Hong, S. (2019). Materials Characterization Microstructure and mechanical / electrochemical properties of friction stir butt welded joint of dissimilar aluminum and steel alloys. *Materials Characterization*, *154*(May), 67–79. https://doi.org/10.1016/j.matchar.2019.05.041

Yuvaraj, N., Aravindan, S., & Vipin. (2015). Fabrication of Al5083/B4C surface composite by friction stir processing and its tribological characterization. *Journal of Materials Research and Technology*, *4*(4). https://doi.org/10.1016/j.jmrt.2015.02.006

Yuvaraj, N., Aravindan, S., & Vipin. (2017). Comparison studies on mechanical and wear behavior of fabricated aluminum surface nano composites by fusion and solid state processing. *Surface and Coatings Technology*, *309*, 309–319. https://doi.org/10.1016/j.surfcoat.2016.11.076

Zaitoun, N. M., & Aqel, M. J. (2015). Survey on Image Segmentation Techniques. *Procedia Computer Science*, *65*(Iccmit), 797–806. https://doi.org/10.1016/j.procs.2015.09.027

Zhang, C., Cui, L., Wang, D., Liu, Y., & Li, H. (2018). Effect of microstructures to tensile and impact properties of stir zone on 9%Cr reduced activation ferritic/martensitic steel friction stir welds. *Materials Science and Engineering: A*, *27*(8), 558–563. https://doi.org/10.1016/j.msea.2018.05.043

Zhang, Z., Yang, R., Guo, Y., Chen, G., Lei, Y., Cheng, Y., & Yue, Y. (2017). Materials Science & Engineering A Microstructural evolution and mechanical properties of ZrB 2 / 6061Al nanocomposites processed by multi-pass friction stir processing. *Materials Science &*

Engineering A, *689*(February), 411–418. https://doi.org/10.1016/j.msea.2017.02.083

Zhu, S., Xia, X., Zhang, Q., & Belloulata, K. (2007). An Image Segmentation Algorithm in Image Processing Based on Threshold Segmentation. *2007 Third International IEEE Conference on Signal-Image Technologies and Internet-Based System*, 673–678. https://doi.org/10.1109/SITIS.2007.116

APPENDIX A

Clamping of the Aluminum sheet for FSP

APPENDIX B

Vickers Microhardness Tester

APPENDIX C

Polishing Machine

APPENDIX D

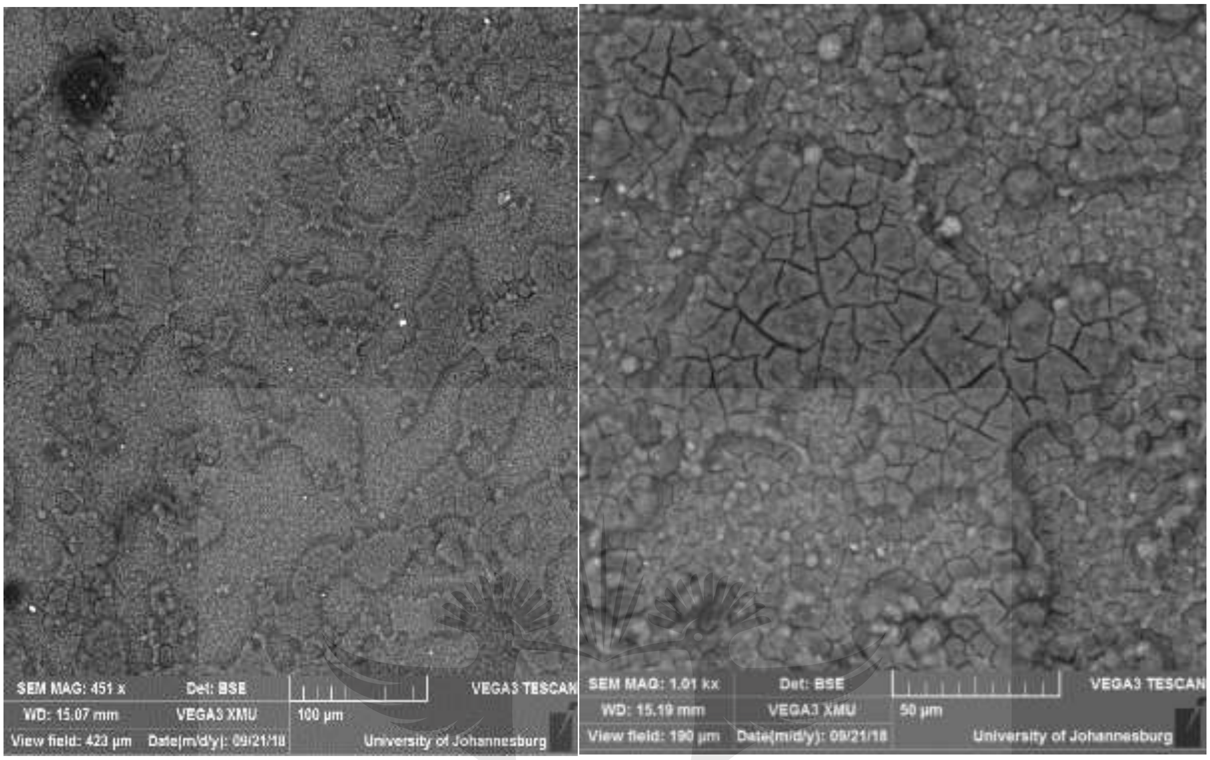

SEM Images of Y1 composite(1-pass/600rpm/Square tool geometry) with low and high magnification

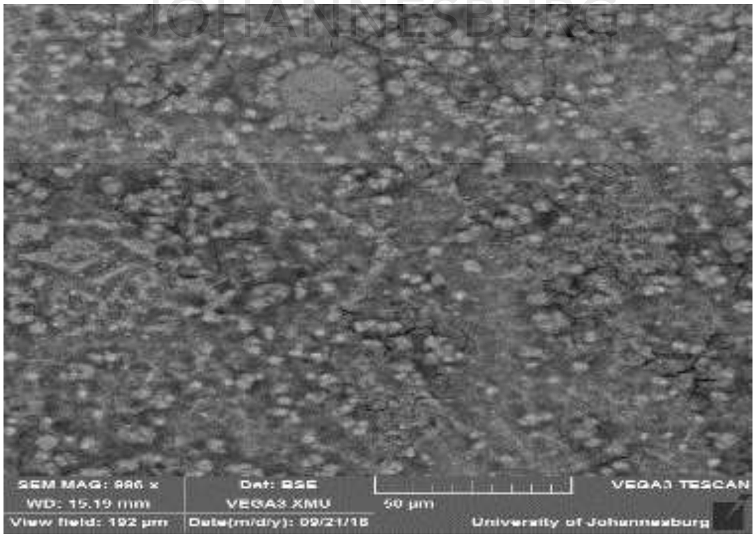

SEM images of Y2(2-pass/1200rpm/Square tool geometry) showing unrefined grain structure

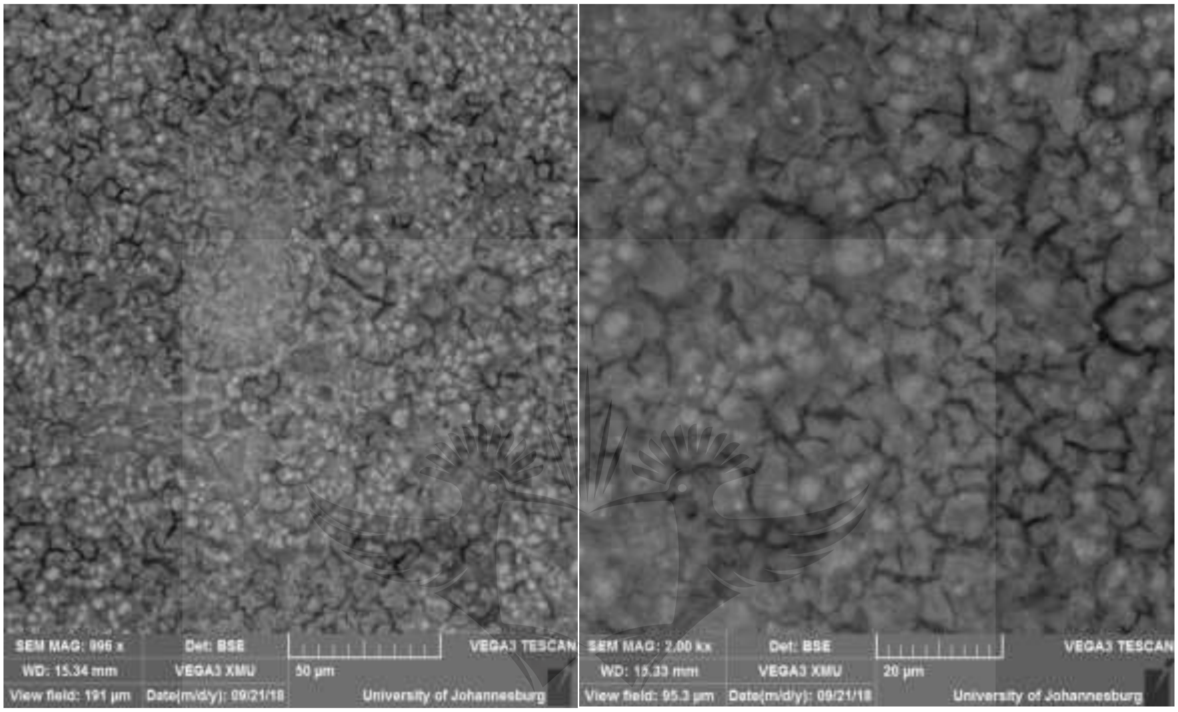

SEM images of B3(3-pass/1200rpm/Threaded taper tool) showing refined grain structure) with low and high magnification

APPENDIX E

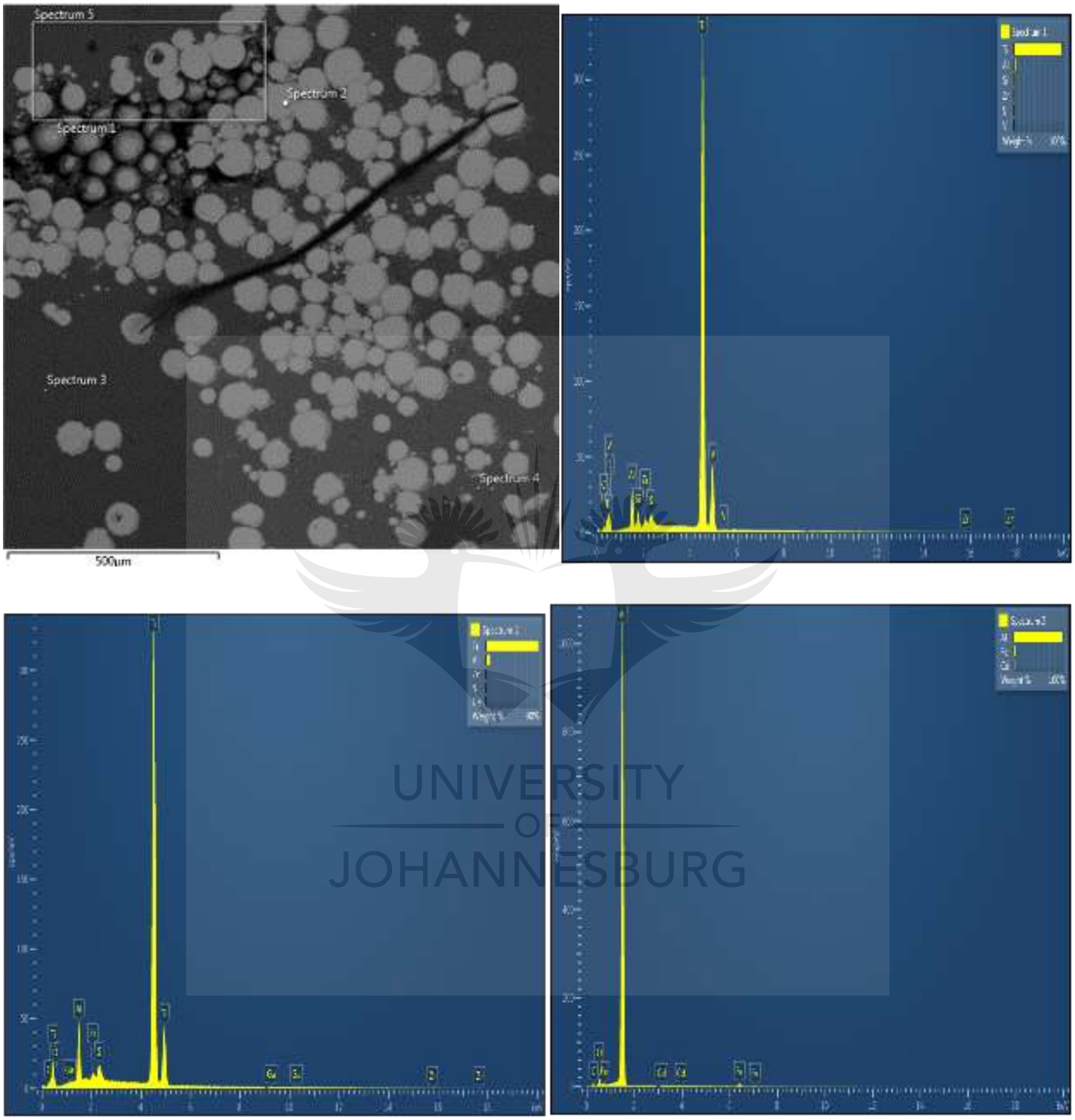
Spectrum 5
Spectrum 2
Spectrum 1
Spectrum 3
Spectrum 4
500µm

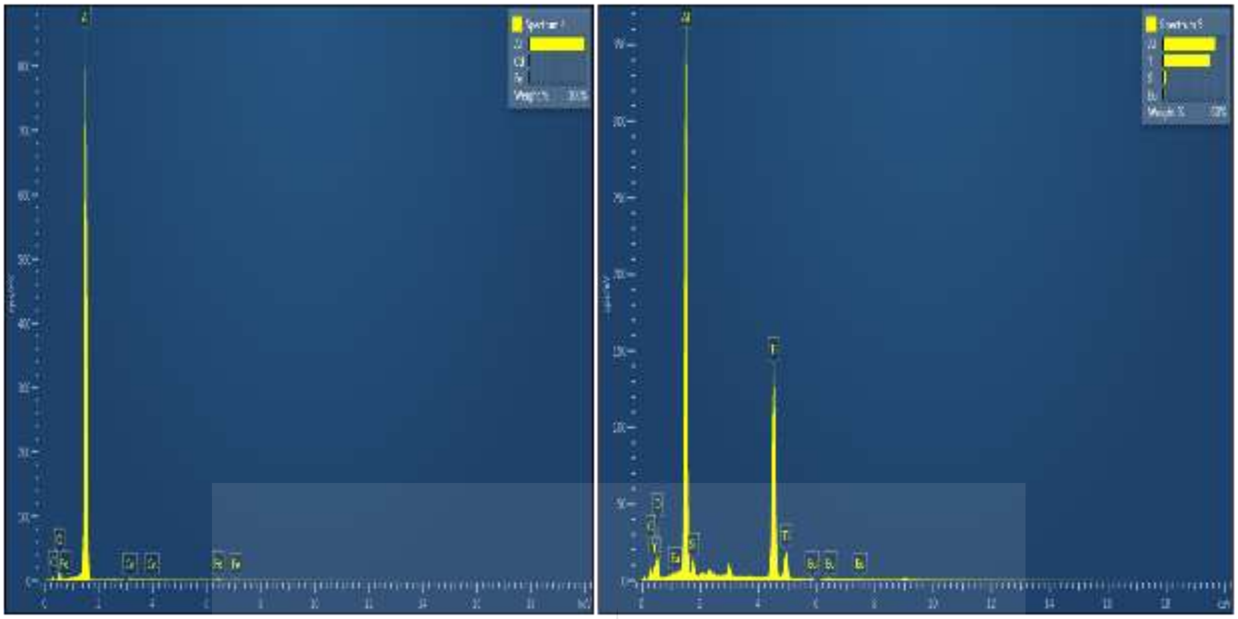

EDS analysis of the A1(1-pass/600rpm/Threaded taper tool geometry) composite showing clustering of Ti particle

APPENDIX F

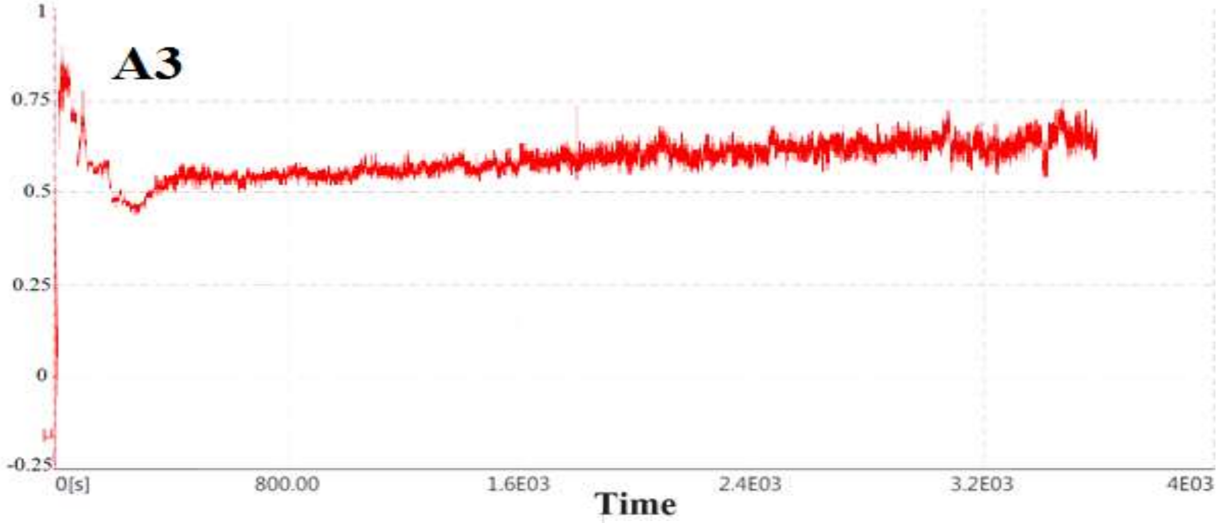
A3
1
0.75
0.5
0.25
0
-0.25
0[s]
800.00
1.6E03
2.4E03
3.2E03
4E03
Time

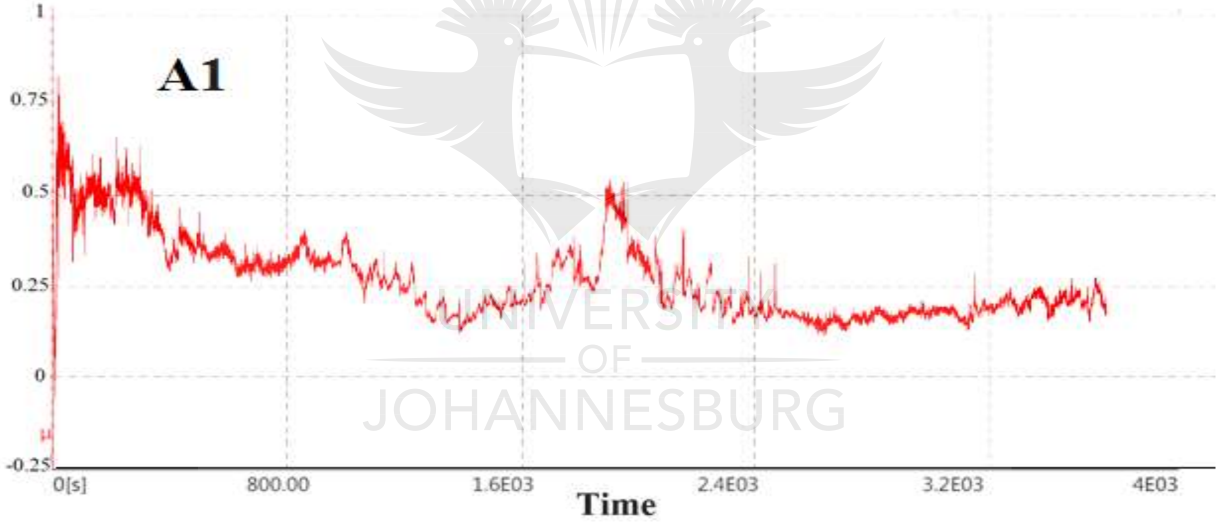
A1
1
0.75
0.5
0.25
0
-0.25
0[s]
800.00
1.6E03
2.4E03
3.2E03
4E03
Time

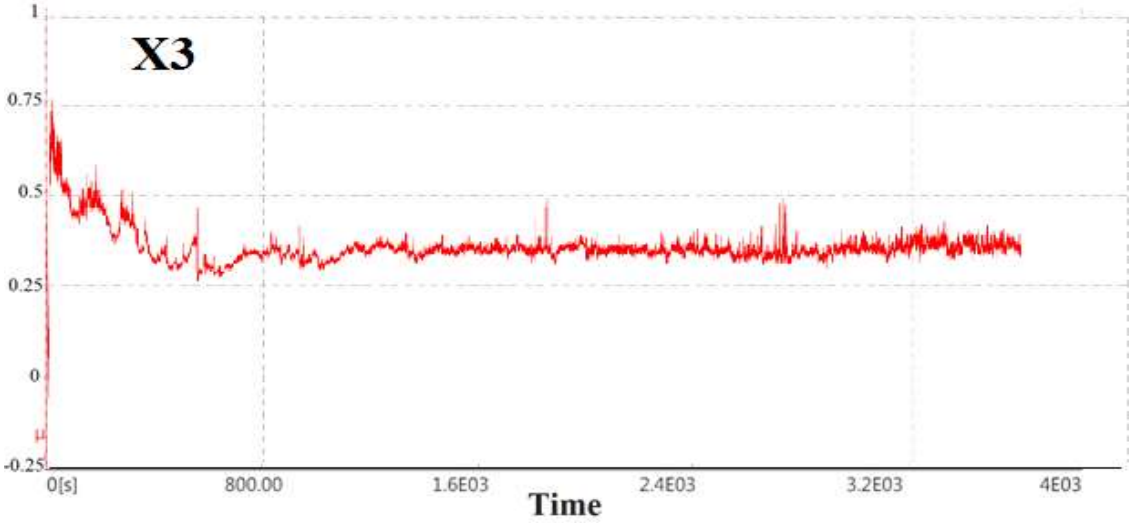

Friction behavior of various composites

APPENDIX G

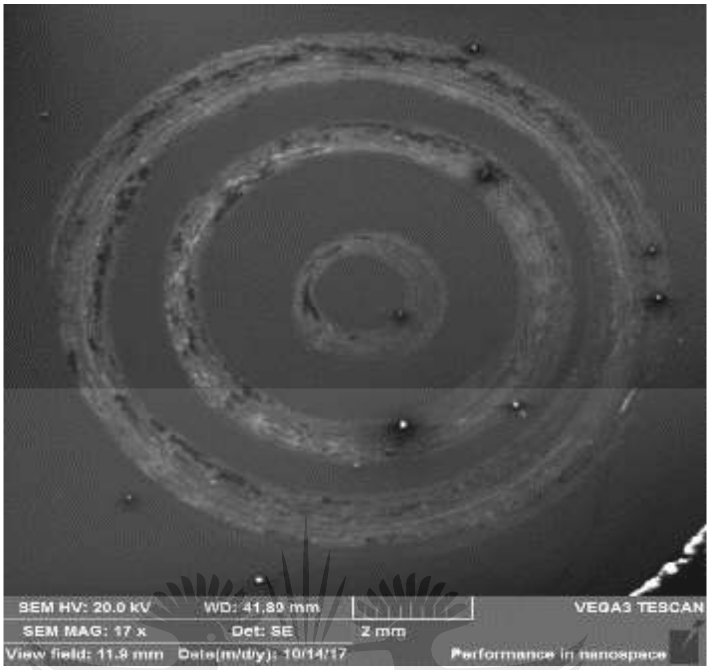

SEM images of the worn surface of the base material(1100 Al)

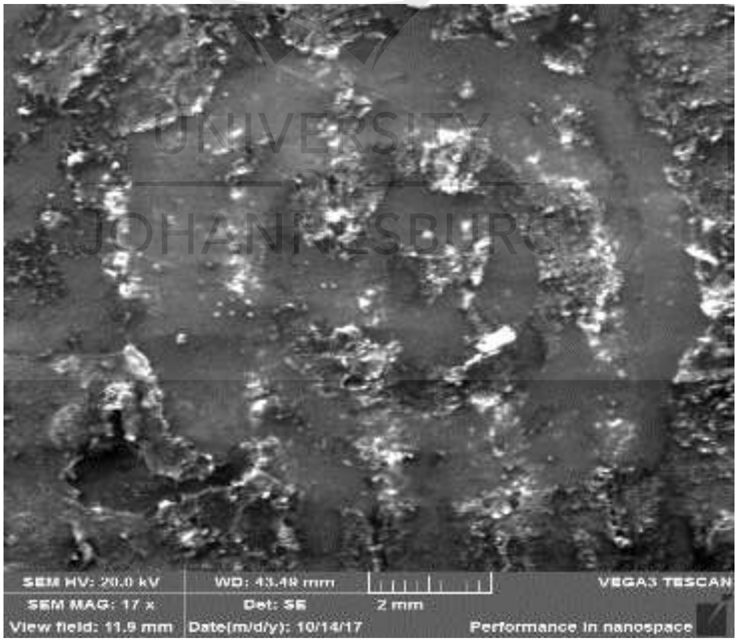

SEM images of the worn surface of B2(2-pass/1200rpm/Threaded taper tool)

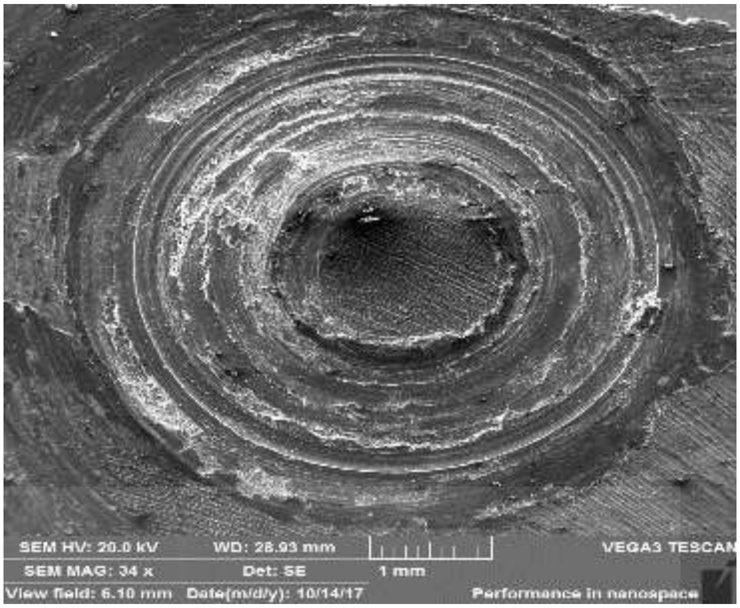

SEM images of Y3 (3-pass/1200rpm/ Square tool geometry)

APPENDIX H

(a)

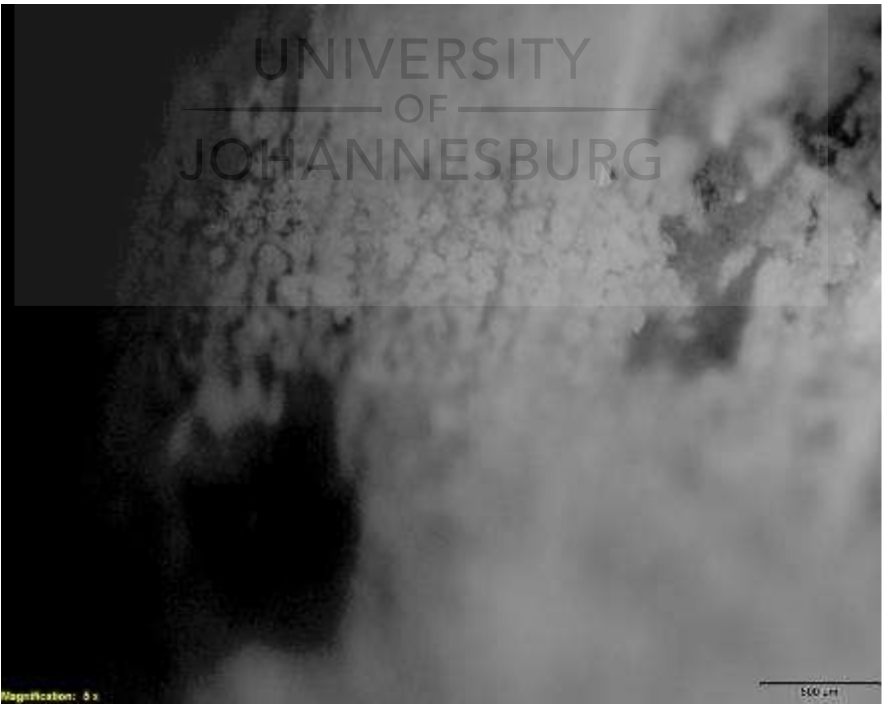

(b)

(c)

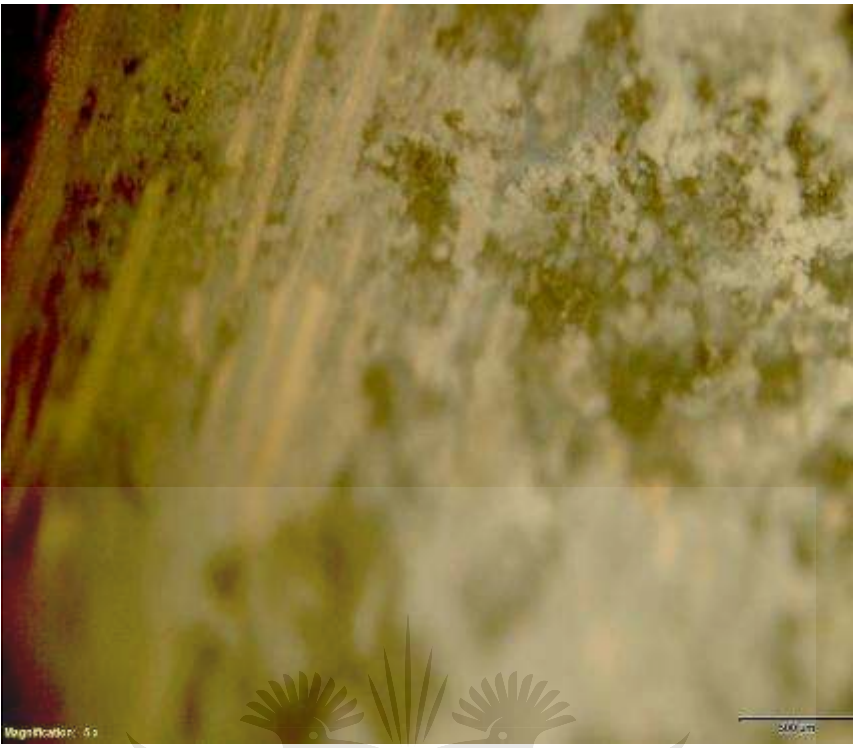

Optical Microscope of the corroded surfaces of composites, (a) A1, (b) Y2 and (c) B3)